~

INSIGHTS ON THE MICROBIAL CARBON PUMP IN THE GLOBAL OCEAN WITH SPECTROSCOPIC TECHNIQUES

Teresa Serrano Catalá

Academic advisors:

Isabel Reche Cañabate
Xosé Antón Álvarez Salgado

Granada, September 2015

Editorial: Universidad de Granada. Tesis Doctorales
Autora: María Teresa Serrano Catala
ISBN: 978-84-9125-267-2
URI: http://hdl.handle.net/10481/41126

Tesis presentada por **Teresa Serrano Catalá** para optar al grado de Doctora con Mención Internacional en el Programa de Doctorado de Biología Fundamental y de Sistemas por la Universidad de Granada.

Fdo. Teresa Serrano Catalá

Tesis dirigida por los Doctores **Isabel Reche Cañabate** y **Xosé Antón Álvarez Salgado**

Fdo. Isabel Reche

Fdo. Xosé Antón Álvarez-Salgado

La doctoranda Teresa Serrano Catalá y los directores de la tesis Isabel Reche Cañabate y Xosé Antón Álvarez Salgado garantizamos, al firmar esta tesis doctoral, que el trabajo ha sido realizado por el doctorando bajo la dirección de los directores de la tesis y hasta donde nuestro conocimiento alcanza, en la realización del trabajo, se han respetado los derechos de otros autores a ser citados, cuando se han utilizado sus resultados o publicaciones.

Granada a de 2015

Doctorando

Fdo. Teresa Serrano Catalá

Directores de la Tesis

Fdo. Isabel Reche Cañabate

Fdo. Xosé Antón Álvarez Salgado

In one drop of water are found the secrets of all endless oceans.
Kahlil Gibram

~

This PhD Thesis has been carried out at the Departamento de Ecología and Instituto del Agua of the University of Granada and the Department of Oceanography of the Marine Research Institute (Spanish Research Council, CSIC). The research was funded by the grants "Expedición de circunnavegación Malaspina 2010: cambio global y exploración, MALASPINA 2010" (Spanish Ministry of Science and Innovation, grant No CSD2008–00077, to C.M. Duarte) and "Zonas de mezcla y frentes en el océano oscuro como "hot–spots" de biodiversidad y flujos biogeoquímicos a través del Mar Mediterráneo y el Atlántico Nordeste–II, HOT–MIX" (Spanish Ministry of Science and Innovation, CTM2011–30010–C02–02, to X.A. Álvarez-Salgado). T.S. Catalá was supported by a FPU grant of the Spanish Ministry of Education, Culture and Sports (No AP2009-2138) and a research contract funded by the project "Reactividad fotoquímica y microbiológica de la materia orgánica disuelta en relación con su composición química y estructura molecular, FOMEM" (Spanish Research Council, CSIC–PIE, No 201030E130, to X.A. Álvarez-Salgado). Research stays at the National Institute for Aquatic Resources of the Technical University of Demark, Charllotelund (Denmark), hosted by Dr. C.A. Stedmon and funded by the Ministry of Education, Culture and Sports (No AP2009-2138), and at the Earth Research Institute, University of California, Santa Barbara (USA), hosted by Dr. N.B. Nelson, were funded by the University of Granada and CEI BioTic Granada.

Ackowledgments

I would like to thank my supervisors Pepe and Isa for their dedication, enthusiasm, simplicity, honesty and transparency at all times. Thanks for letting me participate in the Malaspina Expedition, which not only encouraged my scientific skills; but also let me mature as a human being; thanks to the unique experiences and the variety of personal encounters.

To the Granada research team. Gema· thanks for your permanent smile every time I passed you in the corridor, your kindness, strength and for providing me with accommodation in your Albaicín house; thanks to Natalie for introducing me to the absorbance and fluorescence spectroscopic techniques as well as for your warm personality; to Nacho, for his aptitude to help if I asked for it; to Mohammad for his hospitality even in the institute, he always provided us with persian tea and sweets.

To the Organic Geochemistry Laboratory team in the Instituto de Investigaciones Mariñas (IIM, Vigo). To María, for her innate skill of helping others and making them feel at home in a new place, for her constant smile and positivity even when dealing with 'EPI' and 'BLAS'. To Vanessa, Mar and Alba for their help in everything I needed during my several visits to the IIM. Besides, I thank Bieito for his help with Matlab, for the several trips to excellent places such as 'El Valle del Sil' or 'Cabo Home' and for showing me very local places in Vigo.

To the Palmas de Gran Canaria research group. Javier, thanks for your courtesy and your authenticity in many conversations. Nauzet, thanks for your help in the lab, for resolving all the queries that I had, and for the back and forth daily trips to the university of Las Palmas during my stay. Mine, thanks for treating me as a beloved family member and for showing me the local spots of Arigana with a lot of enthusiasm.

To Colin Stedmon and Norm Nelson for their knowledge sharing, for their kindness and for facilitating me by all kinds of means throughout my stay in both Copenhagen and Santa Barbara. To Linda Jørgensen, for her sweetness, help at any time and introducing me to the Danish traditional cuisine and culture. To Kelsey for her sweetness and introducing me to new people and places in Santa Barbara.

To Resi for helping me to design the front page of this thesis.

To Fidel Echevarría for offering his assistance at any time and for getting me out of some delicate situations I experienced in Cádiz University.

To María Calleja ('little bug' to me), I appreciate all the gratifying times we lived together in the 'cottage', I have very good memories from this time. For example, I remember the continuous test runnings and conversations in the kitchen as well as enjoying the meal after cooking it, or our first chilled days in the house when trying to turn on the fire for the first time. Since I met you, you have always offered your help in both work and personal matters without expecting anything in return. Thanks for your company during this phase of my life!

To Pepón, for demonstrating to me that there is still sensitive men in the world, for introducing me to the musical world as well as the very special lessons and moments shared in our hometown.

To Miguel, for turning upside down some unnecessary beliefs that I had and for helping me to get to know better what love is.

To Cintia because, apart from the exceptional friendship that is shared, she is always available for whatever the issue that concerns me. Thanks for your patience with matlab, and for maintaining our friendship after the police persecution in the Sequoias National Park, the curt turn in a Swedish road when driving at 70 km/h or the hedge overpassing in the shopping mall somewhere in Sweden.

To Ana and Peco for their hospitality during the multiple occasions I have visited Granada. I felt like a real relative.

To Cristina, my sister, and my parents, as they daily inspire me and guide me through the paths of life. Thanks for your company, support and love. Although there is neither words nor material facts that compensate my love towards them, I dedicate this PhD thesis to them.

Contents

General Abstract 16
Resumen General 18
Glossary of abbreviations 20
General Introduction 23
1. Marine dissolved organic matter: one of the largest reduced carbon pools on Earth 23
2. Dissolved organic matter bioreactivity 24
3. Dissolved organic matter distribution in the oceans 26
4. DOM sources, sinks and accumulation 28
5. Ocean carbon pumps 31
6. The forth carbon pump: the microbial carbon pump (MCP) 33
7. Spectroscopic techniques to DOM characterization as tools in the study of the microbial carbon pump 34
8. The Malaspina 2010 circunnavigation 41
9. Goals of this PhD thesis 42
10. Structure of this PhD thesis 42
Chapter 1. Water mass age and ageing driving chromophoric dissolved organic matter in the dark global ocean 45
Abstract 45
Introduction 45
Materials and Methods 47
Results 54
Discussion 64
Conclusions 69
Chapter 2. Chromophoric signatures of long-lived microbial by-products in the dark ocean 71
Abstract 71
Introduction 71
Materials and methods 72
Results and Discussion 77
Conclusions 83
Chapter 3. Turnover time of fluorescent dissolved organic matter in the dark global ocean 85
Abstract 85
Introduction 85
Methods 86
Results 91
Discussion 96
Chapter 4. Drivers of fluorescent dissolved organic matter in the epipelagic global ocean 100
Abstract 100
Introduction 100

Materials and Methods 102
Results 108
Discussion 120
Conclusions 126
General Discussion 128
1. Why it is so difficult to produce a standardized global database of FDOM measurements? 128
2. How recalcitrant the CDOM and FDOM components are? 130
3. Moving a step ahead beyond absorption coefficients and slopes: picking individual chromophores in the dark ocean 131
4. How much carbon holds the fluorescence components? 133
5. Are changes in CDOM and FDOM properties coupled over the global thermohaline circulation? 134
6. Does FDOM and CDOM properties support the size-reactivity continuum model? 136
General Conclusions 137
Conclusiones Generales 139
Appendixes 142
Appendix I. Methodology in sample collection 142
Appendix II. Description of the water masses intercepted during the Malaspina circumnavigation ... 150
Appendix III. Chromophores Toolbox Tutorial 154
Appendix IV. Conversion of Raman units into carbon units 162
Appendix V. Average profiles of the environmental parameters that contribute on FDOM variability in the surface ocean. 163
References 173

General Abstract

The transformation of biologically labile organic matter into refractory compounds by prokaryotic activity has been termed the 'microbial carbon pump' (MCP) and may constitute an effective mechanism to store reduced carbon in the dark ocean. Understanding its generation and its role in carbon sequestration is crucial to assess its relevance in the context of the global carbon cycle. The main aim of this PhD thesis is to test the significance of the chromophoric (CDOM) and fluorescent (FDOM) fractions of dissolved organic matter (DOM) as tracers for the microbial production of recalcitrant DOM in the global ocean. All its content is framed in the Malaspina 2010 circumnavigation, which allowed us to produce the first global inventory of the optical properties of DOM in both the surface ocean (<200 m), gathered by Longhurst's biogeographic provinces, and the dark ocean (>200 m) by the main water masses.

In the dark ocean, ideal age and ageing (apparent oxygen utilization) of the main water masses were tracked along the global thermohaline circulation, allowing the estimation of net production/consumption rates of CDOM and FDOM and their respective turnover times. We found that CDOM was generated *in situ* by microbial metabolism (at a global rate of $3.3 \pm 0.5 \times 10^{-5}$ m^{-1} yr^{-1}), with a turnover time of ca. 625 years and was accumulated in the dark ocean due to its recalcitrant nature, with an increase in the degree of aromaticity and molecular weight along the thermohaline circulation. We identified two distinct chromophores. One was centred at 302 nm (UV chromophore) and the other one at 415 nm (Visible chromophore). The UV chromophore was attributed partially to nitrate and likely to the antioxidant gadusol and presented a turnover time of ca. 345 years. The Visible chromophore was related to the respiratory enzyme cytochrome c and presented a turnover time of ca. 356 years.

The analysis of the fluorescent properties of DOM in both the surface (< 200 m) and dark ocean (> 200 m) allowed us to identify four ubiquitous fluorophores. Two fluorophores were humic-like (C1, C2) components and the other two were amino acid-like (tryptophan-like C3, tyrosine-like C4) components. The robustness in the level of explanation for humic-like and amino acid-like components by biogeochemical variables was much higher for the humic-like components than for the amino acid-like components both in the surface and the dark ocean (~80% vs ~30%). The fluorescent humic-like material was explained by water ageing and showed positive power functions both in the surface and in the dark ocean. In the dark ocean, C1 showed a higher production rate than C2, with a net production rate of $2.3 \pm 0.2 \times 10^{-5}$ and $1.2 \pm 0.1 \times 10^{-5}$ RU yr^{-1} and turnover times of 530 and 740 years, respectively. However, in the surface ocean both rates were similar. In the dark ocean C1 and C2 showed higher conversion efficiencies per unit of utilized oxygen than in the surface ocean, likely due to photobleaching. In the dark ocean, tyrosine-like C4 presented an inverse power relationship with the apparent oxygen utilization, decreasing at a rate of -1.1 ± 10^{-5} RU yr^{-1}. On the contrary, the tryptophan-like component C3 did not show a pattern with ageing. In the surface ocean, the amino acid-like components were apparently more affected by physical processes, although the positive relationship of C4 with Chl *a* also implies a microbial influence on this component.

The *in situ* production of the DOM fractions as by-products of microbial metabolism identified as water masses turned older and the long turnover times of the humic-like components indicated the relevant role of the MCP in the carbon sequestration in the dark ocean. Thus, the initial hypothesis of this PhD thesis that was: "are the chromophoric and fluorescent fractions of DOM key components of the recalcitrant DOM pool?" has been verified. Similarly, the fact that chromophores and fluorophores can be used as tracers of the water mass mixing and biogeochemical processes operating at centennial time scales will bring new insights into the ocean carbon storage.

Resumen General

La transformación de materia orgánica lábil en recalcitrante a consecuencia del metabolismo de los procariotas se ha denominado "bomba microbiana de carbono" y puede constituir un mecanismo efectivo de almacenamiento de carbono reducido en el interior del océano. Comprender la generación de materia orgánica disuelta (MOD) recalcitrante y el papel que esta juega en el almacenamiento de carbono en los océanos es crucial para cuantificar su relevancia en el contexto del ciclo global del carbono. En este contexto, el principal objetivo de esta Tesis Doctoral es comprobar la validez de las fracciones cromófora (CMOD) y fluorescente (FMOD) de la MOD como trazadores de la producción microbiana de MOD recalcitrante en el océano global. El trabajo se enmarca en la expedición de circunnavegación Malaspina 2010, que ha hecho posible producir el primer inventario global de propiedades ópticas de la MOD tanto en la capa superficial (< 200 m), organizado por provincias biogeógraficas, como en el interior del océano (> 200 m), organizado por masas de agua.

En el océano profundo, se trazó la edad y el envejecimiento (utilización aparente de oxígeno) de las principales masas de agua a lo largo de la circulación termohalina, posibilitando la estimación de tasas netas de producción/consumo de CMOD y FMOD y sus respectivos tiempos de renovación. Así, se encontró que la CMOD se produce *in situ* a consecuencia del metabolismo microbiano (a una tasa neta global de $3.3 \pm 0.5 \times 10^{-5}$ m^{-1} a^{-1}), presenta un tiempo de renovación de aprox. 625 años y se acumula en el interior del océano debido a su naturaleza recalcitrante, mostrando un incremento de la aromaticidad y el peso molecular medio con el discurrir de la circulación termohalina. Además, se identificaron dos cromóforos, uno centrado a 302 nm (cromóforo UV) y el otro a 415 nm (cromóforo Visible). El cromóforo UV se atribuyó parcialmente a nitrato y probablemente también al antioxidante gadusol y presentó un tiempo de renovación de aprox. 345 años. El cromóforo visible se relaciona con el enzima respiratorio citocromo y presenta un tiempo de renovación de aprox. 360 años.

Tanto en la capa superficial como en el interior del océano se han identificado cuatro fluoróforos ubicuos, dos de ellos de naturaleza húmica (C1, C2) y los otros dos proteínica (tipo triptófano, C3, y tipo tirosina, C4). Si bien la distribución global de estos fluoróforos puede explicarse en base a ciertas variables ambientales, la robustez estadística de dicha explicación fue mucho mayor para los de naturaleza húmica que para los de naturaleza proteínica tanto en la capa superficial como en el océano profundo (aprox. 80% vs aprox. 30%). La distribución del material de naturaleza húmica se explicó en función del envejecimiento del agua y mostró una correlación potencial positiva con la utilización aparente de oxígeno tanto en la capa superficial como en el interior del océano. En el interior del océano, C1 mostró una tasa de producción neta mayor que C2: $2.3 \pm 0.2 \times 10^{-5}$ frente a $1.2 \pm 0.1 \times 10^{-5}$ RU a^{-1}, y unos tiempos de renovación 530 y 740 años, respectivamente. Sin embargo, en la capa superficial ambas tasas fueron similares. En el interior del océano, las eficiencia de conversión de C1 y C2 por unidad de oxigeno utilizada fueron mayores que en la capa superficial, probablemente debido a la fotodegradación. En el interior del océano, el fluoróforo tipo tirosina (C4) presentó una relación potencial inversa con la utilización aparente de oxígeno que permitió calcular una tasa neta de consumo de -1.1 ± 10^{-5} RU a^{-1} y un tiempo de renovación de aproximadamente 460

años. Por el contrario, el fluoróforo tiempo triptófano (C3) no mostró relación alguna con el envejecimiento de las masas de agua. En la capa superficial, los fluoroforos proteínicos se vieron mas afectados por procesos físicos, aunque la relación positiva entre C4 y clorofila también implica una influencia de la actividad microbiana sobre la distribución de este componente.

La producción *in situ* de estas fracciones de la MOD como subproductos del metabolismo microbiano, su acumulación con el envejecimiento de las masas de agua, y los prolongados tiempos de renovación de los componentes húmicos indican el papel relevante que la bomba microbiana de carbono juega en el secuestro de carbono en el interior del océano. Por tanto, la hipótesis inicial de esta Tesis, Son las fracciones cromófora y fluorescente de la MOD componentes clave del reservorio de MOD recalcitrante?, ha sido verificada. Igualmente, el hecho de estos cromóforos y fluoróforos puedan usarse como trazadores de la mezcla de masas de agua y los procesos biogeoquímicos que ocurren a escala centenaria abre nuevas perspectivas acerca del almacenamiento de carbono en los océanos.

Glossary of abbreviations

Organic matter

AOU	Apparent oxygen utilization
a_{325}	Absorption coefficient at 325nm
$a_{Ch\text{-}UV}$	Absorption coefficient of the UV chromophore at 302 nm
$a_{Ch\text{-}VIS}$	Absorption coefficient of the VIS chromophore at 415 nm
CcO	Citochrome, the respiratory enzyme cytochrome c oxidase.
CDOM	Chromophoric dissolved organic matter
DBC	Dissolved black carbon
DOM	Dissolved organic matter
E_a	Activation energy
EEM	Excitation Emission Matrix
FDOM	Fluorescent dissolved organic matter
Φ_{340}	Fluorescence quantum yield at 340 nm
LDOM	Labile dissolved organic matter
NP	Net production
OUR	Oxygen utilization rate
Peak A/C	Humic-like FDOM peak at Ex/Em <270·370/470 nm
Peak M	Humic-like FDOM peak at Ex/Em 320/400 nm
Peak T	Tryptophan-like FDOM peak at Ex/Em 290/340 nm
Peak B	Tyrosine-like FDOM peak at Ex/Em 270/310 nm
POM	Particulate organic matter
Q_{10}	Temperature coefficient Q_{10}
RDOM	Refractory dissolved organic matter
SLDOM	Semi-labile dissolved organic matter
$S_{275\text{-}295}$	Spectral slope over the wavelength range 275–295 nm
S_R	Ratio of spectral slopes over the ranges 275–295 nm and 350–400 nm
τ	Ideal age

Water masses

EDW	Eighteen Degrees Water
$ENACW_{12}$	Eastern North Atlantic Central Water (12°C)
$ENACW_{15}$	Eastern North Atlantic Central Water (15°C)
13EqAtl	Equatorial Atlantic Central Water (13°C)
$SACW_{12}$	South Atlantic Central Water (12°C)
$SACW_{18}$	South Atlantic Central Water (18°C)
$STMW_I$	Indian Subtropical Mode Water
ICW_{13}	Indian Central Water (13°C)
$STMW_{SP}$	South Pacific Subtropical Mode Water
$SPCW_{20}$	South Pacific Central Water (20°C)
13EqPac	Equatorial Pacific Central Water (13°C)
CMW_{NP}	North Pacific Central Mode Water (12°C)
$STMW_{NP}$	North Pacific Subtropical Mode Water (16°C)
MW	Mediterranean Water
SAMW	Sub-Antarctic Mode Water
$AAIW_{3.1}$	Antarctic Intermediate Water (3.1°C)
$AAIW_{5.0}$	Antarctic Intermediate Water (5.0°C)
NPIW	North Pacific Intermediate Water
$CDW_{1.6}$	Circumpolar Deep Water
$NADW_{2.0}$	North Atlantic Deep Water (2°C)
$NADW_{4.6}$	North Atlantic Deep Water (4.6°C)
AABW	Antarctic Bottom Water

Biogeographical provinces

NASE	North Atlantic Subtropical Gyral
NATR	North Atlantic Tropical Gyral
WTRA	Western Tropical Atlantic
SATL	South Atlantic Gyral
BENG	Bengela Current Coastal
EARF	East Africa Coastal
ISSG	Indian South Subtropical Gyre
SSTC	South Subtropical Convergence
AUSE	East Australian Coastal
SPSG	South Pacific Subtropical Gyre
PEQD	Pacific Equatorial Divergence
NPTG	North Pacific Tropical Gyre
PNEC	North Pacific Equatorial Countercurrent
CARB	Caribbean

General Introduction

1. Marine dissolved organic matter: one of the largest reduced carbon pools on Earth

Natural organic matter comprises organic compounds that were initially formed by life but may have undergone multiple alterations and degradation processes [*Lechtenfeld*, 2012]. The most important carbon source for the synthesis of organic matter is carbon dioxide (CO_2) and the energy for the breakage of the C–O bond is mainly supplied by sunlight, specifically by the photosynthetically active radiation (PAR). Since the carbon atoms in organic matter have an oxidation state lower than in CO_2, it is often referred as "reduced carbon".

Organic matter in marine environments occupies a molecular size continuum from tenths of angstroms to meters [*Verdugo*, 2012; *Verdugo et al.*, 2004; *Azam et al.*, 1993]. To facilitate its classification, two pools of marine organic matter have been operationally distinguished (Fig. I.1): dissolved organic matter (DOM), referred to the fraction that passes through 0.2–1.0 µm pore size filters and is not prone to sink [*Hedges*, 2002], and particulate organic matter (POM), the fraction over 1.0 µm that tends to aggregate and sink.

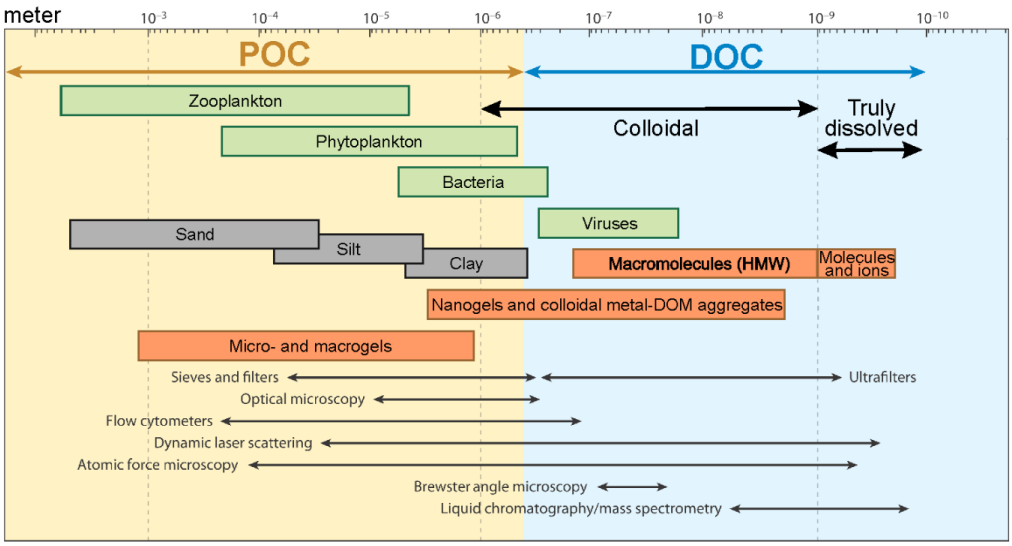

Fig. I.1. Size ranges and scales in meters for different kinds of matter found in seawater. Living matter (green boxes), inorganic material (grey) and organic compounds (orange) all overlap in the nano- to millimetre size range. Operationally defined size classifications separate the continua of sizes into discrete fractions, where the colloidal and " truly" dissolved substances and smallest living cells are subsumed as the dissolved organic carbon (DOC) fraction. Common methods to separate or analyse the size fractions are shown in the lower part of the figure. POC: Particulate organic carbon. *Taken from *Verdugo* [2012] as modified by *Lechtenfeld* [2012].

Given the heterogeneous composition of DOM, the low concentration of specific components (typically less than picomolar to low micromolar) and the ~0.7 M ionic strength inorganic salt matrix, the task of resolving the chemical composition of DOM after isolation and concentration by

ultrafiltration, solid phase extraction or reverse osmosis combined with electrodialysis still remains arduous because the molecules are polyfunctional, heterogeneous, polyelectrolytic and polydisperse in molecular weight [*Mopper et al.*, 2007]. Although less than 10% of the marine DOM has been identified at the molecular level [*Repeta*, 2015; *Dittmar and Paeng*, 2009; *Kaiser and Benner*, 2009; *Hertkorn et al.*, 2006], recent progresses in analytical chemistry have allowed the molecular characterization of DOM in unprecedented detail [e.g. *Hansman et al., in press*; *Medeiros et al.*, 2015; *Osterholz et al.*, 2015; *Chen et al.*, 2014; *Lechtenfeld et al.*, 2014] (for more details see Section 7 of this introduction).

Much effort has been put into understanding the cycling of carbon between the atmospheric, oceanic, and terrestrial pools [*Sarmiento and Gruber*, 2006]. Interconnection of these pools in the ocean occurs predominantly in the ocean surface, where CO_2 rapidly exchanges between atmosphere and marine organic matter, but also at the water-sediment interface, where part of the organic matter is stored for geological times. In this context, oceanic DOM is a collection of reduced carbon compounds in an amount close to the reservoir of atmospheric CO_2 (828 Pg C, 1 Pg = 10^{15} g, *Joos et al.,* 2013*; Prather et al.,* 2012) or the living biomass on land and in freshwater (600 – 1000 Pg C, *Falkowski et al*., 2000). At 662 ± 32 Pg C, DOM exceeds the inventory of organic particles in the oceans by 200–fold [*Hansell et al.*, 2009; *Hansell and Carlson,* 1998]. This pool plays an important role in the global carbon cycle since (1) it supports life in the oceans as it serves as substrate for microbial growth and/or nutrients recycling after microbial and photochemical processes [*Kujawinski*, 2011]; (2) it has an influence on atmospheric chemistry as it exchanges CO_2, carbon monoxide and dimethyl sulphide among other biogases; and (3) its chromophoric fraction controls the intensity and spectral quality of light through the water column [*Nelson and Siegel*, 2013; *Blough and Del Vecchio*, 2002] . The imbalance between the biological processes of carbon fixation and remineralization has controlled carbon sequestration and shaped the composition of the atmosphere throughout the history of life on Earth [*Lechtendeld et al.*, 2015]. The major reservoirs of organic matter are in a continuous interaction and little exchanges among them can have considerable impacts on the Earth's climate. In fact, modelling studies suggest that DOM storage or remineralization have promoted fluctuations in the global CO_2 atmospheric content that have had subsequently impacts on the Earth's climate [*Sexton et al.*, 2011]. For instance, the net mineralization of just 1% of the marine DOM pool would generate an amount of CO_2 close to the 7.8 ± 0.6 Pg C produced annually by fossil fuel combustion [*IPCC, 2013, Section 6.3.1*]. In the past couple of decades, rapid progress has been made in elucidating the roles that basic physical (e.g. ocean circulation or gas exchange) and inorganic geochemical processes (e.g. the equilibrium of the carbonate system) play in regulating the uptake of anthropogenic CO_2 from the atmosphere [*Ridgwell and Arndt*, 2015]. In contrast, the role and response of the "biological carbon pump", and particularly the "microbial carbon pump" (MPC), in the cycling of carbon is much less well understood.

2. Dissolved organic matter bioreactivity

The bulk DOM pool spans a wide range of biological reactivities, ranging from materials that

turn over on timescales of minutes to millennia [*Hansell and Carlson*, 2015]. According to its reactivity or lifetime, *Hansell* [2013] has defined a total of five DOM fractions from shortest to longest lifetimes as: labile (LDOM), semi-labile (SLDOM), semi-refractory (SRDOM), refractory (RDOM) and ultra-refractory (URDOM) (Table I.1).

The term 'labile' refers to the fraction that is removed on timescales of heterotrophic microbial growth rates such that it is not accumulated [*Hansell*, 2013] whereas the term 'recalcitrant' is employed to characterize DOM that accumulates and is more resistant to microbial degradation; the labile fraction presence is fleeting (hours to days), has a production rate of ~15–25 Pg C y^{-1}, which represents half of the carbon that is globally fixed by primary producers [*Chavez et al.*, 2011; *Carr et al.*, 2006], and provides autochthonous support for the euphotic zone microbial loop and its mineralization products remain in the upper ocean for exchange with the atmosphere. The semi-labile pool (SLDOM) is the most important DOM fraction contributing to the biological pump, supports the microbial loop of the upper mesopelagic zone, has a limited role in carbon sequestration and their mineralization products are returned to the air-sea interface within months to years. The semi-refractory fraction (SRDOM) is largely exported to the mesopelagic zone and potentially important in carbon sequestration over decades to centuries. The refractory dissolved organic matter (RDOM) is relevant on centennial to millennial timescales and accounts for more than 95% of the total dissolved organic carbon in the ocean [*Jiao et al.*, 2010]; it is returned to the upper ocean over centuries to millennia and constitutes the fraction of largest average radiocarbon age (4000–6000 yr). Lastly, the ultra-refractory (URDOM) is likely thermogenic and it is termed dissolved black carbon (DBC). Its primary sinks are the sediments and photooxidation, and represents transfer of carbon from the biological to the geological realm. The quantitative characteristics of these fractions are summarised in Table I.1.

Table I.1. Quantitative characteristics of DOM fractions according to their reactivities. *Taken from *Hansell* [2013].

Fraction	Inventory (Pg C)	Gross Production rate (Pg C yr^{-1})	Removal rate (µmol C kg^{-1} yr^{-1})	Lifetime (yr)
Labile (LDOM)	<0.2	~ 15–25	~ 10	~0.001
Semi-labile (SLDOM)	6 ± 2	~ 3.4	~ 2–9	~1.5
Semi-refractory (SRDOM)	14 ± 2	~ 0.34	~ 0.2–0.9	~20
Refractory (RDOM)	630 ± 32	~ 0.043	~ 0.003	~16 000
Ultra-refractory (URDOM)	>12	~ $1.2x10^{-5}$	~ $8x10^{-7}$	~40 000

The size-reactivity continuum model proposed by *Amon and Benner* [1996] provides a conceptual framework depicting the relationships among the size, reactivity and chemical composition of marine

organic matter (Fig. I.2). As decomposition and the decrease of molecular size proceed, the chemical complexity of these residues of organic matter increases, biological reactivity declines, and the radiocarbon ages of molecules increase. Instead, larger size classes of organic matter were more bioavailable and more rapidly remineralised by microbes.

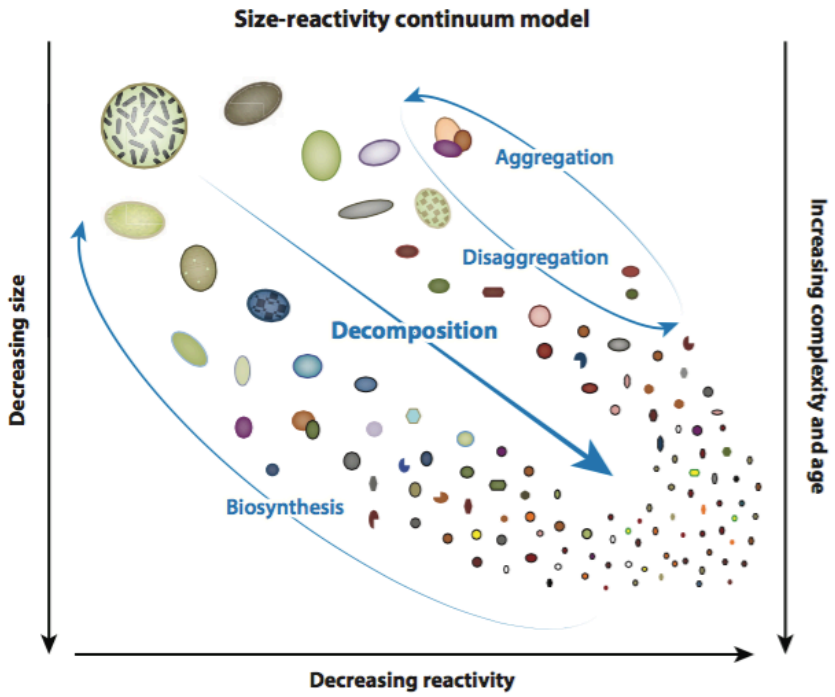

Fig. I.2. A conceptual model of the size-reactivity continuum, showing the net flow of organic carbon from larger to smaller size classes with increasing decomposition. *Taken from *Benner and Amon* [2015].

Contrary to the size-continuum model, other studies found evidence of a dominant content of a more resistant and complex high molecular weight (HMW) DOM with increasing age and decomposition rates [*Hansman et al.*, *in press*; *Helms et al.*, 2008], which, in turn, it might elucidate a coexistence of both formation, transformation and mineralization of the different molecular sizes of DOM in the ocean.

3. Dissolved organic matter distribution in the oceans

High concentrations of 70–80 μmol kg^{-1} C are present at the ocean surface in the tropical and subtropical biogeographic provinces (40°N to 40°S), where vertical stratification favours the slow accumulation of organic matter resistant to biological degradation. Instead, lower concentrations of ~40–50 μmol kg^{-1} C are observed at the surface in equatorial regions, in subpolar seas and in the Southern Ocean (>50°S), where low-DOC deep ocean waters upwells to the surface. Despite its high latitudes, the Arctic Ocean is enriched in DOC by the input of terrigenous organic matter via high fluvial

fluxes from boreal regions to the system [*Benner et al.*, 2005; *Dittmar and Kattner*, 2003]. In this area, there is a massive DOC export to the dark ocean with the North Atlantic Deep Water (NADW) formation (~48 μmol kg^{-1}) and a subsequent DOC loss during thermohaline circulation because of DOM mineralization, reaching the minimum in the North Pacific (~34 μmol kg^{-1}; Fig. I.3). The coastal areas with river discharges have higher DOC concentration than the open ocean, whereas coastal upwelling areas present lower concentrations of DOC because of the DOC-depleted subsurface waters that reach the surface [*Hansell and Carlson*, 2001].

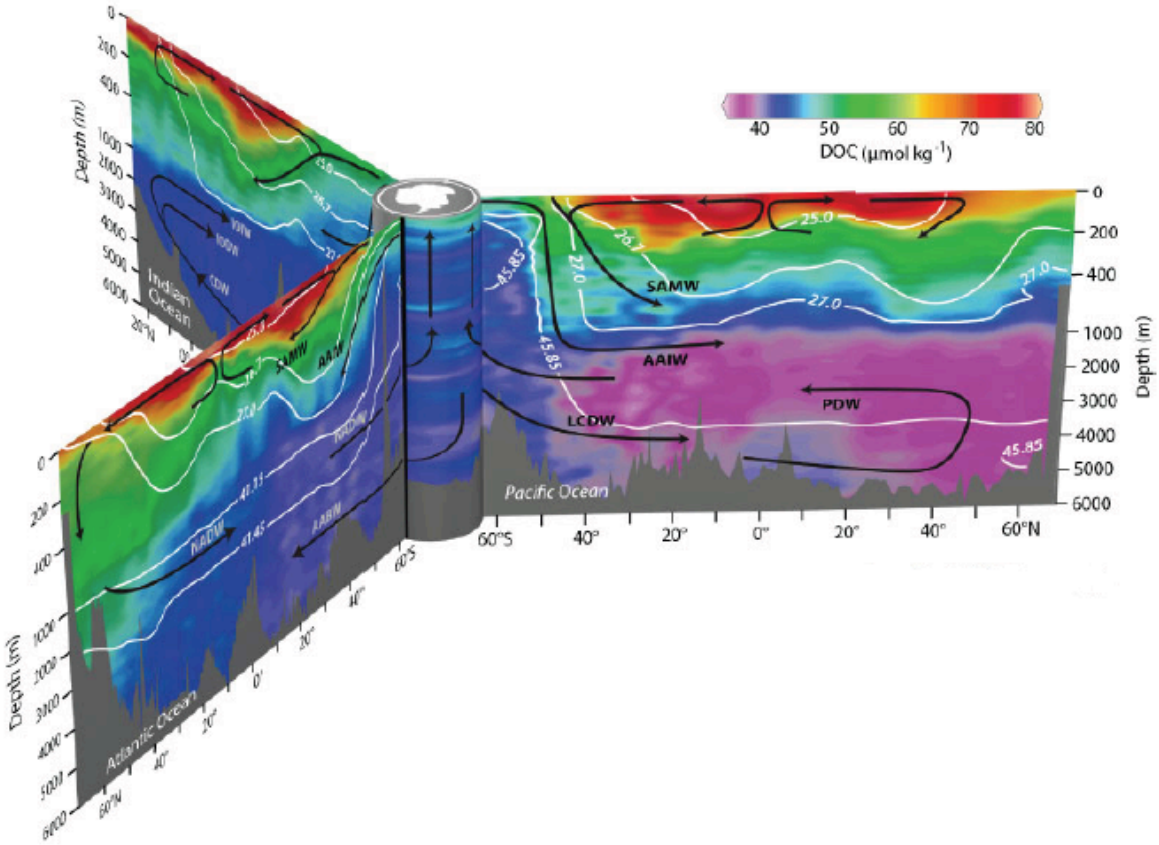

Fig. I.3. Distribution of DOM (μmol kg^{-1} C) along meridional sections of the three oceans basins. Black arrows represent the circulation pathways of the main water masses of the global ocean: North Atlantic Deep Water (NADW), Antarctic Intermediate Water (AAIW), Lower Circumpolar Water (LCW), Pacific Deep Water (PDW), SAMW: Subantarctic Mode Water (SAMW), Antarctic Bottom Water (AABW). White lines represent relevant isopycnal surfaces. *Taken from *Hansell et al.*, [2009].

As for the case of DOC, the lowest mean concentrations of dissolved organic nitrogen (DON) are found in the dark ocean, with a mean value of 3.6 ± 2.2 μmol L^{-1}, whereas the average surface ocean DON concentration is 4.4 ± 0.5 μmol L^{-1} [*Letscher et al.*, 2013]. Concentrations tend to be higher in the eastern boundaries and the equatorial upwelling zones (i.e. >5 μmol L^{-1}), resulting from an enhanced upward flux of NO_3^- supporting biological production within these systems [*Letscher et al.*, 2013]. In the

poleward and westward of the upwelling regions, DON concentrations are lower, so it is assumed that the subtropical gyres are sinks for DON due to biological consumption [*Sipler and Bronk*, 2015]. Concentrations of DON decrease with depth as it is removed through vertical mixing and subsequent remineralization by microbes below the mixed layer [*Letscher et al.*, 2013], which, in turn, is coincident with an increase in NO_3^- [*Torres-Valdés et al.*, 2009].

For the case of dissolved organic phosphorus (DOP), the values range between ~0.09–0.12 and ~0.07–0.09 μmol L^{-1} in the surface (0–200 m) and intermediate-deep waters (>200 m) of the North Atlantic, ~0.18–0.20 and ~0.05–0.15 μmol L^{-1} in the surface-intermediate and deep waters of the South Atlantic [from the National Oceanographic and Atmospheric Administration–National Oceanic Data Center, *Sipler and Bronk*, 2015], and ~0.12–0.24 and ~0.03–0.12 μmol L^{-1} in the surface and intermediate-deep waters of the North Pacific [*from The Hawaii Ocean Time-series Station ALOHA (22° 45'N, 158°W), Sipler and Bronk*, 2015].

Stoichiometric analyses show that the carbon : nitrogen : phosphorus (C:N:P) ratios for surface and deep waters are substantially different. The average C:N:P ratio for RDOM in deep waters, which have low DOM concentrations, is ~3511:202:1, greater than the C:N:P ratio of LDOM (199:20:1) found in surface waters or the POM ratio (106:16:1–the Redfield ratio) [*Hopkinson and Vallino*, 2005]. Both LDOM and RDOM are C-rich relative to the Redfield ratio, which implies that DOM export is C-rich and more efficient that the POM carbon export. This C-rich DOC that is exported to the dark ocean might contribute to the excess respiration estimated to occur in the interior ocean [*del Giorgio and Duarte*, 2002].

4. DOM sources, sinks and accumulation

In the open ocean, the main source of DOM is autochthonous, and this DOM comprises more than 95% of the total organic matter pool [*Nelson and Siegel*, 2013; *Lalli and Parsons*, 1997], whereas terrestrial inputs only represent about 0.7–2.4% of the total DOM [*Opsahl and Benner*, 1997]. Nevertheless, as this thesis mainly focused on the recalcitrant fraction of DOM, apart from describing the sources and sinks of the bulk DOM pool, we thoroughly detail the sources and sinks of recalcitrant DOM in this section.

The biotic formation of DOM includes: (1) extracellular release by phytoplankton [*Marañon et al.*, 2005], (2) grazing and egestion by protists [*Jiao et al.*, 2010; *Nagata and Kirchman*, 1992], (3) release via cell lysis (both viral and bacterial) [*Weinbauer et al.*, 2011; *Jiao et al.*, 2010], (4) release of metabolites by microbes for nutrient acquisition (e.g., metal-binding ligands for metal acquisition; *Ito and Butler*, 2005), for communication (e.g., acyl homoserine lactones for quorum sensing; *Gram et al.,* 2002), or for chemical defence (e.g., polyunsaturated aldehydes for grazing inhibition; *Wichard et al.*, 2008), and (5) programmed cell death of microalgae and prokaryotes [*Bidle and Falkowski, 2004*; *Orellana et al.*, 2013].

The main biotic source of recalcitrant DOM is the *de novo* production from labile DOM by

microbes [*Ogawa et al.*, 2001; *Jiao et al.*, 2010; *Jiao and Azam*, 2011], which has been coined the "microbial carbon pump" (MCP) (see below in Section 6). Abiotic processes that can lead to the synthesis of recalcitrant DOM are (1) the polymerization of low molecular weight (LMW) DOM (condensation reactions catalysed by light and metal complexation [*Kieber et al.*, 1997], (2) new production or modification of chemical bond structure of LDOM and SLDOM by exposure to ultraviolet light [*Hansell*, 2013; *Nagauma et al.*, 1996; Keil and *Kirchman*, 1994], (3) adsorption of labile DOM to colloids [*Nagata and Kirchman*, 1996; *Kirchman et al.*, 1989], (4) assemblage into gels [*Orellana and Hansell*, 2012] and (5) the alteration of biomolecules by excessive heat to large polycyclic aromatic compounds or DBC [*Dittmar and Paeng*, 2009]. DBC accumulated in soils and sediments over decades to thousand years after vegetation fires on land [*Singh et al.*, 2012; *Masiello and Druffel*, 1998]. This fraction is released into rivers to be carried ultimately into the oceans [*Dittmar et al.*, 2012] at a rate of 26.5 ± 1.8 x 10^{12} g C yr^{-1}, which is 10% of the global riverine DOC flux [*Jaffé et al.*, 2013]. A fully unconstrained potential source of DBC to the dark ocean is hydrothermal circulation through marine sediments although, at this point, it has not been directly investigated [*Dittmar and Koch*, 2006].

Heterotrophic prokaryotes, which transport low molecular weigth DOM (<600 Dalton) through their cell membranes [*Nikaido and Vaara*, 1985], as well as formation of POM by spontaneous assembly of DOM polymers [*Chin et al.*, 1998] are recognized as the dominant sinks of DOM in the ocean [*Carlson and Hansell,* 2015]. The removal processes of recalcitrant DOM are little known. It is unclear whether the removal is mainly by photodegradation in surface waters or interactions with the Earth´s crust [*Hansell*, 2013]. In surface waters, UV irradiation is the only mechanism suggested in the literature for recalcitrant DOM removal. Once recalcitrant DOM returns to the ocean surface, a portion of it is photo-oxidized to CO_2 and to a lesser extent CO [*Mopper and Kieber*, 2002; *Mopper et al.*, 1991; *Moran and Zepp*, 1997; *Stubbins et al.*, 2006, 2012]. Photodegradation has been proposed as the probable single most important removal process for DBC in the ocean [*Dittmar*, 2015], being photodegraded at a rate of 20 to 490 x 10^{12} g C yr^{-1} and, thus, balancing the entire riverine input and avoiding its accumulation in the ocean [*Stubbins et al.*, 2012]. *Anderson and Williams* [1999] estimated the photochemical oxidation of recalcitrant DOC to be 282 x 10^{12} g C y^{-1}. Moreover, when the chromophores absorb UV light, it transforms the HMW DOM that comes from the dark ocean to biologically available LMW carbonyl compounds [*Anderson and Williams*, 1999; *Benner and Biddanda*, 1998; *Moran and Zepp*, 1997; *Mopper et al.*, 1991; *Kieber et al.*, 1989], facilitating the uptake and remineralization of DOM by heterotrophic bacterioplankton and playing a significant role in the microbial loop [*Pomeroy et al.*, 2007; *Azam et al.*, 1983]. On the other hand, UV light enhances the cross-linking, humification, and polymerization of labile biomolecules exuded by phytoplankton into more recalcitrant compounds [*Reche et al.*, 2001; *Obernosterer et al.*, 1999; *Benner and Biddanda*, 1998; *Kieber et al.*, 1997].

Removal of recalcitrant forms of DOM is also observed in the ocean interior where UV does not penetrate [*Hansell et al.*, 2012, 2009; *Carlson et al.*, 2010]. In deep waters, deep-sea microorganisms may have the ability to degrade and utilise some of the DOM that was refractory in the upper water column [*Carlson et al.*, 2011; *Kujawinski*, 2011]. However, why is the DOM long-term persisting? Several

hypotheses have been proposed to explain the DOM millennium-scale stability [*Dittmar*, 2015]. The "environmental hypothesis" relates the reactivity of DOM to particular environmental conditions prevailing in certain regions or in different periods of the Earth history [*Dittmar*, 2015]. DOM mineralization can be constrained by the availability of essential resources such as electron acceptors (e.g. oxygen, sulphate, nitrate), nutrients (e.g. phosphorous, iron) or metabolites (e.g. vitamins). For example, in the oligotrophic Mediterranean Sea, the low phosphate concentration limits the growth of phytoplankton and heterotrophic bacteria [*Kritzberg et al.*, 2010; *Zohary et al.*, 2005] or, in the Black Sea, where the microbial oxidation of sinking debris and the lack of deep ocean ventilation has led to very low oxygen levels that unable bacteria to utilize labile materials [*Sexton et al.*, 2011; *Albert et al.*, 1995]. The oxygen availability on heterotrophic DOM degradation is on debate, whereas some authors postulate that preservation of organic carbon tends to increase under anoxic conditions [*Canfield et al.*, 1993], other authors put forward that the amount of organic matter mineralized in anoxic systems is underestimated and the carbon burial efficiencies are not substantially different from those of oxygenated environments with similar sediment accumulation rates [*Bastviken et al.*, 2004; 2003; *Middelburg et al.*, 1993; *Calvert et al.*, 1991]. The increase of DOM preservation could be the result of a thermodynamically limited degradation of recalcitrant material in the absence of the electron acceptor oxygen, the inability of anaerobic organisms to degrade organic matter and a decreased enzymatic activity [*Arndt et al.*, 2013; *Kattner et al.*, 2011]. Therefore, periods of widespread ocean anoxia related to reduced deep ocean ventilation, like in the Eocene, resulted in a larger global ocean DOC inventory [*Sexton et al.*, 2011], whereas once oxic conditions are re-established, the DOC would then be rapidly oxidized to DIC, releasing CO_2 to the atmosphere [*Ridgwell and Arndt*, 2015].

The "molecular diversity hypothesis" postulates that the decomposition rate of an organic substrate depends on its concentration [*Dittmar*, 2015]. Culture experiments indicate that transporter proteins and catabolic pathways are only expressed when a certain threshold concentration of substrate is reached [*Kovarova-Kovar and Egli*, 1998]. So, although there is enough organic material dissolved in the dark ocean (~40 μmol L^{-1}) [*Hansell et al.*, 2009], the low newly-synthesized bacterial DOC concentrations (~10 μmol L^{-1}) [*Lenchtenfeld et al.*, 2015] indicate that the concentration of thousands of individual molecules in picomole amounts in each litre of seawater (>10000 different molecular formulae) [*Dittmar and Paeng*, 2009] are extremely low that reduce the encounter rates between substrates and bacterial enzymes [*Arrieta et al.*, 2015; *Lenchtenfeld et al.,* 2015; *Kattner et al.*, 2011; *Kovarova-Kovar and Egli*, 1998; *Jannasch*, 1967]. However, the link between DOM decomposition rates and the concentration of individual DOM compounds seems a non-exclusive scenario as it is also related to its molecular structure [*Dittmar*, 2015]. In this sense, the "intrinsic stability hypothesis" links the DOM reactivity to its molecular structure [*Dittmar*, 2015] postulating that the chemical complexity of the dissolved molecules limits the availability of organic matter to free-living deep-sea bacteria.

In addition, sorption of DOM onto sinking particles is a potential DOM abiotic removal mechanism within the ocean interior [*Druffel et al.*, 1996, 1998], accounting for ~0.02–0.05 Pg C y^{-1} [*Hansell et al.*, 2009]. HMW DOM spontaneously assembles into gels that are interconnected tangles of covalently or electrostatic cross-linked biopolymers called self-assembled microgels [*Verdugo*, 2012].

Moreover, the entrainment of fluids through porous basalts at high-temperature vent systems within Earth's crust could remove ~0.7–1.4 × 10^{10} g C y^{-1}, a relatively minor DOC sink compared to others discussed above [*Lang et al.*, 2006].

5. Ocean carbon pumps

The processes that relocate carbon away from the surface to the ocean interior are traditionally divided into three conceptual "pumps" [e.g., *Sarmiento and Gruber*, 2006]: (1) the "solubility" pump, (2) the "organic matter" ("organic carbon" or "soft tissue") pump, and (3) the "carbonate" (or "counter") pump (Fig. I.4). The latter two also partition alkalinity with depth [*Wolf-Gladrow*, 2001], thus dictating the speciation of dissolved inorganic carbon (i.e. the balance between CO_2(aq), HCO_3^-, and CO_3^{2-}) to maintain overall charge neutrality.

Oceans take CO_2 from the atmosphere at a net rate of approximately 2 Pg C y^{-1} [*Takahashi et al.*, 2009; *Sarmiento and Gruber*, 2006]. The **solubility pump** (Fig. I.4a) is defined as the CO_2 sequestration by means of the dissolution of CO_2 from the atmosphere. Most of this diffusion occurs in cold, high-latitude surface waters, where deep water forms [*Ridgwell and Arndt*, 2015], and are redistributed throughout the dark ocean by means of the thermohaline circulation until it reaches lower latitudes where they warms up and upwells [*Raven and Falkowski*, 1999].

In the **organic matter pump** (Fig. I.4b), photoautotrophically fixed carbon in the surface layer is transported as dead sinking biogenic particles or as dissolved organic matter to greater depths by convection currents [*Goldberg et al.*, 2009], turbulent diffusion, and meridional overturning circulation where it is remineralised to CO_2, maintaining a vertical gradient of CO_2 in the ocean's interior [*Karl and Bjorkman*, 2015; *Lechtenfeld*, 2012; *Ducklow et al.*, 2001]. It is estimated that ~50 Pg C y^{-1} is fixed by photosynthesis in the global ocean [*Chavez et al.*, 2011; *Carr et al.*, 2006], and ~20% escapes rapid remineralization in the surface and sinks to the ocean interior mostly in the form of particulate material (~8 Pg C y^{-1}), whereas only 2 Pg C y^{-1} enters the ocean interior as DOM [*Hansell et al.*, 2009]. The heterotrophic oxidation of POM back to CO_2 during sinking is highly efficient, with <1–6% of the POM export production reaching the seafloor [*Dunne et al.*, 2007].

The **carbonate pump** (Fig. I.4c) involves the production of calcium and to a lesser extent magnesium carbonate ($CaCO_3$ and $MgCO_3$) by calcifying organisms at the ocean surface. This is an efficient mechanism to sequester particulate inorganic carbon at a short-time scale [*Elderfield*, 2002]. Global new production of $CaCO_3$ ranges from 0.8 to 1.4 Pg of $CaCO_3$–C y^{-1} [*Iglesias-Rodriguez et al.*, 2002; *Lee*, 2001] and the total water column $CaCO_3$ dissolution rate for the global oceans is approximately 45 to 65% of the export production of $CaCO_3$, most of it occurring in the upper 2000 m [*Feely et al.*, 2004]. The present-day accumulation of $CaCO_3$ in marine sediments is about 0.1 to 0.14 Pg of $CaCO_3$–C y^{-1} [*Iglesias-Rodriguez et al.*, 2002; *Milliman et al., 1999*; *Catubig et al.*, 1998], which is no more than 10% of the total amount of $CaCO_3$ that is annually produced. The rest is either dissolved at the sediment-seawater interface or in the upper portion of the sediment column [*Feely et al.*, 2004].

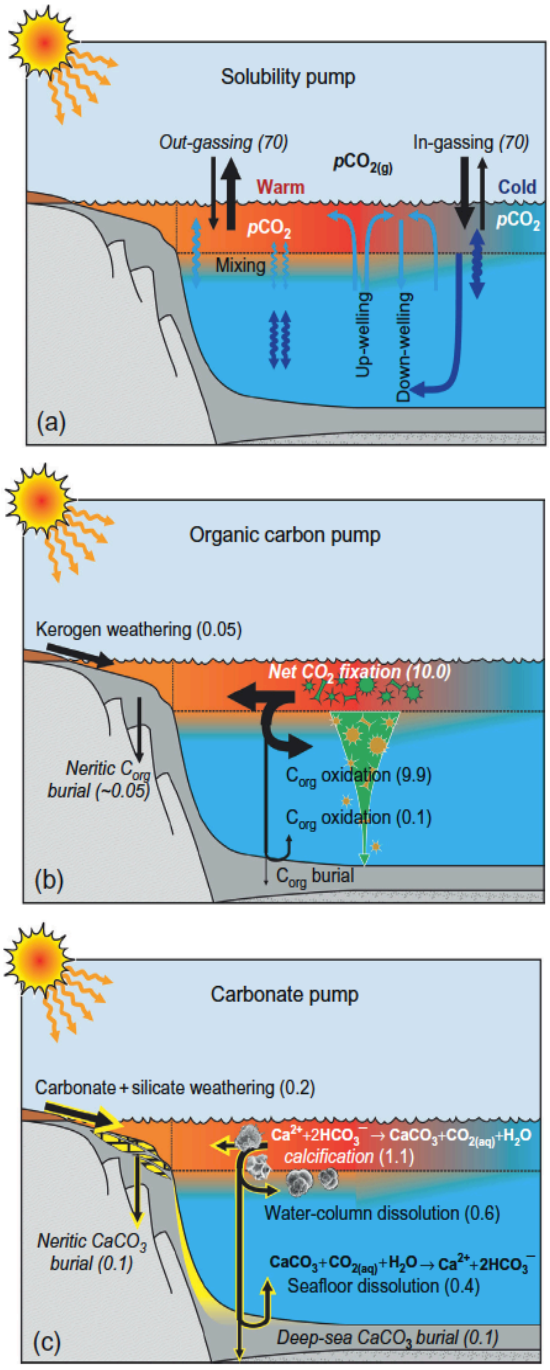

Fig. I.4. Outline of the three classical components of the ocean carbon pump. (a) The solubility, (b) the particulate organic carbon, and (c) the carbonate pump. *Taken from *Ridwell and Arndt* [2015].

On time scales of the order of the ocean turnover time (i.e. ~500–1000 yr), all three of the pumps play an important role in the carbon cycle as they influence on carbon sequestration [*Buesseler et al.*, 2007; *Cameron et al.*, 2005].

6. The forth carbon pump: the microbial carbon pump (MCP)

Recently, a forth carbon pump that involves the conversion of labile organic matter into recalcitrant DOM, which resist subsequent mineralization, has been proposed. It was firstly described by *Ogawa et al.* [2001], and lately conceptualized by *Jiao et al.* [2010] as the microbial carbon pump (MCP) (Fig. I.5). Most of the LDOM derived from photosynthesis material is remineralised (~90%) by heterotrophs. During the microbial processing of organic matter, low-concentration labile (or reactive) carbon is progressively transferred to high-concentration recalcitrant carbon [*Jiao et al.*, 2010] and accumulated in the ocean interior, accounting for the vast majority of the DOM inventory [*Hansell*, 2013]. According to this definition, bacteria, archaea and viruses play an important role in the carbon sequestration by synthesizing or releasing recalcitrant DOM throughout the water column. Concerning virus, *Suttle et al.* [2007] showed that highly labile materials, such as amino acids and nucleic acids, tend to be recycled in the euphotic zone during viral shunt, whereas more recalcitrant carbon-rich material, such as that found in cell walls, potentially increases the efficiency with which carbon is exported to below the pycnocline. Moreover, the labile cell material released during viral lysis could be indirectly promoting the RDOM synthesis by microorganisms, thus contributing to the MCP [*Jiao et al.*, 2010].

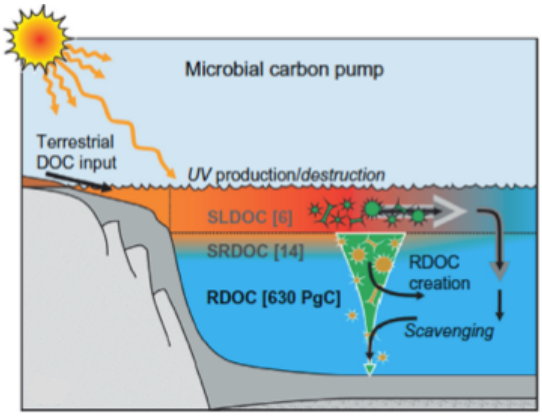

Fig. I.5. Outline of the microbial carbon pump. SLDOC: Semi-labile DOC, SRDOC: Semi-refractory DOC, RDOC: Refractory DOC. *Taken from *Ridwell and Arndt* [2015].

The rate of production of RDOC ranges between 0.043–0.069 Pg C y^{-1} [*DeVries et al.*, 2014; *Hansell*, 2013], but its recalcitrant nature at centennial to millennial time scale permits a net inventory of 656 Pg C. Recent mesocosm experiments indicate that less microbially-produced RDOM than previously thought is generated, but still enough to sustain the global RDOM pool [*Osterholz et al.*, 2015]. Furthermore, the MCP alters the chemical composition of DOM, resulting in changing ratios of carbon to nitrogen, phosphorus and other elements [*Hopkinson and Vallino*, 2005]. It keeps relatively more carbon in the RDOM pool than organic nitrogen and phosphorus, and it releases more inorganic nitrogen and phosphorus into the water, providing essential nutrients for future primary production

[*Jiao et al.*, 2010]. To strengthen this assumption, *Lenchtenfeld et al.* [2015] reported that most of the molecules in bacterial DOM consisted solely of carbon, hydrogen and oxygen (49–52%), whereas molecules containing nitrogen contributed 31–37% of the molecules. These authors reported that up to 32–35% of the carbon in bacterial DOM were accounted for carboxyl-rich alicyclic molecules, which represent > 50% of the molecular diversity in the surface and deep ocean DOM [*Hertkorn et al.*, 2013], with protein and peptide amide carbon being a relatively minor component. This is consistent with the abundance of non-hydrolysable carbohydrates in marine DOM [*Benner et al.*, 1992] and the estimation that DOM is composed of ~8% of carboxylic-rich alicyclic structures [*Hertkorn et al.*, 2006] or ~2% of derivatives of polycyclic aromatic hydrocarbons or DBC [*Dittmar and Paeng*, 2009]. In addition, DOM has a clear molecular overprint in the form of non-hydrolysable D-amino acids, which are only produced by bacteria and archaea, not by algae [*Dittmar et al.*, 2001].

The potential effects of climate-driven changes on the MCP have been recently discussed by *Legendre et al.* [2015]. They suggested that an increase of surface-ocean temperature, water column stratification and ocean acidification may increase DOC production and, thus could potentially enhance carbon sequestration by the MCP. In contrast, other predicted consequences of climate change such as slowing down of the thermohaline circulation, reduction of the phytoplankton mean size and the cloud cover, as well as the increase in anthropogenic nutrient supply via continental waters and the atmosphere [*Jiao et al.*, 2014] could have a negative impact on the carbon sequestration by the MCP. Microbial carbon accumulation is known to occur when mineral nutrients are limiting [*Gasol et al.*, 2009; *Lauro et al.*, 2009].

7. Spectroscopic techniques to DOM characterization as tools in the study of the microbial carbon pump

As marine DOM is the sum of (1) all intact biomolecules exuded, excreted and leached from the living and decaying biota present in a water body; (2) the remnant and transformed biomolecules from organisms, plus (3) chemically and biologically altered biomolecules from surrounding waters, atmospheric deposition, sediments, and terrestrial sources, we can expect the chemical complexity of the marine DOM pool to be orders of magnitude greater than for any single organism [*Mopper et al.*, 2007].

The common techniques used to characterize DOM do not fully reveal the chemical composition of open ocean DOM, although they are offering novel insights and fostering greater recognition of DOM's molecular understanding [*Stubbins et al.*, 2014]. Up to now, the techniques to characterize DOM have been gathered into two categories: (1) DOC concentration, C:N:P ratios, bulk isotopic composition, chromophoric DOM, and fluorescent DOM, and (2) ultra-high-resolution techniques to measure identifiable lignins, amino acids, sugars, proteins, nucleic acids, and other biomolecules [*Mopper et al.*, 2007]. While these approaches have yielded significant advances, as demonstrated by the quantity and scope of the current DOM literature, they remain limited. The most common advanced instrumental approaches for characterization of marine DOM are the nuclear magnetic

resonance (NMR) and ultrahigh resolution Fourier transform ion cyclotron mass spectrometry (FT-ICR-MS) [*Repeta*, 2015; *Kujawinski et al.*, 2009; 2004; *Mopper et al.*, 2007; *Repeta et al.*, 2004]. Extraction and concentration techniques, as well as desalinization, are initially required for taking advantage of the high-resolution capabilities of FT-ICR-MS and NMR as, at natural levels, trace molecules will likely fall below the detection limit [*Mopper et al.*, 2007]. To extract and concentrate, ultrafiltration and solid-phase extraction with styrene divinyl benzene polymer type sorbents (PPLs) are currently the most commonly used procedures, retaining about 20% and 40% of the bulk DOM pool, respectively [*Dittmar et al.*, 2008]. To desalinize the DOM seawater samples, size-exclusion chromatography and electrodialysis (ED) are the most applied procedures. Reverse osmosis (RO) has been shown to be an effective method for desalinization as well as for retention and concentration of DOM [*Vetter et al.*, 2007]. For instance, a bunch of tests performed in the Atlantic Ocean after combining RO and ED recovered more than 60% of marine DOM [*Vetter et al.*, 2007]. Even the sequential isolation of DOM from large water volumes, first with PPL and then via RO/ED of the PPL waste stream achieved a recovery of 98% and 101% for the dark and surface ocean, respectively [*Green et al.*, 2014]. On the other hand, absorption and fluorescence spectroscopic techniques are complementary approaches that provide global information on the nature of DOM pool in the ocean without an intrinsic chemical characterization.

The absorption of light in water contributes to attenuate the penetration of the solar radiation through the water column [*Guéguen and Kowalczuk*, 2013]. In all natural waters the spectral absorption coefficient of water, $a_{tot}(\lambda)$, is defined as the sum of the absorption coefficient of pure water, $a_w(\lambda)$, phytoplankton pigments contained in algae cells, $a_{ph}(\lambda)$, non-algal particulate material, $a_{NAP}(\lambda)$, chromophoric dissolved organic matter (CDOM), $a_{CDOM}(\lambda)$, and inorganic salts dissolved in seawater, $a_s(\lambda)$.

$$a_{tot}(\lambda) = a_w(\lambda) + a_{ph}(\lambda) + a_{NAP}(\lambda) + a_{CDOM}(\lambda) + a_s(\lambda) \quad (1)$$

In marine systems, CDOM absorbs ultraviolet and, to a lesser extent, visible radiation and is considered the dominant source of light absorption throughout the blue and especially in the UV spectral regions of the open ocean [*Nelson and Siegel*, 2013]. For wavelengths lower than 440 nm, CDOM is by far the most important factor regulating total absorption in the upper layers of the open ocean (Fig. I.6).

So far, we know that contributors to the chromophore (and fluorophore) pool include aromatic amino acids [*Yamashita and Tanoue*, 2008; 2003], lignin phenols, and ill-defined humic substances that are operationally characterized by their absorption and fluorescence properties [*Coble*, 1996].

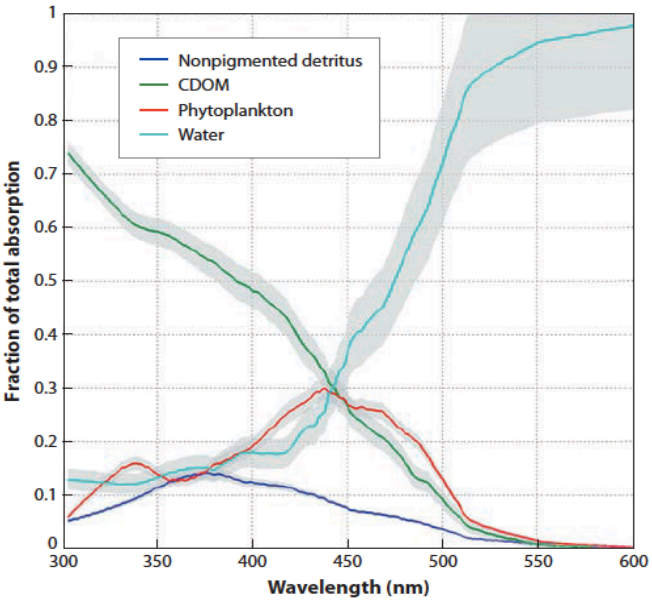

Fig. I.6. Estimated mean relative contributions of CDOM and other components to the total light absorption at wavelengths of 300–600 nm. *Taken from *Nelson and Siegel* [2013].

Spectroscopic techniques to measure CDOM in estuaries, coastal regions and marginal seas commonly use spectrophotometers with a cuvette of 1- or 10-cm pathlength, which are normally valid to measure the CDOM absorption with the accuracy required. However, the use of liquid capillary wave guide cell systems (LWCC) with cuvettes from 0.25 up to 3 m is required for the very low CDOM levels detected in oligotrophic waters such as the core of oceanic subtropical gyres. Furthermore, a latter promising technique that enables CDOM absorption measurements below detection the limits of ordinary spectrophotometers is the integrating sphere [*Röttgers and Doerffer*, 2007]. It enables measurements of the absorption coefficient not disturbed by the presence of small particles, colloids, and viruses or small bacteria [*Guéguen and Kowalczuk, 2013*]. The use of the absorption and beam attenuation meter, the ac-9, which is capable of measuring CDOM *in situ* with very high spatial and temporal resolution, but with the limitation of its coarse spectral resolution (i.e. 10 nm) that make it difficult to calculate the CDOM absorption parameters explained below. Characterization of CDOM through UV-visible (250–700 nm) spectroscopy primarily uses the absorption coefficient as an index of CDOM concentration [*Nelson et al.*, 2010], and the spectral slopes as indices of the molecular structure. Spectral slopes can be calculated through a linear fitting of the log-linearized absorption spectra or through a nonlinear fitting [*Blough and Del Vecchio*, 2002], and the values can be highly variable, almost 75% variability, depending on the estimation wavelength range [*Twardowski et al.*, 2004]. In this regard, the slope wavelength ranges (275–295 nm and 350–400 nm) proposed by *Helms et al.* [2008] are becoming more commonly used since they showed the largest variations in contrasted CDOM samples (river, estuary, coastal and open ocean). Spectral slopes measured in the UV-visible region have been shown in many studies to increase in response to the bleaching of CDOM and have been observed to decrease with increasing water mass age in the dark ocean [*Nelson et al.*, 2007],

hinting at changes in CDOM composition driven by bleaching or production. Spectral slopes measured at wavelengths < 300 nm have been used to quantify the DOC concentration [*Fichot and Benner*, 2011] and the molecular weight distribution [*Helms et al.*, 2008], whereas the SUVA index (i.e. a_{254}/DOC) has been used to account for the abundance of conjugated carbon double bonds [*Weishaar et al.*, 2003]. Furthermore, other parameters measured at longer wavelengths (> 300 nm), such as the spectral slopes between 350 and 400 nm, $S_{350\text{-}400}$ [*Helms et al.*, 2008] or between 300 and 500 nm, $S_{300\text{-}500}$ [*Hong et al.*, 2005], and the ratios $S_{275\text{–}295}/S_{350\text{–}400}$ [*Helms et al.*, 2008] or a_{254}/a_{365} [*Dahlén et al.*, 1996] are commonly applied to the DOM characterization.

A portion of CDOM also emits fluorescence when irradiated with ultraviolet light and is termed fluorescent dissolved organic matter (FDOM) (Fig. I.7) [*Coble*, 2007; 1996], being the coastal areas the marine systems with higher content [*Kowalczuk et al.*, 2010; *Chen and Bada*, 1992] and more distinct sources (e.g. terrestrial, wetland and wastewater inputs; *Tzortziou et al.*, 2011; *Chen et al.*, 2004). Organic matter fluorescence occurs when a loosely held electron in an atom or a molecule is excited to a higher energy level by the absorption of energy, and some energy is lost from the excited electron by collision, non-radiative decay and other processes, prior to emission, where the electron returns to its original energy level (ground state) [*Hudson and Baker*, 2007]. For this reason, the energy of the emitted photon is lower (i.e. larger wavelengths) than the excitation energy (the Stokes' Shift) (i.e. lower wavelengths).

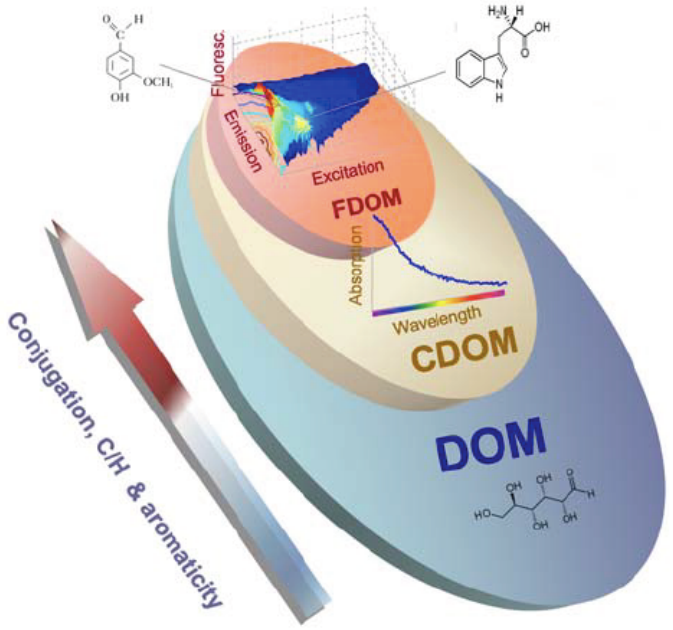

Fig. I.7. Scheme of the chromophoric (CDOM) and fluorescent (FDOM) fraction of total DOM pool. The arrow indicates increasing aromaticity, conjugation, and carbon to hydrogen (C/H) ratio. Over the CDOM and FDOM fractions, examples of CDOM absorption spectra and excitation-emission matrices are shown, respectively. Structure of tryptophan, a natural amino acid, and vanillin, a constituent of lignin, are shown as examples of amino acid-like and humic-like fluorescent CDOM, respectively. The grey lines indicate the position of their respective fluorescence excitation-emission peaks. *Taken from *Stedmon and Álvarez-Salgado* [2011].

Typically, the fluorescence intensity is Raman calibrated (Raman units) or standardised to quinine sulphate units (QSU in ppb). It has been used as a proxy of CDOM absorption since numerous studies have observed a linear relationship between fluorescence and absorption coefficients [*Del Vecchio and Blough*, 2004a; *Ferrari and Dowell*, 1998].

Fluorescence spectroscopy, in particular the excitation-emission matrix (EEM) technique [*Coble*, 1996], is the state-of-the-art method [*Hudson and Baker*, 2007] used to characterize CDOM in terms of its composition and origin, to follow changes from biological or physical processing, and to elucidate its distribution patterns [*Coble*, 1996]. EEMs were first introduced by *Weber* [1961] and consist on a number of fluorescence emission scans at different excitation wavelengths that are compiled into a matrix typically containing > 3000 fluorescence intensities, which can allow the visualization of a range of fluorophores in their relative positions in optical space as a three-dimensional surfaces [*Hudson and Baker*, 2007] (Fig. I.8). Fluorescence is more sensitive than absorption spectroscopy and provides more information as to chemical composition than do absorbance spectra [*Coble*, 2007].

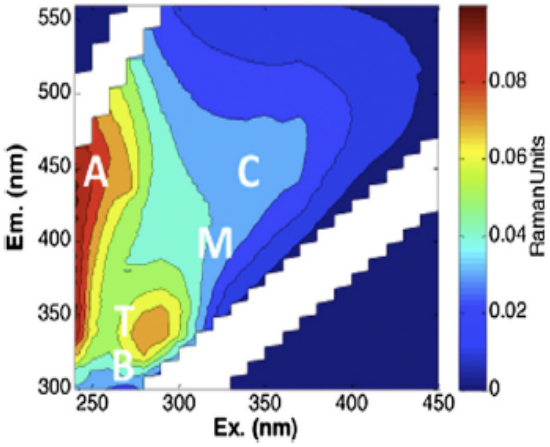

Fig. I.8. Example of a fluorescence excitation-emission matrix for an open ocean sample. White areas are masked due to first- and second-order Rayleigh and Raman scattering. *Taken from *Catalá et al*. [2013].

Six general types of fluorescence peaks have been identified in natural waters [*Guéguen and Kowalczuk*, 2013; *Hudson and Baker*, 2007; *Coble*, 1996]. These peaks are commonly included in two groups: humic-like and amino acid-like substances (Table I.2).

Table I.2. Spectral characteristics of the main FDOM components in marine waters in bulk water.

Peak	Name	Ex wavelength (nm)	Em wavelength (nm)	Nature
1	T	270-280	340-360	Tryptophan-like, amino acid-like, autochthonous
2	B	270-280	300-310	Tyrosine-like, amino acid-like, autochthonous
3	-	260	282	Phenylalanine-like, amino acid-like, autochthonous
4	A	230-260	380-460	Terrestrial humic-like
5	C	320-360	420-480	Terrestrial humic-like
6	M	290-320	370-420	Marine humic-like

The amino acid-like substances fluoresce at wavelengths characteristic of the aromatic amino acids tryptophan (Ex/Em 280 nm/350 nm, peak-T) [*Coble*, 1996], tyrosine (Ex/Em 275 nm/305 nm, peak-B) [*Coble*, 1996] and phenylalanine (260/282) [*Jørgensen et al.,* 2011] in either free or bounded forms. The position of the amino acids in the proteins determines the intensity and Ex/Em wavelengths of the amino acid-like fluorescence peaks [*Lakowicz*, 2006]. Tryptophan dominates the emission and is highly dependent upon polarity and/or local environment [*Lakowicz*, 2006]. Tyrosine fluorescence is negligible when both tyrosine and tryptophan coexist in the same peptides because the emission energy of tyrosine is used as excitation energy for tryptophan [*Creighton*, 1993]. The quantum yield, which is defined as the proportion of light absorbed that is re-emitted as fluorescent light, of both tryptophan and tyrosine is similar (~0.13 and 0.14, respectively). Phenylalanine is generally present in higher concentration than the other two [*Yamashita and Tanoue*, 2003], although is not always visible because its high bioavailability and low quantum yield (~0.03).

The humic-like substances fluoresce at higher emission wavelengths (Ex/Em 250/435 nm for peak-A, Ex/Em 320/410 nm for peak-M and Ex/Em 340/440 nm for peak-C, Fig. I.8). Peaks A and C were thought to represent terrestrial humics, and peak-M were thought to represent marine-derived humics [*Nelson and Siegel*, 2013]. Currently we know that peaks A and C can be generated *in situ* in the oceans by phytoplankton and bacteria [*Romera-Castillo et al.*, 2011; 2010]. Terrestrial humic-like materials display excitation and emission maxima at longer wavelengths than do marine humic-like materials, as would be predicted from their more aromatic chemical nature and presumed higher molecular weight [*Coble*, 2007]. Tannins, lignin, polyphenols and melanins are some components responsible for the humic-like fluorescence [*Coble*, 2007]. Humic substances can be sub-divided into three categories, chemically defined by solubility at different pH. Humic acids are insoluble in aqueous solution at pH lower than 2, but soluble at higher pH. Fulvic acids are soluble in water under all pH conditions. Humins are insoluble in water under any pH conditions [*Aiken et al.*, 1985]. Humic

substances generated in aquatic systems have a fulvic acid nature, whereas allocthonous humic substances mostly generated in soils and transported by fluvial and marine currents have a humic acid nature. International Humic Substances Society (IHSS) isolates have been used as standards for the humic and fulvic fractions [*Senesi et al.*, 1989]. Nevertheless, as there is still no standard for humic substances of marine recalcitrant DOM. *Green et al*. [2014] suggested using the isolated DOM fraction from the Natural Energy Laboratory of Hawaii Authority (NELHA) water as a marine standard of RDOM. This water, pumped from 674 m deep, is termed as North Equatorial Pacific Intermediate Water (NEqPIW) [*Hansman et al.*, *in press*] and is the most aged oceanic water mass and, in turn, it is expected that contains the highest amount of humic substances in the ocean.

The arduous task of developing a statistically consistent deconstruction of fluorescence data contained in EEMs has been circumvented through the application of a powerful multivariate data analysis known as parallel factor analysis (PARAFAC) [*Stedmon and Bro*, 2008], which came into common use to analyse EEM data. PARAFAC can take overlapping fluorescence spectra and decompose them into broadly defined fluorescence components. This has allowed going in depth in the study of the different fluorophores contributing to the FDOM. Besides PARAFAC, principal component analysis (PCA), the laplacian operator and the Nelder-Mead optimisation algorithm, and/or the Self-Organising Maps (SOM) has also been proposed as a tool to explore patterns in large EEM datasets, as well as to discriminate and locate potential peaks in the EEM landscape [*Ejarque-Gonzalez and Butturini*, 2014; *Butturini and Ejarque*, 2013; *Boehme et al.*, 2004]. These multivariate data analysis together with the ongoing application of *in situ* fluorometers can account for higher resolutions in FDOM distribution and lead to a better understanding of the environmental dynamics of FDOM [*Yamashita et al.*, in press].

The combination of both procedures (i.e. low-resolution and high-resolution techniques) encourages to track the bulk pools of DOM and also highlights the complexity of the molecular underpinning of fluorescence signatures for the DOM chemical characterization. For example, a recent study of *Stubbins et al.* [2014] in 11 boreal rivers coupled PARAFAC modelling with FTICR-MS molecular analyses to compare optical and molecular signatures of DOM. In their study, they found that thousands of peaks within a single DOM sample were identified so precisely that elemental formulas (i.e., $C_nH_nO_nN_nS_n$) can be assigned, and that almost 40% of the molecular formulas and 60% of FTICR-MS peak intensities were associated with a PARAFAC fluorescent component. Upcoming studies that correlate fluorescence PARAFAC components and FTICR-MS still remain to be performed in ocean waters but see *Timko et al.* [2015].

While the task of determining the detailed composition and structure of marine DOM is daunting, it offers unparalleled rewards, for representing a unique set of biogeochemical tracers capable of providing important insights into the origins of the waters and the diagenetic alterations that have occurred within those waters during transport [*Mopper et al.*, 2007].

8. The Malaspina 2010 circunnavigation

This PhD thesis and all its content are framed in the Malaspina Expedition 2010, an interdisciplinary research project whose main objectives were: (1) to advance marine science in Spain and promote society's awareness of it, (2) to evaluate the impact of global change on the oceans, (3) to encourage exploration of biodiversity in the ocean depths, (4) to analyse the repercussions of the first Malaspina expedition in 1798–94 leaded by Alejandro Malaspina (1754·1810) and (5) to train and attract young researchers to oceanography. The Malaspina 2010 circumnavigation began in December 2010 with the departure from Cádiz of the research vessel "Hespérides" operated by the Spanish Navy. After a voyage passing through Río de Janeiro, Cape Town, Perth, Sydney, Auckland, Honolulu, Panama and Cartagena de Indias, it returns to Spain in July 2011 (solid lines in Fig. IX). A second cruise of 2 months duration on board the research vessel "Sarmiento de Gamboa" started in January 2011 from Canary Islands to Santo Domingo, and went back to Vigo (dashed yellow lines in Fig. I.9).

Fig. I.9. Cruise track of the Malaspina Expedition 2010. *Taken from www.expedicionamalaspina.es

During the circunnavigation on board R/V Hesperides, 147 stations were sampled spanning latitudes 40°S to 34°N and over 250 scientists carried out an expedition combining cutting-edge scientific research with the training of young researchers. This project formed part of the Consolider-Ingenio Programme, and was headed by the Spanish National Research Council (CSIC), with outstanding collaboration from the Spanish Navy and the Banco Bilbao, Vizcaya, Argentaria (BBVA) Foundation.

9. Goals of this PhD thesis

The overall objective of this PhD thesis is to gain knowledge on the distribution, net production rates and turnover times of DOM as well as its role in the long-term carbon sequestration in the oceans through the study of its optical properties. As this PhD is mostly centred in the dark ocean (>200m), the DOM fraction studied was the recalcitrant DOM, which resist from months to millennia along the ocean circulation. In turn, this study is also aimed at the microbial carbon pump (MCP) since it involves one of the main recalcitrant DOM production pathways in the ocean and therefore a significant mechanism of carbon storage. Our hypothesis was to corroborate that the chromophoric and fluorescent fractions of DOM are key components of the recalcitrant DOM pool in the oceans that can be used as tracers of the water mass mixing and biogeochemical processes operating at centennial to millennial time scales.

To test this hypothesis, the following specific objectives on this PhD have been proposed:

(1) To generate a global ocean database of CDOM and FDOM measurements.

(2) To characterize the CDOM spectra in the different water masses of the dark ocean and to detect discrete ubiquitous chromophores.

(3) To identify the main fluorophores of the global ocean by Parallel Factor Analysis (PARAFAC).

(4) To characterize the FDOM by biogeographic provinces in the epipelagic zone and by water masses in the meso- and bathypelagic zone, respectively.

(5) To evaluate the DOM optical transformations over time by the relationships with ageing indicators such as apparent oxygen utilization (AOU) and oxygen utilization rate (OUR) and ideal age.

(6) To calculate the net production rates and turnover times of CDOM and FDOM in the dark ocean.

10. Structure of this PhD thesis

This PhD dissertation is structured in 4 chapters corresponding to four scientific papers that address the aforementioned objectives through *in situ* measurements in the ocean, empirical modelling and analytical work.

Chapter 1 embraces an inventory of the CDOM optical properties of the water masses intercepted along the Atlantic, Indian and Pacific oceans during the Malaspina 2010 expedition through a water mass analysis in which 22 water types (WT) were detected. We intercepted 13 central WT representing 26.3%, 5 intermediate waters representing 21.5% and 4 abyssal WT that accounted for 52.2% of the total volume sampled. The most abundant WT for the central, intermediate and abyssal layers with respect to the total water volume were the 13ºC water of the Equatorial Pacific (13EqPac) with 5.7%, the Sub-Antarctic Mode Water (SAMW) with 8.0% and the Circumpolar Deep Water with 27.0%, respectively. We also estimated the average OUR of the dark global ocean occupied

during the circumnavigation in 0.5 ± 0.1 μmol kg^{-1} yr^{-1}. Most of this oxygen is consumed in the central waters (58%) followed by the abyssal (25%) and, finally, the intermediate (17%) waters. We also reported that the activation energy (E_a) and coefficient Q_{10} that we obtained for OUR in this study (108 ± 10 kJ mol^{-1} and 5.2 ± 0.9, respectively) were approximately 3 and 2 times higher than the expected values for the labile and the semi-labile DOM.

To trace the differential influence of ageing on CDOM, we studied the relationships of the optical parameters with AOU and OUR. We obtained that the absorption coefficient at 325 nm (a_{325}) and the fluorescence quantum yield at 340 nm (Φ_{340}) increased with water ageing whereas the spectral slope between 275–295 nm ($S_{275\text{-}295}$) and the ratio between the spectral slopes between 275–295 nm and 350–400 nm (S_R) decreased. The AOU–a_{325} positive relationship supports the assumption of *in situ* production and accumulation of CDOM as water masses turn older, and also allowed to estimate the CDOM turnover time in 634 ± 120 yr.

Chapter 2 includes the first robust inventory of two chromophoric recalcitrant microbial by-products in the major oceanic water masses. One chromophore was centred at 302 ± 3 nm and is partly due to the absorption of nitrate and likely an antioxidant species of the gadusol group, and the other one at 415 ± 3 nm with the cytochrome c oxidase (CcO) as the suggested source. These discrete chromophores have revealed as potential markers to trace the antioxidant activity and the respiration processes in the dark ocean at centennial time-scales, given that their turnover times were of ca. 350 yr.

Chapter 3 deals with the identification of four ubiquitous fluorophores intercepted during the Malaspina 2010 expedition, together with the relationships with ageing and the calculation of their turnover times. Two of them were of humic-like nature and presented positive relationships with ageing, having turnover times of 529 ± 49 and 742 ± 67 yr. In parallel, two amino acid-like fluorophores were detected, the tryptophan-like presented a negligible variation with water ageing, whereas the tyrosine-like fluorophore decayed, presenting a turnover time of 461 ± 125 yr.

Finaly, chapter 4 incorporates the global distribution of the four ubiquitous fluorophores intercepted during the Malaspina 2010 expedition in the epipelagic zone (< 200 m) by parcelling the ocean in Longhurst's biogeographic provinces. The relationships between environmental factors and fluorescence PARAFAC components in the surface global ocean revealed to be mostly non-linear, which encourages the use of GAMs for describing the large-scale variability of FDOM. GAMs results showed that the environmental drivers of the humic-like and amino acid-like fluorescent components, as well as the robustness of the relationships are not the same, with the humic-like components being primarily affected by microbial activity (AOU and Chl *a*), and the amino acid-like components by physical processes (S).

Chapter 1

Published in Global Biogeochemical Cycles
DOI: 10.1002/2014GB005048

Water mass age and ageing driving chromophoric dissolved organic matter in the dark global ocean

T. S. Catalá[1], I. Reche[1], M. Álvarez[2], S. Khatiwala[3], E. F. Guallart[4], V. M. Benítez-Barrios[5], A. Fuentes-Lema[6], C. Romera-Castillo[4,7], M. Nieto-Cid[7], C. Pelejero[4,8], E. Fraile-Nuez[5], E. Ortega-Retuerta[4], C. Marrasé[4], and X. A. Álvarez-Salgado[7]

[1]Departamento de Ecología and Instituto del Agua, Universidad de Granada, Granada, Spain, [2]IEO Centro Oceanográfico de A Coruña, Coruña, Spain, [3]Department of Earth Sciences, University of Oxford, Oxford, UK, [4]CSIC Institut de Ciències del Mar, Barcelona, Spain, [5]IEO Centro Oceanográfico de Canarias, Santa Cruz de Tenerife, Spain, [6]Departamento de Ecoloxía e Bioloxía Animal, Universidade de Vigo, Vigo, Spain, [7]CSIC Instituto de Investigacións Mariñas, Vigo, Spain, [8]Institució Catalana de Recerca i Estudis Avançats, Barcelona, Spain

Abstract

The omnipresence of chromophoric dissolved organic matter (CDOM) in the open ocean enables its use as a tracer for biochemical processes throughout the global overturning circulation. We made an inventory of CDOM optical properties, ideal water age (τ) and apparent oxygen utilization (AOU) along the Atlantic, Indian and Pacific Ocean waters sampled during the Malaspina 2010 expedition. A water mass analysis was applied to obtain intrinsic, hereinafter archetypal, values of τ, AOU, oxygen utilisation rate (OUR), and CDOM absorption coefficients, spectral slopes and quantum yield for each one of the 22 water types intercepted during this circumnavigation. Archetypal values of AOU and OUR have been used to trace the differential influence of water mass ageing and ageing rates, respectively, on CDOM variables. Whereas the absorption coefficient at 325nm (a_{325}) and the fluorescence quantum yield at 340 nm (Φ_{340}) increased, the spectral slope over the wavelength range 275–295 nm ($S_{275–295}$) and the ratio of spectral slopes over the ranges 275–295 nm and 350–400 nm (S_R) decreased significantly with water mass ageing (AOU). Combination of the slope of the linear regression between archetypal AOU and a_{325} with the estimated global OUR allowed us to obtain a CDOM turnover time of 634 ± 120 yr, which exceeds the flushing time of the dark ocean (> 200 m) by 46%. This positive relationship supports the assumption of *in situ* production and accumulation of CDOM as a by-product of microbial metabolism as water masses turn older. Furthermore, our data evidence that global-scale CDOM quantity (a_{325}) is more dependant on ageing (AOU), whereas CDOM quality ($S_{275–295}$, S_R, Φ_{340}) is more dependent on ageing rate (OUR).

Introduction

The pool of oceanic dissolved organic matter (DOM) represents, besides soil humus, the largest reservoir of organic matter of the biosphere [*Hedges,* 1992]. It contains around 700 Pg of carbon, which is equivalent to that of CO_2 in the atmosphere (828 Pg) [*Boden et al., 2011*]. Most marine organic matter is originated from phytoplankton photosynthesis in the surface ocean; the vast majority (80%) enters the ocean interior as particulate organic matter (POM), either suspended or sinking,

and the dissolved fraction (DOM) represents 20% of total organic carbon flux [*Carlson et al.,* 1994; *Six and Maier-Reimer,* 1996; *Hansell et al.,* 2009], and serves as substrate supporting heterotrophic prokaryotic metabolism [*Hansell,* 2013]. At present, the global carbon flux to the ocean interior as DOM is about 2 Pg Cyr^{-1} [*Hansell et al.,* 2009; *Hansell*, 2013], which is similar to the annual ocean uptake of anthropogenic CO_2 [*Gruber et al.*, 2009].

Most of the phytoplankton-derived organic matter is biologically labile and has a very short lifetime (hours to days), being quickly respired back to CO_2 in the illuminated zone. However, a portion of the fixed carbon that escapes rapid mineralization is transformed (biotically or abiotically) into resistant material, and accumulates as recalcitrant DOM, creating the enormous ocean reservoir of dissolved organic carbon (DOC) [*Hansell et al.*, 2009, 2012; *Hansell*, 2013]. The microbial-mediated transformation of labile into refractory DOM was first postulated by *Ogawa et al.* [2001] and was termed as 'microbial carbon pump' (MCP) by *Jiao et al.* [2010], who formalized the idea in a wider context. *Benner and Herndl* [2011] estimated that approximately 23% of the bulk oceanic DOC pool (155 Pg C) was sequestered by the MCP in the global ocean and *Kattner et al.* [2011] and *Arrieta et al.* [2015] suggested the low concentration of the thousands of individual DOM constituents in the dark ocean as a possible cause for the inability of prokaryotes to use RDOM as a carbon source. In this study, we provide new insights to the RDOM characterization and its distribution by taking advantage of the ability of a fraction of the RDOM to absorb light.

The fraction of dissolved organic matter (DOM) that absorbs light in the ultraviolet and, to a lesser extent, in the visible range of the spectrum is named chromophoric dissolved organic matter (CDOM). Typically, UV-visible absorption spectra for CDOM increase exponentially with decreasing wavelength [*Twardowski et al.,* 2004]. To obtain information about the origin, processing and fate of CDOM from the spectra, several variables have been described and can be gathered into: (1) 'Quantitative' variables (i.e. absorption coefficients at specific wavelengths), which are a proxy of the CDOM concentration (being 254 and 325 nm the most commonly used wavelengths) and (2) 'Qualitative' variables (i.e. spectral slopes, molar extinction coefficients, absorption coefficient ratios and quantum yields), which are largely independent of the concentration and provide information about the origin, molecular weight and chemical structure of CDOM [*Brown,* 1977; *Weishaar et al.*, 2003; *Helms et al.*, 2008; *Nelson and Siegel*, 2013].

The first attempts to map the CDOM in the surface ocean were conducted to cope with the accuracy of global satellite-based measurements of ocean chlorophyll and primary production [*Siegel et al.,* 2005; *Ortega-Retuerta et al.*, 2010]. Since the interest on CDOM distribution throughout the water column is more recent, global databases are not still very abundant. Furthermore, most studies addressed this matter from a geographical perspective, describing differences among ocean basins and depths in epi-, meso- and bathypelagic layers [*Nelson et al.,* 2007; 2010]. The novelty of our approach is that we describe the distribution of CDOM by

considering the main water masses crossed by the circumnavigation. The aims of this study are (1) to make an inventory of the CDOM optical properties of the main water masses of the dark global ocean by using 'quantitative' (i.e. absorption coefficients) and 'qualitative' spectral variables; (2) to trace the basin scale mineralization processes affecting these CDOM optical properties using a water mass analysis; (3) to estimate the turnover time of the CDOM in the dark ocean; and (4) to assess the effect of 'age' and 'ageing' on CDOM optical properties. In this context, 'age' is defined as the elapsed time since the water was last in contact with the atmosphere, and 'ageing' (traced through apparent oxygen utilization, AOU) refers to the consumption of oxygen over that period. To pursue our goals, we performed the following activities: (1) a water mass analysis to obtain the proportion of the main water types (WT) intercepted during the Malaspina 2010 circumnavigation in the central, intermediate and abyssal waters of the global ocean; (2) an inventory of ideal ages, AOU, oxygen utilization rates (OUR) and spectral variables of the main water masses of the dark ocean; and (3) a regression analyses of the relationship of these spectral variables with the ideal age and 'ageing' (AOU) of the water masses at the global scale.

Materials and Methods

Sampling site and measurements

The Malaspina 2010 circumnavigation was conducted from December 2010 to July 2011 on board R/V Hesperides along the Atlantic, Indian and Pacific oceans, spanning latitudes from 34ºN to 40ºS (Fig. 1.1). During the cruise, 147 CTD stations were carried out with a Seabird 911+ from surface to 4000 m depth. Water samples were collected at each station with a 24–10 L Niskin bottles rosette. The CTD was equipped with a redundant temperature and salinity sensor for intercomparison during the cruise and a polarographic membrane oxygen sensor Seabird SBE-43. Temperature and pressure sensors were calibrated at the SeaBird laboratory before the cruise. On board salinity calibration was carried out with a Guildline AUTOSAL model 8410 A salinometer with a precision higher than 0.002 for single samples and the potentiometric end-point Winkler method for the calibration of the oxygen sensor. Oxygen saturation was calculated from practical salinity and potential temperature with the equation of *Benson and Krause* [1984]. Apparent oxygen utilization (AOU) was calculated as the difference between the saturation and measured dissolved oxygen concentrations.

The UV-visible absorption coefficient of CDOM was determined from 250 to 750 nm at 1 nm intervals in 10-cm path length quartz cuvettes in a double beam Perkin Elmer lambda 850 spectrophotometer. The estimated detection limit of this spectrophotometer for quantifying CDOM absorption is 0.001 absorbance units or 0.02 m^{-1}.

Samples for the determination of the absorption spectrum of CDOM were not filtered because light absorption due to pigments and detrital particles contribute only to a minor fraction of the open ocean CDOM absorption [*Nelson et al.,* 1998; 2007], particularly at the depths (200–4000 m) covered by this study. At

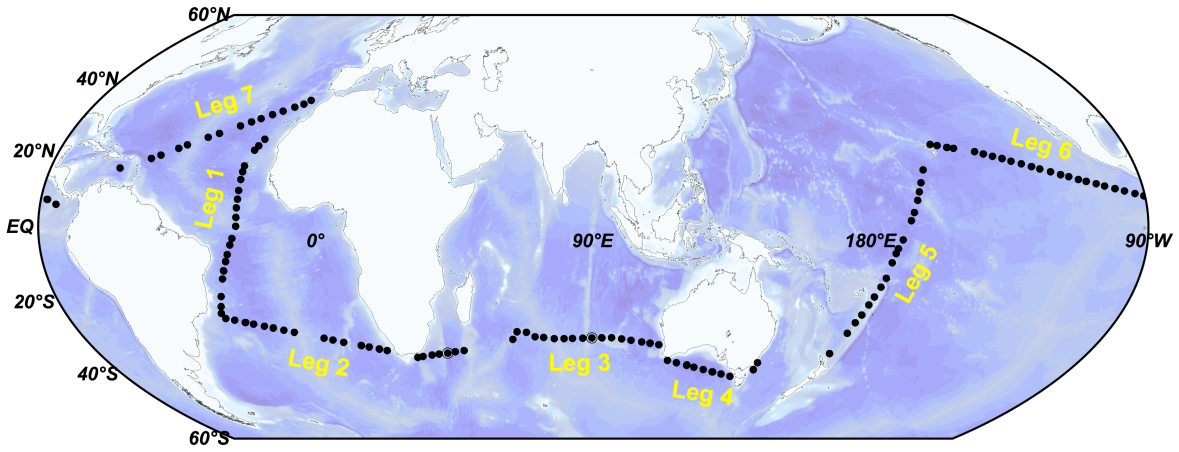

Fig. 1.1. Cruise track of the Malaspina 2010 circunnavigation on board the Spanish R/V Hespérides from 16 December 2010 to 11 July 2011.

each station, samples were drawn from Niskin bottles at 8 discrete depths throughout the water column, poured directly into acid cleaned 250 mL glass bottles and immediately stored in dark conditions to allow equilibration with room temperature and to avoid photobleaching. The time elapsed between sample collection and determination did not exceed 2 hours. A blank was measured every 5 samples to detect and correct (linearly) any instrument drift. To minimize any effect of light scattering by particles and microbubbles, samples were stirred vigorously and then settled to let any particles fall to the bottom of the flask before measuring. During the measurements, we first checked that the differences between sample and baseline absorbance at long wavelengths (> 600 nm) maintained < 0.0005 absorbance units. In the case that difference was > 0.0005 absorbance units, we renewed the water in the sample cuvette and repeated the measurement. In most cases, we got a final difference < 0.0005 absorbance units. To correct this generally minor effect of light scattering we applied a wavelength-independent correction proposed by *Green and Blough* [1994], which consists on subtracting the average absorbance in the 600–750 nm wavelength range to the measured absorption spectrum. We chose the wavelength-independent correction instead of the wavelength-dependent correction proposed by *Bricaud et al.* [1981] because the low differences between sample and baseline absorbance at long wavelengths did not produce measurable differences between both corrections at short wavelengths.

Absorbance at 325 nm was converted into absorption coefficient (m^{-1}, a_{325}) [*Green and Blough*, 1994] using the equation:

$$a_{325} = 2.303 \frac{[Abs_{325} - Abs_{600-750}]}{l} \qquad (1)$$

where Abs_{325} is the absorbance at a wavelength of 325 nm, $Abs_{600-750}$ is the average absorbance between 600 and 750 nm, l is the path length of the cuvette (0.1 m) and 2.303 is the factor that converts from decadic to natural logarithms.

Helms et al. [2008] emphasized the potential of the spectral slopes as a tool for the structural characterization of CDOM and

calculated them from the linear regression of log-transformed absorption spectra. They chose the 275–295 nm and 350–400 nm wavelength ranges because there are intervals identified as the most dynamic regions of the natural log transformed absorption spectra [*Helms et al.*, 2013] and appear to be particularly sensitive to shifts in molecular weight or DOM sources [*Helms et al.*, 2008]. After a previous quality check, those slopes with $R^2 < 0.95$ for $S_{275-295}$ and $R^2 < 0.85$ for $S_{350-400}$ were deleted. As a consequence, the dataset of $S_{275-295}$ and $S_{350-400}$ were reduced from 742 to 737 and 717 samples, respectively. A dimensionless variable, the slope ratio (S_R), was calculated as the ratio of the slope of the shorter wavelength region (275–295 nm) to that of the longer wavelength region (350–400 nm).

The quantum yield of DOM fluorescence at excitation 340 nm, Φ_{340}, is the proportion of light absorbed at 340 nm, a_{340}, that is re-emitted as fluorescent light between 360 and 560 nm, $F_{360-560}$, and was calculated as in *Green and Blough* [1994]:

$$\Phi_{340} = \Phi_{340(\mathrm{QS})} \cdot \frac{F_{360-560}}{a_{340}} \cdot \frac{a_{340(\mathrm{QS})}}{F_{360-560(\mathrm{QS})}} \quad (2)$$

where $\Phi_{340(\mathrm{QS})}$ is the dimensionless fluorescence quantum yield of quinine sulphate (the standard used to calibrate fluorescence measurements), 0.54 [*Melhuish*, 1961], and $F_{360-560}$ is the integral of fluorescence intensity at an excitation/emission of 340/360–560 nm. Fluorescent measurements were taken with a JY-Horiba Spex Fluoromax-4 spectrofluorometer and the sample scan was reported at an emission interval between 350–560 nm after exciting it at 340 nm. Fluorescence units were converted to Raman units dividing by the Raman area for further comparison with other studies [see more details in chapter III of this PhD thesis]. Whereas simple chemical structures containing carbon double bounds are capable of absorbing radiation, fluorescence emission is uniquely produced under the presence of the more complex aromatic rings. Therefore, higher values of Φ_{340} are indicative of a higher proportion of aromatic compounds [*Green and Blough,* 2004; *Romera-Castillo et al.,* 2011].

Estimation of the water sample age

Water sample ages (τ) were derived from *Khatiwala et al.* [2009; 2012] by interpolating their gridded mean age estimates to our sample time, locations and depths. As described by these authors, they used an inverse technique to estimate the ocean's mean age from tracer observations. A mathematically rigorous approach that accounts for the multiplicity of transport pathways and transit times characteristic of an eddy-diffusive flow such as the ocean allowed them to quantify ventilation in terms of a probability distribution that partitions fluid parcels according to the time and location of their last contact with the surface. Such a distribution is known as a boundary propagator (or more generically a Green function). The ideal mean age is the first moment of the boundary propagator integrated over the entire surface of the ocean (sometimes called a 'transit time distribution' or TTD) and is interpreted as the average time since a water parcel was last in contact with the surface. *Khatiwala et al.* [2009; 2012] developed a maximum entropy-based inverse technique to deconvolve the ocean's boundary propagator

from tracer observations, which they applied to gridded fields of radiocarbon, cluorofluorocarbons (CFCs) and hydrographic (temperature, salinity, phosphate, and oxygen) data.

Water mass analysis

The dark ocean (from 200 m to the bottom) can be described by the mixing of distinct water masses. A water mass is a body of water defined by its intrinsic thermohaline and chemical characteristics that, in turn, can be described by one or more water types (WT) [*Tomczak,* 1999].

The strategy to sample the dark ocean during the Malaspina circumnavigation was not in favour of collecting water from fixed depth levels but from extreme values of salinity, temperature and dissolved oxygen. This procedure allowed us covering the cores of flow of the most abundant WT of the dark global ocean (depth ≥ 200m, θ < 18ºC, AOU > 0) and, therefore, performing a robust calculation of the different WT proportions that contribute to any of the 742 CDOM samples collected during the circumnavigation by means of a classical water mass analysis [*Kartensen and Tomczak,* 1998]. We have characterized the WT on basis of its salinity (S) and potential temperature (θ), which are assumed to be conservative variables.

The equations to be solved for a specific water sample j are:

$$100 = \sum_i x_{ij} \qquad (3)$$

$$\theta_j = \sum_i x_{ij} \cdot \theta_i \qquad (4)$$

$$S_j = \sum_i x_{ij} \cdot S_i \qquad (5)$$

where x_{ij} is the proportion of WT i in sample j; θ_j and S_j are the thermohaline characteristics of sample j; θ_i and S_i are the fixed thermohaline characteristic of WT i in the area where it is defined. Furthermore, the solution of the multi-parameter water mass analysis includes an additional constrain: all contributions must sum up to 100% and have to be non-negative.

We have identified 22 water types in the route followed during the Malaspina 2010 circumnavigation (chapter 3 of this PhD thesis; see Appendix II). They were divided into three domains according to their depth: central (200-500 m), intermediate (500-1500 m) and abyssal (>1500 m). In the central domain we identified Eighteen Degrees Water (EDW), Eastern North Atlantic Central Water (ENACW), defined by two WT of 12ºC and 15ºC, 13ºC water of the Equatorial Atlantic (13EqAtl), South Atlantic Central Water (SACW), defined by two WT of 12ºC and 18ºC, Indian Subtropical Mode Water ($STMW_I$), Indian Central Water of 13ºC (ICW_{13}), South Pacific Subtropical Mode Water ($STMW_{SP}$), South Pacific Central Water of 20ºC ($SPCW_{20}$), 13ºC water of the Equatorial Pacific (13EqPac), North Pacific Subtropical Mode Water ($STMW_{NP}$), and North Pacific Central Mode Water (CMW_{NP}). In the intermediate domain we found Mediterranean Water (MW), Antarctic Intermediate Water (AAIW), defined by two WT of 3.1ºC and 5.0ºC, Sub-Antarctic Mode Water (SAMW) and North Pacific Intermediate Water (NPIW). In the abyssal domain we identified

Circumpolar Deep Water (CDW), North Atlantic Deep Water (NADW), defined by two types of 2°C and 4.6°C, and Antarctic Bottom Water (AABW).

Equations (3)–(5) allow solving the simultaneous mixing of a maximum of three WT on basis of reasonable vertical and geographical constraints to the water mass mixing. Concerning the vertical constraints, for a given region of the ocean, every WT will mix only with the water types situated immediately above and below according to their density. Regarding the geographical constraints, every WT will mix preferentially with water types in their surroundings. With these considerations in mind, we deconvolved the 742 samples collected during the circumnavigation into 24 pairs/triads that group water samples with common WT composition (see Fig. 1 in Appendix II).

Volume of each water type collected during the Malaspina circumnavigation

Once the WT proportions (x_{ij}) are known, the fraction of the total volume of water sampled during the Malaspina 2010 circumnavigation that corresponds to WT i (%VOLi) can be calculated as:

$$\%VOL_i = \frac{\sum_j x_{ij}}{n} \qquad (6)$$

where n is the number of samples.

Archetypal values and oxygen utilization rate (OUR) estimation

The archetypal value of variable N for water type i (Ni) is the weighted-average value of N in the center of mass of WTi in the study area. According to *Álvarez-Salgado et al.* [2013], archetypes retain information about the variability of N that can be attributed to mixing of water types and basin-scale mineralization processes from the site where the water types were defined to their respective centers of mass along the circumnavigation. Archetypal values of depth (z), water age (τ), apparent oxygen utilization (AOU), a_{325}, $S_{275\text{-}295}$, S_R and Φ_{340} were calculated for the 22 WT intercepted by the Malaspina cruise track as follows:

$$N_i = \frac{\sum_j x_{ij} \cdot N_j}{\sum_j x_{ij}} \qquad (7)$$

where N_j is the value of variable N (z, τ, AOU, OUR, a_{325}, $S_{275\text{-}295}$, S_R and Φ_{340}) in sample j; and x_{ij} is the proportion of WT_i in sample j.

The standard deviation of N_i (SDN_i), which should be interpreted as an estimate of the robustness of the calculation, was obtained as:

$$SDN_i = \frac{\sqrt{\sum_j x_{ij} \cdot (N_j - N_i)^2}}{\sum_j x_{ij}} \qquad (8)$$

Similarly, the archetypal value of N in every sample ($<N_j>$) was calculated as:

$$< N_j > = \frac{\sum_i x_{ij} \cdot N_i}{100} \qquad (9)$$

The determination coefficient (R^2) and standard deviation of the residuals (SD res) of the linear regressions between the measured (N_j) and arquetypal values ($<N_j>$) of variable N were obtained. Whereas, R^2 allows assessing the degree of dependence of variable N on WT mixing and basin scale mineralization in the dark ocean, SD res informs on the average error incurred when estimating the measured from the archetypal values.

Division of AOU_i (in μmol kg^{-1}) by τ_i (in yr) provides a measure of the archetypal oxygen utilization rate (OUR) of each water type, an indicator of the velocity at which the

mineralization of organic matter occurs in oxygenic environments [*Jenkins,* 1982]. Specifically, the archetypal oxygen utilization rate of each WT, OUR_i (in μmol kg^{-1} yr^{-1}), represents the average rate of oxygen consumption from the area where the WT_i is formed to its center of mass along the Malaspina cruise track. To perform this calculation, we have assumed that water masses are in equilibrium with the atmosphere in their formation areas (i.e. the initial AOU of any WT is 0). Since we are aware that this assumption may not be totally accurate [*Ito et al.,* 2004], the OUR_i values obtained with this procedure could be, to some extent, overestimated.

Calculation of the global production of CDOM and its turnover time

To estimate the CDOM production in the dark global ocean (see the results in section 3.4), we have followed the procedures applied by *Yamashita and Tanoue* [2008] and *Catalá et al.* (chapter III of this PhD thesis) to calculate the global production of marine fluorescent humic-like substances on the basis of the slope of the relationship between fluorescent dissolved organic matter (FDOM) and AOU, but applied in our case to CDOM and AOU. Therefore, the global net production of a_{325}, NP_{a325} (in m^{-1} yr^{-1}), was obtained as:

$$NP_{a325} = \left(\frac{\partial a_{325}}{\partial AOU}\right) \cdot OUR_{global} \qquad (10)$$

where $\frac{\partial a_{325}}{\partial AOU}$ is the absorption coefficient rate of change per AOU unit for the global dark ocean and OUR_{global} is the total oxygen consumption rate that is obtained as:

$$OUR_{global} = \frac{\sum_i VOL_i \cdot OUR_i}{100} \qquad (11)$$

Once the NP_{a325} was obtained, we calculated the CDOM turnover time as:

$$Turnover\ time = \frac{\sum_i VOL_i \cdot a_{325_i}}{100 \cdot NP_{a325}} \qquad (12)$$

Where $\frac{\sum_i VOL_i \cdot a_{325i}}{100}$ is the WT proportion weighted-average absorbance of the dark global ocean.

Statistical analysis

Linear regression analyses between the different values (measured, archetypal) of τ, AOU, OUR, a_{325}, $S_{275-295}$, S_R and Φ_{340}, were performed using the Statistica 7.0 software. Linear regression analyses were also used for the Arrhenius plot. We applied model II regressions because we have no control of the variables used [*Sokal and Rolf*, 1995].

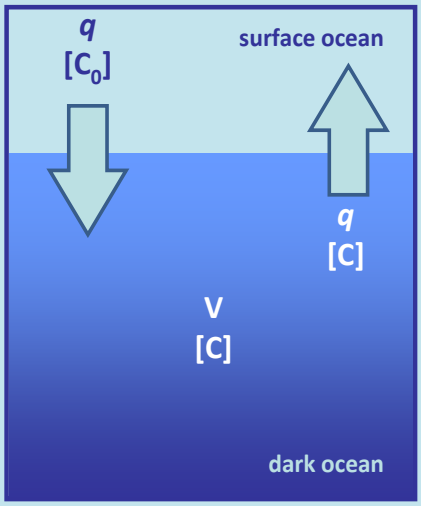

The differential equation defining the rate of change of any substance, C, in the global dark ocean is:

$$Vx\frac{d[C]}{dt} = q\ x\ ([C_o] - [C]) + NP \qquad \textbf{[1]}$$

Where *V* is the volume of the dark global ocean; [C_0] and [*C*] the average concentrations of C in the global surface and dark ocean, respectively; *q* the exchange rate of water between the global surface and dark ocean; and *NP* the net production rate of C in the global dark ocean.

Assuming that C is in steady-state, *d*[*C*]/*dt* = 0 and, therefore:

$$NP = -\ q \times ([C_0] - [C]) \qquad \textbf{[2]}$$

The turnover time of any substance, C, is calculated as the ratio between the total amount of C in the dark global (*V x [C]*) and its net production rate (*NP*). If *NP* ≥ 0 (as for the case of CDOM), the turnover time is calculated as:

$$turnover\ time = \frac{Vx[C]}{NP} = \frac{[C]}{(NP/V)} \qquad \textbf{[3]}$$

In this manuscript, we calculated the total amount of CDOM ([*C*]) as the water mass weighted average absorption coefficient at 325 nm (a_{325}, in m^{-1}). The volumetric net production rate (*NP/V*, in m^{-1} yr^{-1}) was obtained by multiplying the slope of the linear correlation between a_{325} and AOU (in m^{-1} µmol kg^{-1} yr^{-1}) by the water mass weighted average oxygen utilization rate (OUR, in µmol yr^{-1}).

On the contrary, when NP ≤ 0, i.e. if net consumption of C occurs, then the turnover time should be calculated as:

$$turnover\ time = -\frac{Vx[C]}{NP} \qquad \textbf{[4]}$$

This is the case of DOC. Following *Hansell et al.* [2009], about 1.8 Pg C yr^{-1} of DOC are exported to the dark global ocean (defined by these authors as depths > 100m), where it has to be mineralized or removed by other processes to keep the global amount of DOC (662 Pg) constant. Therefore, *V x [C]* = 662 Pg C and NP = -1.8 Pg C yr^{-1} producing a turnover time of 370 yr. In fact, *Hansell et al.* [2009] did this calculation but named it as 'residence time'. In *Hansell* [2013], he refers ageing to a net production of recalcitrant DOC of about 1.9 Pg C yr^{-1} and a total amount of recalcitrant DOC of 662 Pg C, which would translate into a turnover (or residence) time of about 350 yr in the dark global ocean.

In summary, since the turnover times of CDOM and DOC are calculated in the same way, they are directly comparable. Furthermore, it should be noted that if *NP* is replaced by $-\ q \times ([C_0] - [C])$ in equation **[4]** then:

$$turnover\ time = \frac{Vx[C]}{NP} = -\frac{V}{q}x\frac{[C]}{[C_o]-[C]} = -t_R\ x\frac{[C]}{[C_o]-[C]} \qquad \textbf{[5]}$$

Results

Water types (WT) distribution in the three ocean basins

A classical water mass analysis of the thermohaline properties of the central, intermediate and abyssal waters (200–4000 m) of the North and South Atlantic, South Indian and South and North Pacific Oceans was used to determine (i) the water mass proportions on each individual sample collected during the circumnavigation; (ii) the water mass proportion-weighted average value of the different CDOM variables; and (iii) the variability of CDOM due to water mass mixing and basin-scale mineralization processes from the source point to the center of mass of the WT within the circumnavigation.

In this study, 22 WT were identified (see Appendix II). We intercepted 13 central WT representing 26.3% of the total water volume sampled, with the 13EqPac accounting for 5.7% and spreading on the South and North Pacific at an archetypal depth (Z_i) of 483 ± 35 m (Fig. 1.2a). We sampled 5 intermediate waters, representing 21.5% of the total volume, and the most prominent were: SAMW, corresponding to 8.0% of the total volume and located mostly in the Indian Ocean and the Great Australian Bight at an archetypal depth (Z_i) of 719 ± 42 m (Fig. 1.2b), AAIW, which accounted for 7.4% including its two branches (3.1 and 5.0°C) and was basically located in the South Atlantic and below the SAMW in the Indian Ocean and the Great Australian Bight, at a Z_i of 1066 ± 80 m (Fig. 1.2c), and NPIW, corresponding to 5.9% of the total volume and located in the North Pacific at a Z_i of 671 ± 65 m (Fig. 1.2d). Finally, we intercepted 4 abyssal WT that accounted for 52.2% and the CDW was the dominant WT in the deep Indian, South and North Pacific basins at a Z_i of 2412 ± 76 m, representing 27.0% of the total volume sampled (Fig. 1.2e). The deep Atlantic waters were dominated by the upper + middle (4.6°C) and lower (2°C) branches of the NADW, representing 20.5% of the total sampled water at Z_i of 1582 ± 99 m and 3780 ± 64 m, respectively (WT weighted-average equals to 2649 ± 78 m) (Fig. 1.2f).

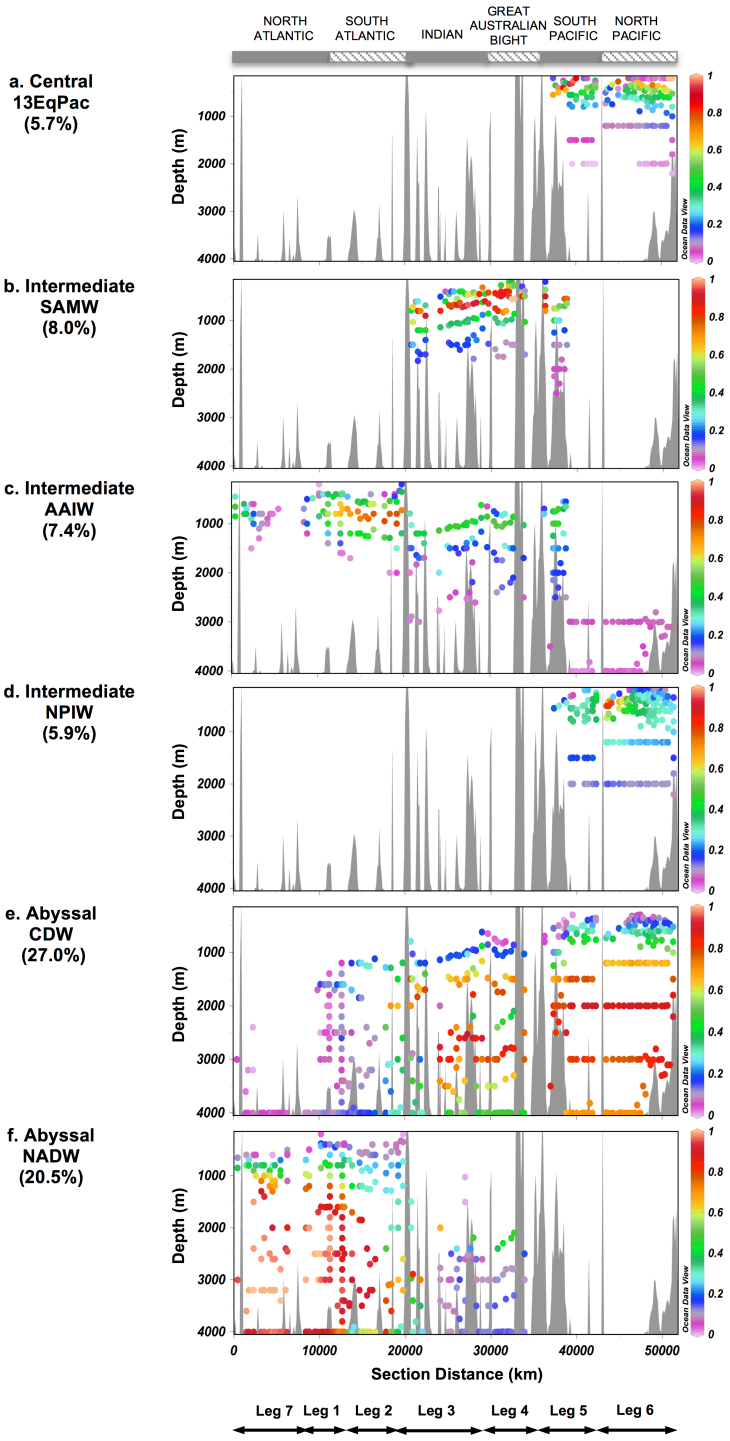

Fig. 1.2. Distribution of the most representative water masses of the dark global ocean during the Malaspina 2010 circumnavigation: (a) Equatorial Pacific Central Water at 13 °C (13EqPac), (b) Sub-Antarctic Mode Water (SAMW), (c) Antarctic Intermediate Water (AAIW), (d) North Pacific Intermediate Water (NPIW), (e) Circumpolar Deep Water (CDW) and (f) North Atlantic Deep Water (NADW). Note that the proportion ranges from 0 (0%) to 1 (100%) and the depth range starts at 200 m.

Basin-scale characterization: ideal water age (τ), apparent oxygen utilization (AOU) and oxygen utilization rate (OUR)

Water ages (τ) of the samples collected in the dark ocean during the circumnavigation ranged between 0 and 1900 yr. The oldest waters were tracked in the southern region o the South Pacific at around 2000 m (Fig. 1. 3a). AABW and CDW presented the oldest archetypal ages with 745 ± 47 and 821 ± 22 yr, respectively (Table 1.1). The youngest waters were located in the central domain of all ocean basins except in the North Pacific, with ages of 259 ± 16 and 433 ± 34 yr for the CMW_{NP} and 13EqPac, respectively. Note that the young waters of the North Atlantic sank deeper into the water column (Fig. 1.3a). The youngest archetypal ages of all WT were 11 ± 4 yr for the EDW formed in the Sargasso Sea and 14 ± 17 yr for the STMWI formed in the subtropical gyre of the Indian Ocean (Table 1.1). The average age of the central, intermediate and deep waters intercepted by the cruise track were 170 ± 17, 367 ± 33 and 638 ± 20 yr, respectively. Overall, the average age of the waters from 200 to 4000 m was 454 ± 22 yr.

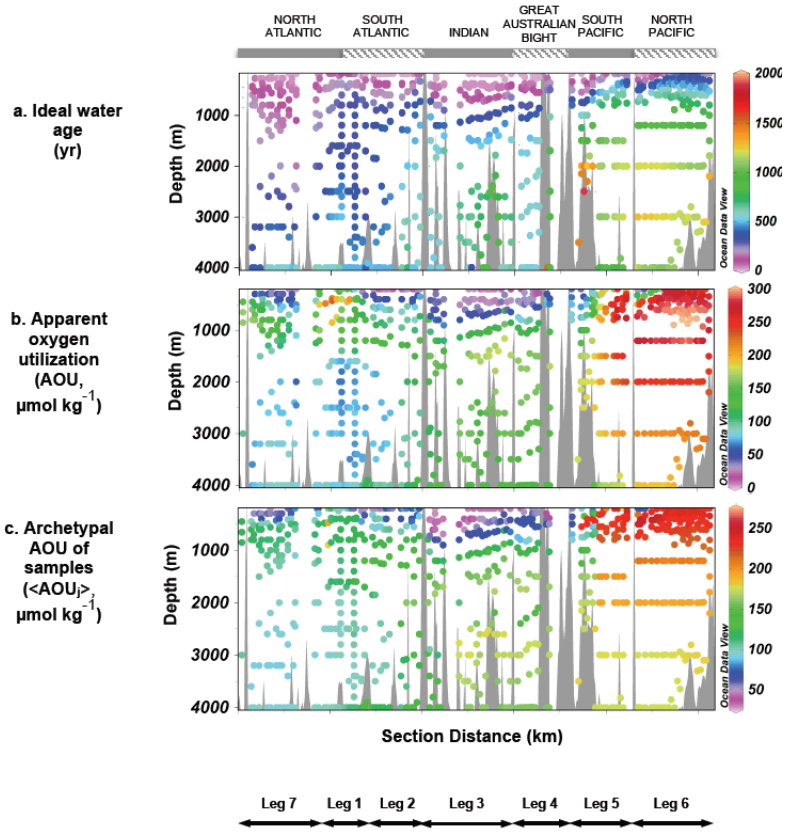

Fig. 1.3. Distribution of (a) ideal water age (τ, yr), (b) apparent oxygen utilization (AOU, µmol kg^{-1}), (c) arquetypal apparent oxygen utilization (<AOU_i>, µmol kg^{-1}) of the water samples intercepted during the Malaspina 2010 expedition. Note that the depth range starts at 200 m.

AOU varied between 5 and 299 μmol kg^{-1} (Fig. 1.3b) showing an increase with water mass age along the global overturning circulation (Fig. 2.3a). Maximum AOUi values were recorded in the central and intermediate waters of the Equatorial and North Pacific: NPIW (255 ± 10 μmol kg^{-1}), CMW_{NP} (234 ± 10 μmol kg^{-1}), 13EqPac (231 ± 6 μmol kg^{-1}) (Table 1.1). Minimum archetypal values corresponded to the central waters of the South Indian and South Atlantic oceans, with $STMW_I$, ICW_{13}, $SACW_{18}$ presenting 26 ± 2, 32 ± 2 and 38 ± 12 μmol kg^{-1}, respectively (Table 1.1). The linear regression between the measured (AOU_j) (Fig. 1.3b) and arquetypal ($<AOU_j>$) (Fig. 1.3c) values of AOU in the dark global ocean (R^2 = 0.80; Table 2.1), indicates that 80% of the variability of AOU is retained by the basin-scale mineralization processes from the source region of each water mass to its center of mass in the Malaspina 2010 cruise track.

OUR_i values ranged from 0.2 to 4 μmol kg^{-1} yr^{-1} (Table 1.1), exhibiting the characteristic power law decrease with depth ($OUR_i = 0.5\ (\pm 0.1) \cdot (Z_i)^{-0.75(\pm 0.12)}$; R^2 = 0.67; $p<0.05$, Fig. 1.4a). The WT with maximum and minimum OUR_i were the EDW with 4 ± 2 μmol kg^{-1} yr^{-1} and the $NADW_2$ with 0.19 ± 0.01 μmol kg^{-1} yr^{-1}, respectively. The average OUR of the central, intermediate and abyssal waters occupied during the circumnavigation were 1.1 ± 0.4, 0.39 ± 0.06 and 0.23 ± 0.01 μmol kg^{-1} yr^{-1}, respectively, and the average OUR of the waters occupied during the circumnavigation from 200 to 4000 m, hereinafter OUR_{global}, was 0.5 ± 0.1 μmol kg^{-1} yr^{-1}. Extrapolating this rate to the dark global ocean (with a total mass of 1.38 $x10^{21}$ kg at a depth > 200m) yields a total oxygen consumption of 0.68 ± 0.18 Pmol O_2 yr^{-1}. Most of this oxygen is consumed in the central waters (58%) followed by the abyssal (25%) and, finally, the intermediate (17%) waters.

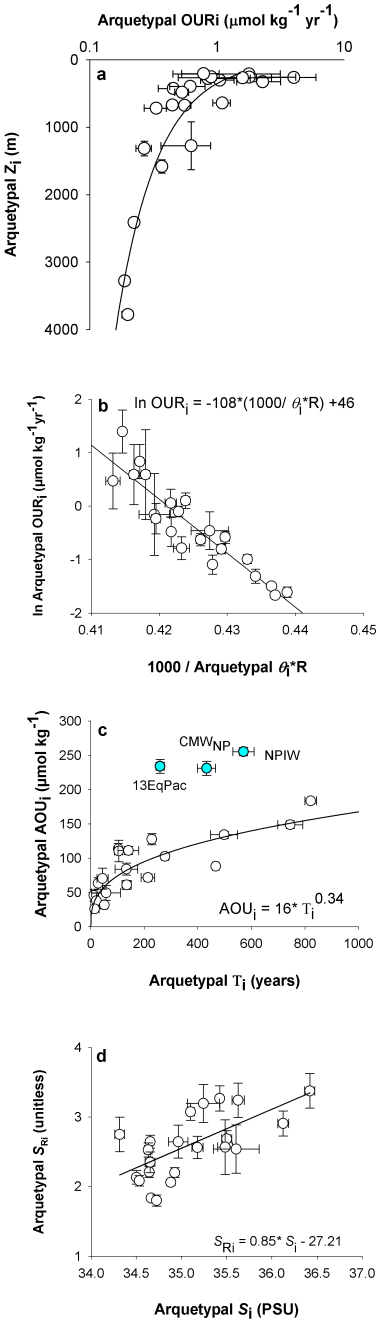

Fig. 1.4. Relationships between (a) OUR_i (µmol kg^{-1} yr^{-1}) and depth (Z_i), (b) OUR_i (µmol kg^{-1} yr^{-1}) and 1000/(R.(273.15+θ)), (c) τi (yr) and AOU_i (µmol kg^{-1}), and (d) Salinity (S_i) (PSU) and S_{Ri} (unitless). The relationships were fitted to the following functions: OUR_i = 0.5 (±0.1) x Z_i -0.75(± 0.12), R^2 = 0.67 (p <0.05, n = 22); ln OUR_i = -108 (±10) x 1000/(TxR) + 46 (±4), R^2 = 0.85 (p <0.001, n = 22); AOU_i = 16 (±5) x τ_i 0.34(±0.06), R^2 = 0.72 (p < 0.001, n = 19 (the NPIW, 13EqPac and CMW_{NP} were ruled out from the power law regression); S_{Ri} = 0.85 (±0.22) x S_i - 27.21 (± 7.97), R^2 = 0.43 (p = 0.001, n = 22).

Table 1.1. Archetypal depth (Z_i, m), potential temperature (θ_i, °C), ideal water age ($\boldsymbol{\tau_i}$, yr), apparent oxygen utilization (AOU_i, µmol kg^{-1}), oxygen utilization rate (OUR_i, µmol kg^{-1} yr^{-1}), absorption coefficient at 325 nm (a_{325i}, m^{-1}), slope between 275-295 nm ($S_{275-295i}$, µm^{-1}), ratio of the slope between 275-295 nm divided by the slope between 350_400 nm (S_{Ri}, unitless) and the quantum yield at 340 nm (Φ_{340i}, %) of the central, intermediate, and abyssal water mass intercepted during the Malaspina 2010 expedition. The percentage of the total volume of water sampled that corresponded to each water mass (VOL_i, %) is also reported.

Acronym	VOL_i (%)	Z_i (m)	θ_i (ºC)	τ_i (yr)	AOU_i (µmol kg^{-1})	OUR_i (µmol kg^{-1} y^{-1})	a_{325i} (m^{-1})	$S_{275-295i}$ (µm^{-1})	S_{Ri} (unitless)	Φ_{340i} (%)
EDW	0.7	264 ± 20	17.1 ± 0.3	11 ± 4	46 ± 8	4 ± 2	0.26 ± 0.04	28 ± 2	3.4 ± 0.2	0.7 ± 0.1
$ENACW_{12}$	3.2	641 ± 40	10.7 ± 0.4	103 ± 9	114 ± 8	1.1 ± 0.2	0.24 ± 0.02	25 ± 1	2.7 ± 0.1	1.0 ± 0.1
$ENACW_{15}$	1.8	327 ± 25	15.3 ± 0.4	28 ± 7	63 ± 8	2.3 ± 0.9	0.26 ± 0.02	28 ± 1	2.9 ± 0.2	0.8 ± 0.1
13EqAtl	1.6	427 ± 37	11.1 ± 0.8	134 ± 18	61 ± 7	0.5 ± 0.1	0.17 ± 0.02	30 ± 2	2.6 ± 0.2	1.1 ± 0.1
$SACW_{12}$	2.2	303 ± 26	12.2 ± 0.6	104 ± 16	110 ± 16	1.1 ± 0.3	0.20 ± 0.01	26 ± 1	2.6 ± 0.2	1.0 ± 0.1
$SACW_{18}$	1.4	211 ± 11	15.9 ± 0.4	21 ± 9	38 ± 12	2 ± 1	0.18 ± 0.02	31 ± 2	3.2 ± 0.2	0.8 ± 0.1
$STMW_I$	0.9	259 ± 35	14.7 ± 0.4	14 ± 17	26 ± 3	2 ± 2	0.14 ± 0.01	36 ± 2	3.3 ± 0.2	0.9 ± 0.1
ICW_{13}	4.5	395 ± 28	12.2 ± 0.3	51 ± 12	32 ± 2	0.6 ± 0.2	0.15 ± 0.01	33 ± 1	3.1 ± 0.1	0.9 ± 0.1
$STMW_{SP}$	0.2	269 ± 26	13.8 ± 1.5	58 ± 54	49 ± 11	0.9 ± 1.0	0.10 ± 0.03	40 ± 7	3.2 ± 0.3	1.7 ± 0.4
$SPCW_{20}$	0.5	277 ± 84	18.1 ± 21	44 ± 21	70 ± 15	2 ± 1	0.15 ± 0.04	33 ± 4	2.6 ± 0.4	1.1 ± 0.4
13EqPac	5.7	483 ± 35	9.3 ± 0.4	433 ± 34	231 ± 10	0.53 ± 0.07	0.27 ± 0.01	19 ± 1	2.2 ± 0.1	1.0 ± 0.1
CMW_{NP}	3.5	253 ± 13	11.4 ± 0.2	259 ± 16	234 ± 10	0.90 ± 0.09	0.28 ± 0.01	20 ± 1	2.5 ± 0.1	1.0 ± 0.1
$STMW_{NP}$	0.2	207 ± 36	13.7 ± 0.4	141 ± 39	111 ± 6	0.8 ± 0.3	0.21 ± 0.02	26 ± 1	2.7 ± 0.2	1.1 ± 0.1
MW	0.2	1276 ± 354	8.4 ± 1.8	133 ± 42	84 ± 9	0.6 ± 0.3	0.21 ± 0.06	27 ± 5	2.5 ± 0.3	1.3 ± 0.4
SAMW	8.0	719 ± 42	8.1 ± 0.3	214 ± 26	72 ± 6	0.33 ± 0.07	0.16 ± 0.01	29 ± 1	2.6 ± 0.1	1.1 ± 0.1
$AAIW_{5.0}$	2.9	1317 ± 108	4.0 ± 0.2	228 ± 13	128 ± 5	0.56 ± 0.07	0.20 ± 0.02	24 ± 1	2.3 ± 0.1	1.2 ± 0.1
$AAIW_{3.1}$	4.5	677 ± 36	6.9 ± 0.4	499 ± 50	134 ± 5	0.27 ± 0.04	0.18 ± 0.01	23 ± 1	2.1 ± 0.1	1.2 ± 0.1
NPIW	5.9%	671 ± 65	7.3 ± 0.4	571 ± 39	255 ± 6	0.45 ± 0.04	0.28 ± 0.01	18 ± 1	2.1 ± 0.1	1.1 ± 0.1
CDW	27.0%	2412 ± 76	2.5 ± 0.1	821 ± 22	183 ± 4	0.22 ± 0.01	0.21 ± 0.01	19 ± 1	1.8 ± 0.1	1.3 ± 0.1
$NADW_{2.0}$	12.9%	3279 ± 66	2.2 ± 0.1	467 ± 13	88 ± 2	0.19 ± 0.01	0.21 ± 0.01	24 ± 1	2.1 ± 0.1	1.3 ± 0.1
$NADW_{4.6}$	7.6%	1582 ± 99	4.8 ± 0.3	277 ± 13	103 ± 4	0.37 ± 0.03	0.21 ± 0.01	24 ± 1	2.2 ± 0.1	1.3 ± 0.1
AABW	4.7%	3780 ± 64	1.1 ± 0.0	745 ± 47	149 ± 6	0.20 ± 0.02	0.19 ± 0.01	21 ± 1	1.8 ± 0.1	1.5 ± 0.1
R^2 (N_j vs <N_j>)					0.80		0.28	0.51	0.42	0.16
SD err of the estimate					36		0.02	3	0.24	0.2
Determination error					1		0.02	2	0.1	0.12

EDW: Eighteen Degrees Water, $ENACW_{12}$: Eastern North Atlantic Central Water (12°C), $ENACW_{15}$: Eastern North Atlantic Central Water (15°C), 13EqAtl: Equatorial Atlantic Central Water (13°C), $SACW_{12}$: South Atlantic Central Water (12°C), $SACW_{18}$: South Atlantic Central Water (18°C), $STMW_I$: Indian Subtropical Mode Water, ICW_{13}: Indian Central Water (13°C), $STMW_{SP}$: South Pacific Subtropical Mode Water, $SPCW_{20}$: South Pacific Central Water (20°C), 13EqPac: Equatorial Pacific Central Water (13°C), CMW_{NP}: North Pacific Central Mode Water (12°C), $STMW_{NP}$: North Pacific Subtropical Mode Water (16°C), MW: Mediterranean Water, SAMW: Sub-Antarctic Mode Water, $AAIW_{3.1}$: Antarctic Intermediate Water (3.1°C), $AAIW_{5.0}$: Antarctic Intermediate Water (5.0°C), NPIW: North Pacific Intermediate Water, $CDW_{1.6}$: Circumpolar Deep Water, $NADW_{2.0}$: North Atlantic Deep Water (2°C), $NADW_{4.6}$: North Atlantic Deep Water (4.6°C), AABW: Antarctic Bottom Water. The determination error refers to the measurement error for the case of AOU and a_{325}, the propagation of the measurement errors of $F_{(340/360\text{-}560)}$ and a_{340} for Φ_{340}, the estimation error of the regression slope for the $S_{275-295}$, and the propagation of the estimation error of the regression slope of $S_{275-295}$ and $S_{350-400}$ for the S_R.

The dependence of archetypal OUR (OUR_i) on archetypal potential temperature (θ_i) responds to the Arrhenius's law [*Arrhenius*, 1889], exhibiting the expected linear relationship between ln (OUR_i) and the inverse of the absolute potential temperature (Fig. 1.4b):

$$\ln OUR_i = 46\ (\pm 4) - 108(\pm 10) \cdot \frac{1000}{R \cdot (273.15 + \theta_i)} \quad (13)$$

(R^2 = 0.85, n = 22, $p < 0.001$)

where R is the gas constant (8.314 J mol^{-1} K^{-1}) and $273.15 + \theta_i$ is the absolute archetypal potential temperature. The slope of this relationship, 108 ± 10 kJ mol^{-1}, would represent the activation energy (E_a) of the mineralization of organic matter in the dark global ocean, which translates into a temperature coefficient Q_{10} of 5.2 ± 0.9 as derived with the equation:

$$Q_{10} = e^{\frac{E_a}{R} \cdot \frac{10}{(273.15+\theta_1)\cdot(273.15+\theta_2)}} \quad (14)$$

where θ_1 and θ_2 are the archetypal potential temperatures of the coldest (1.10 ± 0.04 °C for AABW) and warmest (18.1 ± 0.8 °C for $SPCW_{20}$) WT sampled during the circumanvigation.

Basin-scale characterization: CDOM quantity and quality

The values of a_{325} ranged between 0.07 to 0.50 m^{-1} and changed mostly with section distance, although the a_{325} changes in the Indian Ocean with depth were also relevant (Fig. 1.5a).

The spectral slope $S_{275\text{-}295}$ ranged from 8 to 50 μm^{-1}, varying with section distance and diminishing with depth. Inversely to the pattern of a_{325}, the highest values were observed at the central and intermediate waters of the South Indian Ocean and the lowest values were located in the intermediate waters of the North Pacific (Fig. 1.5b).

S_R varied between 0.79 and 5.22. It decreased with depth, its maximum values were found in the central waters of the South Indian and the lowest values were located in the deep waters of Antarctic origin that were less than 1 in some samples (Fig. 1.5c).

Finally, Φ_{340} ranged from 0.3 to 2.9 and increased with depth, presenting maximum values in bottom waters of the South and North Pacific and minimum values in the central waters of the North Atlantic (Fig. 1.5d).

The archetypal values of a_{325}, $S_{275\text{-}295}$, S_R and Φ_{340} in every sample ($<a_{325j}>$, $<S_{275\text{-}295j}>$, $<S_{Rj}>$ and $<\Phi_{340j}>$, respectively) explained 28%, 51%, 42% and 16% of the total variability of the measured variables (a_{325j}, $S_{275\text{-}295j}$, S_{Rj} and Φ_{340j}, respectively) in the dark global ocean (Table 1.1). In the case of a_{325} and Φ_{340}, the fact that the percentages of explained variability were low but significant likely resides in the lack of precision of the CDOM measurements. Note that we have obtained that the standard deviation of the residuals (SD res) of the linear regression between the measured and the arquetypal values of a_{325} and Φ_{340} and the corresponding measurement error of a_{325} and estimation error of Φ_{340} are of the same magnitude (Table 1.1). Consequently, R^2 were low not because most of the variability of a_{325} and Φ_{340} was not retained by basin scale changes (or because the unexplained variability at the basin scale was due to variability at the study area) but because of the low sensitivity of the analytical method.

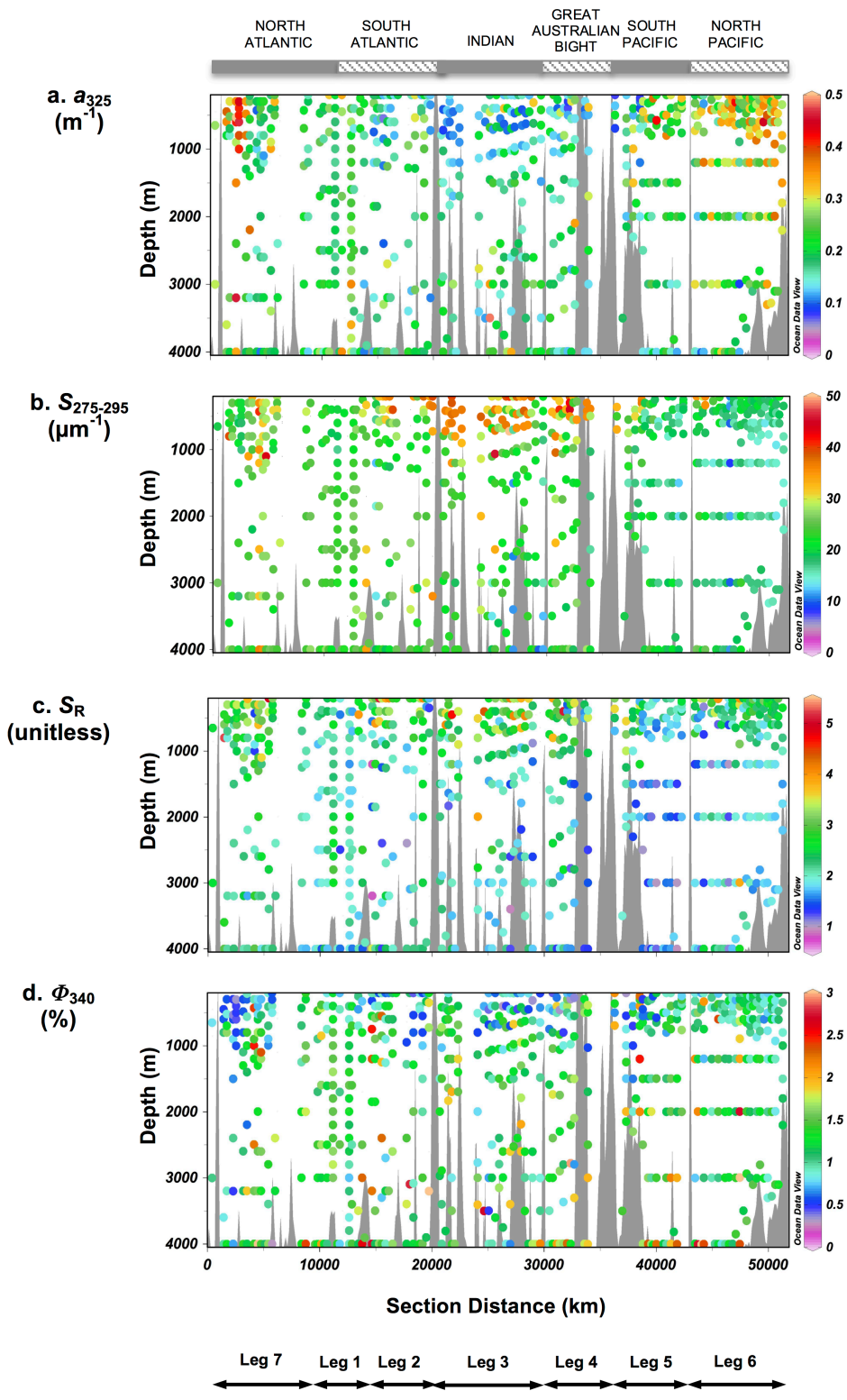

Fig. 1.5. Distribution of (a) a_{325} (m^{-1}), (b) $S_{275\text{-}295}$ (μm^{-1}) (c) S_R (unitless) and (d) Φ_{340} (%) of the water samples intercepted during the Malaspina 2010 expedition. Note that the depth range starts at 200 m.

Dependence of CDOM variables on water mass ageing

Since 80% of the variability of AOU is constrained by basin-scale mineralization processes and water mass mixing, we have used it as tracer of the dynamics of the CDOM variables (Fig. 1.6). In this figure we show the measured (gray dots) and archetypal values for each sample (black dots) and the archetypal values for each water type (white dots) of a_{325}, $S_{275-295}$, S_R and Φ_{340}.

The highest a_{325i} values were found in the central and intermediate waters of the North Pacific (NPIW and CMW_{NP} = 0.28 ± 0.01 m^{-1}, 13EqPac = 0.27 ± 0.01 m^{-1}) and in a more specific region of the North Atlantic (18–32 °N, 17-58 °E) ($ENACW_{15}$ = 0.26 ± 0.02 m^{-1}, EDW = 0.26 ± 0.04 m^{-1}), whereas the lowest a_{325i} were found in the central and intermediate waters of the South Pacific Ocean, with an a_{325i} of 0.10 ± 0.03 m^{-1} in the $STMW_{SP}$ (Table 1.1). The relationship between AOUi and a_{325i} was positive and significant (a_{325i} = 6 (± 1) x $10^{-4}AOU_i$ + 0.13 (± 0.01), R^2 = 0.76, p < 0.001, n = 20, Fig. 1.6b). Note that $ENACW_{15}$ and EDW were ruled out of the relationship (indigo dots in Fig. 1.6a, b). The slope of this relationship (6 ± 1 x 10^{-4} m^{-1} µmol^{-1} kg) substituted $\frac{\partial a_{325}}{\partial AOU}$ in equation [10] and was multiplied by the previously obtained OUR_{global} of 0.5 ± 0.1 µmol kg^{-1} yr^{-1} in equation [11] to obtain a CDOM net production rate NP_{a325} of 3.3 ± 0.5 x 10^{-4} m^{-1} yr^{-1} for the global dark ocean excluding the previously ruled out central waters of the North Atlantic Ocean, which represented only 2.5% of the total volume of sampled water. Following equation [12], dividing the WT proportion weighted-average a_{325} of the dark ocean (0.21 ± 0.01 m^{-1}) by the NP_{a325} calculated above (3.3 ± 0.5 x 10^{-4} m^{-1} yr^{-1}), we obtained a CDOM turnover time of 634 ± 120 yr.

Contrary to a_{325i}, the qualitative indices $S_{275-295i}$ and S_{Ri} decreased with water mass ageing at an exponential ($S_{275-295i}$ = 0.037 (± 0.002) $e^{-0.0032\ (\pm 0.0004)\ AOU_i}$, R^2 = 0.82, p < 0.001, n = 22, Fig. 1.6c, d) and linear (S_{Ri} = –0.011 (±0.002) AOU_i + 3.6 (±0.1), R^2 = 0.74, p < 0.001, n = 19, Fig. 1.6e, f) rate, respectively. The maximum estimated archetypal values of $S_{275-295i}$ were 40 ± 7, 36 ± 2 and 33 ± 1 µm^{-1} for the $STMW_{SP}$, $STMW_I$ and ICW_{13}, respectively, and the minimum was 18 ± 1 µm^{-1} for the NPIW (Table 1.1). The maximum estimated archetypal values of S_{Ri} were 3.4 ± 0.2 for the EDW, 3.3 ± 0.2 for the $STMW_I$ and the minimum S_{Ri} were recorded in the Antarctic WT: AABW and CDW with 1.8 ± 0.1 (Table 1.1). The Φ_{340i} values increased linearly with water mass ageing (Φ_{340i} = 0.006 (±0.003) AOU_i + 0.60 (±0.08), R^2 = 0.49, p = 0.001, n = 19, Fig. 1.6g, h). Note that the most aged water types (13EqPac, CMW_{NP} and NPIW; sky blue dots in Fig. 1.6e, f, g, h) were ruled out from both AOU_i – S_{Ri} and AOU_i – Φ_{340i} relationships.

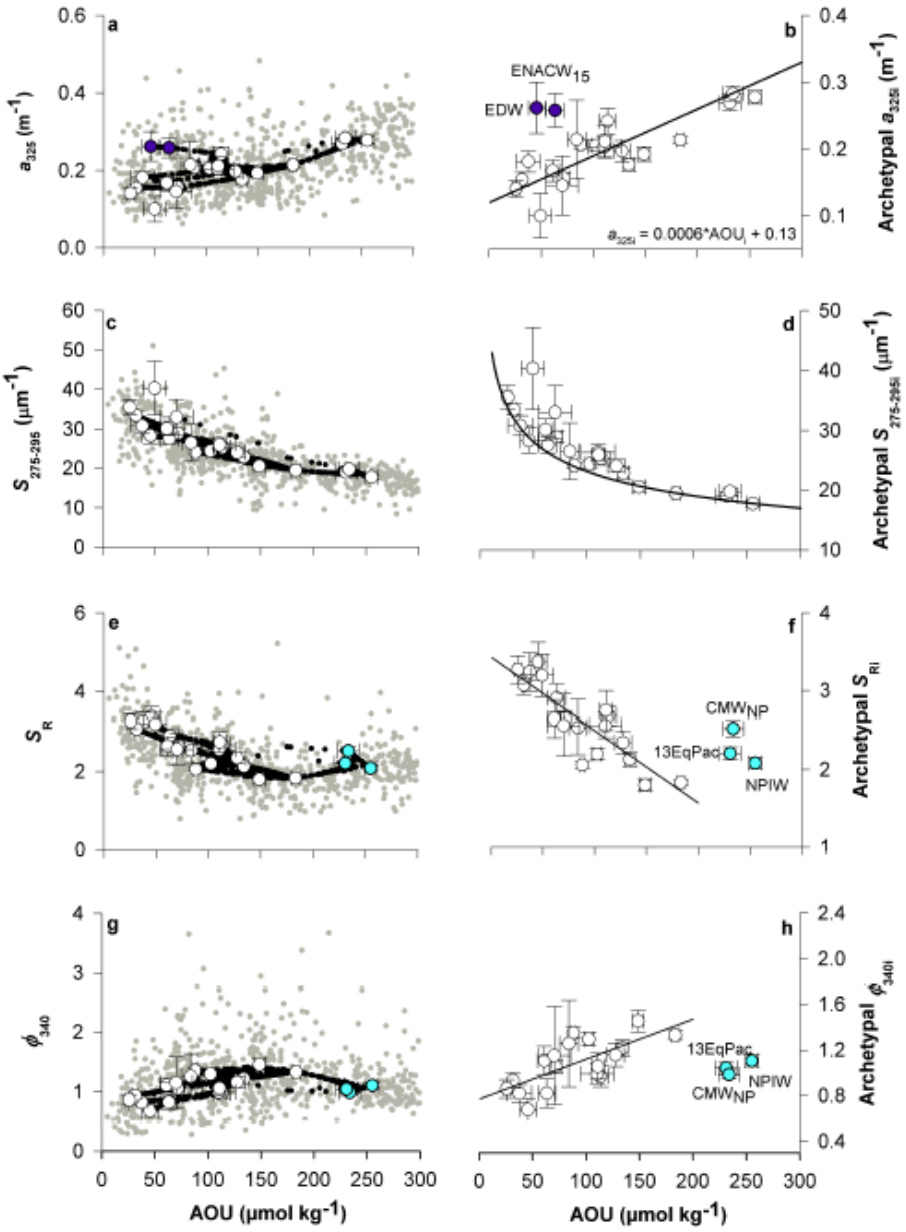

Fig. 1.6. Relationships between the CDOM parameters (a) a_{325}, (m^{-1}), (b) $S_{275\text{-}295}$ (μm^{-1}) (c) S_R (unitless) and (d) Φ_{340} (%) with apparent oxygen utilization (AOU, µmol kg^{-1}) in the global dark ocean. In the plots on the left, measured concentrations (grey dots), archetypal concentrations for each water type (white dots) and archetypal concentrations for each sample (black dots) are presented. The plots on the right column show the relationship between archetypal concentrations of the WT for each studied variable. We obtained the following functions: (b) a_{325i} = 6 (± 1) x 10^{-4} AOU_i + 0.13 (± 0.01), R^2 = 0.76 (p <0.001, n = 20); (d) $S_{275\text{-}295i}$ = 0.037 (± 0.002) $e^{-0.0032(\pm 0.0004)\ AOU_i}$, R^2 = 0.82 (p <0.001, n = 22); (f) S_{Ri} = –0.011 (±0.002) AOU_i + 3.6 (±0.1), R^2 = 0.74 (p < 0.001, n = 19); (h) Φ_{340i} = 0.006 (±0.003) AOU_i + 0.60 (±0.08), R^2 = 0.49 (p = 0.001, n = 19). Indigo and sky-blue dots were excluded from their respective regression models (see the text for justification).

Discussion

DOM optical characterization at the global ocean scale can provide insights on the DOC dynamics and the relevance of the microbial carbon pump (MCP) [*Jiao et al.*, 2010]. So far, the first attempts to obtain a global inventory of marine CDOM have been focused on the optical characterisation of pelagic layers (epi–, meso– and bathypelagic) and ocean basins [*Nelson et al.,* 2007, 2010]. The novelty of our work resides in the fact that we have been able to sort the global ocean by water masses (WT), each one showing their intrinsic characteristics of CDOM quantity and quality, and related them with water ageing along the global overturning circulation. Our approach, oceanographic rather than geographic, allows to overcome the difficulties encountered by previous attempts: (i) several water masses can mix within a given pelagic layer; and (ii) the intermediate and abyssal water masses are not usually restricted to a given ocean basin.

It should be noted that *Nelson et al.* [2010] indicated that the average a_{325} of the global ocean at depths between 3000 and 6000 m was 0.14 ± 0.03 m^{-1} and in the Malaspina circumnavigation the average a_{325} of the 4000 m samples was 0.19 ± 0.05 m^{-1}. It is also relevant to note that the slope of the a_{325}–AOU relationship that we obtained during the circumnavigation (0.6 ± 0.1 x 10^{-4} m^{-1} µmol^{-1} kg) did not differ significantly from the values reported by *Nelson et al.* [2010] for the Indian (0.62 x 10^{-3} m^{-1} µmol^{-1} kg) and Pacific (0.57 x 10^{-3} m^{-1} µmol^{-1} kg) oceans. Therefore, a constant offset of about 0.05 m^{-1} exists between our a_{325} and those reported by other authors. It is improbable that the fact that we did not filter the samples is the reason behind this dissimilarity (see the detailed description of our procedure in materials and methods). Note that in the unlikely case that particles represented 10% of the light absorption [*Nelson et al.*, 1998], a constant offset of 0.03 m^{-1} would still be present. We surmise that the different methodologies used (double·beam spectrophotometer with linear 10 cm cell versus single·beam spectrophotometer Ultrapath with a 2 m·long liquid waveguide capillary cell) may be a feasible cause. An intercalibration between methods would be needed to assess under what conditions both procedures are directly comparable.

Water mass age versus ageing

Water mass 'age' and 'ageing' provide different information; age is defined as the time elapsed since the water was last in contact with the atmosphere, whereas ageing (traced through AOU) refers to the consumption of oxygen over that period, which depends on the time elapsed (age) but also on the rate at which dissolved oxygen is consumed during the organic matter mineralization (OUR). Therefore, the AOU variable integrates the OUR over time giving information about how old a water sample is and how fast the mineralization processes occur in that water sample. Although we found a positive and significant power law relationship between AOU and age in the water masses intercepted during the circumnavigation (AOU_i = 16 (± 5) $\tau_i^{\,0.34\ (\pm\ 0.06)}$, R^2 = 0.72, $p < 0.001$, n = 19, Fig. 1.4c) which explains 72% of their respective global scale variability, our interest is focused on the 28% of the AOU variability that is not explained by age and is attributed to the quantity and

quality of the substrates (particulate, suspended and dissolved organic matter) that cause a different 'ageing' for each WT, i.e. a different OUR_i. Note that CMW_{NP}, 13EqPac and NPIW were ruled out of the AOU–age correlation because they undergo excessive ageing for its age (sky-blue dots in Fig. 1.4c).

The average age for the dark global ocean that we obtained (454 ± 22 yr) is coherent with previous estimates of 500 yr according to *Stuiver* [1983] and 345 yr according to *Laruelle et al.* [2009]. It should be noted that *Stuiver* [1983] restricted his estimate to depths > 1500 m. Unlike the Malaspina expedition that only covers a latitude range of 30°N–40°S at depths between 200 and 4000 m, *Laruelle et al.* [2009] estimated the age with a global ocean model considering depths > 200m. Hence, the absence of central and intermediate waters in the calculation of *Stuiver* [1983] and the consideration of high latitudes (i.e. areas of recent WT formation) in the calculation of *Laruelle et al.* [2009] resulted in a value higher than ours in the case of *Stuiver* [1983] and lower in the case of *Laruelle et al.* [2009].

Our estimate of the dark global ocean oxygen consumption rate (OCR) (0.68 ± 0.18 Pmol O_2 yr^{-1}) is comparable to the 0.83 Pmol O_2 yr^{-1} obtained by *Anderson et al.* [2004] with an ocean biogeochemical model. The difference between these two estimates resides again in the covered domain. The dark global ocean OCR of *Anderson et al.* [2004], which covered the entire ocean, were slightly higher than our estimation (i.e. with a latitude region of 34 ° N–40 ° S) because the younger WT of the high latitudes present more elevated OUR which, in turn, raises the dark global ocean OCR. On the contrary, the Malaspina dark global ocean OCR is not comparable with the commonly much higher respiration rates of 2.6–3.5 Pmol O_2 yr^{-1} calculated using in vitro approaches [e.g. *del Giorgio and Duarte, 2002*]. The main reason for this discrepancy is likely that we considered a long- timescale that accounts for slower mineralization rates, whereas these authors estimated the mineralization rates at a local- and short-timescales that reflects mostly the labile carbon.

Our OUR_i values for each WT (0.19–4 µmol O_2 kg^{-1} yr^{-1}) were lower than those found in previous studies [*Álvarez-Salgado et al.*, 2014; *Aristegui et al.*, 2003; *Sarmiento et al.*, 1990; *Jenkins,* 1998]. The higher OUR estimations of 7–16 µmol O_2 kg^{-1} yr^{-1} reported by *Aristegui et al.* [2003] are based on short-term (days) that include mainly the mineralization of labile organic matter. The use of a tracer age equation (applicable to local, short timescale) in *Sarmiento et al.* [1990] and Jenkins [1998] also resulted in higher values of 13 µmol O_2 kg^{-1} yr^{-1} and 9 µmol O_2 kg^{-1} yr^{-1}, respectively. In contrast, the use of a tritium box model (applicable to the basin, long timescale) [*Sarmiento et al.*, 1990] led to values of 4–5 µmol O_2 kg^{-1} yr^{-1}, which are closer to our OUR estimations. Furthermore, the high OUR values obtained by *Álvarez-Salgado et al.* [2014], ranging from 6.3 to 18 µmol O_2 kg^{-1} yr^{-1}, are likely associated to their age calculations. Their water age estimate from chlorofluorocarbon (CFC) concentrations tends to underestimate turbulent mixing leading to an underestimation of water mass ages, and consequently overestimation of OUR values [*Sonnerup,* 2001; *Mecking et al.,* 2004].

Recalcitrant nature of CDOM and its origin

The turnover time of 634 ± 120 yr that we obtained by combining the NP_{a325} rate (3.3 ± 0.5 x 10^{-4} m^{-1} yr^{-1}) and the water mass weighted average CDOM (0.21 ± 0.01 m^{-1}) gives evidence of the recalcitrant nature of this DOM pool. This turnover time is about 40% longer than the 454 ± 22 yr age of the dark global ocean and the 435 ± 41 yr turnover time of the humic-like fluorescence component 1 (Ex/Em maximum in the UVA/visible at 270–370/470 nm), but not significantly different from the turnover time of the humic-like fluorescence component 2 (Ex/Em maximum in the UVA/visible at 320/400 nm, 610 ± 55 yr) recently reported by Chapter III of this PhD thesis. Similarly, the CDOM turnover time, which represents a minimum fraction of the DOC pool, was about 70% longer than the lifetime of the bulk DOC pool (370 yr according to *Hansell et al.* [2009]), or the tyrosine-like component 4 (Ex/Em maxima in the UVA/visible at 270/310 nm, 379 ± 98 yr according to Chapter 3 of this PhD thesis, which implies a more recalcitrant nature of the CDOM pool than the bulk DOC pool and, therefore, a larger capability to sequester anthropogenic CO_2.

The E_a and Q_{10} that we obtained for OUR in this study (108 ± 10 kJ mol^{-1} and 5.2 ± 0.9, respectively) were approximately 3 and 2 times higher than the expected values for the labile and the semi-labile DOM. *Seiki et al.* [1991] analysed the temperature dependence of the decomposition of labile phytoplankton-derived organic matter and obtained E_a and Q_{10} values of 37 ± 3 kJ mol^{-1} and < 2, respectively. *Bussmann* [1999] reported E_a and Q_{10} values of 67 ± 11 kJ mol^{-1} and about 3, respectively, for the decomposition of semi-labile humic substances. As for the case of the decomposition of soil organic carbon, the association of a higher refractivity to a higher sensitiveness to temperature changes [*Davison and Janssens*, 2006] and the elevated E_a and Q_{10} of decomposed organic matter in the dark global ocean indicates an enhanced response to temperature which may have implications for the response of the ocean carbon cycle to global warming.

AOU on the charge-transfer model of *Del Vecchio and Blough's* [2004b], which proposed that the fluorescence signal of DOM is in part due to intramolecular charge transfer interactions between electron donors and acceptors formed through the partial oxidation of lignin and other aromatic polymeric precursors of terrestrial origin. On the contrary, other studies demonstrated that marine CDOM is generated *in situ* from bacterioplankton during its active growth [*Kramer and Herndl,* 2004; *Ortega-Retuerta et al., 2009*], as well as directly by phytoplankton via extracellular release [Romera-Castillo *et al.*, 2010] or indirectly by zooplankton grazing [*Urban-Rich et al.*, 2006]. Recently, *Jørgensen et al.* [2014] observed an increase in recalcitrant CDOM fluorescence associated with prokaryote utilization of either glucose or natural colourless semi-labile DOM as carbon sources. Our positive relationship of a_{325} with AOU (Fig. 1.6a, b) is compatible with both hypotheses, which are not mutually exclusive. The terrestrial discharges do not seem to be provoking the elevated initial a_{325i} values of the North Atlantic central water types EDW and $ENACW_{15}$. It should be noted that the low latitudes where these WTs are formed involve

warm initial temperatures (θ) of 18 ºC for the EDW and 15 ºC for the $ENACW_{15}$ but also elevated photobleaching rates, which should result in relatively high S_{Ri} but low a_{325i} values. In fact, the archetypal S_R values of these WTs are high, 3.4 ± 0.2 for EDW and 2.9 ± 0.2 for $ENACW_{15}$, however, the archetypal values of a_{325} are relatively high and favour us to propose that, prior to winter mixing, enhanced microbial production of CDOM in these warm water masses exceeded removal by photobleaching leading to high initial a_{325} and S_R during their formation. The high a_{325} values of the central North Atlantic are of the same level than those found in the thermocline waters of the North Pacific, specifically CMW_{NP}, 13EqPac and NPIW (Table 1.1, Fig. 1.5a, Fig. 1.6a, b). However, in this case, they are not due to high initial a_{325} values but to the excessive ageing experienced by these WT for its age, which is associated with (i) the sluggish circulation of the North Pacific that allows recalcitrant CDOM accumulation, (ii) the large size of the North Pacific subtropical gyre, resulting in large distances from the edge to the center of the gyre, where downwelling occurs, and (iii) the export of particulate organic material that results in high oxygen utilization rates [*Feely et al.,* 2004] and production of recalcitrant CDOM [e.g. *Hayase and Shinozuka,* 1995; *Yamashita et al.,* 2007; *Yamashita and Tanoue,* 2008, 2009].

Factors controlling the CDOM quantity and quality in the global ocean

Not only the magnitude (AOU) but also the rate of mineralization (OUR) is a key variable to understand the basin-scale variability of the quantity and quality of CDOM. In general terms, an old water mass presents slow mineralization rates caused by either an insufficient (limiting) or biologically recalcitrant substrate, leading to low OUR [*Jenkins*, 1998].

To check the variable —ageing (AOU) or substrate quantity and quality (OUR) — that better contributes to explain the variability of CDOM in the dark global ocean, we performed two simple regression analyses, one considering the AOU_i and another considering OUR_i as independent variables. The a_{325i} values represent quantity, and Φ_{340}, which is an appropriate (but still not broadly used) proxy to CDOM aromaticity, was taken as a 'qualitative' variable (Fig. 1.6). For the case of a_{325i}, the regression analysis was positive and significant with AOU_i, explaining 76% of the variability of a_{325i} (R^2 = 0.76, Fig. 1.6b), but was not significant with OUR_i (Fig. 1.7a). This means that ageing is the key variable to explain the accumulation of CDOM in the dark global ocean (i.e. for a same age, the WT that has experienced faster mineralization rates will have more CDOM). Conversely, for the case of Φ_{340i}, it is not AOU_i (Fig. 2.6h) but OUR_i (Fig. 1.7.b) the variable that best explains its variability, with the following inverse relationship, $\Phi_{340i} = 1.28\ (\pm\ 0.05)\ e^{-0.20\ (\pm 0.04)\ OUR_i}$ (R^2 = 0.55, p = 0.001, n = 22). This means that the lower the rate of mineralization, the higher the aromaticity of the CDOM generated by microbial respiration. Therefore, the lower the quality for microbial consumption of the mineralised organic matter, the more complex the DOM molecular structures and the more content in aromatic compounds, promoting the ability to emit fluorescence. This assumption matches with the novel results of *Jørgensen et al.* [2014] that confirms that the more recalcitrant the mineralised materials the

larger the production rate of fluorescent DOM. It can also be coherent with the charge-transfer model of Del Vecchio and Blough regarding the terrestrial origin of CDOM in the ocean that were previously mentioned.

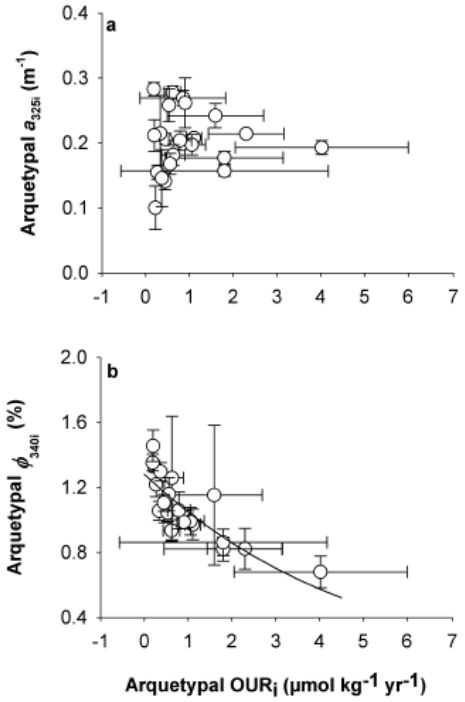

Fig. 1.7. Relationships between archetypal OUR_i (µmol kg^{-1} yr^{-1}) and (a) archetypal a_{325i} (m^{-1}) and (b) archetypal Φ_{340i}. The fitted equation is: Φ_{340i} = 1.28 (± 0.05) $e^{-0.20\ (\pm 0.04)\ OUR_i}$, R^2 = 0.55 (p = 0.0001, n = 22).

Linked to the same postulation, we found that the lowest $S_{275\text{-}295i}$ and S_{Ri} values corresponded to the oldest WT (Fig. 1.6d, f), and, according to *Helms et al.* [2008], low values are attributed to a dominant content of aromatic and high molecular weight (HWM) DOM fraction. However, this hypothesis, indicating that the low molecular weight (LMW) DOM turns into to a more recalcitrant HMW DOM with ageing, does not appear to apply to the bulk of natural DOM according to *Amon and Benner* [1996]. Instead, they found that the bulk of HMW DOM is more bioreactive and fresher than the LMW DOM. Consequently, it seems that both synthesis and transformation of the HMW RDOM happen during the DOM mineralization.

Our study is the first in presenting a global data set of S_R for the entire dark ocean, allowing to differentiate the S_R of the various WT within the ocean rather than just contrasting the wide difference between terrestrial and marine sources of CDOM in coastal areas. Similar to *Helms et al.* [2008], we obtained a linear and positive relationship between salinity (S) and S_R, but within the much narrower salinity range of the open ocean waters (S_{Ri} = 0.85 (±0.22)· S_i – 27 (±8), R^2 = 0.43, p = 0.001, n = 22, Fig. 1.4d). However, whereas in the case of *Helms et al.* [2008] the relationship is related to the terrestrial versus marine origin of the samples, in the case of our open ocean samples it is presumably produced by photobleaching. The positive relationship can be justified because saltier water masses are generally originated at lower latitudes where photobleaching previous to winter convection is higher. In order to check this, we have used the potential temperature (θ) as a proxy to the exposure of the water masses to solar radiation and, therefore, we have related S_R with θ. It resulted that the linear regression with θ (S_{Ri} = 0.09 (±0.01)· θ_i + 1.77 (±0.12), R^2 = 0.74, p = 0.001, n = 22) explained the global distribution of S_R better than S. Note that higher θ results in higher S_R values and lower molecular weight of CDOM (i.e. lower content in aromatic substances). This means that the relationship between S_R and S may also

express the degree of photobleaching when considering the open ocean.

Conclusions

This study provides (1) the first global inventory of CDOM variables of the main water masses of the ocean; (2) a robust estimate of the turnover time of CDOM in the dark global ocean of 634 ± 120 yr, which exceeds the turnover time of the DOC pool and the water flushing time of the dark ocean by 70% and 40%, respectively; and (3) new evidences on the dependence of CDOM quantity on water mass ageing (AOU) and CDOM quality on the nature of the mineralised organic matter (OUR).

Acknoledgements

We thank C.M. Duarte for the coordination of the Malaspina expedition; the chief scientists of the seven legs, the staff of the Marine Technology Unit (CSIC·UTM) and the Captain and crew of R/V Hespérides for their outright support during the circumnavigation.

This study was financed by the Malaspina 2010 circumnavigation expedition (grant number CSD2008–00077); C.R·C. acknowledges funding through a Beatriu de Pinos postdoctoral fellowship from the Generalitat de Catalunya. M.N.·C. was funded by the CSIC Program "Junta para la Ampliación de Estudios" cofinanced by the ESF. S.K. was supported by US NSF grant OCE·1060804. E.F.G. was funded through a JAE·Pre grant from CSIC and the European Social Fund. C. M. was supported by DOREMI (CTM2012·34294) funded by the Spanish Ministry of Economy and Competitiveness.

Chapter 2

Under revision in Geophysical Research Letters

Chromophoric signatures of long-lived microbial by-products in the dark ocean

Abstract

Microbial metabolism is largely responsible for the vast oceanic dissolved organic matter (DOM) reservoir. Examination of the DOM absorption spectra from the dark ocean samples collected during the Malaspina circumnavigation allowed us to identify two chromophores centered at 302 nm (UV) and 415 nm (Visible). We deconvolved the signal attributed to those chromophores from the exponential decay curve characteristic of humic substances. The distribution of the UV chromophore was ubiquitous in intermediate and deep waters of the global ocean and it is partially related to nitrate and to a gadusol-like antioxidant compound. The Visible chromophore was more prominent at central and intermediate depths of the North Pacific and it has been recently assigned to the enzyme cytochrome c. Whilst both water mass age and ageing explain the global distribution of the UV chromophore, only ageing dictates the Visible chromophore distribution. The turnover time of these chromophores was ~350 yr.

Introduction

Oceanic dissolved organic matter (DOM) represents one of Earth's largest reservoirs of reduced carbon, and most of it (> 95%) is in the form of recalcitrant DOM (RDOM), being resistant to microbial degradation [*Hansell,* 2013]. Although the labile organic matter from photosynthesis is preferentially respired back to CO_2 in the surface ocean, a minor fraction of it is transformed into RDOM as a by-product of the microbial metabolism thereby preserving fixed carbon in the ocean [*Ogawa et al.,* 2001*; Benner and Herndl,* 2011*; Lechtenfeld et al.,* 2015]. This process has been recently termed as microbial carbon pump (MCP) [*Jiao et al.,* 2010], having implications for the climate as it could contribute to sequester atmospheric CO_2 at centennial to millennial time scales.

A portion of the RDOM pool, known as chromophoric DOM (CDOM), absorbs UV and visible light and has been widely used as an "optical marker" in ocean hydrography and biogeochemistry studies [*Nelson and Siegel,* 2013]. Light absorption by any organic functional group capable of absorbing light (chromophore) is characterized by its intensity and shape. Whilst the intensity results from the molar absorption and concentration of the chromophore, the shape of light absorption (wavelength maxima and band width) depends on the electronic transitions involved [*Stedmon and Nelson,* 2015].

Absorption spectra of natural waters provide both quantitative and qualitative information on CDOM in aquatic environments. Absorption coefficients at specific wavelengths, a_λ, are used as proxies of the concentration of CDOM and a wide variety of spectral indices and slopes have provided key information on the origin and molecular structure of CDOM [*Helms et al.,* 2008*; Twardowski et al.,* 2004]. Most of the research efforts have focused on the characterization of the exponential decay of a_λ with increasing wavelength, traditionally

associated with dissolved humic substances [*Bricaud et al.,* 1981]. Detailed inspection of CDOM spectra has recently resulted in the identification of specific chromophores, particularly in open ocean waters [*Röttgers and Koch,* 2012]. However, this approach is still lacking in the literature. Here, we thoroughly explore a collection of 740 CDOM spectra from the dark global ocean (water depths > 200 m). We identify two distinct chromophores, centered at 302 ± 3 nm and 415 ± 3 nm by statistically isolating the absorption coefficient signal attributable to these chromophores from the standard decreasing exponential curve due to the pool of humic substances. Moreover, we apply a water mass analysis that allow us to quantify the occurrence of both chromophores in the most abundant water masses of the dark global ocean, to explain their occurrence on basis of the ventilation time (ideal age) and the cumulative microbial respiration (apparent oxygen utilization, AOU) of those water masses, and to obtain their global net production rate and turnover time.

Materials and methods

The Malaspina 2010 circumnavigation was conducted from December 2010 to July 2011 on board R/V Hesperides along the Atlantic, Indian and Pacific oceans, spanning latitudes from 34ºN to 40ºS. During the cruise, 147 hydrographic stations were occupied (Fig. 2.1 in Chapter II).

The water column was sampled from the surface to 4000 m depth with a 24–10 L Niskin bottles rosette. Continuous conductivity–temperature–depth and dissolved oxygen profiles were recorded with a Seabird 911+ CTD probe equipped with a redundant temperature and salinity sensor for intercomparison and a polarographic membrane oxygen sensor Seabird SBE-43. Temperature and pressure sensors were calibrated at the SeaBird laboratory before the circumnavigation. On board salinity calibration was carried out with a Guildline AUTOSAL model 8410B salinometer with a precision better than 0.002 for single samples and the potentiometric end-point Winkler method for the calibration of the oxygen sensor. Oxygen saturation was calculated from practical salinity and potential temperature with the equation of Benson and Krause [*Benson and Krauss*, 1984]. Apparent oxygen utilization (AOU) was calculated as the difference between the saturation and measured dissolved oxygen concentrations.

CDOM absorption coefficient spectra

At each station, samples for the determination of the absorption spectra of CDOM were taken from 8 discrete depths between 200 and 4000 m depth, poured directly from the Niskin bottle into acid cleaned 250 mL glass flasks and immediately stored in dark until analysis on board within a few hours after collection. Samples were not filtered because light absorption due to pigments and detrital particles contribute only to a minor fraction of the open ocean CDOM absorption [*Nelson et al.,* 1998; 2007], particularly at meso- and bathypelagic depths.

The UV-visible absorbance of CDOM was determined from 250 to 750 nm at 1 nm intervals in 10-cm path length quartz cuvettes in a double beam Perkin Elmer lambda 850 spectrophotometer and a blank was measured every 5 samples to detect and correct (linearly)

any instrument drift. The estimated detection limit of this spectrophotometer for quantifying CDOM absorption is 0.001 absorbance units or 0.02 m^{-1}. The absorbance was converted into Neperian absorption coefficient (m^{-1}) using the equation [*Green and Blough,* 1994]:

$$a_\lambda = 2.303 \frac{[\mathrm{Abs}_{(\lambda)} - \mathrm{Abs}_{(600-750)}]}{l} \quad (1)$$

where $\mathrm{Abs}_{(\lambda)}$ is the absorbance at a given wavelength (nm), $\mathrm{Abs}_{(600-750)}$ is the average absorbance between 600 and 750 nm, *l* is the path length of the cuvette (0.1 m) and 2.303 is the factor that converts from decadic to natural logarithms. During the measurements, we first checked that the differences between sample and baseline absorbance at long wavelengths (> 600 nm) maintained < 0.0005 absorbance units. In the case that difference was > 0.0005 absorbance units, we renewed the water in the sample cuvette and repeated the measurement. In most cases, we got a final difference < 0.0005 absorbance units. To correct this generally minor effect of light scattering by particles and microbubbles we applied a wavelength-independent correction [*Green and Blough*, 1994] by subtracting the mean absorbance from 600 to 750 nm from all spectral absorbance values.

Chromophore identification analysis

To locate and quantify the chromophores centered at 302 nm (UV chromophore) and 415 nm (VIS chromophore) (Fig. 2.1), we developed a Matlab toolbox (Appendix III) to obtain the parameters that best fit (least squares sense) the following equation [*Röttgers and Koch*, 2012; *Breves et al.*, 2003]:

$$a_\lambda = b_1 e^{-b_2(\lambda-\lambda_0)} + b_3 \frac{1}{\sigma\sqrt{2\pi}} e^{\frac{-(\lambda-\lambda_0)^2}{2\sigma^2}} + b_4 \quad (2)$$

The equation was fitted within different wavelength ranges for each chromophore. The **first and third terms** of the equation models the typical exponential decay of any CDOM spectrum with increasing wavelength. It consists of a pre-exponential term ($\mathbf{b_1}$), an exponential slope ($\mathbf{b_2}$), and an absorption parameter to correct for offsets in the absorption at longer wavelength ($\mathbf{b_4}$). The **second term** is a Gaussian function to model the absorption spectra of the UV or VIS chromophore, with $\mathbf{b_3}$ being the height at the reference wavelength $\boldsymbol{\lambda_0}$ of the chromophore and $\boldsymbol{\sigma}$ the width of the Gaussian function, respectively. The absorption coefficient of the UV or VIS chromophore at their respective λ_0 ($\boldsymbol{a_{Ch\text{-}UV}}$ or $\boldsymbol{a_{Ch\text{-}VIS}}$) is calculated as $b_3 \frac{1}{\sigma\sqrt{2\pi}}$. $\mathbf{b_1}$, $\mathbf{b_2}$, $\mathbf{b_3}$, $\mathbf{b_4}$, $\boldsymbol{\lambda_0}$ and $\boldsymbol{\sigma}$ are optimized with the Matlab toolbox. Equation (2) was applied to the wavelength range from 250 to 400 nm to obtain the parameters of the UV chromophore and from 350 to 600 nm to obtain the parameters of the VIS chromophore.

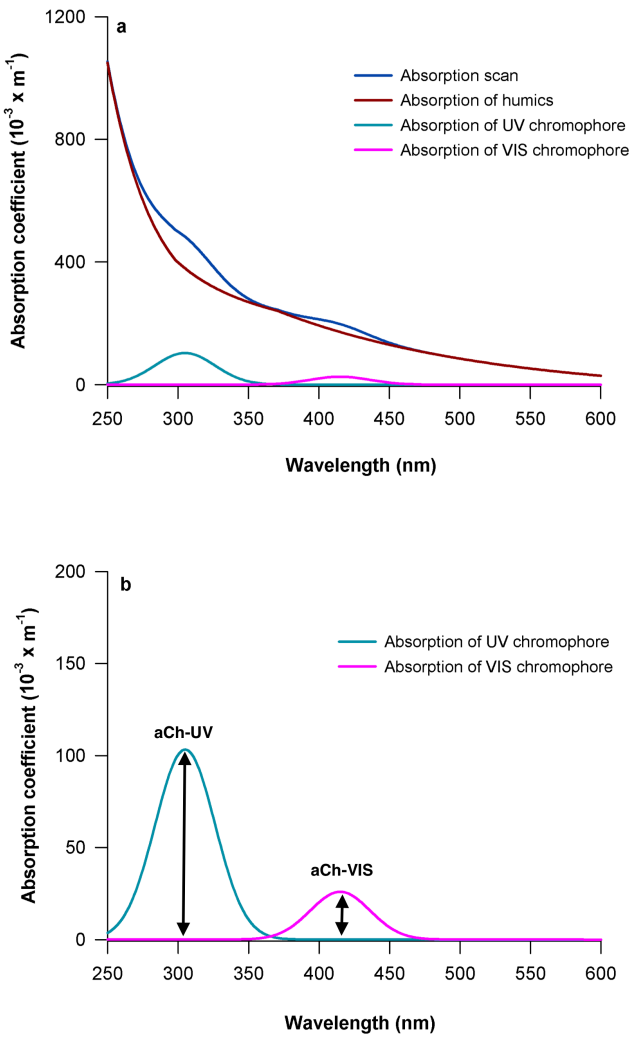

Fig. 2.1. Absorption coefficient spectra of (a) chromophoric dissolved organic matter (CDOM) of the samples collected at station 114 in the North Pacific from the dark ocean and (b) deconvolution of a CDOM absorption coefficient spectrum (dark blue line) into the signal due to the dissolved humic substances plus the residual absorption (brown line), the UV chromophore (green line) and the VIS chromophore (pink line).

Ideal water ages

They were estimated by interpolating the gridded mean ages obtained by *Khatiwala et al.* [2009; 2012] to our sample time, locations and depths. These ages represent the time elapsed from the instant that each water samples was last in contact with the atmosphere. For more details Chapter I.

Water mass analysis

The water mass analysis applied was the same as for CDOM (see methods of chapter I). The WT and samples arquetypal values of both a_{ChUV} and a_{ChVIS} were calculated following the Eq. 7 and 8 from chapter I (Fig. 2.2).

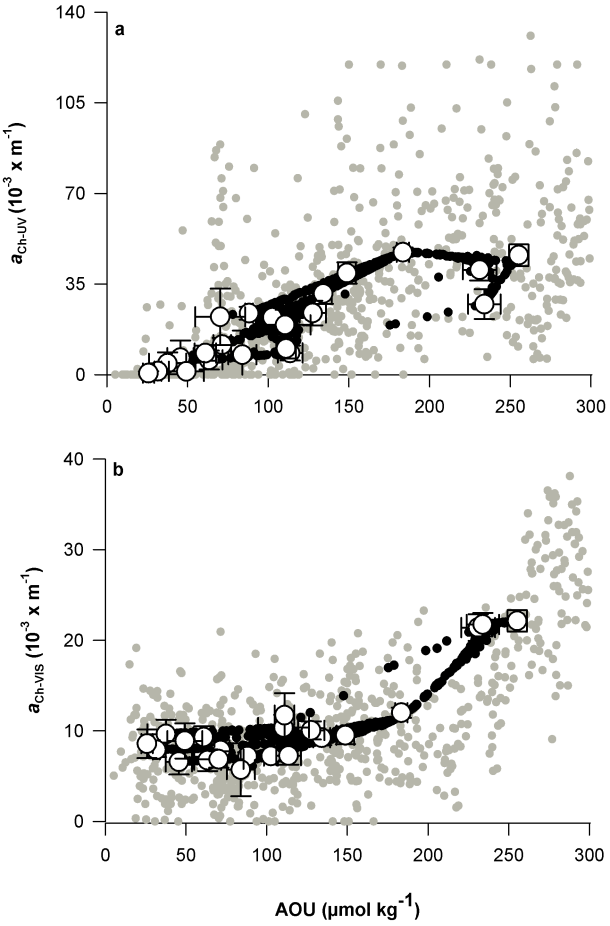

Fig. 2.2. Relationship between (a) the absorption coefficient of the UV chromophore ($a_{Ch\text{-}UV}$, x 10^{-3} m^{-1}) with apparent oxygen utilization (AOU, µmol kg^{-1}) and (b) the absorption coefficient of the Visible chromophore ($a_{Ch\text{-}VIS}$, x 10^{-3} m^{-1}) with apparent oxygen utilization (AOU, µmol kg^{-1}). The measured concentrations (grey dots), archetypal concentrations for each water type (white dots) with their standard deviations of the estimates (SDN_i), and archetypal concentrations for each sample (black dots) are presented.

Table 2.1. Characteristics of the water types (WT) intercepted during the circumnavigation.

Domain	Acronym	VOL_i (%)	Z_i (m)	AOU_i ($\mu mol\ kg^{-1}$)	τ_i (y)	OUR_i ($\mu mol\ kg^{-1}\ y^{-1}$)	NO_{3i} (μM)	$a_{Ch\text{-}UV}$ ($10^{-3}\ m^{-1}$)	$a_{Ch\text{-}VIS}$ ($10^{-3}\ m^{-1}$)	$\lambda_{Ch\text{-}UV}$ (nm)	$\lambda_{Ch\text{-}VIS}$ (nm)	$\sigma_{Ch\text{-}UV}$ (nm)	$\sigma_{Ch\text{-}VIS}$ (nm)
Central (200 – 500 m)	EDW	0.7%	264 ± 20	46 ± 8	11 ± 4	4 ± 2	7.9 ± 1.5	6 ± 7	7 ± 1	298 ± 5	412 ± 5	17.7 ± 1.6	28.2 ± 1.4
	$ENACW_{12}$	3.2%	641 ± 40	114 ± 7	103 ± 9	1.1 ± 0.2	22.6 ± 1.6	8 ± 3	7 ± 1	300 ± 3	418 ± 3	22.1 ± 1.3	26.8 ± 1.3
	$ENACW_{15}$	1.8%	327 ± 25	63 ± 8	28 ± 7	2.3 ± 0.9	11.9 ± 1.6	6 ± 4	7 ± 1	297 ± 3	413 ± 3	19.5± 1.5	27.7 ± 1.3
	13EqAtl	1.6%	427 ± 37	61 ± 7	134 ± 18	0.5 ± 0.1	16.7 ± 1.9	8 ± 3	9 ± 1	303 ± 4	412 ± 3	20.7 ± 1.2	25.4 ± 2.0
	$SACW_{12}$	2.2%	303 ± 26	110 ± 16	104 ± 16	1.1 ± 0.3	19.3 ± 2.8	19 ± 6	10 ± 1	297 ± 2	416 ± 3	24.3 ± 1.4	24.5 ± 1.6
	$SACW_{18}$	1.4%	211 ± 11	38 ± 12	21 ± 9	2 ± 1	6.9 ± 2.2	4 ± 4	10 ± 2	300 ± 3	413 ± 3	24.1 ± 1.6	26.6 ± 1.8
	$STMW_I$	0.9%	259 ± 35	26 ± 3	14 ± 17	2 ± 2	17.6 ± 1.1	0 ± 1	9 ± 2	304 ± 3	418 ± 4	25.5 ± 2.2	25.4 ± 2.7
	ICW_{13}	4.5%	395 ± 28	32 ± 2	51 ± 12	0.6 ± 0.2	6.1 ± 1.4	1 ± 1	8 ± 1	305 ± 2	414 ± 3	22.5 ± 1.0	25.4 ± 1.2
	$STMW_{SP}$	0.2%	269 ± 26	49 ± 11	58 ± 54	0.9 ± 1.0	1.3 ± 0.8	1 ± 3	9 ± 2	305 ± 10	406 ± 4	20.8 ± 2.3	23.9 ± 6.2
	$SPCW_{20}$	0.5%	277 ± 84	70 ± 15	44 ± 21	2 ± 1	10.5 ± 0.8	22 ± 11	7 ± 1	309 ± 7	412 ± 7	19.5 ± 3.1	22.4 ± 4.1
	13EqPac	5.7%	483 ± 35	231 ± 10	433 ± 34	0.53 ± 0.07	5.1 ± 1.2	40 ± 4	21 ± 1	302 ± 2	417 ± 1	26.9 ± 0.8	27.0 ± 0.8
	CMW_{NP}	3.5%	253 ± 13	234 ± 10	259 ± 16	0.90 ± 0.09	19.9 ± 1.1	27 ± 6	22 ± 1	298 ± 2	415 ± 1	23.7 ± 1.3	28.7 ± 0.6
	$STMW_{NP}$	0.2%	207 ± 36	111 ± 6	141 ± 39	0.8 ± 0.3	18.4 ± 1.3	10 ± 4	12 ± 2	307 ± 14	412 ± 6	16.8 ± 2.0	28.7 ± 2.9
Intermediate (500 – 1500 m)	MW	0.2%	1276 ± 354	84 ± 9	133 ± 42	0.6 ± 0.3	9.5 ± 1.6	8 ± 9	6 ± 3	303 ± 11	419 ± 10	19.1 ± 4.4	26.4 ± 4.5
	SAMW	8.0%	719 ± 42	72 ± 6	214 ± 26	0.33 ± 0.07	23.1 ± 0.9	11 ± 3	8 ± 1	304 ± 1	412 ± 3	23.2 ± 0.8	25.1 ± 0.9
	$AAIW_{3.1}$	4.5%	1317 ± 108	134 ± 5	499 ± 50	0.27 ± 0.04	26.8 ± 1.4	31 ± 4	9 ± 1	304 ± 1	415 ± 4	27.2 ± 1.0	26.6 ± 1.1
	$AAIW_{5.0}$	2.9%	677 ± 36	128 ± 8	228 ± 13	0.56 ± 0.07	29.3 ± 1.4	24 ± 5	10 ± 1	303 ± 3	414 ± 2	24.0 ± 1.4	27.9 ± 1.0
	NPIW	5.9%	671 ± 65	255 ± 6	571 ± 39	0.45 ± 0.04	22.5 ± 0.8	46 ± 4	22 ± 1	300 ± 1	418 ± 1	27.7 ± 0.7	28.4 ± 0.6
Abyssal (>1500 m)	CDW	27.0%	2412 ± 76	183 ± 4	821 ± 22	0.22 ± 0.01	26.7 ± 0.4	47 ± 2	11 ± 1	302 ± 0	416 ± 1	28.4 ± 0.3	27.4 ± 0.4
	$NADW_{2.0}$	12.9%	3279 ± 66	88 ± 2	467 ± 13	0.19 ± 0.01	24.7 ± 0.6	24 ± 2	7 ± 0	299 ± 1	418 ± 2	21.9 ± 0.7	25.1 ± 0.7
	$NADW_{4.6}$	7.6%	1582 ± 99	103 ± 4	277 ± 13	0.37 ± 0.03	26.1 ± 0.9	22 ± 3	7 ± 1	300 ± 2	418 ± 2	23.2 ± 0.8	25.5 ± 0.8
	AABW	4.4%	3780 ± 64	149 ± 6	745 ± 47	0.20 ± 0.02	28.1 ± 1.1	39 ± 4	9 ± 1	302 ± 1	415 ± 4	28.4 ± 0.7	26.8 ± 1.0

Results and Discussion

Water masses distribution

The water types (WT) intercepted during the circumnavigation were classified into central (200–500 m), intermediate (500–1500 m) and abyssal (>1500 m) waters according to their depth range, representing 26%, 22% and 52% of the total sampled volume, respectively (Table 2.1; Fig. 2.3a). Central waters originate at temperate latitudes and are restricted to the oceanic area where they are formed. The most abundant central WT was the 13ºC water of the Equatorial Pacific (13EqPac) with around 6% of the total sampled volume. Regarding intermediate waters, their sources are at subpolar latitudes, except for the case of the Mediterranean water (MW), which spills out from the Strait of Gibraltar with elevated salinity and spreads at about 1000 m in the North Atlantic. The most abundant intermediate water sampled during the circumnavigation was the Antarctic Intermediate water (AAIW), which represented 7.4% of the total sampled volume. Finally, abyssal waters are formed at polar latitudes, either in the Northern North Atlantic or the Southern Ocean. Both intermediate and abyssal waters occupy extensive oceanic regions, being unrestricted to a determined ocean basin. The Circumpolar Deep water (CDW) and the North Atlantic Deep water (NADW) are the most abundant WT, representing 27% and 20% of the total sampled volume, respectively. CDW originates in the Antarctic Circumpolar Current and NADW in the Northern North Atlantic.

DOM chromophores: the UV chromophore and Visible chromophore

A careful examination of the absorption coefficient spectra of the samples revealed a consistent and recurrent presence of two discrete absorption chromophores (Fig. 2.1a) The first chromophore is centered at 302 ± 3 nm occupying a wavelength band of 26 ± 6 nm, and had not been described ever in the dark global ocean. The absorption coefficient of this UV chromophore, $a_{Ch\text{-}UV}$, ranged from 0 to 131 x 10^{-3} m^{-1}, with maximum values in the intermediate and deep waters of the Pacific Ocean (Fig. 2.3b). The second ubiquitous chromophore presented a maximum absorption at 415 ± 3 nm and a wavelength band of 27 ± 6 nm. Maximum values of the absorption coefficient of this chromophore, $a_{Ch\text{-}VIS}$, were found at intermediate depths of the North Pacific reaching up to 38 x 10^{-3} m^{-1} (Fig. 2.3c).

The highest $a_{Ch\text{-}UVi}$ values for the UV chromophore were 47 ± 2 x 10^{-3} m^{-1} for the CDW, 46 ± 4 x 10^{-3} m^{-1} for the North Pacific Intermediate water (NPIW), 40 ± 4 x 10^{-3} m^{-1} for the 13EqPac, and 39 ± 4 x 10^{-3} m^{-1} for the Antarctic Bottom water (AABW) (Table 2.1., orange and green dots in Fig. 2.4.a, b, c). Note that these are the less ventilated water masses intercepted during the circumnavigation (as shown from their estimated ideal ages, τ) and exhibit the largest cumulative microbial respiration (as follows from their apparent oxygen utilization, AOU) (Table 2.1.). The lowest values were observed in the central waters of the three ocean basins (Fig. 2.3b). The water masses with minimum $a_{Ch\text{-}UVi}$ values were the subtropical mode waters of the Indian ($STMW_I$, 1 ± 1 x 10^{-3} m^{-1}) and

South Pacific oceans ($STMW_{SP}$, 1 ± 3 x 10^{-3} m^{-1}) and the Indian Central Water of 13°C (ICW_{13}, 1 ± 1 x 10^{-3} m^{-1}), which in turn are the most ventilated water masses intercepted during the circumnavigation (Table 2.1).

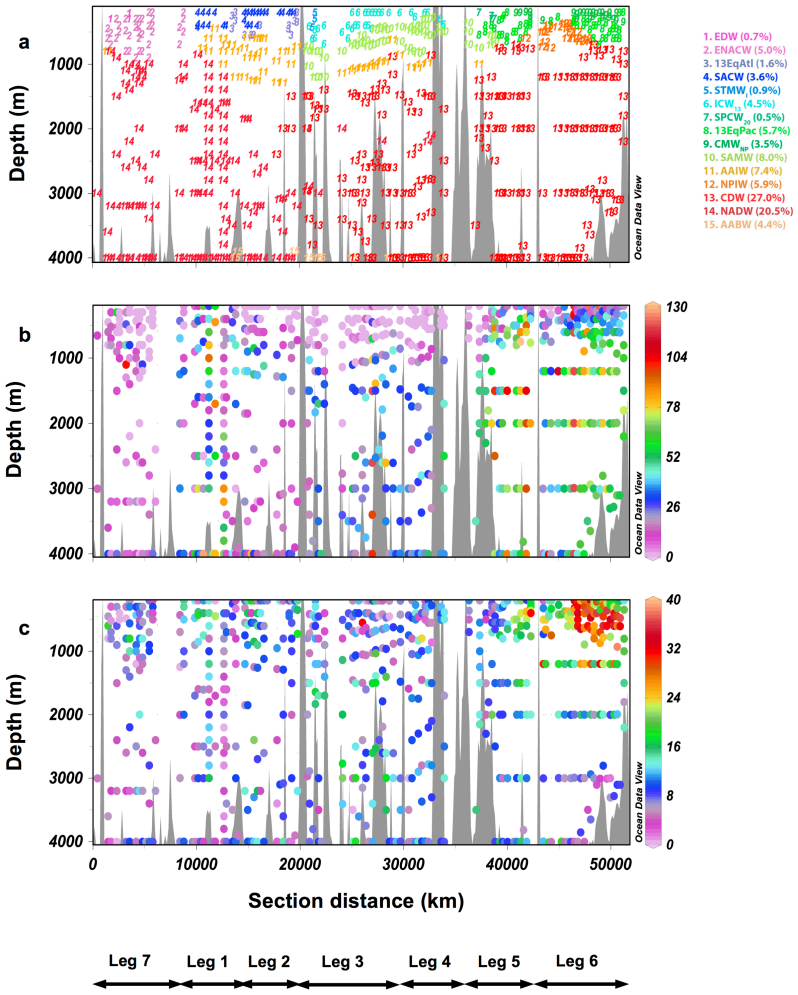

Fig. 2.3. Distribution of (a) the most abundant fifteen WT domains intercepted during the Malaspina 2010 circumnavigation; (b) absorption coefficients of the UV chromophore ($a_{Ch\text{-}UV}$, x 10^{-3} m^{-1}), n= 740; and (c) absorption coefficients of the Visible chromophore ($a_{Ch\text{-}VIS}$, x 10^{-3} m^{-1}), n = 713. Note that the depth scale starts at 200 m.

Green and orange dots are water masses with distinctive characteristics (see the text for clarification). Equations for (a), (b), (d) and (e) are shown in Table 2.2. The dashed grey line in (c) represents the expected absorption coefficient due to nitrate on basis of its molar absorption coefficient (7.14 M^{-1} cm^{-1} [*Jankowski et al.,* 1999]).

Consequently, highly significant (p < 0.001) positive simple linear regressions were obtained for $a_{Ch\text{-}UVi}$ with archetypal AOU (AOU_i), and with archetypal ideal age (τ_i) (Fig. 2.4a, b; Table 2.2). Moreover, the distribution of $a_{Ch\text{-}UVi}$ was modelled better by a multiple linear regression with τ_i and AOU_i (R^2 = 0.91, p < 0.001):

$$a_{\mathrm{Ch-UVi}} = c \cdot \tau_i + d \cdot \mathrm{AOU_i} \qquad (3)$$

where c and d are the regression coefficients reported in Table 2.2 (c = 3.5 ± 0.6 x 10^{-5} m^{-1} yr^{-1}, d = 10 ± 2 x 10^{-5} m^{-1} μmol^{-1} kg). Age (τ_i) was the primary (normalized regression coefficient, 0.57 ± 0.01) and ageing (AOU_i) the secondary (normalized regression coefficient, 0.46 ± 0.01) explanatory variable (Table 2.2). By deriving equation (3) with respect to τ_i, we calculated the net production (NP) of $a_{Ch\text{-}UV}$ for each water mass as follows:

$$\mathrm{NP}a_{\mathrm{Ch-UVi}} = \frac{\partial a_{\mathrm{Ch-UVi}}}{\partial \tau_i} = c + d \cdot \frac{\partial \mathrm{AOU_i}}{\partial \tau_i} = c + d \cdot \mathrm{OUR_i} \qquad (4)$$

This derivate highlights the positive dependence of the net production of $a_{Ch\text{-}UVi}$ ($NPa_{Ch\text{-}UVi}$) with the oxygen utilization rate ($OUR_i = AOU_i/\tau_i$). A higher OUR_i is indicative of a higher respiration rate related to a larger amount of organic substrate available for microbial utilization or higher temperatures in a given water mass [*Brown et al.,* 2004; *Mazuecos et al.,* 2015]. Substituting the water mass proportion weighted average OUR of the global dark ocean in Eq. 4, 0.5 ± 0.1 µmol kg^{-1} yr^{-1} ($= \sum_i \%\mathrm{VOL_i} \cdot \mathrm{OUR_i}/100$), we obtained a global average net production rate of $a_{Ch\text{-}UVi}$ of 8.6 ± 1.1 x10^{-5} m^{-1} yr^{-1}. Finally, dividing the water mass proportion weighted-average $a_{Ch\text{-}UVi}$ of the dark ocean, 30 ± 3 x10^{-3} m^{-1} ($=\sum_i \mathrm{VOL_i} \times a_{\mathrm{Ch-UVi}}/100$), by the $NPa_{Ch\text{-}UVi}$ yields a turnover time of 345 ± 80 yr for this chromophore. This turnover time is not significantly different from the water mass weighted average ideal age of our samples, 454 ± 22 yr, but significantly shorter (p < 0.05) than the turnover time of the total humic fraction of CDOM, 634 ± 120 yr, as calculated from the absorption coefficient at 325 nm (a_{325}) (Chapter I of this PhD thesis) Therefore, the recalcitrant nature of the UV chromophore dictates its accumulation over time, but its net production depends on the microbial respiration rate characteristic of each water mass, i.e. for two water masses that were last in contact with the atmosphere at the same time, the largest $a_{Ch\text{-}UVi}$ is detected in the one that underwent the highest OUR_i.

The UV chromophore is partly due to the absorption of nitrate in the UVB region of the spectrum [*Johnson and Coletti*, 2002]. Nitrate has two principal absorption bands, the first is an intense π → π* band occurring in the far UV at 201 nm, while the second is a weak absorption band centred at 302 nm [*Jankowski et al.,* 1999], which coincides in position and shape with the UV chromophore. In fact, addition of sodium nitrate to seawater causes an initial increase in the absorption coefficient for wavelengths <330 nm associated with the absorption properties of nitrate in the UVB region [*Swan et al.,* 2012]. However, an overall

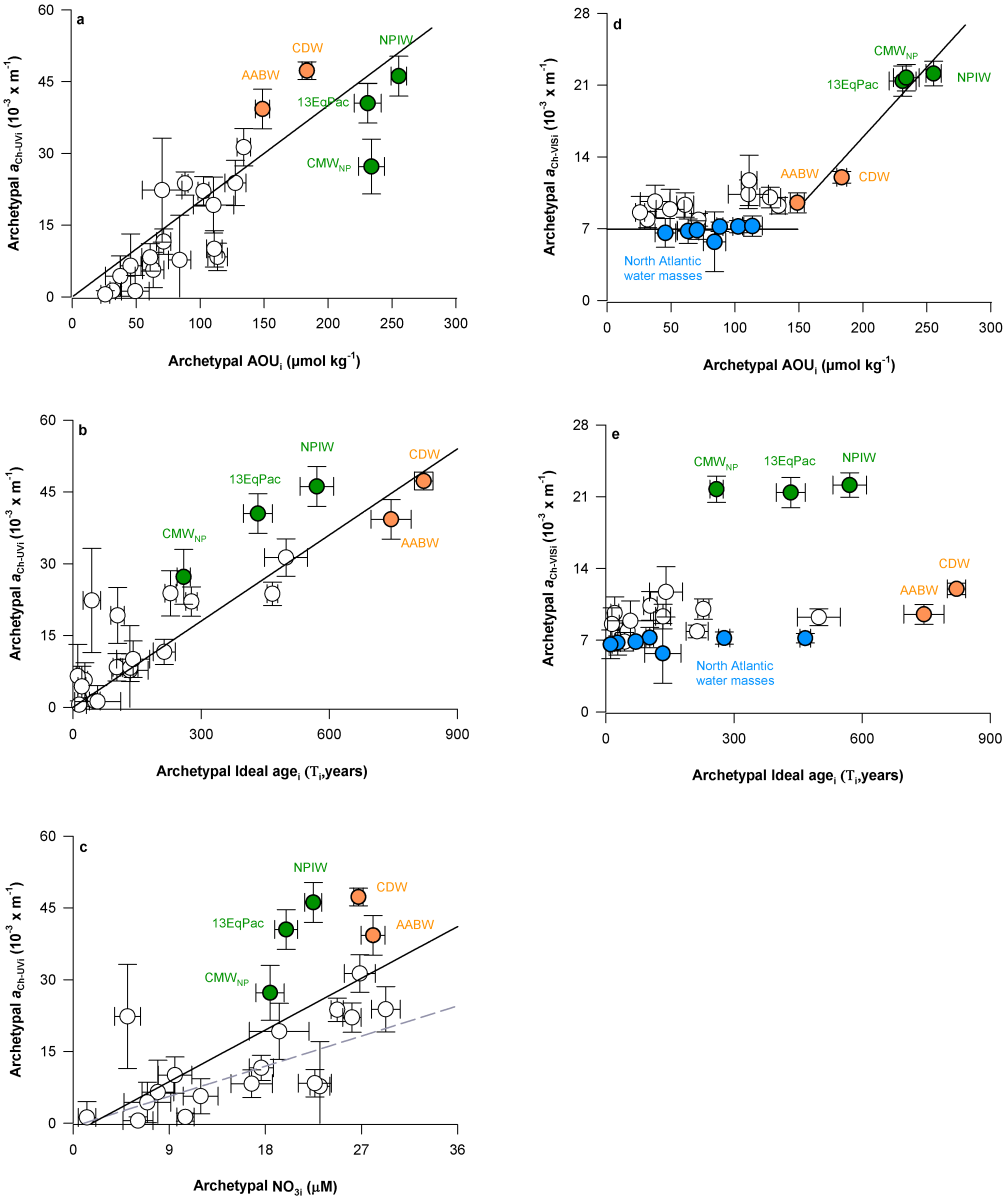

Fig. 2.4. Archetypal absorption coefficient of the UV chromophore ($a_{Ch\text{-}UVi}$, x 10^{-3} m^{-1}) versus (a) archetypal apparent oxygen utilization (AOU_i, µmol kg^{-1}); (b) archetypal ideal age (τ, yr); and (c) archetypal nitrate concentration (NO_{3i}, µM, black line). Archetypal absorption coefficient of the Visible chromophore ($a_{Ch\text{-}VISi}$, x 10^{-3} m^{-1}) versus (d) archetypal apparent oxygen utilization (AOU_i, µmol kg^{-1}); and (e) archetypal ideal age (τ_i, yr). n = 22. The corresponding standard deviations of the estimates are shown.

Table 2.2. Linear relationships of the archetypal apparent oxygen utilization (AOU) and ideal water age (τ) with the absorption coefficient maximum of the UV ($a_{Ch\text{-}UV}$) and visible ($a_{Ch\text{-}VIS}$) chromophores of the water masses intercepted during the Malaspina 2010 circumnavigation.

	UV chromophore	VIS chromophore
AOU (μmol kg^{-1})	$a_{Ch\text{-}UVi} = 2.2 \pm 0.3 \times 10^{-4}$ AOU_i $R^2 = 0.74$***, n = 22	$a_{Ch\text{-}VISi} = 1.4 \pm 0.2 \times 10^{-4}$ AOU_i $R^2 = 0.95$***, n = 5
τ (y)	$a_{Ch\text{-}UVi} = 6.2 \pm 0.7 \times 10^{-5} \tau_i$ $R^2 = 0.74$***, n =22	$a_{Ch\text{-}VISi} = 8 \pm 4 \times 10^{-6} \tau_i + 8 \pm 1 \times 10^{-3}$ $R^2 = 0.17$ (ns), n = 22
AOU (μmol kg^{-1}) τ_i (y)	$a_{Ch\text{-}UVi} = 10 \pm 2 \times 10^{-5}$ $AOU_i + 3.5 \pm 0.6 \times 10^{-5} \tau_i$ $R^2 = 0.91$***, n = 22	
Production rate	$8.6 \pm 1.1 \times 10^{-5}$ m^{-1} y^{-1}	$3.1 \pm 0.4 \times 10^{-5}$ m^{-1} y^{-1}
Turnover time	345 ± 80 y	356 ± 74 y

Notation: ***, $p < 0.001$; *, $p < 0.05$; ns, non significant
For AOU vs $a_{Ch\text{-}VIS}$, the regression is applied to water types with AOU > 150 μmol kg^{-1}.

lack of correlation between the concentration of nitrate and the absorption coefficient of CDOM at 300 nm has been reported in the global ocean [*Nelson et al.,* 2007; *Swan et al.,* 2012]. Consistently, the relationship between the archetypal concentration of nitrate (NO_{3i}) and the archetypal absorption coefficient of CDOM at 302 nm (a_{302i}) for the water masses intercepted during the circumnavigation was not significant (R^2 = 0.11, p > 0.13; data not shown). However, it is noticeable that the linear relationship of NO_{3i} with $a_{Ch\text{-}UVi}$ is significant (R^2 = 0.41, p< 0.001; black line in Fig. 2.4c), indicating that the lack of correlation between NO_3 and a_{300} is simply due to the fact that humic substances are causing most of the variability of the absorption coefficient of CDOM at that specific wavelength. Furthermore, for most of the water masses, $a_{Ch\text{-}UVi}$ is higher than expected from the molar absorption coefficient of nitrate (7.14 M^{-1} cm^{-1}) [*Jankowski et al.,* 1999] (see the dashed grey line in Fig. 2.4c), denoting that nitrate is not the only responsible for the absorption of the UV chromophore. Based on the positive multiple relationship of $a_{Ch\text{-}UVi}$ with τ_i and AOU_i and, therefore, of the production of $a_{Ch\text{-}UVi}$ with OUR_i, we hypothesize that $a_{Ch\text{-}UV}$ may primarily be due to the absorption of a colored antioxidant species of the gadusols group. Gadusols are mycosporine-like precursors synthesized by bacteria, cyanobacteria, phytoplankton, macroalgae, plants and fungi with the absorption maximum at 294 nm at physiological pH [*Shick and Dunlap*, 2002]. Besides its most spread function as an UV sunscreen compound [*Shick and Dunlap*, 2002; *Rozema et al.*, 2002; *Oren and Gunde-Cimerman*, 2007], evidence is accumulating that this family of molecules may serve also as

antioxidants scavenging harmful reactive oxygen species produced during the aerobic respiration (e.g. singlet oxygen, superoxide anions, hydroperoxyl and hydroxyl radicals) [*Oren and Gunde-Cimerman*, 2007; *Bandaranayake and Des Rocher*, 1999].

Regarding the Visible chromophore, it has been previously found in subsurface waters of the eastern Atlantic Ocean, the West Pacific and the Santa Barbara Channel [*Röttgers and Koch*, 2012] and the Arabian Sea [*Breves et al.,* 2003]. It was more pronounced in and below the deep chlorophyll maximum (DCM) and extended into the oxygen minimum layer [*Röttgers and Koch*, 2012; *Breves et al.,* 2003]. Here, we provide further evidence of the presence of this chromophore in the dark global ocean. Maximum archetypal $a_{Ch\text{-}VIS}$ values were observed in the poorly ventilated NPIW, North Pacific Central Mode water (CMW_{NP}) and 13EqPac, with values around 22 ± 1 x 10^{-3} m^{-1} (Table 2.1, green dots in Fig. 2.4d). The lowest values were recorded in the central, intermediate and deep waters of the North Atlantic, ranging from 6 to 8 x 10^{-3} m^{-1} (Table 2.1, blue dots in Fig. 2.4d). The scatterplot between $a_{Ch\text{-}VISi}$ and AOU_i (Fig. 2.4d) indicates that for AOU_i < 150 µmol kg^{-1}, $a_{Ch\text{-}VISi}$ remains constant at 7 ± 1 x 10^{-3} m^{-1} and for AOU_i > 150 µmol kg^{-1} a significant positive linear relationship (R^2 = 0.95, p <0.001) was observed between $a_{Ch\text{-}VISi}$ and AOU_i (Fig. 2.4d, Table 2.2). Conversely, we did not find a significant relationship between $a_{Ch\text{-}VISi}$ and τ_i (Fig. 2.4e, Table 2.2), which means that ageing, but not age, is the key factor controlling the accumulation of this chromophore in the dark global ocean. As AOU_i was the only explanatory variable, the water mass weighted average net production rate of $a_{Ch\text{-}VIS}$ was 3.1 ± 0.4 x10^{-5} m^{-1} yr^{-1} and was obtained as:

$$\mathrm{NP}a_{\mathrm{Ch-VIS}} = \sum_i \frac{\mathrm{VOL_i}}{100} \cdot \left(\frac{\partial a_{\mathrm{VISi}}}{\partial \mathrm{AOU_i}}\right) \cdot \left(\frac{\partial \mathrm{AOU_i}}{\partial \tau_i}\right) = \sum_i \frac{\mathrm{VOL_i}}{100} \cdot \left(\frac{\partial a_{\mathrm{VISi}}}{\partial \mathrm{AOU_i}}\right) \cdot \mathrm{OUR_i} \quad (5)$$

As for the case of $a_{Ch\text{-}UV}$, dividing this number by the average concentration of $a_{Ch\text{-}VIS}$ (11.2 ± 0.8 x 10^{-3} m^{-1}) we obtained a turnover time of 356 ± 74 yr for this chromophore, which is not significantly different from the turnover time of $a_{Ch\text{-}UV}$.

The respiratory enzyme cytochrome c oxidase (CcO) has been suggested as a plausible source for the absorption of the Visible chromophore [*Röttgers and Koch*, 2012]. This enzyme presents an absorption maxima around 410 to 415 nm and is one of the most important components of cellular respiration, which reduces molecular oxygen to water coupled to the pumping of protons across the mitochondrial or bacterial membrane [*Yoshikawa et al.,* 2011]. Previous studies demonstrated absorption at 415 nm by bio-detritus [*Kishino et al.,* 1985; *Bricaud and Stramski,* 1990] and by heterotrophs such as bacteria, ciliates and flagellates [*Morel and Ahn,* 1990; *Stramski and Kiefer,* 1998]. Hence, it is probable that a noteworthy source of this chromophore originates from the particulate fraction, either from bacteria or detrital particles sinking down from the euphotic zone [*Röttgers and Koch*, 2012]. Another enzyme as the ribulose-1,5 bisphosphate carboxylase/oxydase (RuBisCO) has been observed well-preserved at high concentrations in intermediate and deep waters of the North Pacific Ocean [*Orellana and Hansell,* 2012] suggesting a very effective export from surface

waters. Likewise, the stable $a_{Ch\text{-}VISi}$ values around 7 ± 1 x 10^{-3} m^{-1} for water masses with AOU_i < 150 µmol kg^{-1} may be CoC remnants produced by phytoplankton during respiration and accumulated in the surface layer due to their slow degradation rates until water mass formation during winter mixing.

Conclusions

In this study, we have identified two chromophores related to microbial respiration. We propose nitrate as certain and gadusols as likely generators of the UV chromophore. Gadusols are active secondary metabolite synthesized to counteract the harmful oxygen reactive species during microbial respiration. Both water mass age and ageing contribute significantly to explain the global distribution of $a_{Ch\text{-}UV}$, reflecting that its synthesis is enhanced with the respiration rate and its recalcitrant nature let its accumulation over time. We assigned the Visible chromophore to CcO, which is considered a residue released after cell ruptures. The fact that only ageing contributed to explain the global distribution of $a_{Ch\text{-}VIS}$ reflects that this chromophore is more dependent on the cumulative respiration than on the time that the water mass has not been in contact with the atmosphere. In summary, we suggest that the UV chromophore could be a proxy of oxidative stress, whereas the Visible chromophore can be a feasible proxy of long-term respiration processes in the dark ocean.

Acknowledgments

We thank C.M. Duarte for the coordination of the Malaspina expedition; the chief scientists of the seven legs, the staff of the Marine Technology Unit (CSIC-UTM) and the Captain and crew of R/V Hespérides for their outright support during the circumnavigation. Also, we thank the Physics block for collecting, calibrating and processing the CTD data; Dolors Blasco for facilitating the nitrate data; Antonio Fuentes-Lema, Eva Ortega-Retuerta, Celia Marrasé, Mar Nieto-Cid, Cristina Romera-Castillo and Francesca Iuculano for their contribution to sampling collection and measurements; Bieito Fernandez-Castro for Matlab support, as well as Eulogio Corral Arredondo for the "Chromophores Toolbox" web page design. This study was financed by the Malaspina 2010 circumnavigation expedition (grant number CSD2008–00077).

Chapter 3

Published in Nature Communications

DOI: 10.1038/ncomms6986

Turnover time of fluorescent dissolved organic matter in the dark global ocean

T. S. Catalá[1], I. Reche[1], A. Fuentes-Lema[2], C. Romera-Castillo[3], M. Nieto-Cid[3], E. Ortega-Retuerta[4], E. Calvo[4], M. Álvarez[5], C. Marrasé[4], C. A. Stedmon[6], X. A. Álvarez-Salgado[3]

[1] Departamento de Ecología and Instituto del Agua, Universidad de Granada, 18071 Granada, Spain, [2] Departamento de Ecoloxía e Bioloxía Animal, Universidade de Vigo, 36310 Vigo, Spain, [3] CSIC Instituto de Investigacións Mariñas, 36208 Vigo, Spain,[4] CSIC Institut de Ciencies del Mar, 08003 Barcelona, Spain, [5] IEO Centro Oceanográfico de A Coruña, 15006 A Coruña, Spain,[6] National Institute of Aquatic Resources, Technical University of Denmark, 2920 Charlottenlund, Denmark.

Abstract

Marine dissolved organic matter (DOM) is one of the largest reservoirs of reduced carbon on Earth. In the dark ocean (> 200 m), most of this carbon is refractory DOM (RDOM). This RDOM, largely produced by microbial mineralization of organic matter, includes humic-like substances generated *in situ* and detectable by fluorescence spectroscopy. Here we show two ubiquitous humic-like fluorophores with turnover times of 529 ± 49 and 742 ± 67 yr, which persist significantly longer than the ca. 350 yr that the dark global ocean takes to renew. In parallel, decay of a tyrosine-like fluorophore with a turnover time of 461 ± 125 yr is also detected. We propose using DOM fluorescence to study the cycling of resistant DOM that is preserved at centennial time scales and could represent a mechanism of carbon sequestration (humic-like fraction); and decaying DOM injected in the dark global ocean, where it decreases at centennial time scales (tyrosine-like fraction).

Introduction

The biological pump has long been recognized as a mechanism to remove CO_2 from the atmosphere, through photosynthesis and export of particulate and dissolved organic matter to the dark ocean [*Ducklow et al.*, 2001]. More recently, the transformation of biologically labile organic matter into refractory (long lifetime in the dark ocean) compounds by prokaryotic activity has been termed the 'microbial carbon pump' and may constitute also an effective mechanism to accumulate reduced carbon in the dark ocean [*Hansell*, 2013; *Ogawa et al.*, 2001]. Given the large pool of RDOM in the oceans (ca. 656 Pg C) [*Hansell*, 2013], understanding its generation, transformation and role in carbon sequestration is crucial under present and future CO_2 emission scenarios.

Some components of the marine RDOM pool absorb light and a fraction of them also emit fluorescence (fluorescent dissolved organic matter, FDOM) [*Yamashita and Tanoue*, 2008; *Jørgensen et al.*, 2011]. These optical properties are used as tracers for circulation and biogeochemical processes in the dark ocean [*Nelson and Siegel*, 2007].

Here, we obtained the distribution of FDOM in the ocean interior by measuring fluorescence intensities scanned over a range of excitation/emission wavelengths during the Spanish Malaspina 2010 circumnavigation of the globe (Fig. 1.1 in Chapter 1). Discrete fluorescent fractions can be discriminated

from the measured spectra by applying Parallel Factor Analysis [*Stedmon and Bro*, 2008]. Four fluorescent components were isolated from the whole dataset and appear to be ubiquitous and common in the dark global ocean [*Yamashita and Tanoue*, 2008; *Jørgensen et al.*, 2011]. Two components (C1, C2) had a broad excitation and emission spectra, with excitation and emission maxima in the UVA and visible region, respectively. These are traditionally referred to as humic-like components, which accumulate and have turnover times of 529 ± 49 and 742 ± 67 yr, respectively. These turnover times are longer than the ca. 350 yr that the dark (>200 m) global ocean takes to renew [*Laruelle et al.*, 2009]. The two other components (C3, C4) had narrower spectra with excitation and emission maxima below 350 nm and are similar to the spectra of tryptophan and tyrosine, respectively [*Coble*, 1996]. The dark global ocean appears to be a sink for fluorescent tyrosine-like (C4) component and has a turnover time of 461 ± 125 yr that is comparable to turnover time of DOC pool (estimated in 370 yr [*Hansell et al.*, 2009]. Thus, we propose that the fluorescent fractions of DOM are suitable proxies for determining the cycling of the RDOM that produces (humic-like) and decays (tyrosine-like) in the dark ocean at centennial time scales.

Methods

Sample collection

A total of 147 stations were sampled from 40°S to 34°N in the Atlantic, Indian and Pacific Oceans (Malaspina Expedition, December 2010 to July 2011). Vertical profiles of salinity (S), potential temperature (θ) and dissolved oxygen (O_2 μmol kg^{-1}) were recorded continuously with the conductivity–temperature–depth (CTD) and oxygen sensors installed in the rosette sampler. Salinity and dissolved oxygen were calibrated against bottle samples determined with an on board salinometer and the Winkler method, respectively. The apparent oxygen utilization (AOU) was calculated as the difference between the saturation and measured dissolved oxygen. Oxygen saturation was calculated from salinity and potential temperatura [*Benson and Krauss*, 1984]. Bottle depths were chosen on basis of the CTD-O_2 profiles to cover as much water masses as possible of the dark global ocean. Seawater samples for fluorescence measurements, collected in 12 L Niskin bottles, were immediately poured into glass bottles and stored in dark conditions until measurement before 6 hours from collection. We collected 800 water samples from 200 m to 4000 m depth.

Fluorescence spectral acquisition

When the chromophoric fraction of marine dissolved organic matter (CDOM) is irradiated with ultraviolet light, it emits a fluorescence signal characteristic of both amino acid- and humic-like compounds, which is collectively termed fluorescent DOM (FDOM) [*Coble*, 1996]. Fluorescence Excitation-Emission matrices (EEMs) were collected with a JY-Horiba Spex Fluoromax-4 spectrofluorometer at room temperature (around 20°C) using 5 nm excitation and emission slit widths, an integration time of 0.25 s, an excitation range of 240–450 nm at 10 nm increments, and an emission range of 300–560 nm at 2 nm

increments. To correct for lamp spectral properties and to compare results with those reported in other studies, spectra were collected in signal·to·reference (S:R) mode with instrument·specific excitation and emission corrections applied during collection, and EEMs were normalized to the Raman area. In our case, the Raman area (RA) and its baseline correction were performed with the emission scan at 350 nm of the Milli·Q water blanks and the area was calculated following the trapezoidal rule of integration [*Stubbins et al.*, 2014].

Furthermore, to track that the variability of the instrument during the 147 working days of the expedition affected similarly to the Raman, amino acid· and humic·like regions of the spectrum, the following three standards were run daily: (1) a P·terphenyl block (Stranna) that fluoresces in the amino acid region, between 310 nm and 600 nm exciting at 295 nm; (2) a Tetraphenyl butadiene block (Stranna) that fluoresces in the humic region, between 365 nm and 600 nm exciting at 348 nm; and (3) a sealed Milli·Q cuvette (Perkin Elmer) scanned between 365 nm and 450 nm exciting at 350 nm. Fig. 3.1a shows that the temporal evolution of the Raman area of the Milli·Q water used on board and the reference P·terphenyl and Tetraphenyl butadiene reference materials were parallel, which confirms that the Raman normalization was successful in both the amino acid· and the humic·like region of the EEMs. Therefore, no extra corrections were needed. The comparison between the reference sealed Milli·Q (sMQ) and the daily Milli·Q water allowed us to demonstrate that the Milli·Q water used on board was of a good quality (Fig.3.1b). The average coefficient of variation (CV) between the sMQ and Milli·Q water throughout the circumnavigation was only 0.81%. Similarly, two scans of the reference sealed Milli·Q were measured at the beginning (sMQ_1) and at the end (sMQ_2) of each session, which reveals a slight shift of the fluorescence intensities along each working day (Fig.3.1c). The initial and final sMQ spectra where separated about 10 hours of continuous work of the spectrofluorometer. We found that the average coefficient of variation (CV) between sMQ_1 and sMQ_2 was 1.62%. Therefore, the daily instrument shift was low and about twice the long·term variability throughout the circumnavigation.

Inner·filter correction was not applied due to the low absorption coefficient of CDOM of the samples collected during the circumnavigation: 1.01 ± 0.04 m^{-1} (average ± standard deviation) at 250 nm, i.e. much lower than the threshold of 10 m^{-1} above which this correction is required [*Stedmon and Bro*, 2008]. Raman·normalized Milli·Q blanks were subtracted to remove the Raman scattering signal [*Murphy et al.*, 2010; *Stedmon et al.*, 2003]. Raman area normalization, blank subtraction, and generation of EEMs were performed using MATLAB (version R2008a).

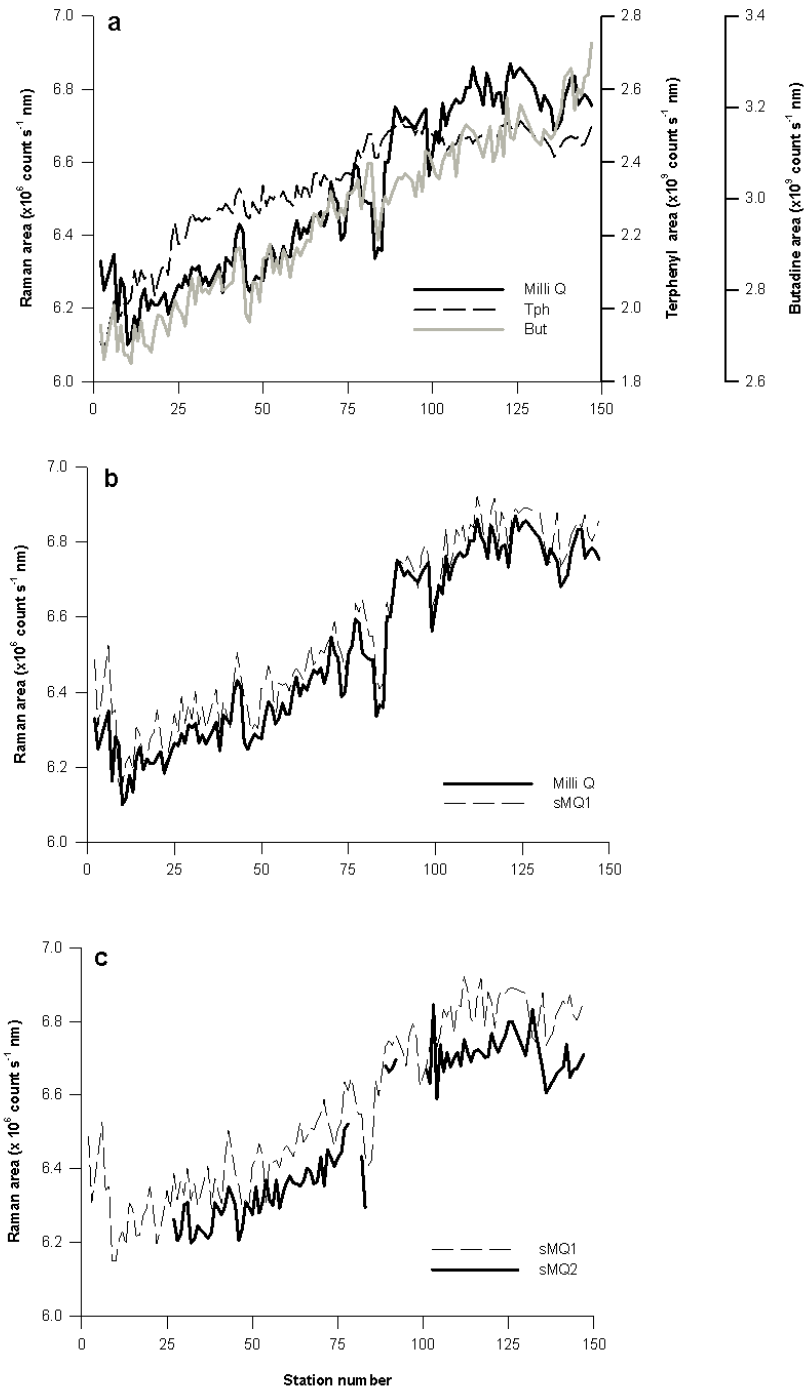

Fig. 3.1. Testing the reliability of the fluorescence measurements during the Malaspina 2010 circumnavigation. Time course ofthe fluorescence intensities of (a) p-Therphenyl (Tph, dotted line), Tetraphenyl butadiene (But, gray line) and R/V Hespérides Milli-Q water (black line); (b) R/V Hespérides Milli-Q water (black line) and sealed initial Milli-Q (sMQ1, dotted line); (c) initial (sMQ1) and final (sMQ2) sealed Milli-Q water along the Malaspina circumnavigation.

Global PARAFAC modelling

Parallel factor analysis (PARAFAC) was used to identify the fluorescent components that comprise the EEMs in the global ocean. PARAFAC was performed using the DOMFluor 1_7 Toolbox8. Prior to the analysis, Rayleigh scatter bands (first order at each wavelength pair where Ex = Em ± bandwidth; second order at each wavelength pair where Em = 2 * Ex ± (2 * bandwidth)) were trimmed. The global PARAFAC model was derived based on 1574 corrected EEMs and was validated using split-half validation and random initialization. A four-component model was obtained (Fig. 3.2), two of them of humic-like nature, Peak A/C (at Ex/Em <270-370/470 nm) and Peak M (at Ex/Em 320/400 nm) and two of amino acid-like nature, attributed to tryptophan and tyrosine at 290/340 nm and 270/310 nm [*Stedmon and Bro,* 2008], respectively. Here we report the maximum fluorescence (Fmax) in Raman units (RU) [*Stubbins et al.*, 2014; *Benson and Krauss*, 1984].

Multi-parameter water mass analysis

For the case of fluorescence measurements (Fmax1, Fmax2, Fmax3, Fmax4), the multi-parameter water mass analysis was applied to the 800 samples from the dark ocean (θ <18°C, AOU >0). For more details of the calculations and the water masses see the methods section of chapter 1 and Appendix II.

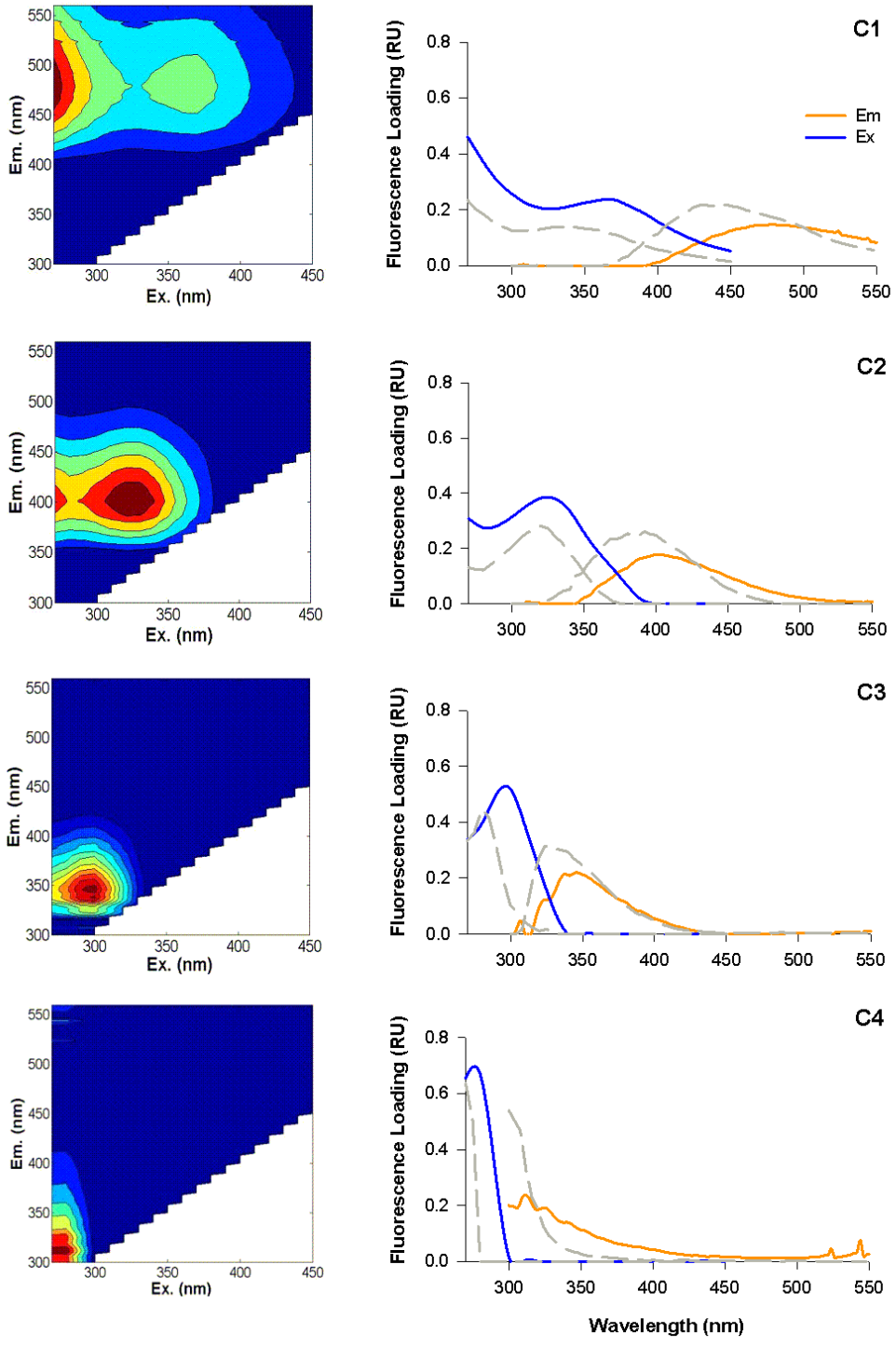

Figure 3.2. Fluorescence matrixes of the 4 identified PARAFAC components (C1-4) in the Malaspina 2010 circumnavigation. C1 represents a combination of peaks A and C, C2 corresponds to peak M, C3 corresponds to peak T (tryptophan-like) and C4 corresponds to peak B (tyrosine-like). The excitation (blue lines) and the emission (orange lines) fluorescence intensities of the four components are compared with previously reported components (gray lines) by *Jørgensen et al.*, [2011].

Results

Water masses across the circumnavigation

The water mass composition of each water sample was described through the mixing of prescribed water types (WT) with a multi-parameter analysis (see the methods section of Chapter I). We identified 22 WT (see Table 3.1) with 12 of them representing 90% of the total volume of water samples collected during the global cruise (Fig. 3.3). Circumpolar Deep Water (CDW) was widely distributed in the Indian and Pacific Oceans accounting for up to 25.6 % of the total volume sampled. North Atlantic Deep Water of 2.0°C ($NADW_{2.0}$) and 4.6°C ($NADW_{4.6}$) accounted 21.4 % of the total volume and mostly located in the Atlantic basin; Antarctic Intermediate Water of 3.1°C ($AAIW_{3.1}$) and 5.0°C ($AAIW_{5.0}$) accounted for 7.6% of the total volume and spread out through the South Atlantic and Indian basins; and North Pacific Intermediate Water accounted for 5.7 % of the total volume sampled.

Global distribution of fluorescent components

The maximum fluorescence intensity (Fmax) of the two humic-like components (C1 and C2) obtained during the Malaspina circumnavigation showed a global distribution similar to the apparent oxygen utilization (AOU) (Fig. 3.4a, b, c), reaching their maxima in the Eastern North Pacific central and intermediate waters and their minima in the Indian Ocean central waters. In contrast, this global trend with AOU was not evident for the two amino acid-like components (C3 and C4) (Fig. 3.4d, e).

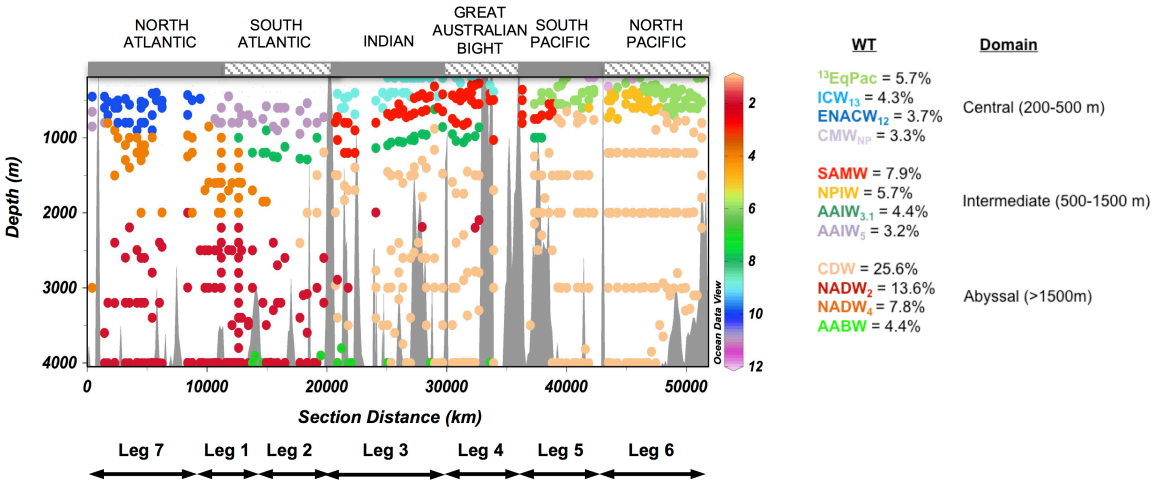

Fig. 3.3. Proportions of the main water types intercepted during Malaspina 2010. The percentages represent the proportion of the total volume of water sampled during the cruise that corresponds to each water type (WT). Here, the 12 most abundant WT are presented. Note that the depth range starts at 200 m. For more details see Table 3.1.

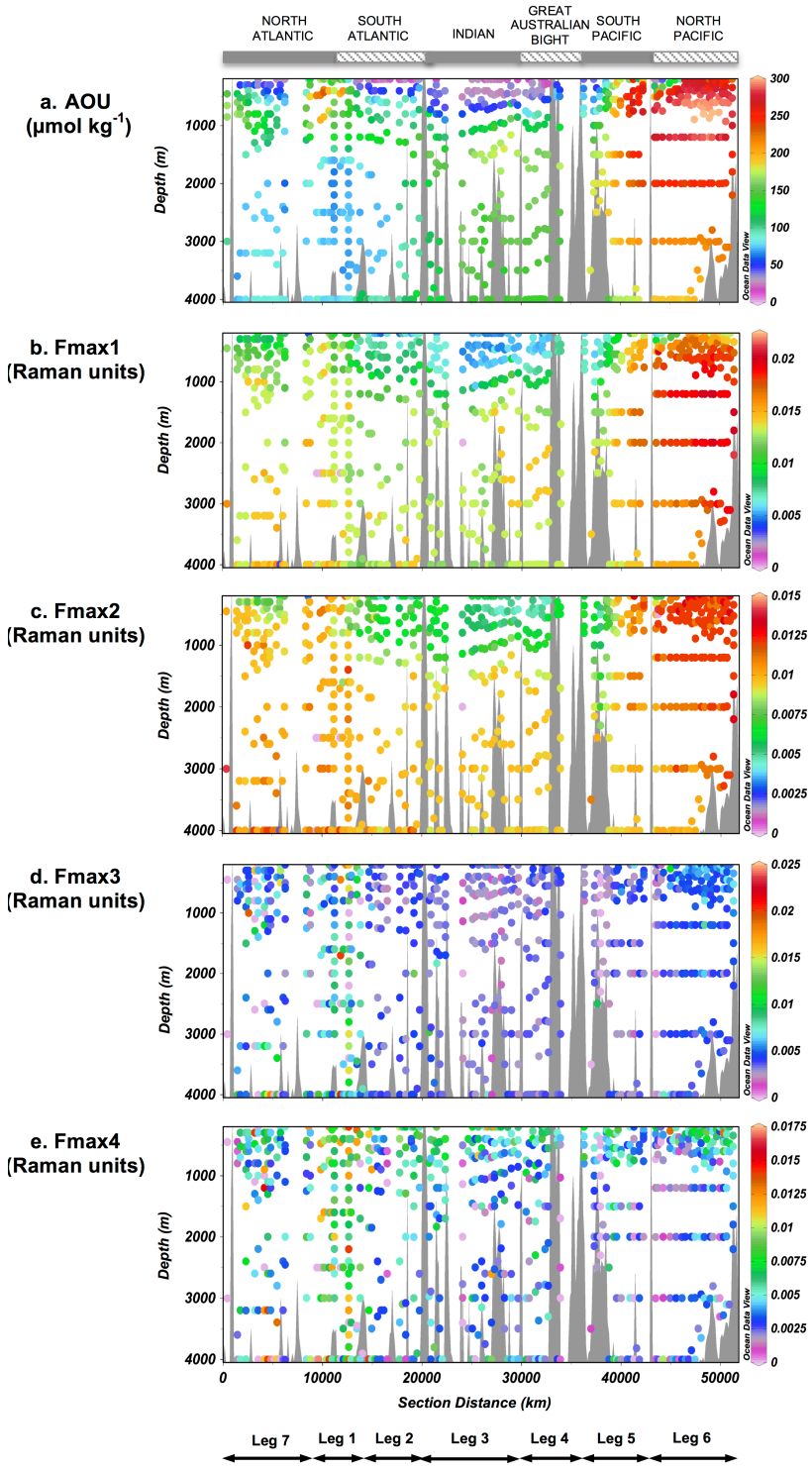

Fig. 3.4. Global distribution of the (a) apparent oxygen utilization (AOU) and the fluorescence intensity at the excitation-emission maxima of the four components (b) Fmax1, (c) Fmax2, (d) Fmax3 and (e) Fmax4 discriminated by the PARAFAC analysis in the global ocean data set of the Malaspina 2010 Expedition are plotted. Note that the depth range starts at 200 m. See methods and Fig. 3.2. for a detailed description of the four fluorescence components.

Table 3.1. Characteristics of the water types (WT) intercepted during the circunnavigation.

Source Water Type	Acronym	VOL_i (%)	Z_i (m)	AOU_i (μmol kg^{-1})	$Fmax1_i$ (× 10^{-3} R.U.)	$Fmax2_i$ (× 10^{-3} R.U.)	$Fmax3_i$ (× 10^{-3} R.U.)	$Fmax4_i$ (× 10^{-3} R.U.)
Eighteen Degrees Water	EDW	0.7	264 ± 20	46 ± 8	8.2 ± 0.6	6.9 ± 0.7	6.0 ± 1.4	6.4 ± 1.9
Eastern North Atlantic Central Water (12ºC)	$ENACW_{12}$	3.7	641 ± 40	114 ± 7	11.6 ± 0.2	9.3 ± 0.1	5.3 ± 0.6	5.0± 0.5
Eastern North Atlantic Central Water (15ºC)	$ENACW_{15}$	1.8	327 ± 25	63 ± 8	9.1 ± 0.4	8.0 ± 0.4	5.8 ± 0.9	6.6 ± 0.9
Equatorial Atlantic Central Water (13ºC)	13EqAtl	1.6	427 ± 37	61 ± 7	7.4 ± 0.3	6.9 ± 0.3	4.9 ± 0.8	6.8 ± 0.9
South Atlantic Central Water (12ºC)	$SACW_{12}$	2.6	303 ± 26	110 ± 16	9.3 ± 0.6	8.4 ± 0.5	5.9 ± 0.8	7.8 ± 0.7
South Atlantic Central Water (18ºC)	$SACW_{18}$	1.5	211 ± 11	38 ± 12	6.6 ± 0.5	6.6 ± 0.6	5.7 ± 1.2	8.3 ± 0.9
Indian Subtropical Mode Water	$STMW_I$	0.8	259 ± 35	26 ± 3	5.4 ± 0.2	5.7 ± 0.2	3.5 ± 0.4	7.3 ± 0.8
Indian Central Water (13ºC)	ICW_{13}	4.3	395 ± 28	32 ± 2	5.5 ± 0.1	5.4 ± 0.1	3.2 ± 0.2	5.8 ± 0.4
South Pacific Subtropical Mode Water	$STMW_{SP}$	0.2	277 ± 84	49 ± 11	6.2 ± 0.4	6.2 ± 0.3	2.8 ± 0.1	6.0 ± 1.1
South Pacific Central Water (20ºC)	$SPCW_{20}$	0.5	269 ± 26	70 ± 15	6.5 ± 0.5	7.8 ± 0.5	2.9± 0.3	5.3 ± 0.8
Equatorial Pacific Central Water (13ºC)	13EqPac	5.7	483 ± 35	231 ± 10	14.5 ± 0.6	10.8 ± 0.3	4.5 ± 0.3	4.8 ± 0.4
North Pacific Central Mode Water (12ºC)	CMW_{NP}	3.3	253 ± 13	234 ± 10	14.1± 0.5	12.0 ± 0.2	5.3 ± 0.3	5.9 ± 0.5
North Pacific Subtropical Mode Water (16ºC)	$STMW_{NP}$	0.2	207 ± 36	111 ± 6	9.0 ± 0.4	11.8 ± 1.7	6.3 ± 1.6	6.8 ± 0.1
Mediterranean Water	MW	0.4	1276 ± 354	84 ± 9	11.8 ± 0.8	9.4 ± 0.3	4.5 ± 0.9	4.3 ± 1.5
Sub-Antarctic Mode Water	SAMW	7.9	719 ± 42	72 ± 6	6.9 ± 0.3	5.9 ± 0.2	2.7 ± 0.1	4.4 ± 0.2
Antarctic Intermediate Water (3.1ºC)	$AAIW_{3.1}$	4.4	1317 ± 108	134 ± 5	10.5 ± 0.4	7.8 ± 0.2	3.1 ± 0.3	3.8 ± 0.4
Antarctic Intermediate Water (5.0ºC)	$AAIW_{5.0}$	3.2	677 ± 36	128 ± 8	10.1 ± 0.4	8.1 ± 0.3	5.2 ± 0.8	6.1 ± 0.6
North Pacific Intermediate Water	NPIW	5.7	671 ± 65	255 ± 6	16.4 ± 0.4	11.4 ± 0.2	4.3 ± 0.2	4.0 ± 0.3
Circumpolar Deep Water	$CDW_{1.6}$	25.6	2412 ± 76	183 ± 4	14.6 ± 0.2	9.9 ± 0.1	3.6 ± 0.1	3.4 ± 0.2
North Atlantic Deep Water (2ºC)	$NADW_{2.0}$	13.6	3279 ± 66	88 ± 2	13.3 ± 0.1	10.1 ± 0.1	6.2 ± 0.4	6.1 ± 0.4
North Atlantic Deep Water (4.6ºC)	$NADW_{4.6}$	7.8	1582 ± 99	103 ± 4	12.5 ± 0.2	9.6 ± 0.2	6.2 ± 0.5	6.3 ± 0.4
Antarctic Bottom Water	AABW	4.4	3780 ± 64	149 ± 6	13.4 ± 0.2	9.6 ± 0.1	3.7 ± 0.3	3.9 ± 0.4
			R^2 (N_i vs $<N_i>$)	0.81	0.77	0.75	0.24	0.26
			SD err of the estimate	34	1.8	1.0	2.4	2.6
			Analytical error	1.0	0.09	0.06	0.11	0.17

%VOLi is the contribution of WT i to the total volume of water collected along the Malaspina cruise, Zi is the arquetypal depth, Fmax1i, Fmax2i, Fmax3i and Fmax4i are the archetypal fluorescent intensities of components 1, 2, 3 and 4. Determination coefficient (R^2), standard deviation of the estimate (SD err).

Relationships between the archetypal AOU and fluorophores

Combining the outputs from the water mass, AOU and fluorescence analyses, we calculated WT proportion-weighted average values, hereafter referred to as archetypal, for the AOU and the fluorescence intensities of the 4 components (see Methods of Chapter I). Archetypal values retain the variability associated with the initial concentrations at the site where each WT is defined and its transformation by basin-scale mineralization processes up to the study site [*Álvarez-Salgado et al.*, 2013]. Archetypal concentrations explained 81%, 77%, 75%, 24%, and 26% of the total variability of AOU, C1, C2, C3, and C4 during the circumnavigation, respectively (Table 3.1).

In the Fig. 3.5. we show the measured maximum fluorescence intensity (grey dots), archetypal values for each water type (white dots) and archetypal values for each sample (black dots) for the components C1 (a), C2 (b), C3 (c) and C4 (d). We obtained direct relationships between the archetypal humic-like components (C1 and C2) and AOU_i (Fig. 3.5a, b) suggesting a net production of these components in parallel with the water mass ageing. The relatively high archetypal fluorescence of C1 (blue dots in Fig. 3.5a) for North Atlantic Deep water (NADW) is related to the high load of terrestrial fluorescent materials transported by the Arctic [*Jørgensen et al.,* 2011] whereas the cause of the high value for the Mediterranean water (MW) is due to the low proportion of this water mass (9 ± 14%) in the samples that contained MW during the circumnavigation, whereas the proportion of NADW was 76 ± 33% in the same samples. Therefore, it is expectable that the archetypal concentration of C1 that our dataset produces for the MW should be close to the NADW archetype. For C2, the North Pacific Subtropical Mode Water ($STMW_{NP}$) (green dot in Fig. 3.5b) also departed from the general archetypal C2–AOU trend. Archetypal C1 and C2 can be modelled with archetypal AOU values using power functions (Fig. 3.5a, b). Given that the high fluorescence of NADW and MW in C1 and of $STMW_{NP}$ in C2 are not related to ageing, these water masses were excluded from their corresponding regression models. It is noticeable that the power factor for C1 (0.51 ± 0.04) is almost twice than for C2 (0.31 ± 0.04), indicating a higher C1 production rate per unit of consumed oxygen. Furthermore, in hypoxic waters (dissolved oxygen concentrations < 60 μmol kg^{-1} [*Naqvi et al.*, 2010]; orange dots in Fig. 3.5a, b) C1 and C2 also behave differently; whereas C1 production was enhanced, C2 did not change substantially.

In contrast, we do not observe a significant relationship between the archetypal values of the tryptophan-like fluorescence component (C3) and AOU (R^2 = 0.001, n = 22, p = 0.88; Fig. 3.5c). This lack of correlation is caused by the low archetypal fluorescence (< 4 x 10^{-3} RU) of the relatively young (AOU < 75 μmol kg^{-1}) central waters of the Indian and South Pacific oceans (ICW_{13}, $STMW_I$, SAMW, $SPCW_{20}$ and $STMW_{SP}$; Table 3.1) (purple dots in Fig. 3.5c). However, such low archetypal values are not observed in the tyrosine-like component (C4), leading to a weak but significant inverse power relationship with AOU (Fig. 3.5d). The archetypal tyrosine-like fluorescence of the aged Central waters (AOU

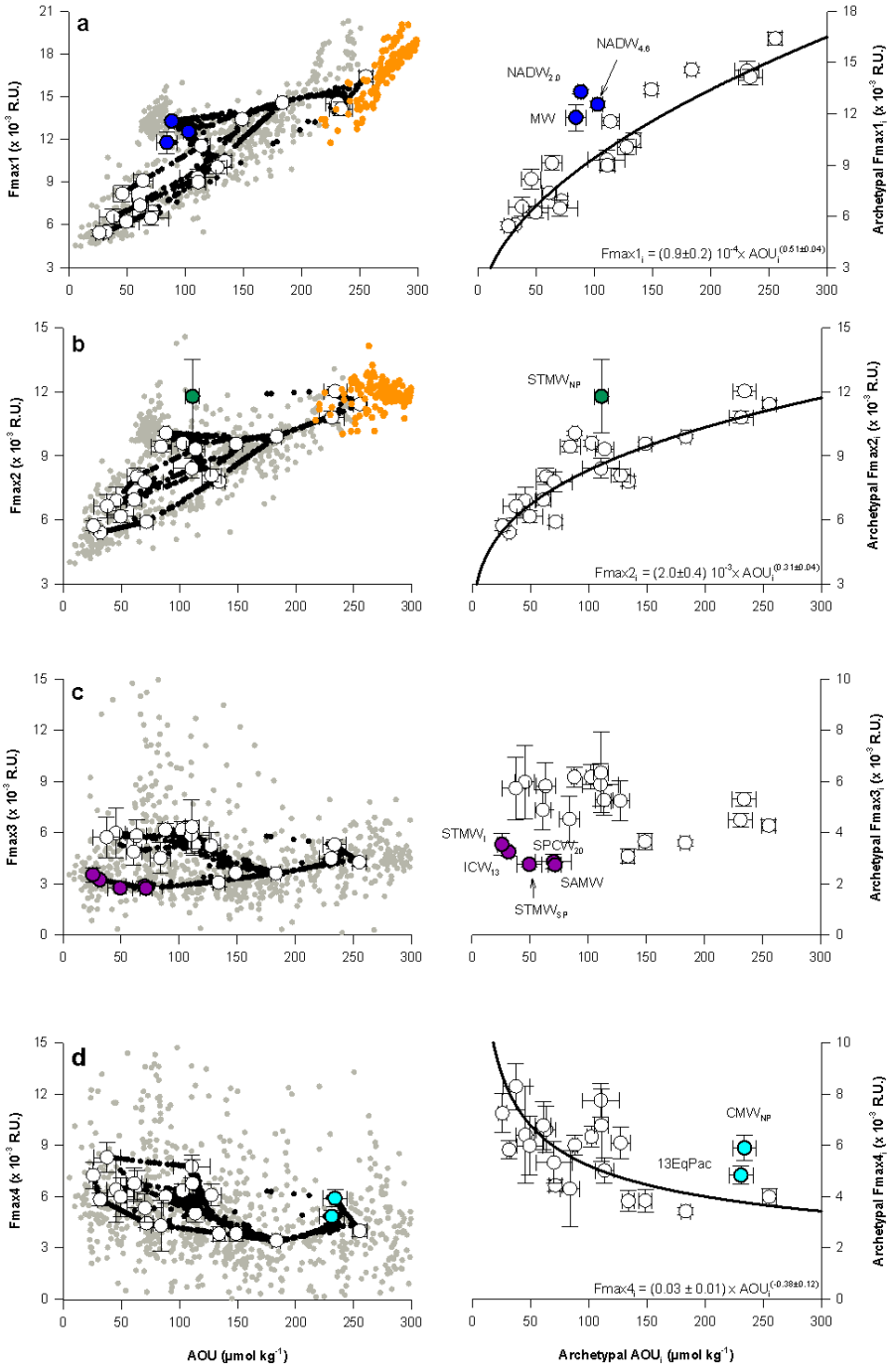

Fig. 3.5. Relationships between the apparent oxygen utilization and the fluorescence components (a) C1, (b) C2, (c) C3 and (d) C4. Grey dots represent measured concentrations, white dots archetypal concentrations for each water type and black dots archetypal concentrations for each sample. Orange dots represent hypoxic samples. In the right column are presented the regression models and fitting equations between archetypal values for C1 (R^2 = 0.90, p <0.001, n = 19), C2 (R^2 = 0.79, p <0.001, n = 21) and C4 (R^2 = 0.31, p < 0.05, n = 20). Water types showed in blue, green, and cyan dots were excluded from their respective regression models. Error bars represent the standard deviation (SD) of the estimated archetypal values of AOU and the four fluorescent components for each water types (see Methods of Chapter I, equation 8).

>200 μmol kg^{-1}) of the Equatorial (13EqPac) and Central North Pacific (CMW_{NP}) exceeded the expected value from their AOU (cyan dots in Fig. 3.5d). These two WT were excluded from the regression model.

Net fluorescent DOM production and turnover times

On the basis of the relationships observed between the archetypal fluorescence intensity of 3 out of 4 fluorescence components (C1, C2 and C4) and AOU, we calculated the net production rate of each component, termed Net Fluorescent DOM Production (NFP). A positive value of NFP indicates net production, as for the case of the humic-like components C1 and C2, and a negative value indicates net decay, as for the case of the amino acid-like C4. The NFP of each component was calculated by multiplying the WT proportion-weighted average fluorescence production values per unit of AOU by the oxygen consumption rate for the dark ocean (OUR_{global}) (see Methods). Here, we have used our OUR_{global} estimate of 0.68 ± 0.18 Pmol O_2 yr^{-1}. The net humic-like fluorescence production rate obtained was 2.3 ± 0.2 x 10^{-5} Raman units yr^{-1} (RU yr^{-1}) for C1 and 1.2 ± 0.1 x 10^{-6} RU yr^{-1} for C2, whereas C4 was consumed at a net rate of –1.1 ± 0.2 x 10^{-5} RU yr^{-1} in the dark global ocean.

Turnover times of components C1, C2 and C4 were calculated dividing the WT weighted-average fluorescence values of the dark global ocean by its corresponding NFP rate (see Methods in Chapter 1). These values represent the time required to produce (C1, C2) or consume (C4) a fluorescence signal of the same intensity than the actual fluorescence of the dark ocean. The resulting turnover of C2, 742 ± 67 yr, was significantly longer than the turnover of C1, 529 ± 49 yr, and both exceeded the turnover times of the bulk DOC pool —estimated in 370 yr [*Hansell et al.*, 2009]— and the terrestrial DOC in the open ocean —estimated in <100 yr [*Hernes and Benner*, 2003] — as well as the renewal time of the dark ocean (water depths > 200 m), estimated in 345 yr [*Laruelle et al.*, 2009]. Conversely, the turnover time of the tyrosine-like component C4 in 461 ± 125 yr was compatible with the turnover time of the bulk DOC.

Discussion

The global pattern in the dark ocean of an increase of the humic-like components concomitant to water mass ageing (high AOU values) has been previously reported [*Yamashita and Tanoue*, 2008; *Jørgensen et al.*, 2011; *Chen and Bada*, 1992; *Hayase and Shinozuka*, 1995]. Although it has been recently hypothesised that this relationship could also be caused by further transformations of terrestrial humic-like materials in the open ocean [*Andrew et al.*, 2013], culture experiments have unequivocally demonstrated that these materials can be produced *in situ* in the oceans [*Jørgensen et al.*, 2014]. In fact, we observe positive and significant relationships between the archetypes of both humic-like components (C1 and C2) and the AOU (Fig. 3.5a, b). The higher C1 production rate per unit of consumed oxygen in comparison with C2 could be related to different mechanisms of production [*Jørgensen et al.*, 2011] that might be linked to the phylogenetic nature of

producers (bacteria, archaea or eukarya) [*Romera-Castillo et al.*, 2011] and/or the sensitivity to environmental oxygen concentration.

The particularly high archetypal fluorescence of C1 for North Atlantic Deep water (NADW) has been previously described and appears to be clearly related to the high load of fluorescent dissolved organic matter of terrestrial origin transported from the Arctic rivers to the North Atlantic Ocean [*Jørgensen et al.*, 2011; *Amon et al.*, 2003; *Benner et al.*, 2005] with a relevant proportion of unaltered high molecular weight lignin [*Hernes and Benner*, 2006]. However, the cause of the high C2 signature for the North Pacific Subtropical Mode Water has not been previously reported. We hypothesize that it could be related to intense rainfall south of the Kuroshio extension where these water mass is formed [*Qiu*, 2002] since it is known that rainwater is particularly enriched in these fluorescent compounds [*Kieber et al.*, 2006; *Santos et al.*, 2009] and this WT is very shallow (archetypal depth = 277 ± 84 m, Table 3.1), which means that rainwater would dilute in a few tenths of meters during formation of that warm water mass. Indeed, lignin-derived phenols, highly modified by photooxidation, have been found in dissolved and submicron particles suspended in the North Pacific Subtropical Mode Water, suggesting an aerosol source for these fluorescent materials [*Hernes and Benner*, 2002]. The high archetypal tyrosine-like fluorescence (C4) of the aged Central waters (AOU > 200 μmol kg^{-1}) of the Equatorial (13EqPac) and Central North Pacific (CMW_{NP}) might be due also to both WT occupy shallow layers (archetypal depths 253 ± 13 m for CMW_{NP} and 483 ± 35 m for 13EqPac; Table 3.1), where amino acid-like fluorescence is higher because of the proximity to the epipelagic waters, where these materials are usually produced [*Jørgensen et al.*, 2011].

The turnover times of the fluorescent materials (time scale of centuries) are of the same order of magnitude than the turnover time of the bulk DOC [*Hansell et al.*, 2009], but an order of magnitude faster than the apparent age of the ocean DOC as derived from ^{14}C measurements (time scale of millennia) [*Hansell*, 2013]. However, it should be noted that mean age, derived from ^{14}C involved by nuclear tests, is not homologous with turnover time (mean transit time), derived from total reservoir and fluxes entering/leaving the reservoir.

It is remarkable the observed decrease of the tyrosine-like fluorescence in the dark ocean at centennial time scales. It has been reported that these fluorophore turns over in the surface ocean in a time scale of days [*Jørgensen et al.*, 2011; *Løngborg et al.*, 2010] but the long-term decline in the dark global ocean in parallel to water mass ageing has never been reported. We can hypothesise that a minor fraction of the tyrosine-like fluorescence turns over in centuries but the bulk signal does it in days-weeks. Furthermore, this apparent discrepancy could also be related to the different turnover of the set of compounds that are represented by this fluorescence signature [*Stubbins et al.*, 2014].

We conclude that humic-like fluorescence (C1 and C2) reveals as a suitable marker of the production of optically active RDOM with turnover times of ~300–800 yr. Using the oceans as an incubator, our

measurements indicate that the *in situ* microbial production of fluorescent humic-like materials in the dark global ocean is a sink of reduced carbon in the time scale of hundreds of years. Conversely, the turnover time of the tyrosine-like component (C4) was compatible with the turnover time of the bulk DOC and both decline with water mass ageing. This coincidence between the turnover times of the bulk DOC pool and the tyrosine-like component could also have applications for tracing long-term DOC reactivity in the dark ocean.

Acknowledgements

We thank C.M. Duarte for the coordination of the Malaspina expedition; the members of the physical oceanography party for collecting, calibrating and processing the CTD data; the chief scientists of the seven legs, the staff of the Marine Technology Unit (CSIC-UTM) and the Captain and crew of R/V Hespérides for their outright support during the circumnavigation; N. Mladenov for the initial protocols; F. Iuculano for fluorescence measurements; Cintia L. Ramón for support with Matlab software; this study was financed by the Malaspina 2010 circumnavigation expedition (grant number CSD2008–00077); C.R-C. Acknowledges funding through a Beatriu de Pinos postdoctoral fellowship from the Generalitat de Catalunya. M.N.-C. was funded by the CSIC Program "Junta para la Ampliación de Estudios" cofinanced by the ESF.

Chapter 4

Manuscript to be submitted to Progress in Oceanography

Drivers of fluorescent dissolved organic matter in the epipelagic global ocean

Abstract

Fluorescent dissolved organic matter (FDOM) in open surface waters (<200 m) of the Atlantic, Pacific and Indian oceans was analysed by excitation-emission matrix (EEM) spectroscopy and parallel factor analysis (PARAFAC). A four-component PARAFAC model was fit to the EEMs, which included two humic- (C1 and C2) and two amino acid-like (C3 and C4) components previously identified in ocean waters. Generalized-additive models (GAMs) were used to explore the environmental factors that drive the global distribution of these PARAFAC components. The explained variance for the humic-like components C1 and C2 (>70%) was substantially larger than for the amino acid-like components C3 and C4 (<35%). The environmental variable that exhibited the largest effect on the global distribution of C1 and C2 was the apparent oxygen utilisation (AOU) followed by chlorophyll a (Chl *a*). Positive non-linear relationships were observed between both predictor variables and the PARAFAC components, suggesting a microbiological control of their distributions. Comparing with the dark ocean (> 200 m), the relationships of C1 and C2 with AOU there suggest a higher conversion efficiency of the humic-like substances in the dark ocean than in the surface ocean where a net effect of photobleaching in also detected. Unexpectedly, C3 (tyrosine-like) and C4 (tryptophan-like) variability was mostly dictated by salinity (S), by means of positive non-linear relationships as well, suggesting a primary physical control of their distributions at the global scale that could be related to the changing evaporation-precipitation regime and, therefore, that the fraction of these amino acid-like components measured in the water column is the one that accumulates after consumption of the most labile portions. Remarkably, bacterial biomass (BB) only contributed to explain a minor part of the variability of C1 and C4.

Introduction

Dissolved organic matter (DOM) is the largest pool of reduced organic carbon in the marine environment and is defined as the organic material that passes through a submicron filter, usually of 0.2–0.7 μm equivalent pore size [*Carlson and Hansell*, 2015]. Within this pool, the fraction that is able to absorb light over a broad range of ultraviolet (UV) and visible wavelengths is named chromophoric dissolved organic matter (CDOM). Especially in the UV and blue light region, the non-water absorption in the ocean is dominated by CDOM [*Nelson and Siegel*, 2002], reaching more than 90% of the total absorption in the clearest waters of the South Pacific [*Bricaud et al.*, 2010; *Tedetti et al.*, 2010; *Morel et al.*, 2007], and thus playing a major role in determining underwater light availability and spectral quality [*Morel and Gentili*, 2009; *Nelson and Siegel*, 2002; *Siegel et al.*, 2002; 1995]. Furthermore, CDOM can influence the accuracy of global satellite-based estimates of ocean chlorophyll and primary production because of its impact on the underwater light field [*Ortega-Retuerta et al.*, 2010; *Siegel et al.*, 2005]. More than half a century ago, *Kalle* [1949] found that a portion of CDOM was also able to emit blue

fluorescence when excited by UV radiation and it is termed as fluorescent dissolved organic matter (FDOM). Recently, these spectroscopic properties of DOM have allowed tracing long-term biogeochemical processes in the global ocean [e.g. chapters I, II and III of this PhD thesis; *Stedmon and Nelson*, 2015; *Nelson and Siegel*, 2013; *Jørgensen et al.*, 2011].

In surface ocean waters, primary producers determine the maximal DOM production rate (*Carlson*, 2002 and references therein). However, complementary processes, besides the extracellular release by phytoplankton, are responsible for DOM production and transformation, such as grazer and prokaryotes release and excretion, viral cell lysis, and solubilisation of detrital and sinking particles [*Carlson and Hansell*, 2015; *Romera-Castillo et al.*, 2010; *Ortega-Retuerta et al.*, 2009; *Suttle*, 2007; *Steinberg et al.*, 2004]. The main abiotic DOM removal process is the photochemical degradation [*Moran and Zepp*, 1997; *Miller and Zepp*, 1995; *Mopper et al.*, 1991), which results in the partial or complete remineralisation of the chromophoric fraction of DOM by the absorption of UV light. Photodegradation plays an important role in global biogeochemical cycles, by turning over carbon, nitrogen, sulphur, and phosphorus in the photic zone [*Stedmon and Nelson*, 2015; *Mopper et al.*, 1991], and in ecological processes through the production of bioavailable substrates for microbes [*Kieber et al.*, 1989] and increasing light penetration in surface waters since the optically active fraction of DOM is depleted. Conversely, DOM exudates from phytoplankton have been also proposed as substrates for DOM photohumification, i.e. the sunlight-mediated condensation from smaller molecules into polymers with higher absorption properties [*Reche et al.*, 2001; *Kieber et al.*, 1997]. Apart from photochemical processes, heterotrophic microbes remove DOM from the water column as they incorporate and mineralise DOM to satisfy their metabolism. However, this is not an isolated process since they also can modify and release DOM by-products, therefore altering its optical properties [*Ortega-Retuerta et al.*, 2009; *Nelson et al.*, 1998].

Excitation emission matrices (EEMs) consisting on recording the fluorescence emission spectra at a series of successively increasing excitation wavelengths is the most common tool used to characterise FDOM in aquatic environments. Six general types of fluorescence peaks, which are usually included in two groups, have been identified in ocean waters from EEMs [*Hudson and Baker*, 2007; *Coble*, 2007; 1996]. The amino acids tryptophan (peak T, *Coble*, 1996), tyrosine (peak B, *Coble*, 1996) and phenylalanine [*Jørgensen et al.*, 2011] are included in the amino acid-like group, with Ex/Em fluorescence maxima at Ex/Em wavelengths of 280 nm/350 nm, 275 nm/305 nm and 260/282 nm, respectively. Peak A, M and C belong to the humic-like group and fluoresce at higher emission wavelengths than the amino acid-like group, with Ex/Em wavelengths of 250/435 nm, 320/410 nm and 340/440 nm, respectively. Parallel factor analysis (PARAFAC) allows discriminating independent fluorescent groups (or fluorophores) and trace their distributions and changes in the environment [*Stedmon and Markager*, 2005a]. This technique has undoubtedly contributed to improve the understanding of production and degradation

processes of FDOM in aquatic systems [*Jørgensen et al.*, 2014; *Murphy et al.*, 2013; *Maie et al.*, 2012; *Stedmon and Markager*, 2005b). Other statistical methods such as principal component analysis, the laplacian operator and the Nelder-Mead optimisation algorithm, and/or Self-Organising Maps has also been proposed as tools to discriminate and locate potential peaks in the EEM landscape [*Ejarque-González and Butturini*, 2014; *Butturini and Ejarque*, 2013; *Boehme et al.*, 2004].

Several studies on FDOM distribution in open ocean waters have been recently published. *Jørgensen et al.* [2011] presented the unique global dataset of the main FDOM components, whereas other studies covered partial oceanic regions of the Atlantic [*Lønborg et al.,* 2015; *De la Fuente et al.*, 2014; *Heller et al.*, 2013; *Kowalczuk et al.*, 2013], Pacific [*Kim and Kim*, 2015; *Tanaka et al.*, 2014; *Dainard and Guéguen*, 2013; *Omori et al.*, 2011; *Yamashita et al.*, 2010; *Kaiser and Benner*, 2009], Indian [*Coble et al.*, 1998], Arctic [*D'Sa et al.*, 2014; *Guéguen et al.*, 2014; 2007; *Jørgensen et al.*, 2014] and Southern oceans [*Yamashita et al.*, 2007]. The present study complements a previous work focused on the distribution of PARAFAC components in the main water masses of the dark global ocean during the Spanish Circumnavigation Malaspina 2010 (see Chapter III). Here, we describe the global distribution of those PARAFAC components in the illuminated global ocean by parcelling it in Longhurst's biogeographic provinces, analysing the variability of the fluorescence components among and within provinces and determining the environmental drivers controlling their distribution.

Materials and Methods

Division of the epipelagic layer by Longhurst's biogeographic provinces

The Malaspina 2010 circumnavigation was conducted from December 2010 to July 2011 on board R/V Hesperides along the Atlantic, Indian and Pacific oceans, spanning latitudes from 34°N to 40°S (Fig. 4.1). To expedite the study of the FDOM distribution in the surface ocean, the Malaspina cruise track was parcelled according to Longhurst´s biogeographic provinces. This partition is based on physical forces in ocean and atmosphere (i.e. turbulence, temperature, irradiance and nutrients) that affect phytoplankton distribution [*Longhurst*, 1998; 1995]. According to this division, four domains can be recognised in every ocean basin: Polar, Westerlies, Trade-Winds, and Coastal Boundary Zone. At the second level of resolution, the ocean basins are partitioned into 56 biogeographic provinces (*Ducklow*, 2003; www.marineregions.org).

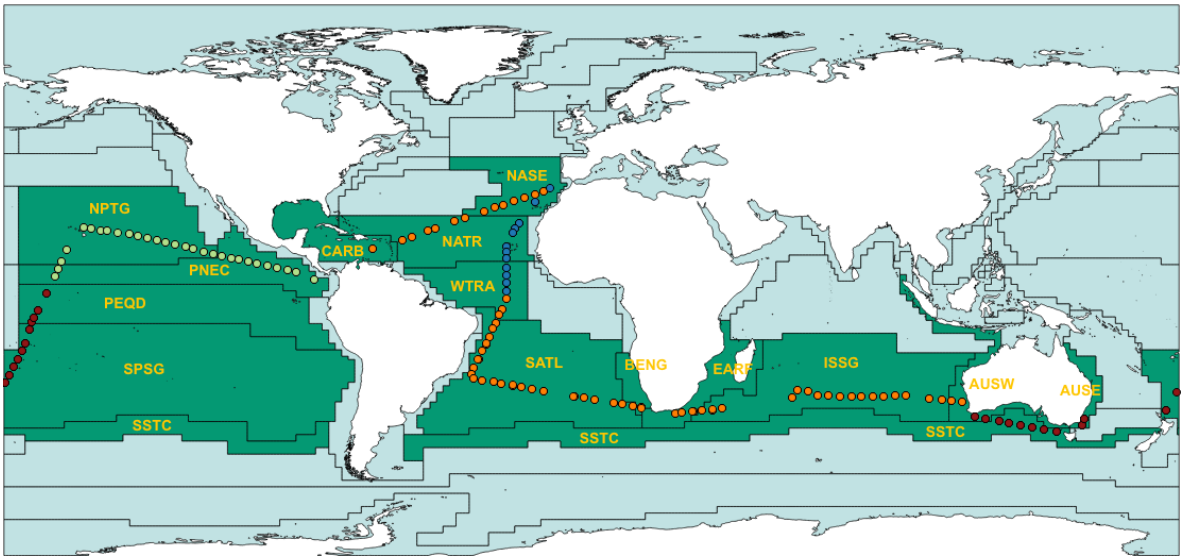

Fig. 4.1. Map of the biogeographic provinces crossed during the Malaspina 2010 circumnavigation. NASE: North Atlantic Subtropical Gyral, NATR: North Atlantic Tropical Gyral, WTRA: Western Tropical Atlantic, SATL: South Atlantic Gyral, BENG: Benguela Current Coastal Province, EARF: East Africa Coastal, ISSG: Indian South Subtropical Gyre, SSTC: South Subtropical Convergence, AUSE: East Australian Coastal Province, SPSG: South Pacific Subtropical Gyre, PEQD: Pacific Equatorial Divergence, NPTG: North Pacific Tropical Gyre, PNEC: North Pacific Equatorial Countercurrent, CARB: Caribbean Province. Circles indicate the position of the 147 stations sampled during the circumnavigation. The colour of the circles accounts for the season. Blue (winter), orange (summer), brown (autumn), green (spring).

A total of 147 stations were occupied and they were assigned to Longhurst's biogeographic provinces according to their geographical coordinates covering all the domains except the Polar (Fig. 4.1). A more exhaustive analysis of the vertical profiles of salinity, potential temperature, dissolved oxygen and fluorescence of chlorophyll *a* was performed in the stations closer to the boundary between two provinces. The Malaspina 2010 circumnavigation crossed a total of 15 provinces (distinguished by green colour in Fig. 4.1). Six provinces were in the Atlantic Ocean: the North Atlantic Subtropical Gyral (NASE), the North Atlantic Tropical Gyral (NATR), the Western Tropical Atlantic (WTRA), the South Atlantic Gyral (SATL), the Benguela Current Coastal Province (BENG) and the Caribbean Province (CARB); four provinces were in the Indian Ocean: the East Africa Coastal (EARF), the Indian South Subtropical Gyre (ISSG), the South Subtropical Convergence (SSTC) and the East Australian Coastal Province (AUSE); and five provinces in the Pacific Ocean: the South Pacific Subtropical Gyre (SPSG), Pacific Equatorial Divergence (PEQD), North Pacific Tropical Gyre (NPTG), the North Pacific Equatorial Countercurrent (PNEC) (Table 4.1). The provinces NASE and NATR were sampled in winter (NASE_W, NATR_W) and summer (NASE_S and NATR_W).

Data acquisition

Every of the 147 sampling days of the circumnavigation a Rosette sampler equipped with 24 Niskin bottles of 10 L was dipped at about 10:00 a.m. (local time) to collect water samples in the epipelagic layer (< 200 m). Seven nominal levels were sampled coinciding with the 70%, 20% and 7% of photosynthetically active radiation (PAR), deep chlorophyll maximum (DCM), DCM plus 20 m (DCM+20) and plus 50 m (DCM+50), and 200 m. For chlorophyll *a*, only samples at 70%, 20% and 7% of PAR, DCM and DCM+20 were collected. For bacterial biomass, only samples at 20% and 7% of PAR, DCM and DCM+20 were collected. Vertical profiles of salinity (S), potential temperature (θ), dissolved oxygen (O_2), *in vivo* fluorescence of chlorophyll *a* (FISP) and PAR were recorded continuously with a conductivity–temperature–depth (CTD) probe Seabird 911+, a polarographic membrane oxygen sensor Seabird SBE-43, a fluorometer Seapoint and a radiometer Biospherical/Licor installed in the rosette sampler. The CTD was equipped with redundant temperature and salinity sensors for intercomparison during the cruise. Temperature and pressure sensors were calibrated at the SeaBird laboratory before the cruise. On board salinity calibration was carried out with a Guildline AUTOSAL model 8410B salinometer [*Pérez-Hernández et al.*, 2012], the potentiometric end-point Winkler method for the calibration of the oxygen sensor [*Álvarez et al.*, 2012] and the fluorimetric method for the calibration of the fluorescence of chlorophyll a (Chl *a*) profiles [*Estrada*, 2012]. The squared Brunt-Väisälä frequency (N^2), commonly used to quantify the stratification of the water column, was calculated following *Millard et al.* [1990]:

$$N^2 = -\frac{g}{\rho}\cdot\frac{\partial\rho}{\partial z} = -g\cdot\frac{\partial \ln(\rho)}{\partial z} \qquad 1)$$

Where g is the gravity acceleration constant (9.8 m s^{-2}), z is the water depth, and ρ is the water potential density at depth z. Integration of Eq. 1 between two depth levels (1 and 2), $N^2 = -g\cdot\ln(\rho_1/\rho_2)/(z_2 - z_1)$ provides a measure of the average stability of the water column between z_1 and z_2 [*Lønborg et al.*, 2015]. Here, we have calculated N^2 between the 70% PAR (3 m) and 150 m. Furthermore, we have also calculated the gradients of potential temperature and salinity (Dθ and DS) over the upper 150 m, which were obtained as the difference between the potential temperature or salinity at 70% PAR (3 m) and 150 m divided by the difference in depth (147 m). The mixed layer depth (MLD) was calculated as the depth where potential density exceeded by 0.1 kg m^{-3} the value at the 70% PAR [*Fernández-Castro et al.*, 2014].

Table 4.1. Averages and standard deviations of potential temperature (θ, °C), salinity (S), short wave radiation (SWR, W m^{-2}), apparent oxygen utilization (AOU, µmol kg^{-1}), chlorophyll *a* (Chl *a*, µg L^{-1}) and bacterial biomass (BB, µg C l^{-1}) of the biogeographic provinces intercepted during the Malaspina 2010 expedition.

Province CODE	Province Description	Biome	Sampling date	Stations	θ (ºC)	S (pss)	SWR (W m^{-2})	AOU (µmol kg^{-1})	Chl *a* (µg L^{-1})	BB (µg C L^{-1})
CARB	Caribbean Province	T	110623	130 (Leg 7)	-	-	-	-	-	-
NATR	N. Atlantic Tropical Gyral Province (TRPG)	T	Summer: 110626-110703	132-139 (Leg 7)	23.6 ± 1.8	37.1 ± 0.3	333.9 ± 32.0	3.3 ± 6.8	0.19 ± 0.06	3.7 ± 1.1
			Winter: 101222-101227	6-11 (Leg 1)	22.1± 1.5	36.4 ± 0.5	202.0 ± 72.7	45.0 ± 25.9	0.30 ± 0.09	3.7 ± 1.1
NASE	N. Atlantic Subtropical Gyral Province (East) (STGE)	W	Summer: 110705-110711	141-147 (Leg 7)	20.2 ± 1.0	36.8 ± 0.2	304.9 ± 69.2	0.0 ± 3.7	0.17 ± 0.07	3.3 ± 0.7
			Winter: 101217-101219	2,3 (Leg 1)	-	-	-	-	-	-
WTRA	Western Tropical Atlantic Province	T	101228-110103	12-18 (Leg 1)	20.0 ± 1.4	35.7 ± 0.2	310.8 ± 27.0	71.1 ± 17.8	0.40 ± 0.14	5.4 ± 1.5
SATL	South Atlantic Gyral Province (SATG)	T	110104-110202	19-41 (Leg 1, 2)	20.7 ± 2.3	36.3 ± 0.4	358.3 ± 73.1	2.0 ± 15.0	0.19 ± 0.05	2.6 ± 0.8
BENG	Benguela Current Coastal Province	C	110203-110205	42-44 (Leg 2)	-	-	-	-	-	-
EARF	E. Africa Coastal Province	C	110213-110215	45-47 (Leg 3)	-	-	-	-	-	-
ISSG	Indian S. Subtropical Gyre Province	T	110216-110309	48-65 (Leg 3)	18.7 ± 1.3	35.6 ± 0.1	282.7 ± 56.0	2.8 ± 5.3	0.16 ± 0.06	3.6 ± 1.4
AUSW	Australia-Indonesia Coastal Province	C	110310-110319	66-69 (Leg 3, 4)	18.7 ± 1.8	35.6 ± 0.2	293.7 ± 76.6	6.1 ± 3.1	0.22 ± 0.09	4.2 ± 1.6
SSTC	S. Subtropical Convergence Province	W	110320-110326	70-76 (Leg 4)	14.2 ± 0.9	35.2 ± 0.1	275.0 ± 27.5	6.2 ± 4.0	0.24 ± 0.10	6.3 ± 2.7
AUSE	East Australian Coastal Province	C	110328-110329	77, 78 (Leg 4)	-	-	-	-	-	-
SPSG	S. Pacific Subtropical Gyre Province	T	110417-110426	79-89 (Leg 5)	24.3 ± 2.8	35.5 ± 0.3	229.3 ± 50.7	16.6 ± 8.2	0.23 ± 0.05	2.7 ± 1.5
PEQD	Pacific Equatorial Divergence Province	T	110427-110504	90-97 (Leg 5)	23.5 ± 3.6	35.2 ± 0.5	303.2 ± 67.8	49.9 ± 40.4	0.27 ± 0.05	5.2 ± 2.3
NPTG	N. Pacific Tropical Gyre Province	T	110505-110523	98-110 (Leg 5, 6)	21.4 ± 1.7	34.8 ± 0.3	356.6 ± 62.1	12.6 ± 11.2	0.24 ± 0.09	5.0 ± 1.4
PNEC	N. Pacific Equatorial Countercurrent Province	T	110529-110608	116-126 (Leg 6)	17.1 ± 2.3	34.6 ± 0.2	288.8 ± 60.2	176.1 ± 43.6	0.36 ± 1.18	6.3 ± 2.8

C: Coastal, T: Trades, W: Westerlies. We have not calculated the average and standard deviation of biogeographic provinces with less than 4 stations.

Daily short wave solar radiation data (in W m^{-2}) were obtained from the National Centres for Environmental Predictions NCEP/DOE 2 Reanalysis database provided by the NOAA/OAR/ESRL PSD, Boulder, Colorado, USA, from their website at http://www.esrl.noaa.gov/psd/ and interpolated for each location of the CTD stations cruise. AOU was calculated as the difference between the saturation and measured dissolved oxygen concentrations. Dissolved oxygen saturation was calculated from practical salinity and potential temperature with the equation of *Benson and Krause* [1984]. Inorganic nutrients (nitrate, phosphate and silicate) were collected from the Niskin bottles in 20-mL acid-washed polyethylene flasks and determined on board using standard segmented flow analysis methods with colorimetric detection [*Blasco et al.*, 2012].

Bacterial biomass (BB) was determined by flow cytometry using standard protocols after fixation with 1% paraformaldehyde and 0.05% glutaraldehyde and staining with SybrGreen I (Molecular Probes, Invitrogen) at a 1/10,000 dilution [*Gasol and del Giorgio*, 2000]. A previously-published calibration curve relating relative side scatter to cell size [*Calvo-Díaz and Morán*, 2006] was used to transform the cytometric signal into cell size, and cell size was converted to biomass using the *Gundersen et al.* [2002] relationship.

Collection and spectral acquisition of fluorescent DOM samples

We collected 835 water samples for FDOM measurements. They were poured from the Niskin bottles into 250 mL acid-washed glass flasks and stored in dark conditions until measurement before 6 hours from collection. Once in the on board laboratory, aliquots were immediately filtered through precombusted (450°C, 4 h) glass fibre filters (GF/F) in an acid-cleaned all-glass filtration system, under positive pressure with low N_2 flow.

Fluorescence EEMs were collected with a JY-Horiba Spex Fluoromax-4 spectrofluorometer at room temperature (around 20 °C) using 5 nm excitation and emission slit widths, an integration time of 0.25 s, an excitation range of 240–450 nm at 10 nm increments, and an emission range of 300–560 nm at 2 nm increments. To correct for lamp spectral properties and to compare results with those reported in other studies, spectra were collected in signal-to-reference (S:R) mode with instrument-specific excitation and emission corrections applied during collection, and EEMs were normalized to the Raman area (RA). In our case, RA normalization and its baseline correction were performed with the emission scan at 350 nm of the Milli-Q water blanks and the area was calculated following the trapezoidal rule of integration [*Lawaetz and Stedmon*, 2009].

Furthermore, to track that the variability of the instrument during the 147 working days of the expedition affected similarly to the Raman, amino acid and humic-like regions of the spectrum, the following three standards were run daily: (1) a P-terphenyl block (Stranna) that fluoresces in the amino acid region, between 310 nm and 600 nm exciting at 295 nm; (2) a Tetraphenyl butadiene block (Stranna) that fluoresces in the humic region, between 365 nm and 600 nm exciting at 348 nm; and (3) a sealed Milli-Q cuvette (Perkin Elmer) scanned between 365 nm and 450 nm

exciting at 350 nm. Successful Raman normalization in both the amino acid- and humic-like regions of the EEMs, a good quality of the Milli-Q water produced on board and a slight shift of fluorescence intensities on daily working routine were observed (Fig.3.1 in Chapter 3).

Inner-filter correction was not applied due to the low absorption coefficient of CDOM of the epipelagic water samples collected during the circumnavigation: 1.31 ± 0.23 m^{-1} (average ± standard deviation) at 250 nm, i.e. much lower than the threshold of 10 m^{-1} above which this correction is required [*Stedmon and Bro*, 2008]. Raman-normalized Milli-Q blanks were subtracted to remove the Raman scattering signal [*Murphy et al.*, 2010; *Stedmon and Markager*, 2003]. RA normalization, blank subtraction, and generation of EEMs were performed using MATLAB (version R2008a).

Global PARAFAC modelling

Parallel factor analysis (PARAFAC) was used to identify the different fluorescent components that comprise the EEMs in the epipelagic waters of the global ocean. PARAFAC was performed using the DOMFluor 1_7 Toolbox [*Stedmon and Bro*, 2008]. Prior to the analysis, Rayleigh scatter bands (first order at each wavelength pair where $Em = Ex \pm bandwidth$; second order at each wavelength pair where $Em = 2 * Ex \pm (2 * bandwidth)$) were trimmed. The global PARAFAC model was derived based on the 1574 corrected EEMs collected during the circumnavigation from the surface to 4000 m depth and was validated using split-half validation and random initialization [*Stedmon and Bro*, 2008]. Likewise, we also tested the PARAFAC model using the subset of 835 epipelagic water samples (surface to 200 m) and it turned out in a similar components model. Here we report the maximum fluorescence (Fmax) in Raman units (RU) [*Murphy et al.*, 2010; *Stedmon et al.*, 2003].

Statistical analysis

Intra-province variability: ANOVA

To determine the relevance of intra-province variability for each environmental variable and fluorescent component among PAR levels we performed an analysis of variance (ANOVA). The provinces CARB, NASE_W, BENG and EARF were excluded because they comprised less than 4 stations.

Drivers of fluorescence components: generalised additive models (GAMs)

To test for the effect of the environment on the variability of the fluorescence PARAFAC components we have used generalized additive models (GAMs, *Wood*, 2006). We examined the influence of 11 environmental predictors on each fluorescence component: SWR, S, θ, N^2, DS, Dθ, O_2, AOU, Chl *a*, NO_3^- and BB. Before model fitting, covariability among predictors was examined using variance inflation factors (VIFs, Table 4.2.). GAMs were formulated as follows:

$$Y_{i,l} = \alpha + \sum_j g_j(X^j) + \epsilon_{i,l} \qquad (2)$$

where *Y* is a fluorescence PARAFAC component measured at a station *i* and nominal level *l*, α is an intercept, *X* is a vector of predictor variables where the superscript j identifies each covariate. *g* are non-parametric smoothing functions specifying the effect of the

covariates on the fluorescent component and $\epsilon_{i,l}$ is the error term assumed to be normally distributed. Smoothing functions were fit by penalized cubic regression splines restricted to a maximum of three knots. The smoothness of the functions was estimated by minimizing the generalized cross validation criterion (GCV). Given that BB was measured in 473 of the 835 samples, two models were run for each fluorescence component: first, models were obtained with all predictor variables but BB; and second models with all predictor variables including BB. In the second case, to test for the effect of reducing the dataset by about a half, the models were run for all predictor variables but BB for the samples were BB was measured.

Table 4.2. Variance Inflation Factor (VIF) for each explanatory variable considered in the GAM models. We began with all explanatory variables (2nd column) and estimated successive VIFs once dropped collinear covariates one at a time (3rd to 4th column) until all VIFs values were around 3 (5th column). For abbreviations see the main text.

Covariate	VIF	VIF	VIF	VIF
Daily SWR	1.15	1.14	1.07	1.02
Temperature	224.81	3.09	2.15	2.06
Salinity	3.35	1.94	1.52	1.57
N^2	221.08	220.08		
DS	31.54	31.28	1.85	1.74
Dθ	160.77	159.78	2.02	1.89
O_2	1900.97			
AOU	2438.67	5.71	5.62	2.49
Chl a	1.21	1.13	1.12	1.13
NO_3^-	5.36	5.31	5.20	

Chl *a* and BB were ln-transformed, and Depth was included in all models as a "catch-all" variable to account for potential unmeasured effects on fluorescence. All models were fitted in R 3.1.1 software (R Development Core Team, 2014) and using the 'mgcv 1.8-0' package [*Wood*, 2006].

Regression analysis: parametric relationships

Linear and non-linear power-law regression equations between the environmental variables (SWR, S, θ, DS, Dθ, AOU, Chl *a* and BB) and each fluorescent component (Fmax1, Fmax2, Fmax3 and Fmax4) were fitted in R 3.1.1 software.

Results

PARAFAC components

A four-component model was obtained (see Fig. 3.2. of chapter 3), two of them of humic-like nature —C1 and C2— since they display a broad emission spectra around 400 nm, at Ex/Em <270–370/470 nm and Ex/Em 320/400 nm, respectively, and two of amino acid-like nature —C3 and C4— as the emission spectra is narrower with maxima below 400 nm at 290/340 nm and 270/310 nm, respectively. In the literature, the humic-like C1 has been defined as Peak A/C and C2 as peak M [*Coble*, 1996]. C1 is proposed to be ubiquitous in DOM but enriched in terrestrial/allochthous sources [*Stedmon and Markager*, 2005a], and appears to be photodegradable but biorefractory [*Maie et al.*, 2012]. C2 has previously been reported as marine humic-like substances [*Coble*, 1996]. With respect to the amino acid-like C3 and C4, they have been attributed to tryptophan and tyrosine, which have been shown to represent

more biodegradable and fresh microbially produced DOM [*Fellman et al.*, 2008; *Yamashita and Tanoue*, 2003a] and have been commonly termed as peaks T and B [*Coble*, 1996], respectively. These four peaks are recurrently observed in diverse aquatic environments [e.g. chapter III of this PhD thesis; *Maie et al.*, 2012; *Jørgensen et al.*, 2011; *Yamashita et al.*, 2008; *Stedmon and Markager*, 2005a].

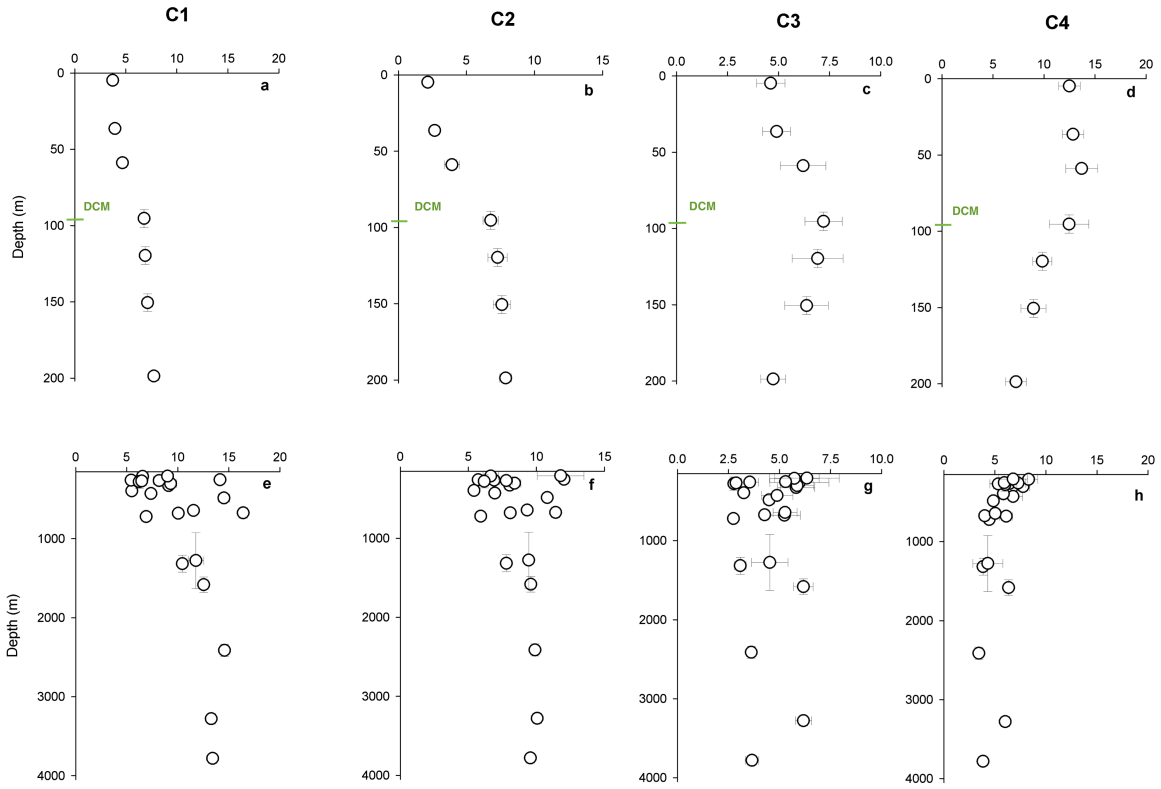

Fig. 4.2. Average profiles of the four PARAFAC components C1 (a), C2 (b), C3 (c) and C4 (d) for each nominal depth in the epipelagic ocean; arquetypal values of the four PARAFAC components C1 (e), C2 (f), C3 (g), C4 (h) for each water mass intercepted in the dark ocean during the Malaspina 2010 circumnavigation. The bars are the standard deviations of the data at each sampling depth. Green line indicates the average depth chlorophyll maximum (DCM).

Gathering our data set according to the seven nominal depth levels sampled during the circumnavigation (Fig. 4.2.) reveals distinct global profiles for the PARAFAC components. Whereas C1 (Fig. 4.2a) and C2 (Fig. 4.2b) increased monotonically with depth, C4 (Fig. 4.2d) exhibited the opposite profile. C3 (Fig. 4. 2c) showed an intermediate behaviour, with maximum values at the depth of the DCM (average ± SD depth, 95 ± 36 m) and minimum either at the surface or 200 m. The global averages of the two humic-like components C1 and C2 showed a very strong positive and linear correlation (Fmax2= 1.47 (±0.06) Fmax1 – 3.1 (±0.4) 10^{-3}; R^2 = 0.99, $p < 0.001$). The

regression slope indicates that the production rate of C2 is ~50% larger than of C1.

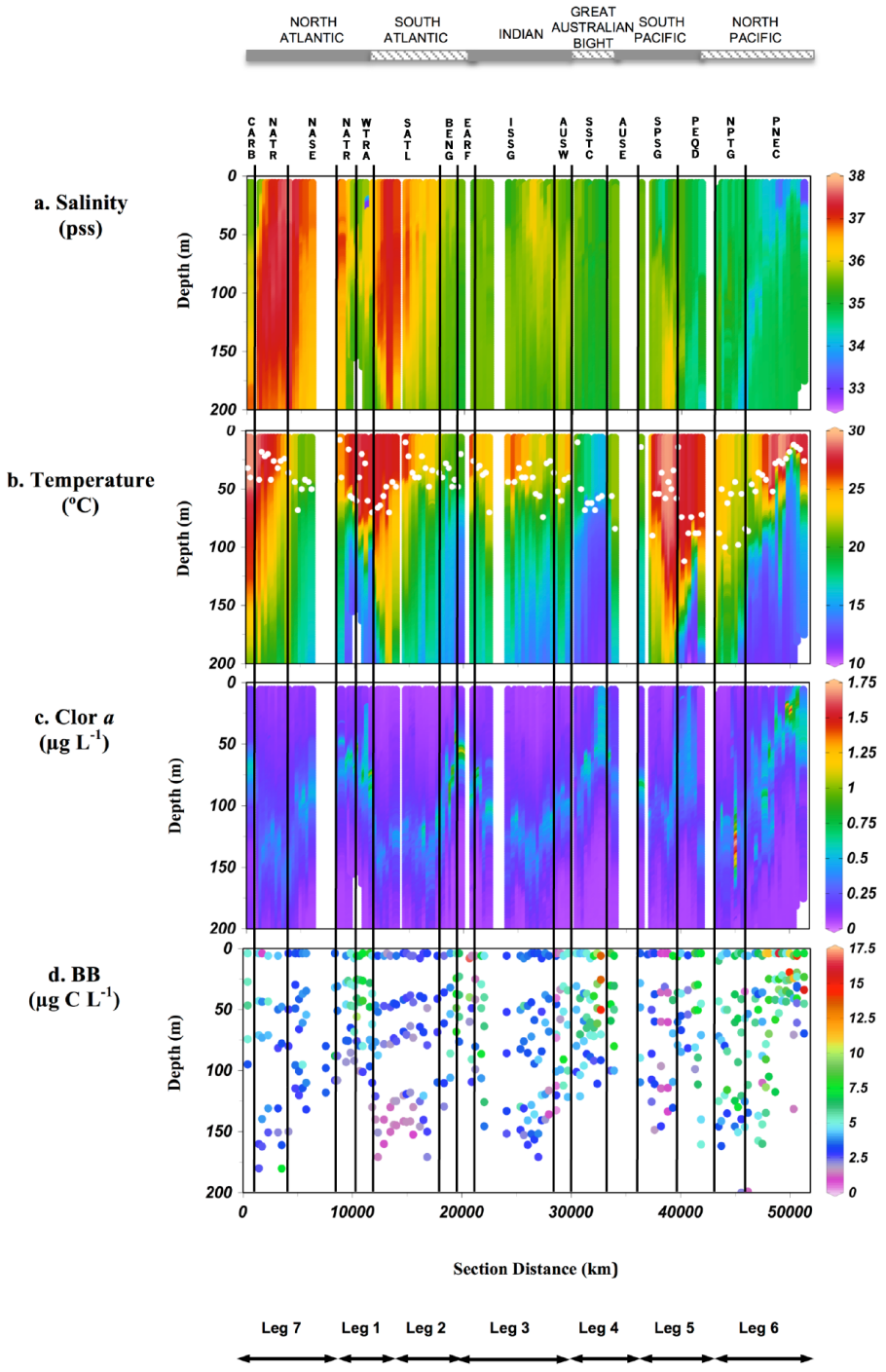

Fig. 4.3. Distribution of (a) salinity, (b) potential temperature, (c) chlorophyll *a* and (d) bacterial biomass during the Malaspina 2010 expedition. White dots in panel b represent the mixed layer depth (MLD).

In contrast, the negative origin-intercept suggests that after full consumption of C2, for example by photodegradation, C1 would be still present in the water column. The relationships between C1·C3, C1·C4, C2·C3 and C2·C4 followed a positive trend above the DCM (see the green line in Fig. 4.2.) and a negative trend below the DCM (R^2 > 0.78). Finally, the relationship between C3 and C4 was positive but followed distinct trends above and below the DCM. The slope was lower for the samples above the DCM (Fmax4 = 0.73 (±0.09) Fmax3 + 9.2 (±0.5) 10^{-3}, R^2 = 0.98) than for the samples below the DCM (Fmax4 = 1.74 (±0.65) Fmax3 – 1.4 (±0.4) 10^{-3}; R^2 = 0.78).

Physical and biogeochemical differences among biogeographic provinces

The mean and standard deviation of all study variables was calculated at each biogeographic province and nominal depth level (70%, 20%, 7% PAR, DCM, DCM+20 and DCM+50). The provinces CARB, NASE_W, BENG and EARF were excluded because they comprised less than 4 stations (Table 4.1). Salinity profiles were very homogeneous in all the study provinces with maximum values about 37 pss in NASE and NATR during summer and minimum values of about 35 pss in PNEC (Fig. 4.3a; Fig. 1a Appendix V). Potential temperature, which ranged from 11°C to 29 °C, showed very homogeneous profiles in some provinces as NASE and NATR_S or strongly stratified in other provinces as PNEC, WTRA, or NATR_W (Fig. 4.3b; Fig. 1b Appendix V). DS ranged between –0.005 and –0.012 pss m^{-1} (Fig. 4.4a) and the maximum were found in NASE_S whereas the minimum in PNEC. Dθ ranged between –0.115 and –0.010 °C m^{-1} (Fig. 4.4b) and the highest values were found in PNEC and the minimum in NASE. The mixed layer depth (MLD) ranged from 8 to 100 m, with an average ± SD of 48 ± 21 m (white dots Fig. 4.3b, Fig. 4.5a). The maximum values were found in NPTG whereas the minimum was found in EARF and PNEC. The total short wave radiation (SWR) ranged from 112 to 497 W m^{-2} (Fig. 4.4c). SATL (occupied in summer) underwent the maximum average SWR with 358 ± 73 W m^{-2}, followed by NPTG (occupied in spring) with 357 ± 62 W m^{-2}. NASE (occupied in in winter) showed the lowest average SWR with 146 ± 37 W m^{-2}. N^2 ranged from 0.1 to 1.2 min^{-2} (Fig. 4.4d), with PEQD showing the maximum and NASE_S the minimum values. AOU ranged from –26 and 266 µmol kg^{-1}. The maximum values were found in PNEC between 100 and 200 m depth, whereas the minimum values were located between 50 and 75 m depth in the South Atlantic and South Indian oceanic gyres, corresponding to the provinces SATL and ISSG (Fig. 4.5a).

Chl *a* ranged from 0.01 to 1.93 µg L^{-1} and the deep chlorophyll *a* maximum (DCM) was located between 37 and 161 m (Fig. 4.3c; Fig. 1d in Appendix V). Maximum Chl *a* values were found in NATR, EARF and PNEC whereas the minima were in the centre of the oceanic gyres. The maximum depths of the DCM were coincident with the centre of the oceanic gyres and were located in the SATL, ISSG and NPTG. BB ranged from 0.1 and 16.7 µg C L^{-1} and the maxima were found in SSTC and PNEC (Fig. 4. 3d). The minimum values were not found in a specific geographic area, although a noticeable group of samples with values near 0 were found around 150 m in the SATL.

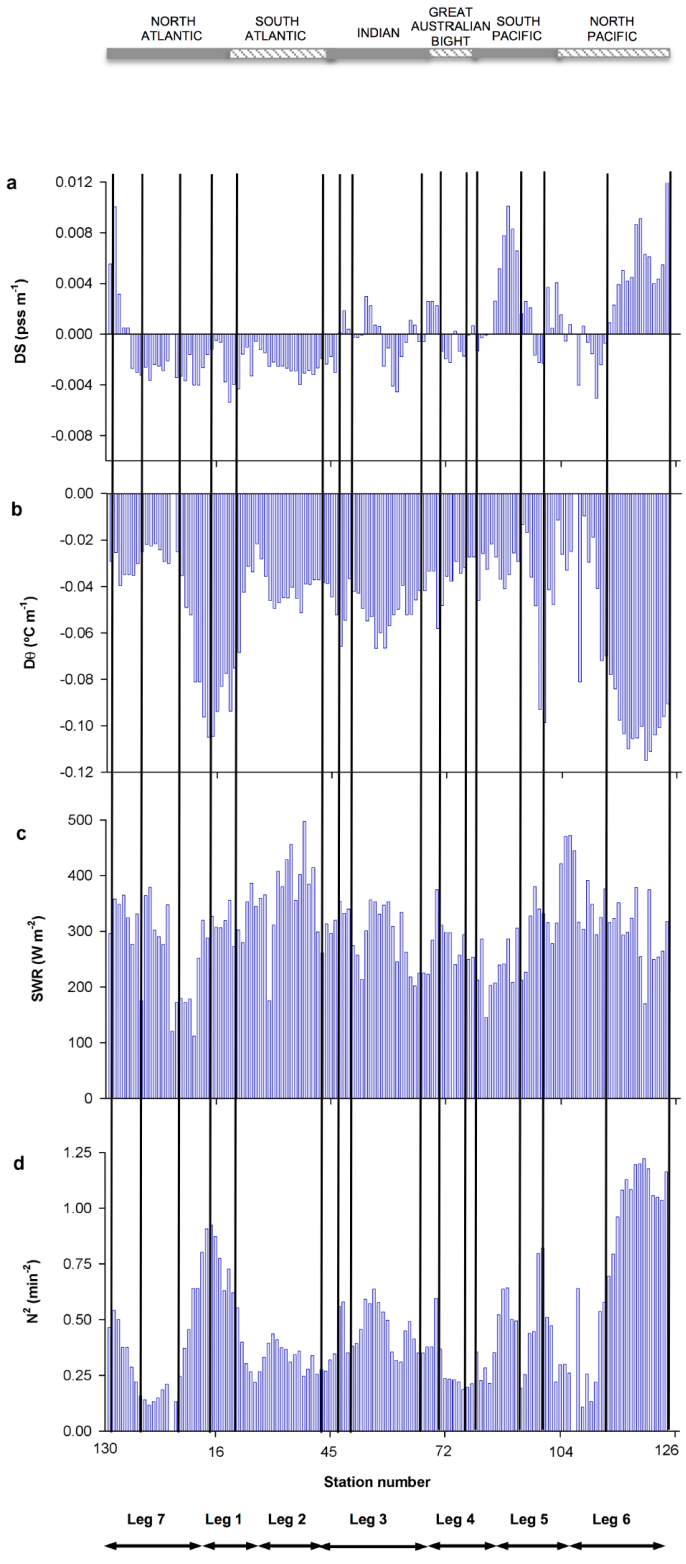

Fig. 4.4. Bar plots of the distribution of the gradients of (a) salinity (pss m^{-1}) and (b) potential temperature (°C m^{-1}), (c) short wave radiation (W m^{-2}), (d) squared Brunt·Väisälä frequency (1 m^{-2}) over the upper 150 m (min^{-2}).

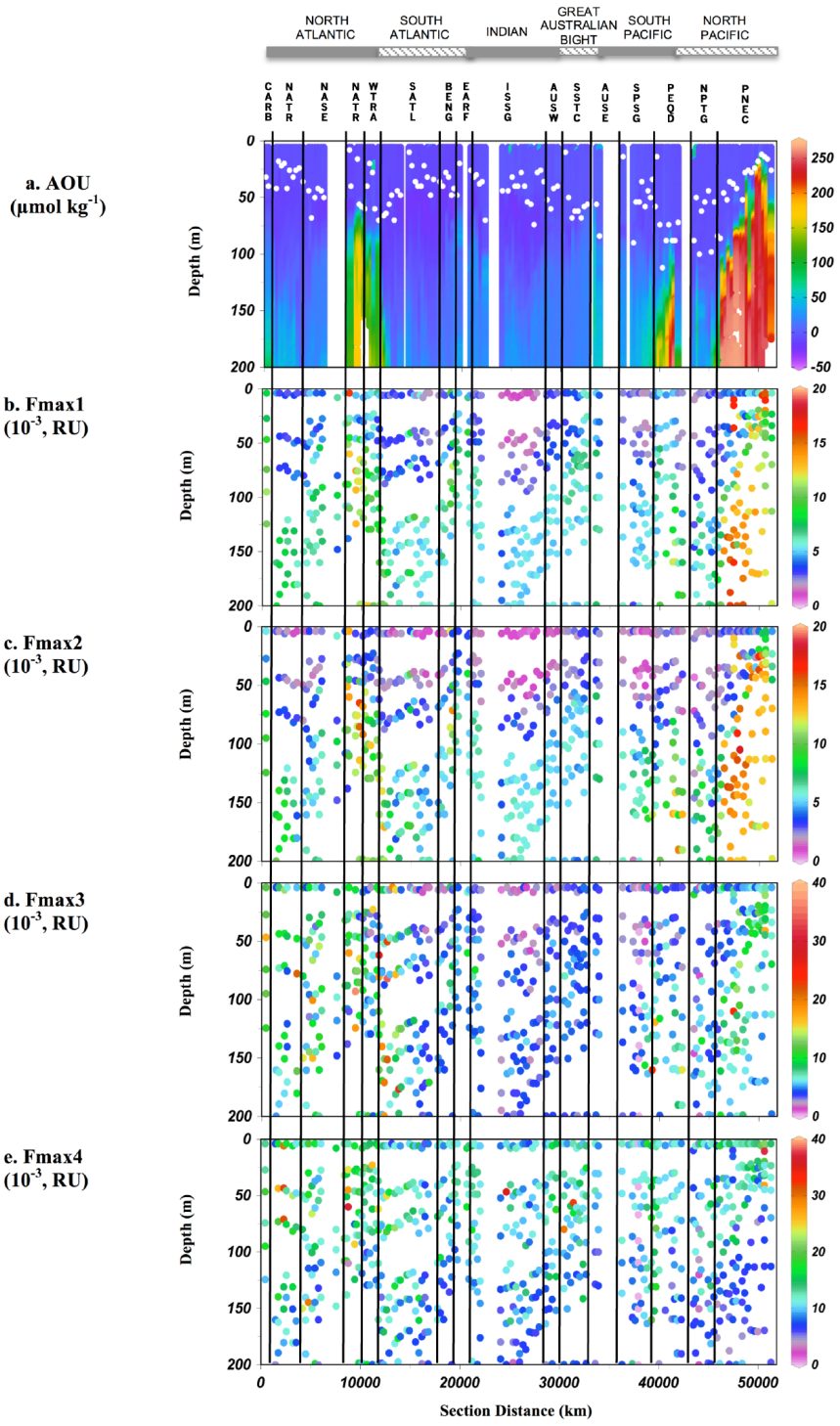

Fig. 4.5. Distribution of the apparent oxygen utilization (AOU) (a), and the maximum fluorescence (Fmax) of the components C1 (b), C2 (c), C3 (d) and C4 (e) delivered by Parallel Factor Analysis (PARAFAC) during the Malaspina 2010 expedition. The black vertical lines show the biogeographic provinces delimitations. Provinces acronyms as in Table 4.1. White dots in the upper panel represent the mixed layer depth (MLD).

The humic-like components C1 and C2 presented Fmax values ranging from 0.6 to 17.2 x 10^{-3} RU and from below the detection limit to 17.7 x 10^{-3} RU, respectively, and their distributions concurred with the AOU distribution (Fig. 4.5a, b, c, Fig. 1c, e, f of Appendix V). The maximum means of Fmax1 and Fmax2 were 11.5 ± 1.8 and 11.6 ± 1.8 x10^{-3} RU, respectively and were found at the PNEC province (Fig. 4.6a, b). The ISSG and SPSG provinces showed the minimum means of Fmax1, with values of 3.7 ± 0.6 and 4.0 ± 0.5 x10^{-3} RU (Fig. 4.6a). The lowest Fmax2 means were found in ISSG and NASE_S with 3.8 ± 0.6 x10^{-3} RU (Fig. 4.6b).

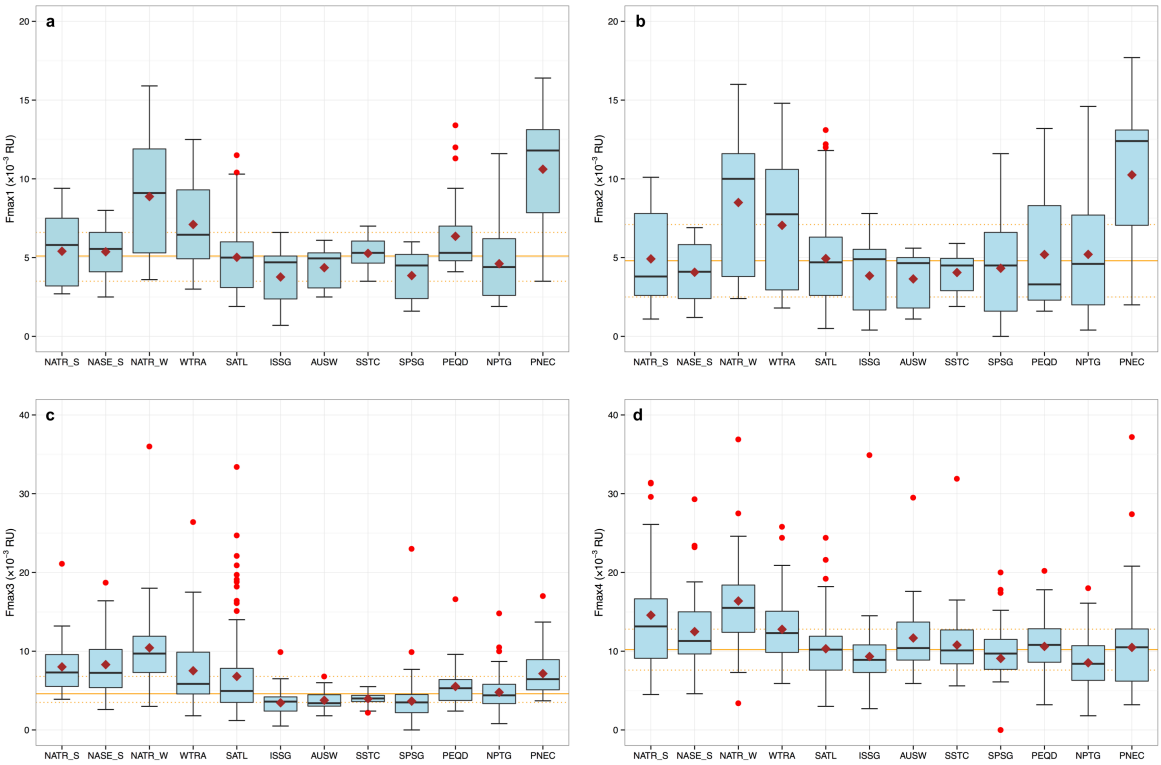

Fig. 4.6. Box and Whisker plots for the four fluorescent components at each biogeographic province. Horizontal line, median; brown diamonds, mean; blue-box, 25–75% percentiles; and whiskers extend from the upper (lower) to the highest (lowest) value that is within 1.5 × inter-quartile range of the hinge. Note that provinces with less than four stations were not included.

The amino acid-like components C3 and C4 were generally higher than the humic-like components, with C4 roughly twice more intense (Fig. 4.2); Fmax3 ranged from below detection limit to 36.0 x 10^{-3} RU and Fmax4 from below detection limit to 37.2 x 10^{-3} RU, respectively. C3 was nearly absent in some oceanic areas such as the South Atlantic, the South Indian Ocean or the South Pacific, corresponding to the provinces SATL, ISSG and SPSG (Fig. 4.5d, Fig. 1g of Appendix V); C4 was the most homogeneously distributed component with a Fmax4 difference of around 10 x 10^{-3} RU throughout the water column

(Fig. 4.5e, Fig. 1h of Appendix V). The NATR_W province presented the maximum means for Fmax3 and Fmax4, 11.5 ± 6.0 and 17.2 ± 0.7 x10^{-3} RU (Fig. 4.6c, d), respectively, whereas the lowest means were 3.5 ± 1.1 x10^{-3} RU at ISSG for Fmax3 (Fig. 4.6c) and 8.5 ± 2.3 x 10^{-3} RU at PNEC for Fmax4 (Fig. 4.6d).

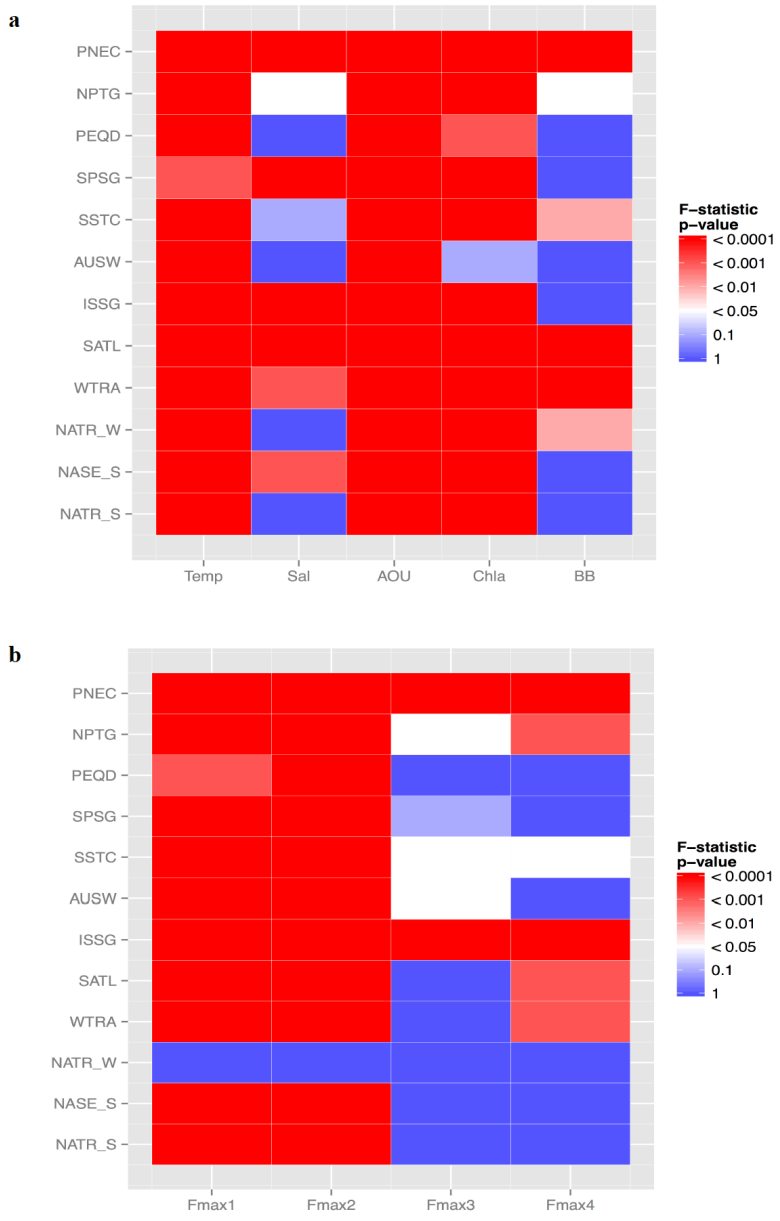

Fig. 4.7. P-value of the F-statistic test resulted from the use of ANOVA applied to the five physical, chemical and biological variables (a), and to the four fluorescent components (b) to evaluate intra-province variability among the sampled PAR levels. Note that each square indicates that average differences in environmental variables or fluorescent components among PAR levels within a specific province are statistically significant or non-significant.

Physical and biogeochemical differences within biogeographic provinces

Results of the ANOVAs to explore the environmental variability are shown in Figure 4.7 the physical and biogeochemical parameters salinity (S), potential temperature (θ), temperature gradient (Dθ), salinity gradient (DS), apparent oxygen utilization (AOU), chlorophyll *a* (Chl *a*) and bacterial biomass (BB) on one side (Fig. 4.7a) and (b) the four PARAFAC components for each study province on the other side (Fig. 4.7b). The red colour is indicative of a marked variability, whereas the blue colour is indicative of homogeneity.

Potential temperature, AOU and Chl *a* (except for NATR_W) presented significant intra-province differences (Fig. 4.7a). AOU increased with depth in all provinces; the AOU in the mixed layer showed negative values for all stations, except in PNEC (Fig. 4.5a), highlighting the predominance of primary production against respiration. Salinity was not as variable as the previous parameters and the provinces NATR_S, NATR_W, AUSW, SSTC and PEQD were homogeneous with depth (blue squares, Fig. 4.7a). The BB was vertically homogeneous in most provinces such as NATR_S, NASE_S, ISSG, AUSW, SPSG and PEQD (blue squares, Fig. 4.7a). The humic-like components C1 and C2 showed a well-defined variability within all provinces, except in NATR_W (Fig. 4.7b). There was a significant difference in Fmax1 and 2 above and below the mixed layer. The values were lower above the MLD except for PNEC, and very uniform below the mixed layer except in PEQD, NPTG and PNEC (Fig. 1e, f of Appendix V). On the contrary, the amino acid-like components were more homogeneous, mostly those situated in the intertropical convergence zone (ITCZ) (i.e. NATR, NATR, WTRA, SPSG and PEQD). The amino acid-like Fmax3 did not present a defined depth profile in most of the provinces (blue squares, Fig. 4.7b). Contrary to the humic-like substances, the depth profiles of Fmax4 tended to display higher values at surface than at depth in some provinces (e.g. PNEC in Fmax4, Fig. 1h of Appendix V).

Drivers of FDOM variability

To explore the environmental factors that drive the global distribution of fluorescence PARAFAC components in epipelagic waters of the world ocean we used generalized-additive models (GAMs) to allow testing the occurrence of non-linear relationships (Fig. 4.8). Early examination of the covariability among predictors allowed us to reject N^2, O_2 and NO_3^- out of the analysis (Table 4.3), thus finally testing a total of 8 predictor variables: SWR, S, θ, DS, Dθ, AOU, Chl *a* and BB. The variable that exhibited the largest effect on Fmax1 was AOU followed by Chl *a* (Table 4.3). The dependence of Fmax1 with both variables was positive and non-linear, with a decrease of the slope as AOU and Chl *a* increases (Fig. 4.8a). Inclusion of bacterial abundance (BB) in the model, thus reducing the number of cases from 680 to 473 samples, resulted in a positive linear dependence that increased the variance explained slightly from 72.1 to 73.3%, although the relationships kept the same trends (Fig. 4.8b), and the variables AOU and Chl *a* still explained most of the variability (Table 4.3). In addition to AOU, Chl *a* and BB, other parameters as SWR, θ and S in a non-linear trend, and DS in a linear trend

also contributed to explain Fmax1 in much lesser extent (Table 4.3).

Table 4.3. Results of the generalized-additive models (GAMs) of the relationship of environmental parameters with the FDOM components. SWR: the daily total solar radiation, θ: temperature, S: salinity, Dθ: differential temperature, DS: differential salinity, AOU: apparent oxygen utilization, Chl *a*: chlorophyll *a*, BB: bacterial biomass.

FDOM components (without BB)	Explicative variables	Function	F	p-value	R^2	FDOM variables (with BB)	Explicative variables	Function	F	p-value	R^2
Fmax1 (n = 680)	S(SWR_D)	Non-linear (-)	6	0.003**	0.72	Fmax 1 (n = 473)	S(SWR_D)	Lineal (-)	3	0.08	0.73
	S (θ)	Non-linear (-) (+)	19	< 0.001***			S (θ)	Non-linear (-) (+)	16	< 0.001***	
	S (S)	Non-linear (-) (+)	36	< 0.001***			S (S)	Non-linear (-) (+)	31	< 0.001***	
	S (D θ)	Lineal (-)	19	< 0.001***			S (Dθ)	Lineal (-)	16	< 0.001***	
	S (DS)	-	-	-			S (DS)	-	-	-	
	S (AOU)	Non-linear (+)	156	< 0.001***			S (AOU)	Non-linear (+)	110	< 0.001***	
	S (lChla)	Non-linear (+)	95	< 0.001***			S (lChla)	Lineal (+)	67	< 0.001***	
	S (Depth)	Non-linear (+)	6	0.003**			S (Depth)	Lineal (n)	0	0.51	
	-	-	-	-			S (log(BB))	Lineal (+)	7	0.006**	
Fmax2 (n = 680)	S(SWR_D)	-	-	-	0.79						
	S (θ)	Lineal (-)	6	0.01*							
	S (S)	Non-linear (-) (+)	23	< 0.001***							
	S (D θ)	Non-linear (-)	9	< 0.001***							
	S (DS)	-	-	-							
	S (AOU)	Non-linear (+)	294	< 0.001***							
	S (lChla)	Non-linear (+)	86	< 0.001***							
	S (Depth)	Lineal (+)	26	< 0.001***							
Fmax3 (n = 669)	S(SWR_D)	-	-	-	0.33						
	S (θ)	Non-linear (+)	14	< 0.001***							
	S (S)	Non-linear (-) (+)	69	< 0.001***							
	S (D θ)	-	-	-							
	S (DS)	Lineal (-)	12	< 0.001***							
	S (AOU)	Non-linear (+) (-)	61	< 0.001***							
	S (lChla)	Lineal (+)	39	< 0.001***							
	S (Depth)	-	-	-							
Fmax4 (n = 678)	S(SWR_D)	Lineal (-)	4	0.03*	0.28	Fmax4 (n = 473)	S(SWR_D)	Lineal (-)	3	0.08	0.31
	S (θ)	Non-linear (-) (+)	8	< 0.001***			S (θ)	Non-linear (-) (+)	4	0.01*	
	S (S)	Non-linear (n) (+)	37	< 0.001***			S (S)	Non-linear (n) (+)	44	< 0.001***	
	S (D θ)	Lineal (-)	6	0.01			S (D θ)	Lineal (n)	2	0.20	
	S (DS)	Non-linear (+) (-)	4	0.02			S (DS)	Non-linear (+) (-)	5	0.01*	
	S (AOU)	Lineal (-)	10	0.001**			S (AOU)	Non-linear (n) (-)	2	0.09	
	S (lChla)	Lineal (+)	11	0.001**			S (lChla)	Non-linear (-) (+)	2	0.15	
	S (Depth)	Lineal (-)	23	< 0.001***			S (Depth)	Non-linear (n) (-)	13	< 0.001***	
	-	-	-	-			S (log(BB))	Non-linear (n) (+)	8	< 0.001***	

Positive, constant and negative relationships are indicated with (+), (n) and (-).

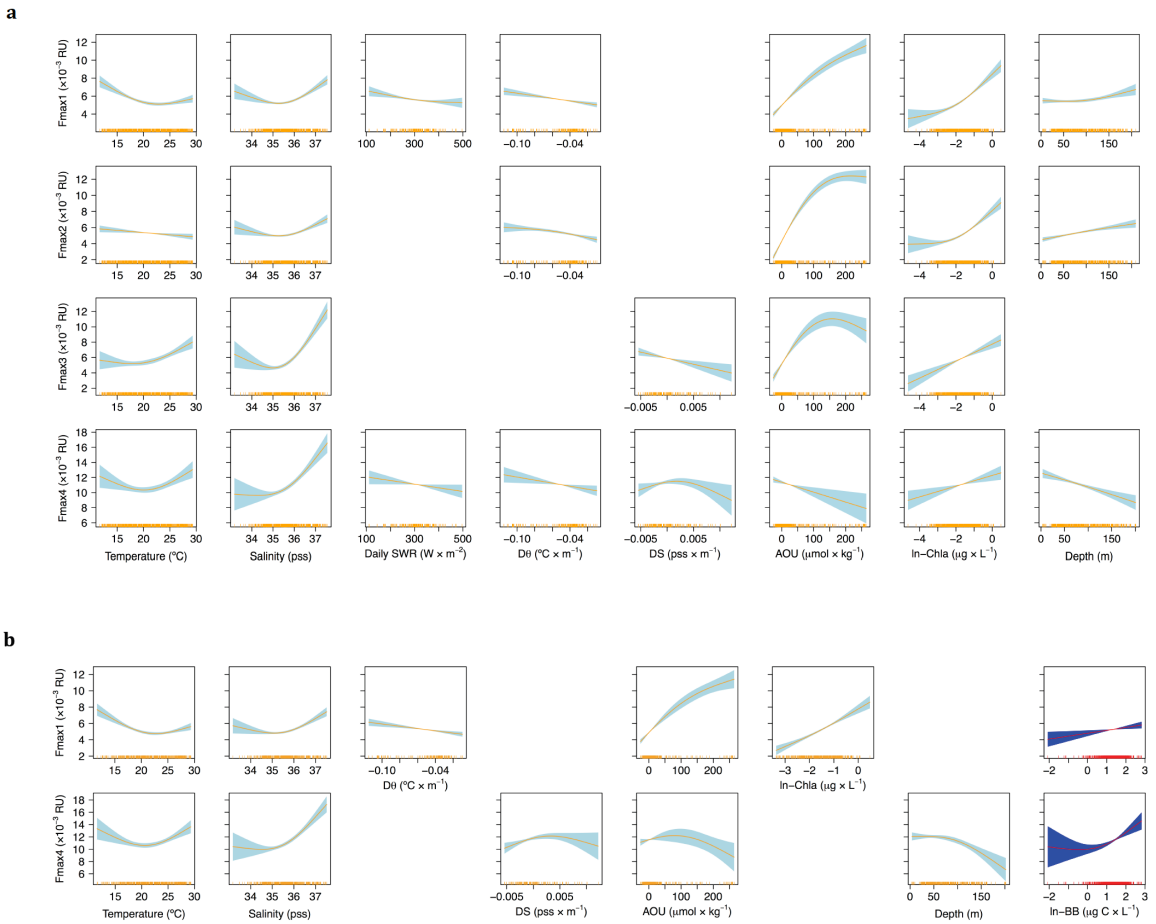

Fig. 4.8. Partial plots showing the additive effects of the physical, chemical and biological covariates on the four fluorescent components. The orange lines are the smoothing functions and the blue shaded areas represent 95% point-wise confidence intervals. Rugs on *x*-axis indicate the distribution of the data.

Likewise, Fmax2 variability was controlled by the same parameters, having the AOU also the largest influence on this variable (Table 4.3). In this case, the AOU·Fmax2 relationship reached a plateau approximately at 170 μmol kg^{-1} (Fig. 4.8a, b) whereas for Fmax1, the relationship was more lineal. It is remarkable that SWR and BB did not contribute significantly to explain Fmax2 in contrast with Fmax1.

The explained variance for the fluororophores C3 and C4 (ca. 30%) was substantially lower than for the fluorophores C1 and C2 (ca. 75%) (Table 4.3). Fmax3 variability was mostly controlled by S and AOU (Table 4.3), being θ, DS and Chl *a* also contributors to explain 33% of the total Fmax3 variability. In this case, the relationship S · Fmax3 was linear and positive from ~35 pss and the relationship AOU · Fmax3 shifted from positive to negative at around 170 μmol kg^{-1} (Table 4.3, Fig. 4.8a).

Fmax4 variability was mainly explained by S and depth (Table 4.3), and along with temperature, AOU, Chl-*a* and SWR, the explained variance was only 28%. In the S·Fmax4 relationship, Fmax4 started to increase linearly with S for values over ~35 pss. The relationship between AOU and Fmax4 was linear and negative all over the AOU range, which contrast with the relationships of AOU with Fmax1, Fmax2 and Fmax3. Concerning Chl *a*, the relationship was positive. By taking BB into consideration, we observed that BB showed a positive relationship with Fmax4 and the explained variance reached up to 31 % (Table 4.3), being S and depth still the dominant explanatory variables of Fmax4 (Table 4.3). Noticeably, BB did no contribute significantly to explain the distribution of Fmax3.

In summary, whereas the environmental factors AOU and Chl *a* explained most of the variability of Fmax1 and 2, the variability of Fmax3 and Fmax4 was mostly explained by S and AOU and by S and depth, respectively. BB only contributed to explain significantly the variability of two (Fmax1 and 4) out of the four PARAFAC components.

Discussion

Comparison of the Malaspina PARAFAC components with other studies

All the fluorescence PARAFAC components identified in this study have been reported earlier in the oceans and in other aquatic environments. The results of the global fluorescence inventory carried out by *Jørgensen et al.* [2011] revealed for the first time in the oceans the ubiquitous signal of the two humic-like fractions that we found in our study. As well as in other marine FDOM studies [e.g. *Timko et al.*, 2015; *Yamashita et al.*, in press; *Jørgensen et al.*, 2011; *Yamashita et al.*, 2010], our C1 revealed as a mixture of the classical humic-like peaks A and C defined by Coble (1996). This component has also been frequently detected in terrestrial and low salinity coastal environments [e.g. C3 in *Wang et al.*, 2014; *Catalá et al.*, 2013; C2 in *Yamashita et al.*, 2013; C3/P3 in *Murphy et al.*, 2008; C4 in *Stedmon and Markager*, 2005a; *Conmy et al.*, 2004), as well as in rivers [e.g. C3 in *Chen et al.*, 2013; *Hong et al.*, 2005] or lakes such as a tropical lake [C3 in *Bittar et al.*, 2015] or a vegetation-free Antarctic lake [*Cory and McKnight*, 2005]. Thus, C1 is related to the

microbial processing of organic matter in both terrestrial and oceanic regions. Our C2 was similar to the marine humic-like components found in other PARAFAC models performed in the ocean [C4 in *Jørgensen et al.*, 2011; C2 in *Yamashita et al.*, 2010], as well as others from coastal environments [*Catalá et al.*, 2013; *Murphy et al.*, 2008; C6 in *Yamashita et al.*, 2008]. Similarly, it was also found in rivers and lakes such as the same vegetation-free Antarctic lake [*Cory and McKnight*, 2005]. Thus, C2 also represents a group of fluorescent substances associated with biological activity.

Unlike other studies that found up to four amino acid-like components [e.g. *Jørgensen et al.*, 2011; *Yamashita et al.*, 2008], we solely found two amino acid-like C3 and C4, which fluorescence characteristics were almost identical to those of free tryptophan and tyrosine [*Yamashita and Tanoue*, 2003b], and also were similar to those of tryptophan- and tyrosine-like components found in previous PARAFAC studies either in the ocean [*Murphy et al.*, 2008; *Yamashita et al.*, 2008; *Murphy et al.*, 2006] and in coastal or inland waters [*Cory and McKnight*, 2005; *Stedmon and Markager*, 2005a].

Comparing our 4-component PARAFAC model with the first global inventory of 7-component PARAFAC model carried out by *Jørgensen et al.* [2011], we believe that the exclusive coverage of remote oceanic areas during the Malaspina 2010 expedition results in the absence of more fluorescent components. Likely, the sampling of coastal areas in *Jørgensen et al.* [2011] allowed them to find two other amino acid-like peaks that were attributed to phenylalanine and to a tyrosine remnant, and a peak with intermediate fluorescence spectrum of the humic- and amino acid-like materials.

Our selection of the 4-component PARAFAC model does not mean that the FDOM exclusively contained these four fluorophores, but it is an indicator of the most representative ones in the EEM database. Regarding fluorescence intensities (FI), *Jørgensen et al.* [2011] and ours global FDOM inventories are directly comparable since they are standardized in Raman units (RU). For the case of the four PARAFAC components that we have in common, the FI ranges are very similar, except for the tryptophan peak that slightly outstands in Jørgensen's et al. study, ranging approximately between below detection limit and 20 x 10^{-3} RU for the humic-like substances, below detection limit and 40 (up to 60 in Jørgensen's study) x 10^{-3} RU for the tryptophan peak, and below detection limit and 40 x 10^{-3} RU for the tyrosine peak.

The lack of uniformity concerning instrument settings, fluorescence normalization and conversion units hinder the comparison with other studies. Apart from the Raman normalization, the other two usual procedures to normalize fluorescence intensities in aquatic environments are the quinine sulphate units (QSU) and the normalized fluorescence units (NFI). Hence, the range of fluorescence units normalization prevents direct comparison with all FDOM studies in the marine environment, and only those values that reported their fluorescence intensities in RU are directly comparable.

Humic-like components and its major drivers

The increase with depth of the humic-like FDOM components in the upper 200 m

followed the regular pattern previously reported for open ocean waters (Fig. 4.2a, b) of the Atlantic [*Lønborg et al.*, 2015; *Timko et al.*, 2015; *Kowalczuk et al.*, 2013; *Determann et al.*, 1996; *Chen and Bada*, 1992; *Mopper et al.*, 1991], the Southern ocean [*Yamashita et al.*, 2007; *Wedborg et al.*, 1998], the equatorial Pacific [*Hayase and Shinozuoka*, 1995; *Chen and Bada*, 1992], the Okhotsk Sea and the northwestern North Pacific [*Yamashita et al.*, in press; *Omori et al.*, 2010; *Yamashita et al.*, 2010; *Tani et al.*, 2003], the Arabian Sea [*Coble et al.*, 1998] or the global cruise of *Jørgensen et al.* [2011] that covered the Atlantic, Pacific, Indian and Southern Oceans. Generally, the humic-like FDOM intensity is lower in surface waters where sunlight penetrates and photolyses these compounds, which has been shown to be very vulnerable to natural solar radiation [*Omori et al.*, 2011; 2010]. Photobleaching has a significant influence upon the optical properties of DOM in the open ocean [*Helms et al.*, 2013] and its vertical extent is limited to the penetration of the ultraviolet radiation in the ocean [*Kowalczuk et al.*, 2013]. In our study, the SWR does not contribute substantially to explain the fluorescence component profiles. We only found a slight negative relationship between Fmax1 and 4 with SWR (Fig. 4.8., Table 4.3), and, for the case of Fmax2 and 3, significant relationships were not found. We presume that the prolonged exposure of surface water bodies to sunlit results in a photobleaching saturation in any oceanic region. Consequently, the photochemical degradation will affect equally regardless of the solar radiation received by any biogeographic province. In fact, previous irradiation experiments with natural waters showed high humic-like substances depletion rates were in the first hours [*Timko et al.*, 2015; *Nieto-Cid et al.*, 2006; *Del Vecchio and Blough*, 2002], showing a slow down after twenty days [*Helms et al.*, 2013]. Likewise, the humic-like peak A/C experienced the lowest losses after 24-h irradiation in the surface samples compared to greater depths [*Timko et al.*, 2015], which is likely a result of the highly photodegraded material that was already present.

Distinct changes in FDOM composition occur above and below the MLD, which limits vertical mixing and thus exposure of DOM to UV solar radiation. The DOM below the MLD is characterized by low amino acid-like to humic-like fluorescence intensity ratios. Indeed, we found significant differences above and below the MLD for the four fluorescent components. Famx1, Fmax2 and Fmax3 showed lower values above than below the MLD (4.22 ± 0.18 vs 6.39 ± 0.13 $x10^{-3}$ RU for C1, 2.76 ± 0.15 vs 6.76 ± 0.15 $x10^{-3}$ RU for Fmax2 and 4.89 ± 0.23 vs 6.16 ± 0.16 $x10^{-3}$ RU for Fmax4, respectively), and Fmax4 showed higher values above the MLD (12.2 ± 0.29 vs 10.0 ± 0.19 $x10^{-3}$ RU for Fmax4). This suggests that DOM may consist of more aromatic humic-like compounds produced mostly by bacterial processing of organic matter in the dark ocean [*Yamashita et al.*, 2010; *Yamashita and Tanoue*, 2008]. In this regard, the fluorescence intensities of the humic-like components differed between surface and dark waters sampled during the Malaspina 2010 expedition. The values of the humic-like components Fmax1 and 2 in the surface ocean (< 200 m) were lower than those from the dark ocean. Whereas half of Fmax1 and Fmax2 values for the surface were lower than 5.2 x

10^{-3} RU and 4.9 x10^{-3} RU, respectively, half of the values in the dark ocean were lower than 12.7 x10^{-3} RU and 9.2 x10^{-3} RU, respectively. In addition, we might expect that the large-scale downwelling circulation of the gyres limit the input of humic-like DOM from deep waters, and the solar exposure photobleaches the humic-like fluorescent components. These two features create the scenario that we reported in the subtropical oligotrophic gyres of the South Atlantic, South and North Pacific and South Indian (i.e. SATL, ISSG, SPSG and NPTG), where the strongest depletion of the humic-like components was found. In our circumnavigation, the minimum values of Fmax1 and 2 at both surface and deep ocean were found in the South Indian Ocean —a mean value of 3.7 ± 0.6 x 10^{-3} RU for ISSG and a water mass proportion-weighted average value (i.e. arquetypal value) of 5.4 ± 0.2 x10^{-3} RU in the Indian Subtropical Mode Water ($STMW_I$) for Fmax1, and a mean value of 3.8 ± 0.6 x 10^{-3} RU for ISSG and an arquetypal value of 5.4 ± 0.1 x10^{-3} RU in the Indian Central Water (ICW_{13}) for Fmax2 [Chapter III of this PhD thesis]. Regarding the depletion of the humic-like components in surface waters and the increase with depth, *Timko et al.* [2015] found that in the eastern North Atlantic Ocean and the northern Sargasso Sea, the humic-like C1 and C2 were on average 5.9 and 3.4 times higher below 1000 m than at the surface. Contrary to *Morel et al*. [2007], we did not find the clearest natural waters in the South Pacific Ocean likely because (1) the Malaspina 2010 expedition crossed the South Pacific in autumn whereas the BIOSOPE expedition did it in spring-summer and (2) the BIOSOPE expedition covered longitudes 70°W to 150°W and found the clearest waters near Easter Island, whereas our transect was located within the range 117°E to 170°E and remained further west from their "clearest" waters spot.

In addition, after comparing the geographical distribution of FDOM on this paper with that from the dark ocean (>200 m) during the same circumnavigation [Chapter III of this PhD thesis], we found that the maximum were located in the Western North Pacific. This area is peculiar, not only because both maximum values of Fmax1 and 2 were found there but also because this is the only geographic area in which the values of Fmax1 and 2 in the surface and dark ocean are similar (i.e. the depth profiles do not increase with depth). At the surface, the highest values for both Fmax1 and 2 were found in the PNEC province (i.e. 11.8 and 12.4 x10^{-3} RU, respectively), and at the deep in the North Pacific Intermediate Water (NPIW) (16.4 ± 0.2 x10^{-3} RU) and in the North Pacific Central Mode Water (CMW_{NP}) (12.0 ± 0.2 x10^{-3} RU) [Chapter III of this PhD thesis]. This unique oddity was not reported previously in other regional or global studies because this region was not covered previously [*Jørgensen et al.*, 2011; *Morel et al.*, 2010; *Yamashita et al.*, 2010]. Instead, the North Atlantic and the Equatorial upwelling regions deviated from the aforementioned increasing depth profile for the humic-like substances and showed the maximum values in the surface [*Jørgensen et al.*, 2011; *Kowalzcuk et al.*, 2013]. In our case, the depth profiles did not deviate from the standard increasing fluorescence intensities with depth but the equatorial provinces (i.e. NATR, WTRA, PEQD and PNEC) showed the largest mean values of the humic-like components, ranging from 6.6 ± 1.6 to 11.5 ±

1.8 x10^{-3} RU for Fmax1 and from 5.9 ± 1.9 to 11.6 ± 1.8 x10^{-3} RU for Fmax2. The reasons behind why upwelling regions are very abundant in humic-like materials are (1) the high microbial productivity in response to nutrient fertilization by deep waters and (2) the net upward advection flux of deep water enriched in humic-like materials [*Siegel et al.*, 2002].

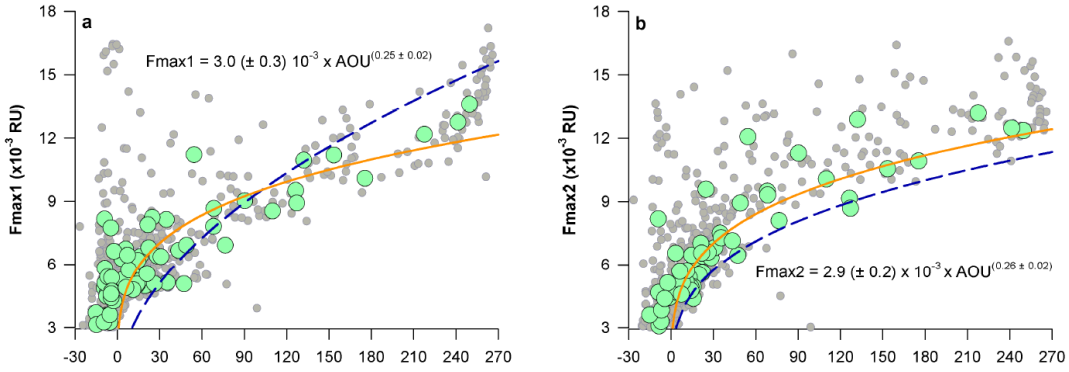

Fig. 4.9. Relationships between the apparent oxygen utilization and the fluorescence components (a) C1 and (b) C2. Grey dots represent measured concentrations, white dots archetypal concentrations for each water type and black dots archetypal concentrations for each sample. The power-law regression curves for the surface (in orange) and for the dark ocean (in dashed blue after Chapter III of this PhD thesis). AOU-C1: $R^2 = 0.73$, $p < 0.0001$, $n = 45$; AOU-C2: $R^2 = 0.80$, $p < 0.0001$, $n = 45$. Note: the values with AOU < 0 were not considered in the AOU-Fmax relationships.

The GAMs analysis of the humic-like Fmax1 and Fmax2 indicate that microbial heterotrophic metabolism (AOU as a surrogate) and primary production (Chl *a* as a surrogate) are the factors that mostly affect to these fluorophores generation. For the case of Fmax1, BB was also a selected explanatory variable, whereas for Fmax2 the contribution of BB was negligible. It is well known that microbes are directly releasing humic-like fractions during its metabolism [*Fukuzaki et al.*, 2014; *Romera-Castillo et al.*, 2010; 2011], but also primary production is likely indirectly boosting the Fmax1 humic-like synthesis by generating labile substrates that enhance bacterial growth, thus contributing to the microbial carbon pump (MCP) [*Jiao et al.*, 2010; *Ogawa et al.*, 2001]. However, the fact that C2 was not explained by BB in our study gives evidence of a less direct bacterial influence than for C1. The photo-degradation and photo-production might be plausible explanations since previous studies have reported that the bleaching of the fluorophore responsible for C1 (peak C) leaves behind residual peak M fluorophores [*Helms et al.*, 2014].

Since AOU was the most significant parameter explaining Fmax1 and Fmax2, we have explored their parametric relationships to compare with previous works (Fig. 4.9a, b). As in the dark ocean, the AOU-Fmax1 and AOU-

Fmax2 relationships were power law, positive and highly significant (Fmax1= 3.0 (± 0.3) x 10^{-3} AOU $^{(0.25 \pm 0.02)}$; R^2 = 0.73, p < 0.0001, n = 45; Fmax2= 2.9 (± 0.2) x 10^{-3} AOU $^{(0.26 \pm 0.02)}$; R^2 = 0.80, p < 0.0001, n = 45; Fig. 4.9a, b). As we were interested in the effect of microbial metabolism on Fmax1 and Fmax2 production, the values in which primary production rates prevails over respiration rates (i.e. AOU < 0 µmol kg^{-1}) were ruled out from this analysis. Note that the average values per province and nominal depth have been used to perform these correlations. However, unlike the dark ocean, where the Fmax2 conversion efficiency exceeded that of Fmax1, in the illuminated ocean the conversion efficiencies of both humic-like components were similar (i.e. almost identical AOU-Fmax exponents). By comparing these regressions with those from the dark ocean (chapter III of this PhD thesis), we found that in both cases the exponents were higher in the dark ocean (i.e. 0.51 ± 0.04 for Fmax1 and 0.31 ± 0.04 for Fmax2, respectively), meaning a higher conversion efficiency of the humic-like substances in the dark ocean than is the surface ocean, where a net effect of photobleaching is also detected.

Amino acid-like components and its major drivers

The decrease of the amino acid-like components with depth suggests that those substances were autochthonously produced and likely more resistant to photobleaching [*Helms et al.*, 2013] (Fig. 4.2d, Fig. 4.8a, b). In previous studies, the vertical distribution of the amino acid-like components displayed dominance in the surface waters and decreasing values with depth. These bioavailable components were linked to primary production [*Kowalczuk et al.*, 2013; *Guéguen et al.*, 2012; *Jørgensen et al.*, 2011; *Yamashita and Tanoue*, 2003b; *Determann et al.*, 1996]. In fact, there was consistent amino acid-like fluorescence intensity dominance in the surface waters of the Atlantic Meridional Transect [*Kowalczuk et al.*, 2013], the eastern Atlantic Ocean and in the northern Sargasso Sea [*Timko et al.*, 2015] or in the southern Canada Basin and in the East Siberia Sea [*Guéguen et al.*, 2012] after studying the DOM composition. Here, we present larger values of the tyrosine-like Fmax4 at the surface than at the dark ocean, with half of the data exceeding 10.2 x10^{-3} RU, whereas for the dark ocean half of the data exceeded 4.9 x10^{-3} RU. Regarding the fluorophore tryptophan-like C3, it was the least variable out of the four fluorescent components throughout the whole water column, being half of the data lower than 4.2 x10^{-3} RU in the surface ocean and 4.9 x10^{-3} RU in the dark ocean. The vertical patterns of both Fmax3 and 4 are coincident with those of *Jørgensen et al.* [2011] and *Timko et al.* [2015], as they found that tyrosine-like Fmax4 was approximately 1.5 times higher at the surface than in waters > 1000 m depth and that tryptophan-like Fmax3 did not show a clear depth-dependence. The province with the maximum average of Fmax3 and 4 was NATR_W, whereas the water mass with the highest archetypal value was the South Atlantic Central Water (18 °C) ($SACW_{18}$) (i.e. 8.3 ± 0.9 x10^{-3} RU). The provinces that showed the minimum value for Fmax 3 and 4 were AUSW and NPTG, whereas in the dark ocean, the minimum was assigned to the Circumpolar Deep Water ($CDW_{1.6}$) (i.e. 3.4 ± 0.2 x10^{-3} RU).

The amino acid-like components showed a positive relationship with Chl *a* for both Fmax3 and 4, and only with BB for Fmax4, which implies a more relevant role of bacteria on the distribution of Fmax4 (Table 4.3; Fig. 4.8). The relationship Fmax4-AOU was negative and less significant than for the humic-like components (Table 4.3; Fig. 4.8). In the dark ocean, *Catalá et al.* (Chapter 3 of this PhD thesis) obtained the same result, explaining the negative relationship by the microbial consumption of the more recalcitrant fraction of the amino acid materials represented by this fluorescence signature with a timescale of centuries. In the surface ocean, we are likely observing the bulk of the recently produced tyrosine-like materials that scape rapid microbial utilisation and the negative relationship with AOU would also be a consequence of the microbial utilization of a less recalcitrant fraction of the amino acid-like substances or the absence of microbial cell communication by exometabolites under less favourable conditions. It has been reported that microbial quorum sensing releases exometabolites like peptides [*Pereira and Giani*, 2014] that content chromophoric groups. This assumption, as well as the microbially produced humic-like substances, is supported by a 72 h incubation experiment in the darkness where the amino acid-like fluorescence decayed by 29 ± 9 % and the marine humic-like fluorescence increased by 20 ± 9 % [*Lønborg et al.*, 2015]. Fmax3 did not show any trend with AOU throughout the whole water column although we saw a shift in the trend from positive to negative at around 170 μmol kg^{-1} due to the subsurface waters of PNEC (Fig. 4.5a, d; Fig. 4.8a). However, unlike the dark ocean, we found a positive and significant relationship of the amino acid-like components with salinity ($F_{S\text{-}Fmax3}$ = 69 and $F_{S\text{-}Fmax4}$ = 37, $p < 0.0001$, Table 4.3), that could be related to the atmospheric influence within the upper 200 m. The areas submitted to intense solar radiation results in both higher water evaporation (i.e. higher salinity) and photobleaching rates of the most sensitive (i.e. humic like components) chromophoric material [*Omori et al.*, 2011; 2010] and likely an accumulation of the less photoreactive (i.e. amino acid-like) components. In addition, as it has been reported that photodegradation shifts the higher molecular weight (HMW) materials to lower MW (LMW) fractions [*Omori et al.*, 2011; 2015], we could expect that the LMW DOM become more available to microbes that, in turn, could synthesize fresh tryptophan- and tyrosine-like materials.

Conclusions

The relationships between environmental factors and fluorescence PARAFAC components in the surface global ocean are mostly non-linear, which encourages the use of GAMs for describing the large-scale variability of FDOM. GAMs results showed that the environmental drivers of the humic-like and amino acid-like fluorescent components, as well as the robustness of the relationships are not the same, with the humic-like components being primarily affected by microbial activity (AOU and Chl *a*), and the amino acid-like components by physical processes (S).

Acknowledgements

We thank C.M. Duarte for the coordination of the Malaspina expedition; the

chief scientists of the seven legs, the staff of the Marine Technology Unit (CSIC-UTM) and the Captain and crew of R/V Hespérides for their outright support during the circumnavigation. Also, we thank the Physics block for collecting, calibrating and processing the CTD data; Dolors Blasco for facilitating the nutrients data; Antonio Fuentes-Lema and Eva Ortega- Retuerta for their contribution to sampling collection and measurements. J. Otero was supported by a "Junta para la Ampliación de Estudios" Fellowship (JAE-Doc program 2011) from the CSIC and ESF. This study was financed by the Malaspina 2010 circumnavigation expedition (grant number CSD2008–00077).

General Discussion

This dissertation presents the first global inventory of DOM optical properties, classified by water types (WT) in the dark ocean and by Longhurst's biogeographic provinces and PAR levels in the illuminated ocean. Both WT and provinces show intrinsic values of CDOM (absorption coefficients, indices and slopes) and FDOM (fluorescence components) properties dictated by relevant environmental variables including WT age and ageing (i.e. AOU) in the dark ocean and salinity, chlorophyll *a*, bacterial biomass and AOU among others in the illuminated ocean. For the case of the dark ocean, previous works by *Nelson et al.* [2007; 2010] have already reported a global inventory of CDOM absorption coefficients and slopes but gathered by pelagic layers (epi–, meso– and bathypelagic) and ocean basins. We stepped forward by presenting an oceanographic rather than geographic approach based on WT that, in turn, overcomes some difficulties that are not solved with the approach based on layers and basins. These difficulties are (1) the mixing of multiple water masses of contrasting origin within a given pelagic layer and (2) the presence of intermediate and abyssal water masses in more than one ocean basin. Concerning FDOM, the global ocean was previously sampled during the Galathea III expedition in 2006–7 [*Jørgensen et al*., 2011], but the number of samples collected in the dark ocean was very limited (about 50) compared with the number of samples collected during the Malaspina 2010 circumnavigation (about 800). Regarding the surface ocean, some studies have attempted to describe the DOM optical properties of a determined oceanic region by Longhurst's biogeographic provinces [e.g. *Kowalczuk et al.*, 2013], but none, except that of *Jørgensen et al*. [2011], covered the entire global surface ocean. However, whereas *Jørgensen et al.'s* study occupied more coastal provinces and arrived to polar latitudes, our study was centred in the open ocean at tropical and temperate latitudes. Given this coverage disparity, joining both global databases as well as those from regional studies would be very convenient to perform a global analysis on FDOM optical properties. However, consideration of fluorescence data collection and unit standardization is mandatory before conducting this effort (see below).

1. Why it is so difficult to produce a standardized global database of FDOM measurements?

The lack of uniformity concerning instrument settings, fluorescence normalization and conversion units hinder the comparison with other studies or the assemblage of all the data produced in individual studies into a unique normalised database. Apart from the Raman normalization, the other two usual procedures to normalize fluorescence intensities in aquatic environments are the quinine sulphate units (QSU), which consists in dividing the fluorescence units by the QSU fluorescence intensity at Ex/Em 340–350/440–450 nm, and the normalized fluorescence units (NFI), which comprises the measurement of the quinine sulphate fluorescence intensity at the same Ex/Em wavelengths of the peak of interest. For instance, in *Yamashita et al.* [2010] or *Yamashita and Tanoue* [2008] the fluorescence intensities of the marine humic-like peak M were reported in NFI units by calibrating the spectrofluorometer measuring the fluorescence of quinine sulphate at Ex/Em 320 nm/420 nm. The latter are valid only for the humic-like peaks given that quinine sulphate does not

fluoresce at the Ex/Em wavelengths of the amino acid-like substances. For this reason, *Nieto-Cid et al*. [2005] proposed standardization based on a mixture of quinine sulphate and tryptophan to overcome this difficulty. Furthermore, the Raman and QSU normalizations are not always performed similarly. The wavelength range of the Raman area can vary among authors as well as the consideration of subtracting or not the baseline. Regarding the QSU normalization, quinine sulphate has the inconvenient of being commercialized in several forms and with different molecular weights, which leads to different fluorescence intensities at the same concentrations of these commercial forms. Similarly, the Ex/Em wavelengths of the peaks of interest can vary according to the study site and, thus in fluorescence intensity. As a consequence, fluorescence units will depend on the chosen peak of interest and its position in the Ex/Em landscape (see an example in the box below). In this sense, as a matter of the aquatic environment, the results exhibited by PARAFAC models will vary not only in the number of components but also in the peak positions. Hence, the range of fluorescence unit normalization prevents our direct comparison with all FDOM studies in the marine environment, and only those values that reported their fluorescence intensities in RU with the same procedure are comparable with ours. Furthermore, when using PARAFAC modelling, all EEM form the different databases should be processed together to obtain a global PARAFAC model with consensus components. In the future, a general consensus regarding the homogeneity in the fluorescence units is required to make all the oncoming studies on FDOM comparable. Hereafter, we propose a standardization of the methodology based on the one we applied in the Malaspina circumnavigation. It consists on obtaining Raman units by calculating the Raman area (RA) between 381 and 426 nm following the trapezoidal rule of integration [*Lawaetz and Stedmon*, 2009] and its baseline correction with the emission scan at 350 nm of the daily Milli-Q water blanks (see section 4.6 of Appendix I for more details). Also, EEM should be acquired in a standardized way (excitation and emission slit wide, wavelength range and step) to facilitate collective treatment with any statistical technique.

Furthermore, continued improvement at the molecular level characterization of marine DOM with accompanying optical spectroscopic characterization will provide deeper knowledge of how changes in DOM composition impact the optical properties of CDOM and FDOM. A better understanding of these relationships has implications for the use of *in situ* optical measurements [*Menon et al.,* 2011; *Spencer et al.,* 2007] and remote sensing technology [*Griffin et al*., 2011; *Del Castillo and Miller*, 2008; *Kutser et al*., 2005; *Del Vecchio and Subramaniam*, 2004; *Carder et al*., 1989] to track biogeochemically and ecologically important processes over comprehensive temporal and spatial scales.

A CASE OF DISPARITY BETWEEN FLUORESCENT UNITS

In order to obtain a conversion factor and convert our Raman units into quinine sulphate units and make them comparable with *Yamashita and Tanoue* [2008] we did a calibration curve of quinine hemisulphate monohydrate. Given that *Yamashita and Tanoue* [2008]'s centred their study on the marine humic-like peak M, we also used the same peak, which in our case was attributed to component C2. However, the direct comparison was not possible because of three dissimilarities in (1) quinine sulphate standards, (2) peak positions and (3) normalization units.

(1) In our case, we used quinine hemisulphate monohydrate (fw = 391.47 g mol^{-1}) and in Yamashita and Tanoue's they used quinine sulphate monohydrate (fw = 440.51 g mol^{-1}). Therefore, our values should be multiplied by a factor of 1.125 to be comparable with those of *Yamashita and Tanoue* [2008].

(2) In *Yamashita and Tanoue* [2008], the peak position was at Ex/Em 320 nm/420 nm whereas in our case Fmax2 was located at Ex/Em 320/400 nm. As a consequence, the fluorescence intensity of peak M in Yamashita and Tanoue exceeded about ~10% our value, and a conversion factor of 1.10 have to be applied to our data to make them comparable.

(3) Yamashita and Tanoue [2008] provided their data in NFIU and we calibrated our instrument in QSU. To convert from QSU into NFIU, our data have to be multiplied by a factor of 2.24.

Overall, a conversion factor of 2.78 has to be applied to our fluorescent measurements to make them comparable to those of *Yamashita and Tanoue* [2008].

2. How recalcitrant the CDOM and FDOM components are?

The absorption and fluorescence of DOM measurements preformed during the circumnavigation, their significant relationships with apparent oxygen utilization (AOU) together with the calculation of a global ocean oxygen utilization rate (OUR) allowed us to estimate net production rates and turnover times of 300–800 yr for the different chromophoric and fluorescent fractions of DOM in the dark global ocean (Table D.1). For the case of the bulk CDOM and the humic-like fluorescent components C1 and C2, the turnover times exceeded the dark ocean flushing time, 345 yr according to *Laurelle et al.* [2009], the turnover time of the bulk DOC pool, 370 yr according to *Hansell et al.* [2009] and the water mass weighted average ideal age of the Malaspina 2010 samples, 454 ± 22 yr according to our estimate in chapter I, whereas the turnover time of the amino acid-like fluorescent component C4, as well as the ubiquitous UV- and VIS-chromophores were not significantly different from those estimates (see Table D.1). The fact that the turnover times of some of the CDOM and FDOM components exceed the renewal time of the dark ocean gives evidence of the role of refractory DOM in carbon sequestration at the timescale of hundreds of years.

Table D.1. Summary of the annual net production rates (NPR) and turnover times of the recalcitrant DOM fractions detected with chromophoric and fluorescent spectral techniques.

	Annual NPR (Raman Units)	Turnover time (yr)
FDOM-C1	$2.3 \pm 0.2 \times 10^{-5}$ RU	529 ± 49
FDOM-C2	$1.2 \pm 0.1 \times 10^{-5}$ RU	742 ± 67
FDOM-C4	$-1.1 \pm 0.2 \times 10^{-5}$ RU	461 ± 125
CDOM (a_{325})	$3.3 \pm 0.5 \times 10^{-4}$ m^{-1}	634 ± 120
UV-Chromophore	$8.6 \pm 1.1 \times 10^{-5}$ m^{-1}	345 ± 80
VIS-Chromophore	$3.1 \pm 0.4 \times 10^{-5}$ m^{-1}	356 ± 74

3. Moving a step ahead beyond absorption coefficients and slopes: picking individual chromophores in the dark ocean

An exhaustive inspection of the CDOM spectra from the dark ocean collected during the Malaspina 2010 circumnavigation allowed us to identify two discrete chromophores located at 302 ± 3 nm (Ch-UV) and 415 ± 3 nm (Ch-VIS) and calculated the absorption coefficient signal following the *Röttgers and Koch* [2012]'s equation that is based on *Breves et al.* [2003]'s approximation (chapter 2). Here, we calculate the contribution of these chromophores to the total CDOM absorption spectrum by comparing the spectral slopes in the ranges 250–400 nm and 350–600 nm including and excluding the UV and VIS chromophores in the non-linear regression Eq. 2 of chapter 2. On average, the slopes when considering the chromophores in the equation were 82 ± 14% and 87 ± 11% the value when they are not considered (Fig. D.1). Therefore, in general, the regression slopes used to characterise the exponential decline of the absorption spectra associated to humic materials, are overestimated when the presence of the UV and VIS chromophores is not considered. Furthermore, Table D.2 presents the contributions of the chromophores signal with respect to the total absorption at that specific wavelength for each water mass intercepted during the circumnavigation. Whereas the Ch-UV contributed noticeably in the deep Antarctic waters (i.e. AABW, CDW and $AAIW_{3.1}$) (see Table 2.1 in Chapter 2), the contribution in the Indian and South Pacific Mode Waters was very low (i.e. ICW_{13}, $STMW_I$ and $STMW_{SP}$). For the case of Ch-VIS, 17 out of the 22 water masses represented more than 10% of the total absorption.

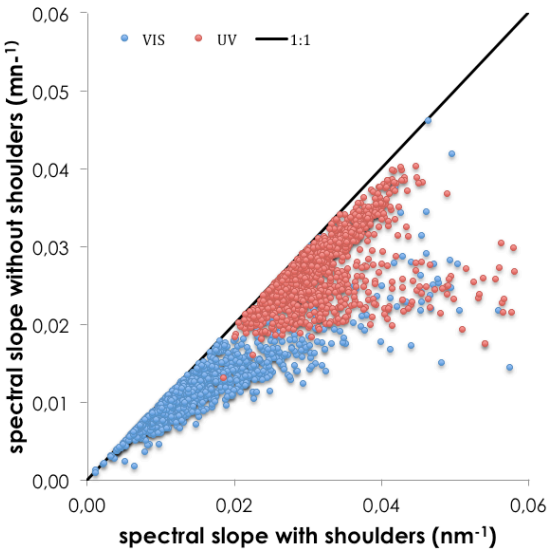

Fig. D.1. Comparison of the spectral slope values in the ranges 250–400 nm (red dots) and 350–600 nm (blue dots) solving Eq. 2 of chapter 2 with and without the UV and VIS chromophore signals, respectively.

Table D.2. Percentage of the Ch-UV and Ch-VIS absorption coefficients with respect to the total absorption signal.

Acronym	VOL_i (%)	$a_{Ch\text{-}UVi}/a_{300i}$ (%)	$a_{Ch\text{-}VISi}/a_{415i}$ (%)
EDW	0.7%	1.5 ± 2.0	6.4 ± 3.4
$ENACW_{12}$	3.2%	1.9 ± 0.8	8.4 ± 3.1
$ENACW_{15}$	1.8%	1.1 ± 1.0	6.5 ± 3.3
13EqAtl	1.6%	2.8 ± 1.4	18.1 ± 7.1
$SACW_{12}$	2.2%	5.0 ± 2.0	15.2 ± 5.0
$SACW_{18}$	1.4%	1.3 ± 1.3	14.5 ± 5.6
$STMW_I$	0.9%	0.1 ± 0.2	19.4 ± 8.3
ICW_{13}	4.5%	0.5 ± 0.4	15.5 ± 4.3
$STMW_{SP}$	0.2%	1.0 ± 3.1	26.1 ± 29.2
$SPCW_{20}$	0.5%	11.0 ± 9.9	12.7 ± 13.0
13EqPac	5.7%	10.6 ± 1.8	19.0 ± 3.1
CMW_{NP}	3.5%	6.2 ± 1.8	17.1 ± 2.8
$STMW_{NP}$	0.2%	3.2 ± 2.9	16.0 ± 8.0
MW	0.2%	2.9 ± 4.9	7.6 ± 8.6
SAMW	8.0%	5.7 ± 1.8	13.6 ± 3.3
$AAIW_{3.1}$	4.5%	12.0 ± 2.4	14.6 ± 3.8
$AAIW_{5.0}$	2.9%	7.9 ± 2.7	15.4 ± 4.1
NPIW	5.9%	11.1 ± 1.7	18.9 ± 2.7
CDW	27.0%	14.4 ± 1.0	15.2 ± 1.7

$NADW_{2.0}$	12.9%	6.5 ± 1.0	11.1 ± 1.7
$NADW_{4.6}$	7.6%	6.6 ± 1.4	11.7 ± 2.2
AABW	4.4%	13.0 ± 2.4	14.3 ± 4.1

4. How much carbon holds the fluorescence components?

To better understand the role played by FDOM in the global carbon cycle, we have made an attempt to estimate the concentration of the fluorescent components as well as the net production rates (NPR) in carbon units on basis of our own conversion factors (for more details see Appendix IV).

With the aim of comparing our conversion factors with those obtained by *Yamashita and Tanoue* [2008], we read up their procedure that was based on *Hayase and Sinozuka* [1995]'s approximation. This approximation is very similar to ours, which consists of obtaining the contribution of the humic-like substances to the bulk DOC pool from the slope of the calibration curve between the concentration of a reference substance and its fluorescence intensity. For the case of *Hayase and Sinozuka* [1995], they used a fulvic acid isolated from the sediments of Tokyo Bay due to the similarity that they find with their FDOM samples in the Pacific Ocean. In our case, we used two International Humic Substances Society (IHSS) reference materials, which were more alike to the humic-like components obtained during the Malaspina 2010 circumnavigation. In addition, *Hayase and Sinozuka* [1995] calculated the amount of FDOM in the Pacific Ocean from the slope of the relationship between FDOM and AOU and their conversion factor of fluorescence into carbon. However, what they really obtained with this calculation was the fraction of the mineralised organic matter that is converted to FDOM. As a result, they inaccurately reported that the contribution of humic-like FDOM to DOM in the marine environment was 1.2%, when they were really reporting that 1.2% of the organic matter mineralised in the Pacific Ocean ends as humic-like FDOM rather than as CO_2. Considering our humic-like NFP in carbon units of 0.20 ± 0.01 Pg C y^{-1} (see Appendix IV) and assuming that 10 Pg C are annually respired in the dark global ocean [*Hansell et al.*, 2009], the global production of humic-like FDOM would represent about 2% of the organic carbon consumption, which is not significantly different from the 1.2% obtained by *Hayase and Sinozuka* [1995]. Furthermore, If one considers the humic-like FDOM measured in the samples of the Pacific Ocean (around 6 fluorescence units (flu) according to Fig. 2 of their manuscript), multiply it by their conversion factor (50 flu per 1mg L^{-1} of fulvic substance), and the assumption that the carbon content in their fulvic acid is 50% of the total weight (i.e. 0.5 mg C/1mg of fulvic substance), they would obtain a final concentration of humic-like FDOM of 0.06 mg C L^{-1} or 5 µmol C L^{-1}. Extrapolating this estimation to the Pacific Ocean, which has a DOC concentration of ~ 35–40 µM, it would result in a global DOC estimation of 12.5–14.2% accounted by humic substances, which is not significantly different to our estimation of 15 ± 3% (see Appendix IV) or the estimation of *Nieto-Cid et al.* [2005] of 6–22% in the coastal upwelling system of the Ría de Vigo (NW Spain), where the terrestrial inputs are more abundant than in the open ocean.

In summary, using the oceans as a bioreactor, our estimates indicate that the *in situ* microbial production rate of fluorescent humic-like materials in the dark global ocean (0.20 ± 0.01 Pg C yr^{-1})

might be a carbon sink in the time scale of hundreds of years, equivalent to the input of organic carbon produced in the coastal seas that is exported to the global open ocean (0.28 Pg C yr^{-1}) [*Chen*, 2004] or the carbon sequestered in the ocean sediments by the biological pump (0.2 Pg C yr^{-1}) [*Sarmiento and Gruber*, 2002].

However, we are aware that our conversion factors, as well as those from *Yamashita and Tanoue* [2008], *Nieto-Cid et al.* [2005] or *Hayase and Sinozuka* [1995], are overestimated after considering that the total amount of the reference materials is fluorescent. A better approximation with nuclear magnetic resonance or ultrahigh resolution Fourier transform ion cyclotron mass spectrometry would contribute to estimate the carbon content of the fluorescent components in the future. Similarly, we suggest using the isolated DOM fraction from Natural Energy Laboratory of Hawaii Authority water proposed by *Green et al.* [2014] as a standard of chromophoric and fluorescent marine RDOM to compare the carbon estimations among studies.

5. Are changes in CDOM and FDOM properties coupled over the global thermohaline circulation?

To test for linkages between the CDOM and FDOM properties in the dark global ocean, we studied the correlation of CDOM absorption coefficients and spectral slopes with the four fluorescent PARAFAC components (see Table D.3). We found a significant negative power law relationship between Fmax1 and Fmax2 with $S_{275\text{-}295}$ and S_R, which points to an increase in aromaticity and in the average molecular weight of CDOM linked to the C1 and C2 humic-like production. The positive trend of Fmax1 and Fmax2 with a_{325} also expresses the accumulation of chromophoric aromatic substances with water mass ageing. However, the shifts into a more aromatic and larger average molecular weight of organic materials are more acute in Fmax1 than in Fmax2, indicating a slowing down in Fmax2 over time, as well as seen in the relationship AOU·Fmax2 (see Figure 3.5 in Chapter3) that could be related to oxygen depletion.

Unlike humic-like components, the amino acid-like Fmax4 showed a positive relationship with $S_{275\text{-}295}$ and S_R, which indicates a lower degree of aromaticity and molecular weight when substantial amounts of C4 are present in the environment. On the contrary, no a_{325}·Fmax3 relationship was found.

Table D.3. Correlations between CDOM absorption coefficient at 325 nm, spectral slopes and the four fluorescent PARAFAC components.

	a_{325}	$S_{275-295}$	$S_{350-400}$	S_R
Fmax1 (Humic-like)	$Fmax1 = 0.05\ (\pm0.02)\ a_{325}^{0.95\ (\pm0.23)}$ $R^2 = 0.50$	$Fmax1 = 5\ (\pm2) \times 10^{-5}\ S_{275-295}^{-1.43\ (\pm0.12)}$ $R^2 = 0.88$	—	$Fmax1 = 0.03\ (\pm0.01)\ S_R^{-1.35\ (\pm0.24)}$ $R^2 = 0.62$
Fmax2 (Humic-like)	$Fmax2 = 0.02\ (\pm0.01)\ a_{325}^{0.67\ (\pm0.16)}$ $R^2 = 0.50$	$Fmax2 = 3\ (\pm2) \times 10^{-4}\ S_{275-295}^{-0.87\ (\pm0.15)}$ $R^2 = 0.65$	—	$Fmax2 = 1.7\ (\pm0.3) \times 10^{-2}\ S_R^{-0.73\ (\pm0.23)}$ $R^2 = 0.35$
Fmax3 (Tryptophan-like)	$Fmax3 = 1.2\ (\pm3.9) \times 10^{-2}\ a_{325}^{0.61\ (\pm0.20)}$ $R^2 = 0.35$	—	$Fmax3 = 7\ (\pm0.01) \times 10^{-5}\ S_{350-400}^{-0.91\ (\pm0.36)}$ $R^2 = 0.24$	-
Fmax4 (Tyrosine-like)	—	$Fmax4 = 0.04\ (\pm0.03)\ S_{275-295}^{0.54\ (\pm0.21)}$ $R^2 = 0.27$	—	$Fmax4 = 2\ (\pm1) \times 10^{-3}\ S_R^{0.85\ (\pm0.22)}$ $R^2 = 0.44$

6. Does FDOM and CDOM properties support the size-reactivity continuum model?

As well as other studies [e.g. *Helms et al.*, 2013; *Helms et al.*, 2008], low $S_{275\text{-}295}$ and S_R values, the high content of humic-like fluorescent components in the oldest water masses of the global ocean, as well as the C1, C2 relationships with $S_{275\text{-}295}$ and S_R allowed us to propose that water mass ageing leads to increased levels of aromatic and likely high molecular weight (HWM) materials in the recalcitrant DOM pool. However, this hypothesis, indicating that the low molecular weight (LMW) DOM turns into a more recalcitrant HMW DOM with ageing, does not appear to apply to the bulk of natural DOM according to *Amon and Benner* [1996], who proposed in their size-reactivity continuum model (Fig. 2 of the introduction) that the bulk of HMW DOM is more bioreactive and fresher than the LMW DOM given that most marine DOM was of LMW (up to 70%) and that the HMW DOM was utilized to a greater extent than LMW DOM in all marine environments investigated. However, considering that the net production of humic-like material is about 2% of the organic matter consumed in the dark global ocean (see section 4 of this chapter) it results that an increase in fluorescent humic like HMW materials would be compatible with the net accumulation of LMW materials in the global ocean.

General Conclusions

I. The quantity of chromophoric dissolved organic matter (CDOM) in the dark ocean was dependent on the cumulative microbial oxygen utilization, whereas the quality (i.e. quantum yield and spectral slopes) was dependent on the microbial oxygen utilization rate with CDOM becoming more aromatic and with higher average molecular weight along the global thermohaline circulation.

II. The net production rate of CDOM was ca. 3.3×10^{-5} m^{-1} yr^{-1} and the turnover time was 624 yr, i.e. significantly longer than the renewal time of the dark ocean indicating that these chromophoric compounds are accumulated, and therefore can be used as tracers of the microbial carbon pump in the dark ocean.

III. Two discrete chromophores have been identified in the dark global ocean: The UV chromophore centred at 302 nm was attributed partially to nitrate and likely to the antioxidant gadusol and presented a net production rate of 8.6×10^{-5} m^{-1} yr^{-1} and a turnover time of 345 years. The Visible chromophore was centred at 415 nm, was related to the respiratory enzyme cytochrome c and presented a net production rate of 3.1×10^{-5} m^{-1} yr^{-1} and a turnover time of 356 years. Omission of the existence of these chromophores leads to an overestimate of the spectral slopes of ca. 15%.

IV. Four ubiquitous fluorescent components both in the illuminated and in the dark ocean were identified, two of humic-like nature (C1, C2) and two of amino acid-like nature (tryptophan-like C3, tyrosine-like C4).

V. The two humic-like fluorophores, C1 and C2 increased as a power function with the water mass ageing at net production rates of ca. 2.3×10^{-5} and 1.2×10^{-5} RU y^{-1} in the dark global ocean. Conversion efficiencies per unit of oxygen in the surface ocean were lower than in the dark ocean, likely because of photobleaching.

VI. The tryptophan-like C3 component did not exhibit any pattern with ageing in the dark ocean, whilst the tyrosine-like C4 presented an inverse power relationship with apparent oxygen utilization leading to a net consumption rate of ca. -1.1 ± 10^{-5} RU yr^{-1}.

VII. The turnover times of the humic-like components C1 and C2 were 529 and 742 yr, significantly longer than the renewal time of the dark ocean suggesting an accumulation of these components in the dark ocean. In contrast, the turnover time of the tyrosine-like C4 was shorter (461 yr) and was not significantly different from the renewal time of the dark ocean.

VIII. In the illuminated ocean, the humic-like component C1 and C2 were also affected by microbial metabolism, being the apparent oxygen utilization and chlorophyll a the environmental variables that drove their distribution.

IX. Unlike the dark ocean, in the illuminated ocean physical processes dictated the variability of the amino acid-like C3 and C4, although C4 was also related to chlorophyll-a implying also a microbial influence.

Conclusiones Generales

I. Mientras que la cantidad de materia orgánica disuelta cromófora (CMOD) en el interior del océano depende de la utilización microbiana de oxígeno acumulada (utilización aparente de oxígeno), la calidad (trazada a través de indicadores como las pendientes espectrales o el rendimiento cuántico de la fluorescencia) depende de la tasa de utilización microbiana de oxígeno (tasa de utilización de oxígeno) con el resultado de que la CMOD gana aromaticidad y peso molecular medio con el discurrir de la circulación termohalina global.

II. La tasa de producción neta de CMOD es de aprox. 3.3×10^{-5} m^{-1} a^{-1} y su tiempo de renovación de aprox. 625 años, que es significativamente mayor que el tiempo de renovación del interior del océano, indicando que la CMOD se acumulan y, por tanto, puede usarse como trazador de la bomba microbiana de carbono en el océano.

III. Se han identificado dos cromóforos en el interior del océano. Uno está centrado en 302 nm (cromóforo UV) y se atribuye parcialmente a la absorción de nitrato y probablemente al antioxidante gadusol. Se produce a una tasa neta de aprox. 8.6×10^{-5} m^{-1} a^{-1} y su tiempo de renovación es de 345 años. El otro está centrado en 425 nm (cromóforo visible), su absorción es probablemente debida al enzima respiratorio citocromo c, se produce a una tasa neta de 3.1×10^{-5} m^{-1} a^{-1} y su tiempo de renovación es de 360 años. Si no se considera la existencia de estos cromóforos, las pendientes espectrales se sobreestiman en aprox. un 15%.

IV. Se han identificado cuatro fluoróforos presentes tanto en la capa superficial como en el interior del océano, dos de naturaleza húmica (C1, C2) y dos de naturaleza proteica (tipo triptófano, C3, y tipo tirosina, C4).

V. Los dos fluoróforos de naturaleza húmica se acumulan en paralelo al envejecimiento de las masas de agua siguiendo funciones potenciales con la utilización aparente de oxígeno y con tasas de producción de aprox. 2.3×10^{-5} y 1.2×10^{-5} RU a^{-1} para C1 y C2 respectivamente en el interior del océano. Las eficiencias de conversión en el océano superficial fueron menores que en el interior del océano probablemente debido a la fotodegradación.

VI. Mientras que el fluoróforo tipo triptófano, C3, no mostró ningún patrón definido con el envejecimiento de masas de agua en el interior del océano, el fluoróforo tipo tirosina, C4, presentó una relación potencial negativa con la utilización aparente de oxígeno, indicando una tasa de consumo neto de -1.1×10^{-5} RU a^{-1}.

VII. Los tiempos de renovación de los fluoróforos húmicos fueron de aprox. 530 años para C1 y 740 años para C2, significativamente mayores que el tiempo de renovación del interior del océano, sugiriendo una acumulación de estos componentes. Por el contrario, el

tiempo de renovación del fluoróforo tipo tirosina fue mas corto (aprox. 460 años), que no es significativamente distinto del tiempo de renovación del interior del océano.

VIII. En la capa superficial del océano los fluoróforos húmicos también se ven afectados por el metabolismo microbiano, siendo la utilización aparente de oxígeno y la concentración de clorofila las variables ambientales que más influyen en su distribución global.

IX. En la capa superficial del océano la distribución global de los fluoroforos proteicos la dictan fundamentalmente procesos físicos, aunque la concentración de clorofila también afecta a la distribución del fluoróforo tipo tirosina lo cual implica que está igualmente afectado por procesos microbianos.

Appendixes

Appendix I.

Methodology in sample collection

Index

1. General concepts
2. Neccesary equipment
3. Calibration
   - 3.1. Absorbance
   - 3.2. Fluorescence
   - 3.3. Daily checks
     - Excitation check
     - Emission check
       - Sealed Milli-Q scan
       - P-tephenyl scan
       - Tetraphenyl butadiene scan
       - Contamination check
       - Water raman scan
4. Description of the technique
   - 4.1. Sample collection for absorbance and fluorescence measurements
   - 4.2. Sample filtration for the absorbance and fluorescence determination
   - 4.3. Absorbance determination on board
   - 4.4. Fluorescence determination on board, 3–Dimensional Matrixes (EEMs) – Blanks & Samples
   - 4.5. Data exporting
   - 4.6. Data pre-treatment with Matlab

1. General concepts

The fraction of dissolved organic matter in the oceans that absorb light in the ultraviolet wavelength range and, to a lesser extent, in the visible range are meant to be chromophoric dissolved organic matter (CDOM). When the CDOM is irradiated with ultraviolet light, it emits fluorescent light characteristic of both amino acid-like and humic-like materials.

The CDOM is characterized by absorption spectra between 250 and 750 nm and excitation-emission matrixes of fluorescence, exciting between 240 and 450 nm and reading the emission between 300 and 560 nm.

In the open ocean, the concentrations of particulate organic matter are considerably low that is not usual to filter the samples in order to minimize the risk of contamination during the filtration process. In the case of Malaspina expedition, only the surface rosette (from 0 to 200 meters) were filtered through GF/F filters of 47 mm of diameter (precombusted at 450ºC during 4h) with a glass ramp filtration under controlled pressure of N_2.

2. Neccesary equipment

- Spectrophotometer Shimadzu UV–2401 with cell holders for 10-cm and prismatic cells.
- Spectrofluorometer FLUOROMAX–4 (Jobin Yvon Horiba) with cell holders for 1-cm and squared cells.

3. Calibration

3.1. Absorbance

The CDOM is characterized with absorption spectra between 250 and 750 nm at 1-nm intervals. Freshly produced Milli-Q water is used as a blank. In double-beam spectrophotometers, the reference substance is inserted in the back cell holder for 10-cm cuvettes.

Absorption spectra were obtained in absorbance units, so there was no need to calibrate them with any reference substance.

3.2. Fluorescence

Previous to start the routine analysis of each station, an emission spectra of several reference substances were done: (1) sealed Milli-Q between 365 nm and 450 nm exciting at 350 nm; (2) the p-terphenyl between 310 nm and 600 nm exciting at 295 nm; and (3) the tetraphenyl butadiene between 365 nm and 600 nm exciting at 348 nm, fixing the excitation and emission bandwidth at 5 nm and the integration time at 0.25 seconds.

3.2.1. Daily checks of the instrument conditions

Excitation Check

- This check lets us know if the lamp intensity (for the pulsed xenon flash tube lamp) has changed over time. Perform this check every 2 or 3 days.
- The chamber has to be empty and completely closed and the settings are at Ex from 200-600 nm, Em set at 350 nm, Ex and Em slits at 1 nm.
- When scan is complete, record the highest peak that should be at 467 nm.

Emission Check

Spectra on the sealed Milli-Q cuvette.

- This test allows checking the lamp decay over time.
- The settings are Ex from 350 nm, Em 365-450 nm, Ex and Em slits at 5 nm.
- When the spectrum finishes, click on the top peak of both modes. The Raman peak should be located at 397±1 nm. If the Raman peak location is within the acceptable range, calculate the integrated area under the peaks.
- At the end of sampling analysis, repeat the emission spectrum of the sealed Milli-Q water with the same settings as above.

Spectra on the p-tephenyl

- This test allows checking the lamp decay in the fluorescence region of the amino acids/aromatic proteins.
- Check that the settings are Ex 295 nm, Em 310-600 nm, Ex and Em “slits” 5 nm. The integration time is set to 0.25 s.
- When the spectrum finishes, click on the top peak. The Raman peak should be located at 338±1 nm.
- If the Raman peak location is within the acceptable range, calculate the integrated area under the peak.

Spectra on the tetraphenyl butadiene

- This test allows checking the lamp decay in the fluorescence region of the humic substances.
- Check that the settings are Ex 348 nm, Em 365-600 nm, Ex and Em “slits” 5 nm. The integration time is set to 0.25 s.
- When the spectrum finishes, click on the top peak. The Raman peak should be located at 422 ± 1 nm. If the Raman peak location is within the acceptable range, calculate the integrated area.

Cuvette check for contamination

- By using vinile or polietilene gloves, fill the QUARTZ cuvette with clean (purged) milliQ water avoiding the formation of bubbles. Make sure to wipe the cuvette clean.
- Settings should be Em from 270-430 nm, Ex set at 240 nm, Ex and Em slits at 5 nm and integration time of 0.1 s.

- The scan should look like a relatively flat but noisy line and have very low intensity (under 2000 CPS). If you can see a peak, even if it is noisy, clean the cuvette or replace the milliQ water and run again. Record intensity of the highest point between 300-350 nm, this range is where amino acids/proteins will fluoresce, so you don't want to see a peak here in milliQ water.
- If you clean the cuvette a lot and peak is still there, rotate cuvette 90 degrees and re-run. If peak changes intensity or position, this is good indication that something is stuck on the cuvette walls. It may take special treatment of methanol/base to remove it, see below.

Water Raman Scan

- This check lets us know if the lamp is drifting. We use the integrated area under the Raman scatter peak for the 3D normalization. This puts everything in Raman units that we can compare with other instruments.
- Check that the settings are at Ex of 350 nm, Em from 365 to 450 nm, Ex and Em slits at 5 nm. The integration time is set to 0.1 s.
- Place a clean milliQ-filled cuvette in the chamber.
- When the scan is finished, click on the highest peak for both modes. The Raman peak should appear at 397 +/- 1 nm. If the Raman peak location is within the acceptable range, calculate the integrated area under the peaks.

4. Description of the technique

4.1. Sample collection for absorbance and fluorescence measurements

The use of vinile gloves is compulsory. Samples were collected with glass flasks of 250 ml. Previous to sampling collection, the flasks were daily washed 3 times with Milli-Q water. Every 3 days, the flasks were introduced in an acid bath (1% HCl) for 24 hours and subsequently washed with plenty of Milli-Q water. The flasks were rinsed 3 times with seawater before filling the flask. The acid bath was replaced every 15 days.

Meanwhile the samples are not measured (less than 2 hours after collection), they were stored in darkness conditions, away from any volatile organic compounds. Samples should warm up until room temperature before starting measurements.

4.2. Sample filtration for the absorbance and fluorescence determination

The use of vinile gloves is compulsory. For depth profiles, the procedure was to start with the largest depths and end up with surface waters. Surface seawater samples (collected at depths higher than 200m) were filtered before measuring its absorbance and fluorescence. For all surface samples (higher than 200m), a volume of 50 mL for absorbance and a volume of 10 mL for fluorescence were filtered through pre-combusted 47mm-diameter GF/F filters with a glass ramp

filtration under controlled pressure of N_2. Previous to filtration, the system and the filter was washed out with 50 mL of Milli·Q water and then with 50 mL of sampling water.

Once the filtration is done, the filtration system was submitted to the same washing procedure of the flasks (see above).

4.3. Absorbance determination on board

- Turn on the spectrophotometer approximately half an hour before starting measuring.
- Set up the instrument to carry out absorption spectra from 250 nm to 750 nm at 1 nm intervals.
- Use vinile or polietile gloves.
- Fill the cuvette with freshly produced Milli·Q water avoiding the bubbles formation. Dry the cuvette walls with tissue and insert it in the back (reference) cell holder.
- Fill the front cuvette with Milli·Q water avoiding the bubbles formation, dry the cuvette walls with tissue and insert it in the front cell holder. Do an absorbance blank. Mind to place the cuvette in the same position at every measurement.
- Rinse the cuvette 3 times with sample water and fill it avoiding the bubbles formation. Mind to place the cuvette in the same position at every measurement.
- Do the spectrum and save it as a compatible excel format (e.g. ascii).
- At the beginning, middle and at the end of the analysis session do a Milli·Q water spectrum to check the spectrophotometer decay.
- After the analysis session, putt he cuvettes in the 1% HCl acid bath for at least 2 hours and wash them with plenty of Milli·Q (3 washes with 25 mL of Milli–Q) before using them again.

4.4. Fluorescence determination on board. 3–Dimensional Matrixes (EEMs) – Blank & Samples

- Excitation·emission matrixes consist of 22 successive emission spectra, starting from a wavelength of 240 nm and finishing in 450 nm at every 10 nm, and a series of emission spectra between 300 and 560 nm at every 2 nm.
- Each scan takes about 20 minutes.
- Note: a blank must always be run first so that you can subtract it later from your sample. Always run the blank and the sample using the same experiment file.
- Rinse the cuvette 3 times with sample water and fill it avoiding the bubbles formation.
- Settings should be for a 3D scan. Ex from 240 to 450 at 10 nm increments. Em from 300·560 nm at 2 nm increments. Ex and Em slits at 5 nm and no Rayleigh masking checked. The integration time is set to 0.25 s.

4.5. Data exporting

- Export your files as ASCII data that you can view with Excel or Matlab and save them in your directory.
- After the analysis session, put the 1·cm cuvette in the 1% HCl acid bath for at least 2 hours and wash them with plenty of Milli·Q (3 washes with 25 mL of Milli–Q) before using them

again. If the cuvette remains dirty, wash it with methanol (3 washes with 5 ml of Milli-Q) and later with plenty of Milli-Q (3 washes with 25 mL of Milli–Q).

- Rinse cuvette several (>10) times with Milli-Q water. Let dry a few minutes. Then place back in protective case and put away.
- Pour out Milli-Q water, put samples back into the refrigerator, and clean workspace.

4.6. Fluorescence data pre-treatment with the Fluoromax 4 software or Matlab

Before applying PARAFAC, a pre-treatment of the fluorescence data is needed. These procedures were done either with Fluoromax 4 or with Matlab software 7.6.0 (2008a).

- **Lamp and instrument correction (done with Fluoromax).** To correct for lamp spectral properties and the instrument-specific excitation and emission spectra and to be able to compare results with fluorescence reported in other studies, spectra were collected in signal-to-reference (Sc:Rc) mode.

  Excitation spectral corrections take into account deviations in the spectral output of the lamp and small imperfections in the instrument's components ability to transmit light. Similarly, every fluorometer is not capable of transmitting the sample emission (fluorescence) from the cuvette to the detector equally efficiently at all wavelengths.

  Another step of the data pretreatment is to handle the effects of Raman and Rayleigh scatter. They originate from the interaction between molecules in the solution and the incident light. The Rayleigh scatter is caused by molecules of the solute oscillating at the same wavelength as the incident light (1st order). It also emits light at twice the excitation wavelength (2nd order), and also at higher multiples of the wavelength [*Rinnan and Andersen*, 2005]. The 1st and 2nd Rayleigh scatter lines were cut off and the region of the EEMs below the Rayleigh peaks were set to zero because there is no fluorescence (emission wavelength > excitation wavelength) [see *Stedmon et al.,* 2003; *Andersen and Bro*, 2003; *Rinnan and Andersen*, 2005]. The Raman scatter is less intense than the Rayleigh scatter and emits light at longer wavelengths than the incident light. The majority of the Raman peak is removed by subtracting the pure water spectrum from the sample spectrum.

- **Inner-filter correction for 3D (EEMs) (done with Matlab).** Because of the low DOC concentration and absorbance of open ocean samples, no inner-filter effect correction was applied.

- **1st and 2nd order Rayleigh Masking (done with Matlab).** Rayleigh scatter bands (first order at each wavelength pair where Em = Ex ± band pass; second order at each wavelength pair where Em = 2 * Ex ± band pass) were trimmed. For instance, at Ex = 240 nm and a band pass = 20 nm, the 1st order Rayleigh masking would cut off the Em wavelengths from 260 nm downwards (Em = 240 + 20 nm) and then filled up with zeros the Em = Ex · 35 nm (Ex = 240 · 35 nm), and the 2nd order Rayleigh masking would cut off the Em wavelengths higher than 460 nm (Em = 2 * 240 · 20) and then filled up with zeros the Em = Ex + 35 nm.

- **Raman area normalization for 3D (EEMs) (done with Matlab).** All samples were normalized to the Raman area to account for lamp decay over time and to express the obtained values in Raman units [*Lawaetz and Stedmon*, 2009]. In our case, the procedure was done with the emission scan at 350 nm of the Milli-Q water blanks.

  The Raman area (RA) and its baseline correction were calculated following the Trapezoidal rule of integration [*Lawaetz and Stedmon*, 2009]. The selected range of the Raman area was between 381 and 426 nm.

$$\mathrm{RA} = \sum F_i - \frac{F_o + F_f}{2} - \frac{F_o + F_f}{2} (\lambda_f - \lambda_i)$$

  Where F_i is the sum of all the fluorescence intensities between 381 and 426 nm, F_o is the fluorescence intensity at 381 nm, F_f is the fluorescence intensity at 426 nm and λ_f is the wavelength at 426 nm and λ_i is the wavelength at 381 nm.

  Furthermore, in order to make sure that either the Raman normalization was done similarly in both the amino acid and humic regions of the EEM (1) and the Milli-Q water used to carry out the Raman normalization was of a good quality (2), daily scans were performed with:

(1) P-terphenyl that fluoresce in the amino acid region, between 310 nm and 600 nm exciting at 295 nm, and Tetraphenyl butadiene that fluoresce in the humic region, between 365 nm and 600 nm exciting at 348 nm, fixing the excitation and emission bandwidth at 5 nm and the integration time in 0.25 seconds. Fig. 1.1a demonstrates that the temporal evolution either of the Milli-Q water used on board and the reference substances of P-tephenyl and Tetraphenyl butadiene were similar, which confirms that the Raman normalization was successful in both the amino acid and the humic region of the excitation-emission matrix. Therefore, no extra correction was needed.

  The first three stations were removed due to some incoherencies in the measurements.

(2) A reference sealed Milli-Q scan between 365 nm and 450 nm exciting at 350 nm.
  The comparison between the reference sealed Milli-Q and the daily Milli-Q water allowed us to demonstrate that the Milli-Q water used on board was of a good quality (Fig. 1.1b of Chapter I).
  Furthermore, two scans of this reference sealed Milli-Q were measured at the beginning and at the end of the journey to check the instrument shift over the day.
  The fluorescence intensities experienced a slight shift along the day after the comparison of sMQ1 and sMQ2 (Fig. 1.1c of Chapter I).
  Note that there is some missing data of sMQ2 along the cruise.
  All reference substances were normalized as well as the excitation-emission matrixes in order to check their decay over time and make them comparable with other studies.

  Finally, we found that whereas the average variability between sMQ1 and sMQ2 during the total oceanic campaign was 1.62%, the average variability between the sMQ1 and Milli-Q

water throughout the campaign was only 0.81%. This demonstrates the fact that the daily instrument shifts are higher than the variations between different substances.

- **Blank Subtraction for 3D (EEMs) (done with Matlab).** Milli-Q water blanks were subtracted to remove Raman scattering. Seven blanks were identified as contaminated and they were replaced with the blank of the previous/forward day.

Appendix II.

Description of the water masses intercepted during the Malaspina circumnavigation

Table 1. Water types intercepted during the Malaspina circumnavigation, brief description of the domain, ocean basin and source point where they belong to, characteristics, and some references with more details about their origin and circulation.

Domain	Ocean basin	Name and acronym	Source	Characteristics	SWT	References
Central	Atlantic	Eighteen degrees water	Sargasso Sea	Mode water observed in the northern Sargasso Sea in winter, weakly stratified with temperature of ~18ºC and salinity of ~36.5.	EDW	Davis, 2013; Istoshin, 1961
Central	Atlantic	Subtropical Eastern North Atlantic Central water	Eastern North Atlantic Subtropical gyre	Mode waters defining the upper (15ºC) and lower (12ºC) limits of the subtropical ENACW formed between the area of the Azores and Portugal currents.	$ENACW_{12}$ $ENACW_{15}$	Harvey, 1982; Pollard and Pu, 1985; Ríos et al., 1992; Álvarez-Salgado et al., 2013
Central	Atlantic	Equatorial Atlantic Central Water (13ºC)	Eastern South Atlantic, near Namibia	Formed by mixing of low salinity water outcropped further south with overlying high salinity water. Transported by the South Equatorial current to the Equator and along the Brazilian coast by the North Brazil current.	13EqAtl	Tsuchiya et al., 1986
Central	Atlantic	South Atlantic Central Water (SACW)	Western Subtropical gyre	Series of mode waters formed south of the Angola-Benguela front (~18ºS).	$SACW_{12}$ $SACW_{18}$	Gordon and Bosley, 1991
Central	Indian	Indian Subtropical Mode Water	Indian Ocean Subtropical gyre	Present in the western subtropical gyre in summer. The distribution area was 27–38ºS, 25–50ºE.	$STMW_{I}$	Tsubouchi et al., 2009
Central	Indian	Indian Central water of 13 ºC	Indian Ocean Subtropical gyre	Mode water formed north of the Subtropical Front.	ICW_{13}	Orsi et al., 1995; Tsubouchi et al., 2009
Central	Pacific	South Pacific Subtropical Mode Water	Southwestern Pacific Ocean	Formed by deep mixing and cooling in the eastward-flowing waters of the East Australia Current.	$STMW_{SP}$	Roemmich and Bruce, 1992
Central	Pacific	South Pacific Central Water	South Pacific subtropical gyre	The Western South Pacific Central Water has θ–S properties identical to those of Indian and South Atlantic Central Water. Formed and subducted in the subtropical convergence between Tasmania and New Zealand. The transition to the fresher Eastern South Pacific Central Water is gradual.	$SPCW_{20}$	Tomczak and Godfrey, 2003
Central	Pacific	Thirteen degrees Equatorial Water	Either side of the Equator	Visible as a thermostad between 5ºS and 5ºN (12–14 ºC at 110ºW or 11–13ºC at 150ºW), associated with narrow eastward jets.	13EqPac	Fiedler and Talley, 2006
Central	Pacific	North Pacific Subtropical Mode Water	North Pacific subtropical gyre	Uniform thermostad of 16–17ºC centred at 150º–160ºE south of the Kuroshio Extension	$STMW_{NP}$	Suga, Takei and Hanawa, 1997
Central	Pacific	North Pacific Central	North Pacific	Thermostads with temperatures ranging from 10 to 13ºC at	CMW_{NP}	Suga, Takei and Hanawa,

		Mode Water	subtropical gyre	160ºW between the Kuroshio Extension and the Kuroshio bifurcation front		1997
Intermediate	Atlantic	Mediterranean Water	Gulf of Cadiz	Formed in the Gulf of Cadiz by entrainment of Eastern North Atlantic Central water on the high-salinity outflow from the Mediterranean Sea, spreads at 800–1300 m, S > 36 and θ ~ 11–12 ºC.	MW	Zenk, 1975; Ambar and Howe, 1979; Castro el al., 1998; Álvarez-Salgado et al., 2013
Intermediate	Atlantic, Indian, Pacific	Antarctic Intermediate Water	Pacific Ocean north of the Sub-Antarctic Front & Malvinas-Brazil Confluence.	Formed north of the Subantarctic Front (SAF) and east of the Drake Passage by ventilation of the Subantarctic Mode Water (SAMW) formed in the Southeast Pacific.	$AAIW_{5.0}$ $AAIW_{3.1}$	McCartney, 1982; Piola and Gordon, 1989; Talley, 1996
Intermediate	Indian, Pacific	Sub-Antarctic Mode Water (SAMW)	Southern Ocean and Southeastern Indian Ocean	Mode water formed by deep convection in late winter just north of the Sub-Antarctic Front (SAF).	SAMW	Tomczak and Leifrink, 2005; Sallee et al., 2006
Intermediate	Pacific	North Pacific Intermediate Water	North Pacific Ocean	Characterized by a salinity minimum (as low as 33.8) with low oxygen (50–150 μmol/kg) and low density (averaging 26.8 σ_θ). Formed by the mixing of different waters in the NW Pacific, in the Okhotsk Sea and at the Oyashio Front.	NPIW	Johnson, 2008; Bostock et al., 2010
Abyssal	Atlantic, Indian, Pacific	Circumpolar Deep Water	Antarctic Circumpolar Current	Also named Common Water, formed by mixing in the Antarctic Circumpolar current of mid-depth Indian, Pacific and Atlantic deep water with WSDW and NADW.	$CDW_{1.6}$	Montgomery et al., 1958; Georgi et al., 1981; Broecker et al., 1985
Abyssal	Atlantic, Indian, Pacific	North Atlantic Deep Water	North Atlantic Ocean	Carried into the South Atlantic by the Deep Western Boundary Current (DWBC). Characterized by salinity maximum and silicate minimum (4.6ºC) ; and θ–S discontinuity and oxygen maximum (2.0 ºC). Defined at their entry in the South Atlantic Ocean off South America.	$NADW_{4.6}$ $NADW_{2.0}$	Wüst, 1935; Speer and McCartney, 1991; Friedrichs et al., 1994
Abyssal	Atlantic, Indian, Pacific	Antarctic Bottom Water	Weddell Sea	Formed by mixing of Weddell Sea Bottom water (WSBW) and Warm Deep water (WDW) (1:1), nutrient rich and oxygen poor. Defined at its entry in the South Atlantic Ocean.	AABW	Reid, 1989; Onken, 1995; Arhan et al., 1999

Table 2. Mixing groups defined to solve the OMP analysis along the Malaspina circumnavigation. The number of samples comprised within each group (n) is shown.

Ocean	Domain	Group	Sub-Group	Water type	n
Atlantic	Central	1	a	$ENACW_{12}$, $ENACW_{15}$	1(
			b	$ENACW_{15}$, EDW	1(
			c	$NADW_{4.6}$, MW, $ENACW_{12}$	1(
			d	$NADW_{4.6}$, $AAIW_{5.0}$, $ENACW_{12}$	2(
			e	$SACW_{12}$, $SACW_{18}$	2(
			f	13EqAtl, $SACW_{18}$	3
			g	$NADW_{4.6}$, $AAIW_{5.0}$, $SACW_{12}$	1(
			h	$NADW_{4.6}$, $AAIW_{5.0}$, 13EqAtl	2(
	Intermediate	2		$NADW_{2.0}$, $NADW_{4.6}$, MW	2(
	Abyssal	3	a	$NADW_2$, $CDW_{1.6}$, $NADW_{4.6}$	8(
			b	$CDW_{1.6}$, $NADW_{4.6}$, $AAIW_{3.1}$	2(
			c	$NADW_{4.6}$, $AAIW_{3.1}$, $AAIW_{5.0}$	1(
Atlantic Indian	Abyssal	4		AABW, $CDW_{1.6}$, $NADW_{2.0}$	9(
Indian	Central	5	a	$SAMW$, ICW_{13}	5(
			b	ICW_{13}, $STMW_t$	1(
	Intermediate Abyssal	6	a	$AAIW_{3.1}$, $CDW_{1.6}$, $NADW_{2.0}$	2(
			b	$AAIW_{3.1}$, $CDW_{1.6}$, SAMW	5(
Pacific	Central	7	a	13EqPac, $SPCW_{20}$	7
			b	CMW_{NP}, $STMW_{NP}$	7
	Intermediate Abyssal	8	a	$CDW_{1.6}$, $AAIW_{3.1}$, SAMW	2(
			b	$CDW_{1.6}$, NPIW, 13EqPac	13
			c	NPIW, CMW_{NP}, 13EqPac	3(
			d	$SAMW_{SP}$, $STMW_{SP}$	3
	Abyssal	9		$CDW_{1.6}$, $AAIW_{3.1}$, AABW	5(
Total					**80**

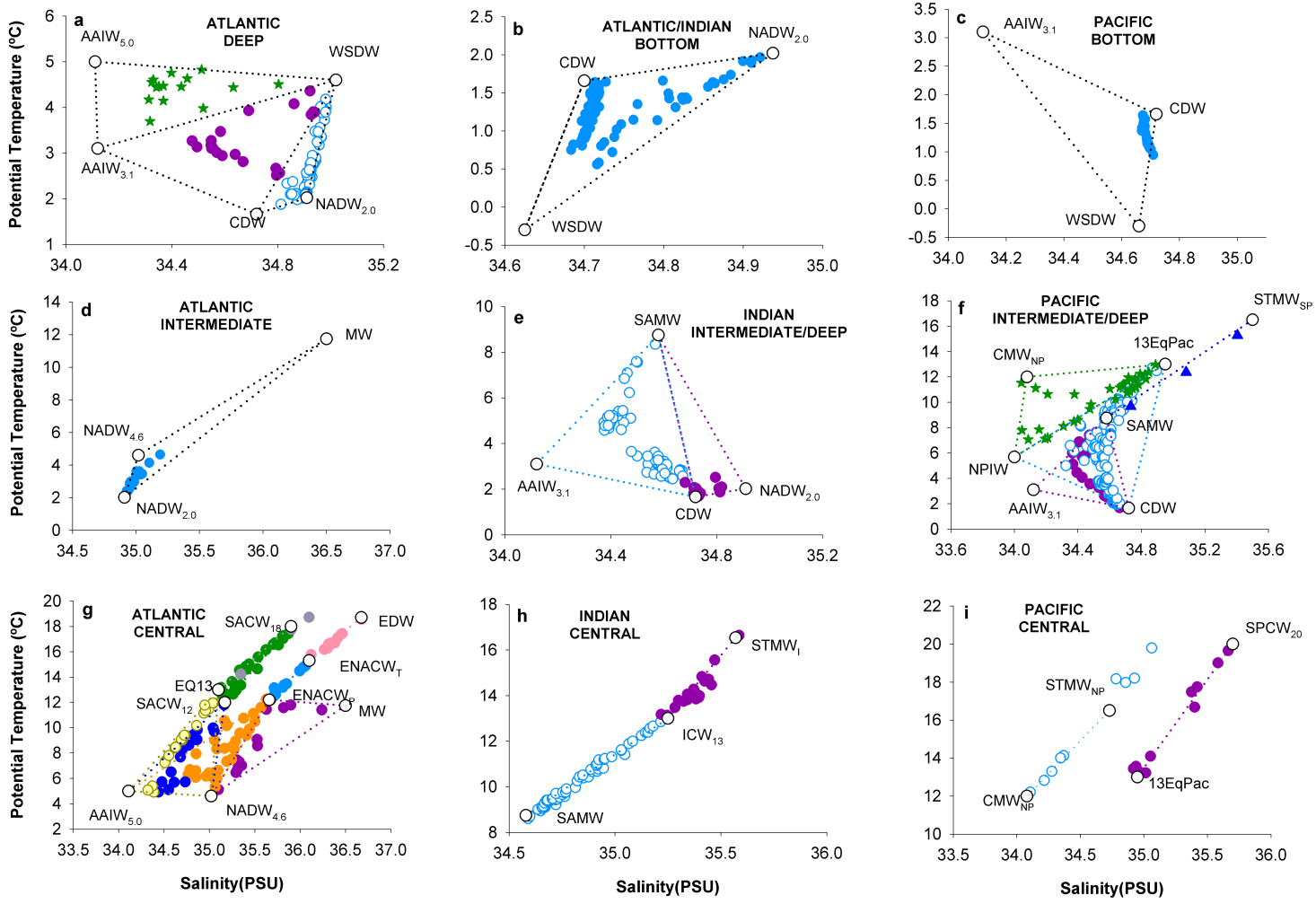

Fig. 1. Potential temperature and salinity (θ/**S**) diagrams of the Malaspina 2010 circumnavigation samples for the nine mixing groups introduced in the water mass analysis.

Appendix III.

Chromophores Toolbox Tutorial

You can consult the Toolbox and manual at the webpage: (http://ecologia.ugr.es/pages/herramientas/toolbox-matlab?lang=en).

Contents

1. Introduction to the Chromophores·Toolbox
2. Chromophores·Toolbox Interface and key concepts
    2.1. Chromophores identification analysis
    2.2. Ch·UV
    2.3. Ch·VIS
    2.4. Chromophores·Toolbox components
    2.5. Chromophores·Toolbox interface
3. Getting started
4. Inputs to the Chromophores·Toolbox: Import data
5. Chromophores·Toolbox analysis
6. Outputs from the Chromophores·Toolbox

1. Introduction to the Chromophores-Toolbox

Absorption coefficients at specific wavelengths, a_λ, are used as proxies of the concentration of CDOM and a wide variety of spectral indices and slopes have provided key information on the origin and molecular structure of CDOM. As the characterisation of specific chromophores is still lacking in the literature we have developed a toolbox to obtain distinct chromophores within CDOM datasets.

The toolbox is adapted to obtain two distinct chromophores centred around 300 nm (named Ch-UV) and 415 nm (named Ch-VIS) by fitting the measured absorption coefficient spectra to the Röttgers and Koch's equation [*Röttgers and Koch*, 2012] and statistically isolating the absorption signal attributable to these chromophores from the standard decreasing exponential curve.

2. Chromophores-Toolbox Interface and key concepts

2.1. Chromophore identification analysis

In order to locate and quantify the absorption chromophores centred around 300 nm (Ch-UV) and 415 nm (Ch-VIS), we developed this Matlab toolbox that obtains the parameters that best fit (least squares sense) the following equation [Breves *et al*., 2003; *Röttgers and Koch,* 2012]:

$$a_\lambda = b_1 \mathrm{e}^{-b_2(\lambda-\lambda_0)} + b_3 \frac{1}{\sigma\sqrt{2\pi}} \mathrm{e}^{\frac{-(\lambda-\lambda_0)^2}{2\sigma^2}} + b_4 \qquad (1)$$

The equation was fitted within different wavelength ranges for each chromophore. The **first and third terms** of the equation models the typical exponential decay of any CDOM spectrum with increasing wavelength. It consists of a pre-exponential term ($\mathbf{b_1}$), an exponential slope ($\mathbf{b_2}$), and an absorption parameter to correct for offsets in the absorption at longer wavelength ($\mathbf{b_4}$). The **second term** is a Gaussian function to model the absorption spectra of the UV or VIS chromophore, with $\mathbf{b_3}$ being the height at the reference wavelength $\boldsymbol{\lambda_o}$ of the chromophore and $\boldsymbol{\sigma}$ the width of the Gaussian function, respectively. The absorption coefficient of the UV or VIS chromophore at their respective λ_o ($\boldsymbol{a_{\text{Ch-UV}}}$ or $\boldsymbol{a_{\text{Ch-VIS}}}$) is calculated as $b_3 \frac{1}{\sigma\sqrt{2\pi}}$. $\mathbf{b_1}$, $\mathbf{b_2}$, $\mathbf{b_3}$, $\mathbf{b_4}$, $\boldsymbol{\lambda_0}$ and $\boldsymbol{\sigma}$ are optimised with the Matlab toolbox.

2.2. Ch-UV

To obtain the parameters of the UV chromophore equation (1) is applied to the wavelength range from **250 to 400 nm**. This chromophore is related with the absorption of nitrate in the UVB region of the spectrum [*Johnson and Coletti*, 2002] or may be caused by the absorption of deoxygadusol, a mycosporine-like precursor synthesized via bacteria, cyanobacteria, phytoplankton, macroalgae (red, brown and green), plants and fungi with an absorption maximum at 294 nm [*Shick and Dunlap*, 2002].

2.3. Ch-VIS

To obtain the parameters of the VIS chromophore equation (1) is applied to the wavelength range from **350 to 600 nm**. A plausible source for the absorption of the VIS chromophore is the respiratory enzyme cytochrome c oxidase. This enzyme presents an absorption maxima around 410 to 415 nm and is one of the most important components of cellular respiration, which reduces molecular oxygen to water coupled to the pumping of protons across the mitochondrial or bacterial membrane [*Yoshikawa et al.,*

2011].

2.4. Chromophores-Toolbox components

The Chromophores-Toolbox is a GUI (Graphical User Interface)-based Matlab toolbox. The Chromophores-Toolbox consists of three parts: (1) a main script related to the Matlab GUI interface (CHROMOPHORES.fig), which is called '***CHROMOPHORES.m***'. This scripts works as a connection (set of commands) between the interface components and the calculus done by Matlab; (2) A folder called **'*functions*',** which contains the Matlab functions that do the fitting analysis (*Ch_UV_fit.m, Ch_VIS_fit.m, rottgers_koch.m*) and the scripts that sends information to the interface log-window (*WriteinWindow.m*); and (3) a folder called **'Help',** which contains information to help the user with the toolbox (this tutorial).

2.5 Chromophores-Toolbox interface

The Chromophores-Toolbox interface is divided in two main modules, (1) one for the UV chromophore and (2) another for the visible chromophore (see Fig. 1). Each module is divided, in turns, into the toolbox inputs (initial parameters), outputs (end parameters) and a "GO" command.

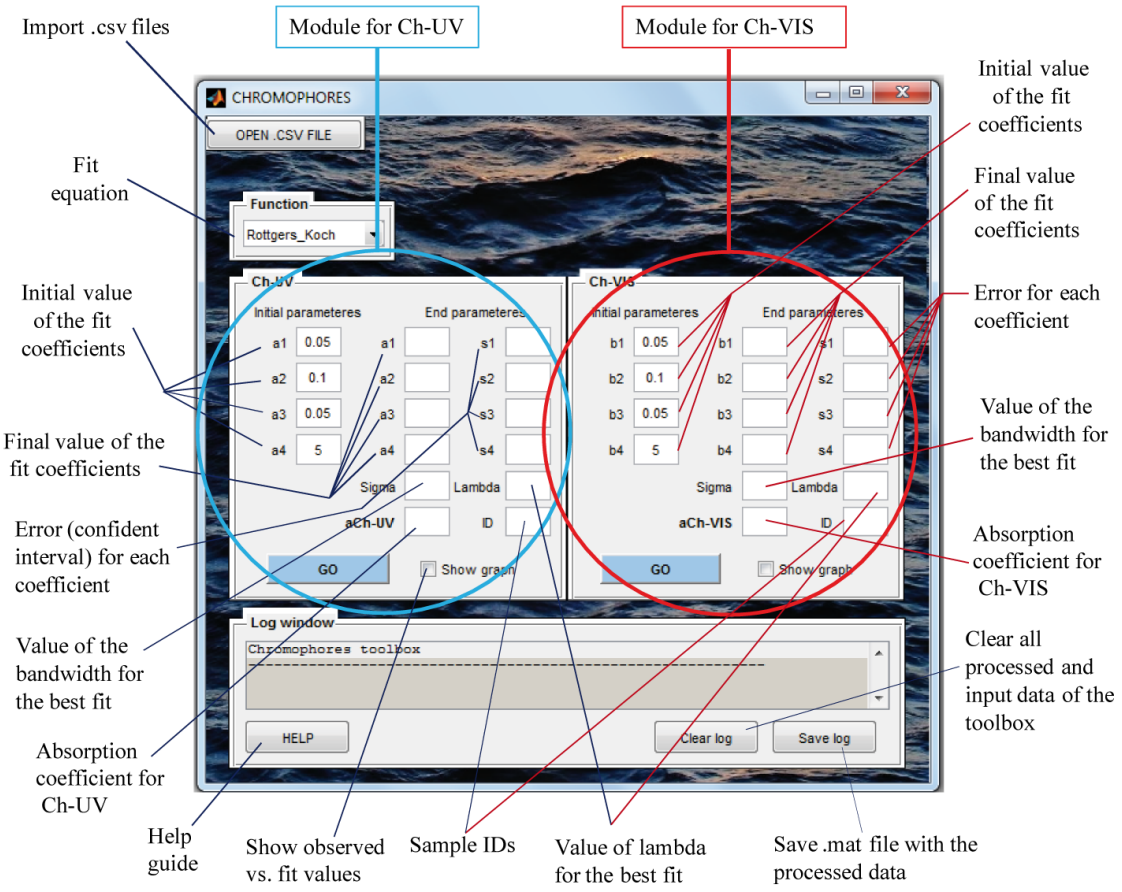

Fig. 1. Chromophores-Toolbox interface

Inputs to the toolbox are the initial value of the a_1-a_4 and b_1-b_4 fitting coefficients for the Ch-UV and Ch-VIS, respectively. These coefficients correspond to the initial value of coefficients *b* in Eq. 1. These initial values are set by default to be $a_1 = 0.05$, $a_2 = 0.1$, $a_3 = 0.05$ and $a_4 = 5$ (the same for the *b* coefficients, see

Fig. 1) but can be changed by the user, before running the analysis, by clicking on the respective coefficient box and introducing a new initial value. Other inputs to the toolbox are the range of '*lambda*' λ_o and '*sigma*' σ (Eq. 1 and Fig. 1) to be tested. For Ch-UV, λ_o is allowed to vary within the range 280:5:320 nm and for Ch-VIS, λ_o is allowed to vary within the range 390:5:440 nm. σ is allowed to vary within the range 15:5:30 nm for both the Ch-UV and Ch-VIS. Although these ranges are fixed in the toolbox, and thus, there is not a direct access to them through the GUI interface, the user can change them by opening the script *CHROMOPHORES.m* and by modifying the values of L (wavelength) and D (bandwidth) in lines 408 and 409 for Ch-VIS and lines 1024 and 1025 for Ch-UV of that .m file.

Outputs of the toolbox (end parameters) consist of the final value (best fit) of the a_1-a_4 and b_1-b_4 fitting coefficients and their respective errors (confident intervals) s_1-s_4, together with the coefficient of determination R^2, the value of λ_o (box *Lambda*), σ (box *Sigma*) and the absorption coefficient of the chromophore –$a_{Ch\text{-}UV}$ or $a_{Ch\text{-}VIS}$– for which the best fit was achieved. The corresponding sample ID (e.g. depth, time, name of the sample) is shown in the box *ID.*

By clicking the '*GO*' button, the fit analysis is run. If the box *Show Graphs* is ticked the toolbox will display a graph showing the measured absorption coefficients together with the best-fit line for each evaluated sample (e.g. Fig. 2).

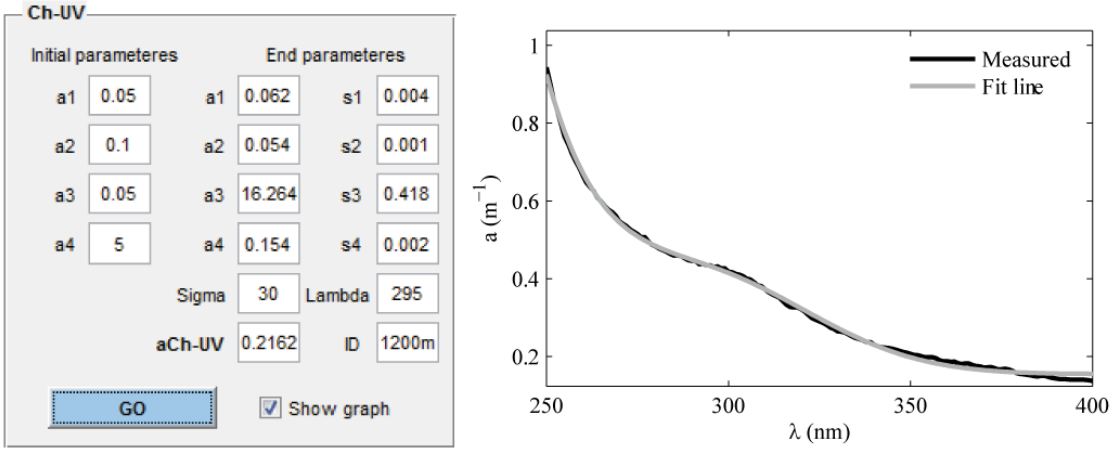

Fig. 2. Example of the interface outputs and graph for the measured and calculated absorption coefficients

The interface also contains a button called '***OPEN .CSV FILE***' to import one or several .CSV files with the measured absorption coefficients (see Section 4 for details), a box called '*FUNCTIONS*' where the fit equation is defined (Eq. 1), a '*Log Window*' where the toolbox displays each of the actions that is carrying out, a '***HELP***' button which contains the basic information to use the Chromophores-Toolbox (this tutorial), a '***Clear log***' button, which erases all the information (imported data and outputs) and a '***Save log***' button, which allows the user to save the outputs in .mat format of the last analysis carried out by the toolbox.

3. Getting started

The Chromophores-Toolbox can be downloaded from 'http://ecologia.ugr.es/pages/herramientas/toolbox-matlab?lang=en'. Once the file is unzipped it is

important to maintain the structure (distribution) of the files within the folder *Chromophores_Toolbox* for a correct function of the toolbox. Once the user has chosen the directory where to locate the toolbox there are two ways to run it:

(1) Open Matlab and in *Current Folder* set the path to the toolbox: Eg: *Current Folder*: C:\User\Chromophores_Toolbox. Once Matlab is in the same directory as the toolbox, write 'CHROMOPHORES' in the Command Window. The GUI interface should open.

(2) Open the CHROMOPHORES.m file in the *Matlab Editor* and run the script (press the play button or go to Debug-Run CHROMOPHORES.m). The GUI interface should open.

It is important not to change the Matlab directory while the toolbox is being used. Otherwise an error would appear in the Matlab command window.

4. Inputs to the Chromophores-Toolbox: Import data

The Chromophores-Toolbox is set to load and read .csv files with information on the measured wavelengths and CDOM absorption coefficients. The first column of the .csv file should contain the wavelength values and the subsequent columns, the absorption coefficient values for each of the samples. The first row should contain identification for each sample (sample ID). This sample ID could be a measured depth, time, etc. Fig. 3 shows an example of an input .csv. It is important to keep the distribution shown in Fig. 3. The analysis will be done no matter the resolution of the sample, i.e. the separation between consecutive values of wavelengths (e.g. each 1 nm, each 5 nm, etc). An example of input .csv file can be downloaded from ('http://ecologia.ugr.es/pages/herramientas/toolbox-matlab?lang=en').

	A	B	C	D	E	F	G	H	I
1		4000m	3000m	2500m	1700m	900m	470m	400m	200m
2	250	0.0532	0.0453	0.0475	0.0469	0.0469	0.0467	0.042	0.0482
3	251	0.0513	0.0435	0.0458	0.0451	0.0452	0.0451	0.0402	0.0465
4	252	0.0501	0.0424	0.0445	0.0438	0.0437	0.0436	0.0388	0.0453
5	253	0.0485	0.0406	0.0428	0.0422	0.0422	0.042	0.0372	0.0436
6	254	0.0475	0.0395	0.0416	0.0411	0.0411	0.0407	0.036	0.0424
7	255	0.0464	0.0386	0.0408	0.0404	0.04	0.04	0.0351	0.0417
8	256	0.0454	0.0374	0.0395	0.0391	0.0389	0.0387	0.0341	0.0406
9	257	0.0443	0.0365	0.0386	0.038	0.0376	0.0378	0.0328	0.0391
10	258	0.0438	0.0358	0.0379	0.0374	0.0374	0.0371	0.0322	0.0386
11	259	0.0431	0.035	0.0371	0.0366	0.0364	0.0365	0.0315	0.0379
12	260	0.0423	0.0344	0.0365	0.0362	0.0357	0.0358	0.031	0.0373
13	261	0.0417	0.0336	0.0356	0.035	0.0351	0.0353	0.0302	0.0365
14	262	0.0412	0.0329	0.0348	0.0345	0.0343	0.0345	0.0295	0.036
15	263	0.0408	0.0322	0.0346	0.0339	0.0338	0.0338	0.0288	0.035
16	264	0.0407	0.032	0.0341	0.0337	0.0339	0.0335	0.0289	0.0351
17	265	0.0392	0.0314	0.033	0.0327	0.0326	0.0326	0.0276	0.0341
18	266	0.0383	0.0301	0.0322	0.032	0.0323	0.032	0.027	0.0333
19	267	0.0383	0.0305	0.0323	0.0319	0.0318	0.0319	0.0267	0.0329
20	268	0.0378	0.0295	0.0314	0.0312	0.0312	0.0313	0.0262	0.0323
21	269	0.0374	0.0293	0.0312	0.0306	0.0308	0.031	0.0259	0.0323
22	270	0.0366	0.0284	0.0302	0.0298	0.0306	0.0302	0.0246	0.031
23	271	0.0354	0.0277	0.0292	0.0288	0.0296	0.0288	0.0238	0.03
24	272	0.0354	0.0267	0.0288	0.0287	0.0291	0.0287	0.0242	0.0298
25	273	0.0349	0.0263	0.0288	0.0281	0.0285	0.0281	0.0234	0.0293
26	274	0.0341	0.026	0.0277	0.0275	0.0283	0.0281	0.023	0.0287
27	275	0.0335	0.0254	0.0271	0.0267	0.0275	0.0269	0.0224	0.0275

Fig. 3. Example of .csv file to be loaded by the toolbox

The user can import one or several .csv files. In case the user loads several .csv files, the analysis for Ch·UV and Ch·VIS will be carried out for all samples within a given .csv file and all the imported .csv files.

5. Chromophores-Toolbox analysis

The Chromophores·Toolbox fits the data in x (wavelengths λ) and y (absorption coefficients) to the function in Eq. 1., with the fitting method of non linear squares, where b_1·b_4 are the coefficients to estimate, and λ_o and σ are the problem parameters. In order to start the fitting iterations, an initial value of the fit coefficients should be given. These initial values are set by default to be b_1 = 0.05, b_2 = 0.1, b_3 = 0.05 and b_4 = 5, but they can be directly changed by the user by changing the initial value of these parameters in the interface (see section 2.5). In order to obtain results, which are realistic in terms of a physical interpretation, the coefficients b_1 and b_3 (the height at λ_o) are forced to be ≥ 0 in the model. By default all coefficients have an upper·limit value of 20 and a lower·limit value of ·10 (except for b_1 and b_3 which is 0). These limits, however, can be modified by the user in lines 393 to 399 and lines 1010 to 1016 (example below) in the '*CHROMOPHORES.m'* file for Ch·VIS and Ch·UV, respectively. The toolbox will show a warning message if the calculated value of a_3 or b_3 is too close (<0.001) to their upper limit, suggesting the user to increase the upper limit for these coefficients.

```
%2. Fit Conditions:
     optionsb = fitoptions('Method','NonlinearLeastSquares',... ;
                           'StartPoint',b0,...
                           'Lower',[0 -10 0 -10],...
                           'Upper',[20 20 20 20],...
                           'Maxiter',1000,...
                           'MaxFunEvals',1000);
```

6. Outputs from the Chromophores-Toolbox

The Chromophores·Toolbox generates two folders, one for each chromophore under study, called '*Ch_UV*' and '*Ch_VIS'*, in the same directory as the imported .csv files, and where the outputs related to the UV chromophore and the visible chromophore will be located, respectively. By default, the Chromophores·Toolbox generates one .csv file after each analysis called '*Parameters_ChUV_[FileName]$_1$_[FileName]$_{end}$.csv'* or '*Parameters_ChVIS_[FileName]$_1$_[FileName]$_{end}$.csv'*, depending on the chromophore, with the information on the fitting coefficients, the goodness of the fitting, the final values of λ_o and σ, and the calculated value for $a_{Ch\text{-}UV}$ or $a_{Ch\text{-}VIS}$. [*FileName*]$_1$ and [*FileName*]$_{end}$ are the names of the first and the last imported .csv files. For example, for three imported files called '*Example1.csv'*, '*Example2.csv'* and '*Example3.csv'*, the Chromophores·Toolbox would generate a .csv file called '*Parameters_ChUV_Example1_Example3.csv*' after the analysis of the UV chromophore. If only one .csv file is imported, the Chromophores·Toolbox will generate a .csv file called '*Parameters_ChVIS_[FileName].csv'*. Fig. 4 shows an example of the '*Parameters_ChUV_[FileName]$_1$_[FileName]$_{end}$.csv'* generated by the Chromophores· Toolbox. Note that the

'*Parameters_ChUV_[FileName]$_1$_[FileName]$_{end}$.csv*' is generated for each 'GO' command. Thus, it will contain the information for several imported files if more than one .csv file has been loaded into the toolbox.

	A	B	C	D	E	F	G	H	I	J	K	L	M
1	Example1.csv												
2	Sample ID	a1	a2	a3	a4	sa1	sa2	sa3	sa4	R2	Lambda(nm	Sigma(nm)	aCh-UV(1/m)
3	4000m	0.4163774	0.0249467	0.4254075	0.0540878	0.0075177	0.0004444	0.2175398	0.0039217	0.9993193	285	15	0.0113142
4													
5	Example2.csv												
6	Sample ID	a1	a2	a3	a4	sa1	sa2	sa3	sa4	R2	Lambda(nm	Sigma(nm)	aCh-UV(1/m)
7	4000m	0.0539624	0.0565319	12.853368	0.0910721	0.002831	0.0012817	0.3435305	0.0018264	0.9984967	295	30	0.1709251
8	3000mR	0.0520134	0.0564041	13.19717	0.1143315	0.002885	0.001355	0.349053	0.0018516	0.998365	295	30	0.175497
9	2000m	0.056018	0.0629067	15.892677	0.1225537	0.0036107	0.0017577	0.4159339	0.002102	0.9981089	290	30	0.211342
10	1200m	0.061799	0.0539483	16.263709	0.1543773	0.0036596	0.0014437	0.4184411	0.0021198	0.9982788	295	30	0.216276
11	600m	0.0789688	0.0509089	16.04699	0.18835	0.0040352	0.001241	0.4307794	0.0020442	0.9986868	295	30	0.2133941
12	370m	0.1188646	0.0383593	11.538134	0.220477	0.0051962	0.000943	0.4644906	0.0019384	0.999007	300	30	0.153435
13	320m	0.119889	0.0407392	11.602415	0.1354628	0.0058734	0.0011548	0.5007417	0.0017863	0.9989714	295	30	0.1542898
14	200m	0.0954071	0.046578	12.841082	0.2021197	0.0055953	0.0014118	0.5426603	0.0023044	0.9982674	295	30	0.1707617
15	150m	0.1905735	0.0350771	10.735813	0.1430252	0.0141942	0.0018141	0.9944459	0.002784	0.9986966	290	30	0.1427657
16	120m	0.438854	0.0221344	1.7511749	0.1425604	0.0088459	0.0004351	0.2268303	0.0051522	0.9993324	290	15	0.0465745
17	100m	0.6370804	0.0225964	1.6038449	0.1538181	0.0049764	0.0001909	0.1400158	0.0028435	0.999811	280	15	0.0426561
18	67m	0.3897257	0.0378461	1.8475391	0.0809438	0.0160487	0.0013242	0.5906189	0.0050372	0.9978379	280	15	0.0491374
19	40m	0.4448933	0.0349249	1.3397668	0.1098756	0.0144798	0.0010113	0.5165056	0.0050853	0.9983023	280	15	0.0356326
20	3m	0.3610886	0.0394763	1.394694	0.0570373	0.0173741	0.001573	0.6494296	0.0051314	0.9973361	280	15	0.0370935
21													

Fig. 4. Example of '*Parameters_ChUV_[FileName]$_1$_[FileName]$_{end}$.csv*' generated by the Chromophores Toolbox. In this example two .csv files called '*Example1.csv*' (with one sample) and '*Example2.csv*' (with 14 samples) were loaded into the toolbox.

It is important to keep the output .csv files closed while the toolbox is doing the analysis. Otherwise an error would appear in the Matlab Command Window.

Alternatively, after each analysis ('GO' command), the Chromophores·Toolbox gives the option to save output data in *.mat* format. After each analysis a question dialog box will open, asking whether the user would like to save the output data in *.mat* format (Fig. 5).

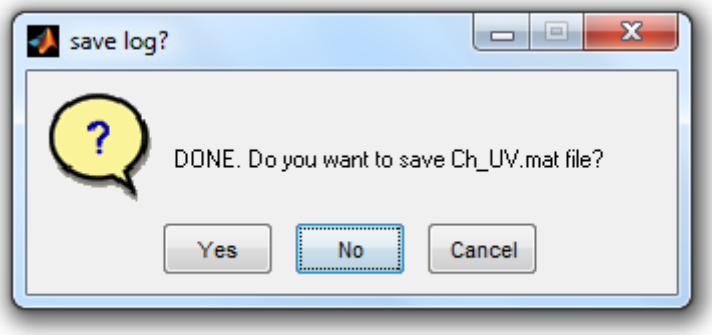

Fig. 5. Question dialog box after the analysis for the Ch·UV

If the user presses '*Yes*', a '*Ch_UV.mat*' file or a '*Ch_VIS.mat*' will be generated and the user will select the directory to save it. This .mat file will contain the following information (Fig. 6):

- Variable *Coeffs*: This contains all the variables in the '*Constants_Ch_UV.csv*' *(or* '*Constants_Ch_VIS.csv*' *)* for each sample and each imported *.csv* file.
- Variable *SampleID*: all the sample IDs

- Variable *x00*: Range of wavelengths for which absorption coefficients were measured (x-variable) for each sample and .csv file (λ in Eq 1). Units = nm.
- Variable *a*: Best fit of the absorption coefficients (Eq. 1) for each sample and .csv file (y-variable). Units = m^{-1}.
- Variable *aChUVrange or aChVISrange*: Absorption coefficients for the Ch-UV range or Ch-VIS range, respectively (term 2 in Eq. 1). Units = m^{-1}.
- Variable *aChUV* or *aChVIS*: absorption coefficients for the UV or visible chrompohores. Units = m^{-1}.
- Variable *Names*: Name of each imported .csv file.

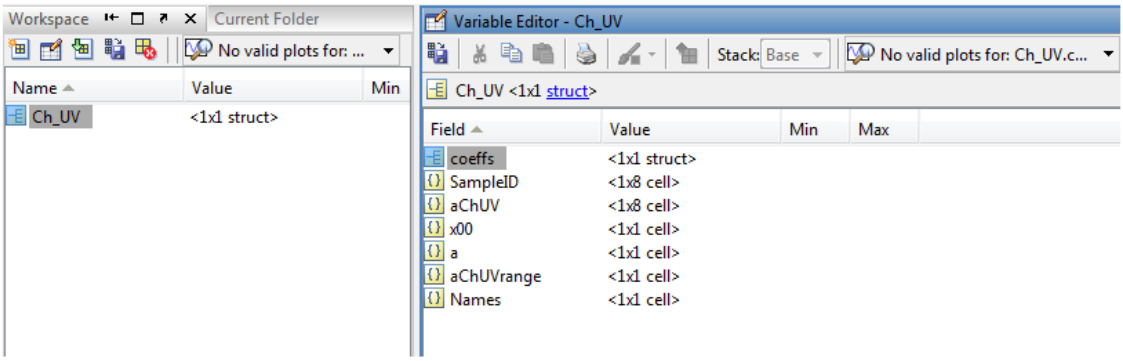

Fig. 6. Example of data in a *Ch_UV.mat* file.

If the user presses '*No*' or '*Cancel*' in the question dialog box, there is still the possibility to save the *.mat* file by clicking on the interface '*Save log*' button. The question dialog box will reopen.

Appendix IV.

Conversion of Raman units into carbon units

Conversion of fluorescence RU of the humic-like components (C1 and C2) into carbon units is complicated as the chemical composition and structure of these materials are essentially unknown. Average fluorescence intensities of C1 and C2 in the dark global ocean were 12.2 (± 0.3) 10^{-3} and 9.2 (± 0.2) 10^{-3} RU, respectively. We obtained a mixed humic-like component C1+2 by combining the EEMs of C1 and C2 in these proportions. The resulting EEM of C1+2 was compared with the EEM of the terrestrial humic isolates available from the International Humic Substances Society (IHSS): Nordic Lake humic (IHSS 1R105H) and fulvic acid (IHSS 1R105F), Waskish Peat fulvic (IHSS 1R107F) and humic acid (IHSS 1R107H), Suwannee River fulvic acid (IHSS, 1R101F), Pahokee peat fulvic acid (IHSS 1R103H) and Pony Lake fulvic acid (IHSS 1R109F). We observed that the EEM of C1+2 could be modelled as a combination of the EEM of the Suwannee River (SRFA) and Pahokee peat (PPFA) fulvic acids in proportions 25% and 75%, respectively. Therefore, we obtained the corresponding conversion factors of these two isolates from the slopes of the linear regressions of fluorescence against dissolved organic carbon of 5 standards of each isolate prepared in milli-Q water (carbon concentration range 83–1667 µM). In this case, fluorescence data were inner filter corrected before the regressions were done. The final conversion factor, resulting from combining the corresponding factors of SRFA and PPFA in proportions 25% and 75%, was 425 ± 66 µM C RU^{-1} (at Ex = 270 and Em = 464 nm).

To allow conversion of fluorescence Raman units (RU) of tryptophan- and tyrosine-like components (C3 and C4) into carbon and nitrogen units, tryptophan (Fluka) (4-point calibration curve, concentration range 7–150 nM of C) and tyrosine (Fluka) (4-point calibration curve, concentration range 8–168 nM of C) were diluted in milli-Q water. The corresponding conversion factors were 16.9 ± 0.1 µM C RU^{-1} (3.08 ± 0.01 µM N RU^{-1}) at Ex/Em 290 nm/340 nm for tryptophan, and 31.5 ± 0.2 µM C RU^{-1} (3.50 ± 0.02 µM N RU^{-1}) at Ex/Em 270 nm/310 nm for tyrosine.

The global carbon content in fluorescence components C1+2 (average fluorescence intensity, 14.5 (± 0.3) 10^{-3} RU), C3 (4.5 (± 0.3) 10^{-3} RU) and C4 (4.9 (± 0.4) 10^{-3} RU) was calculated as $f \cdot \sum_i VOL_i \cdot < Fmax_i > /100$ where f is the corresponding conversion factor: 425 ± 66 µM C RU^{-1} for C1+2, 16.9 ± 0.1 µM C RU^{-1} for C3 and 31.5 ± 0.2 µM C RU^{-1} for C4. Furthermore, the corresponding NPF rates were calculated as f x NFP. Finally, the portions of the dissolved organic carbon (DOC) in the form of humic substances (C1+2), tryptophan (C3) and tyrosine (C4) were calculated dividing $f \cdot \sum_i VOL_i \cdot < Fmax_i > /100$ by the average concentrations of DOC in the dark global ocean: 40 µmol C kg^{-1} [*Hansell*, 2009]. We used the same formulas to calculate the global nitrogen content in fluorescence components C3 and C4, with f being 3.08 ± 0.01 µM N RU^{-1} for C3 and 3.50 ± 0.02 µM N RU^{-1} for C4 and the average concentration of DON in the dark global ocean 2.9 µmol N kg^{-1} [*Bronk*, 2002].

We obtained that the humic-like materials represent about 15 ± 3 % (equivalent to 102 ± 18 Pg C) of the bulk DOC in the dark ocean, and the resultant *in situ* production of humic-like substances in carbon units is 0.2 ± 0.1 Pg C yr^{-1}. Tyrosine-like materials represented 0.39% (equivalent to 2.6 ± 0.2 Pg C) of the bulk DOC and 0.60% (equivalent to 0.34 ± 0.03 Pg N) of the bulk dissolved organic nitrogen (DON), and tryptophan-like compounds 0.19% (equivalent to 1.3 ± 0.1 Pg C) and 0.48% (equivalent to 0.27 ± 0.02 Pg N) of the bulk DOC and DON, respectively.

Appendix V.

Average profiles of the environmental parameters that contribute on FDOM variability in the surface ocean.

-Salinity

-Temperature

-Aparent oxygen utilization (AOU)

-Chlorophyll-a

-Fluorophore C1

-Fluorophore C2

-Fluorophore C3

-Fluorophore C4

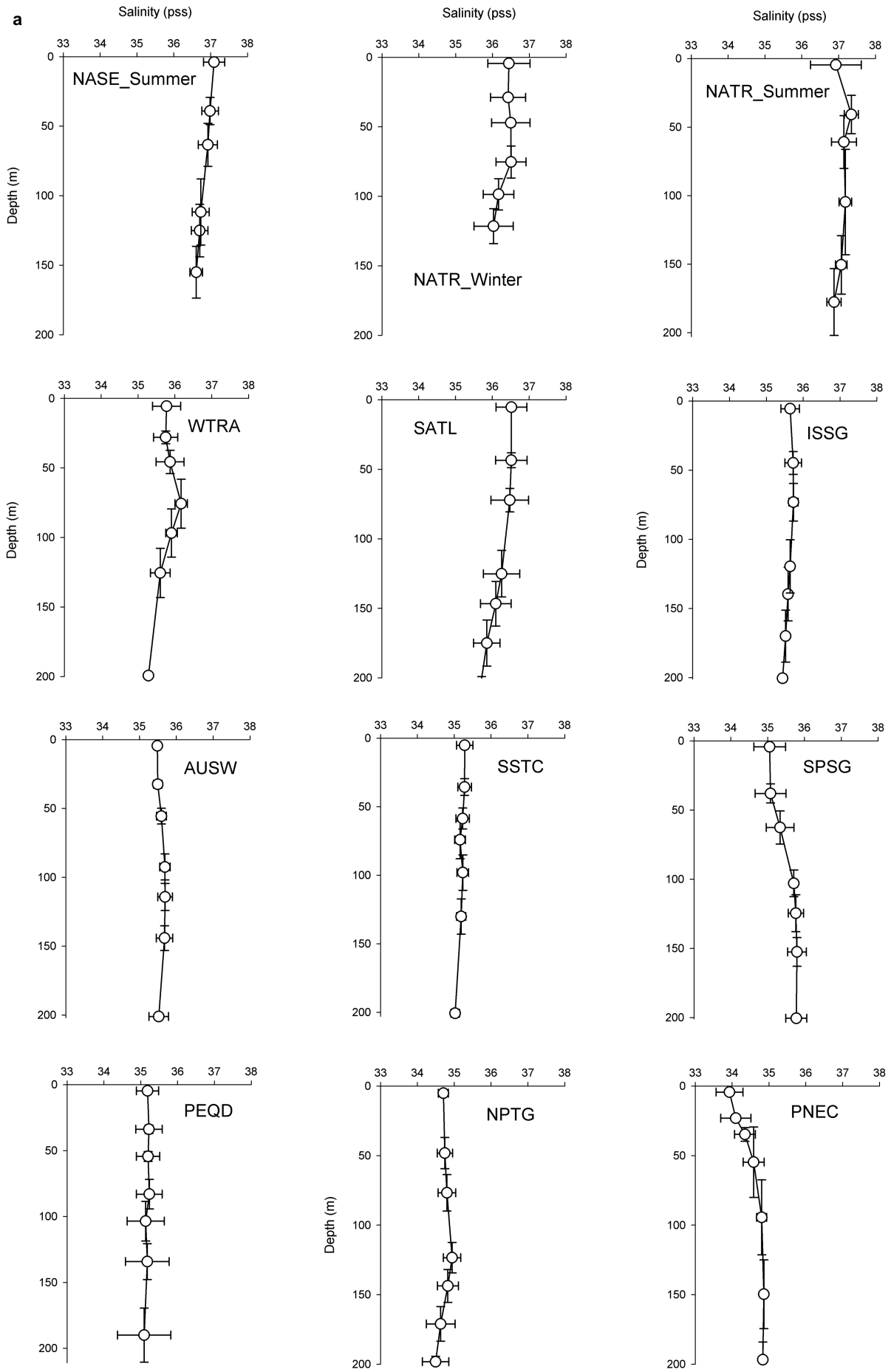
a
Salinity (pss)
33 34 35 36 37 38
0 50 100 150 200
Depth (m)
NASE_Summer
NATR_Winter
NATR_Summer
WTRA
SATL
ISSG
AUSW
SSTC
SPSG
PEQD
NPTG
PNEC

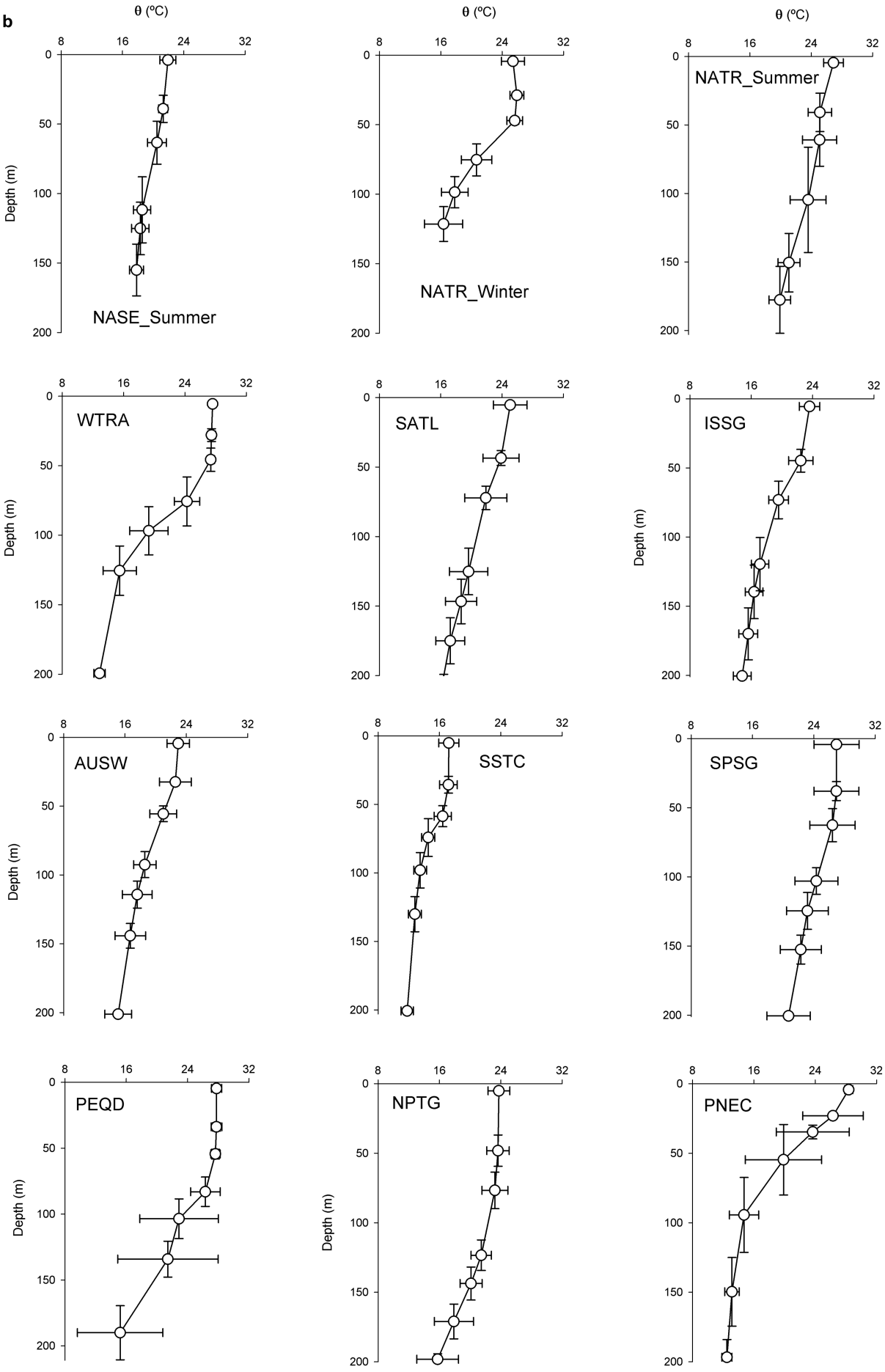
b
θ (ºC)
8
16
24
32
0
50
100
150
200
Depth (m)
NASE_Summer
NATR_Winter
NATR_Summer
WTRA
SATL
ISSG
AUSW
SSTC
SPSG
PEQD
NPTG
PNEC

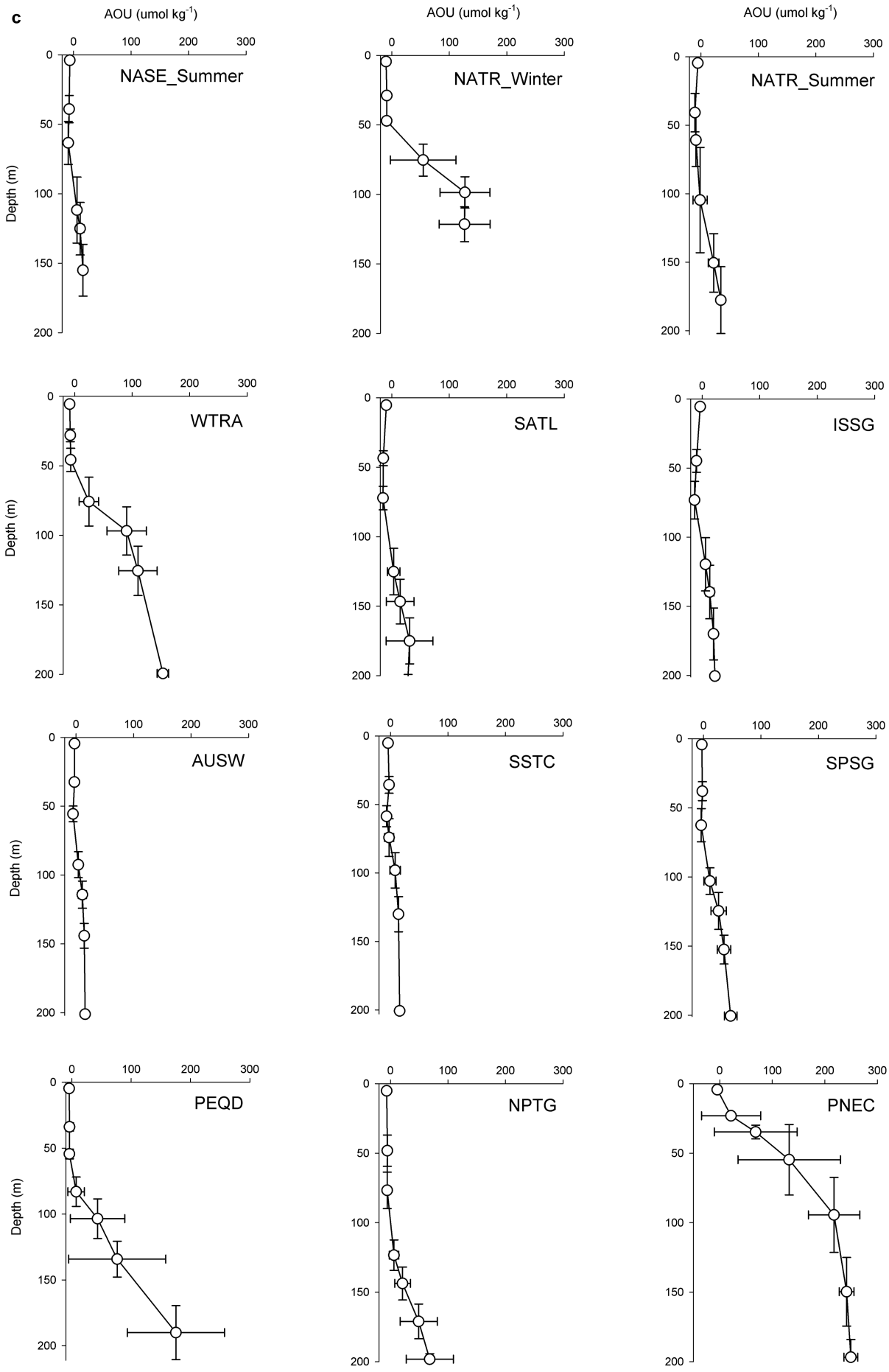
c
AOU (umol kg-1)
Depth (m)
NASE_Summer
NATR_Winter
NATR_Summer
WTRA
SATL
ISSG
AUSW
SSTC
SPSG
PEQD
NPTG
PNEC
0
50
100
150
200
300

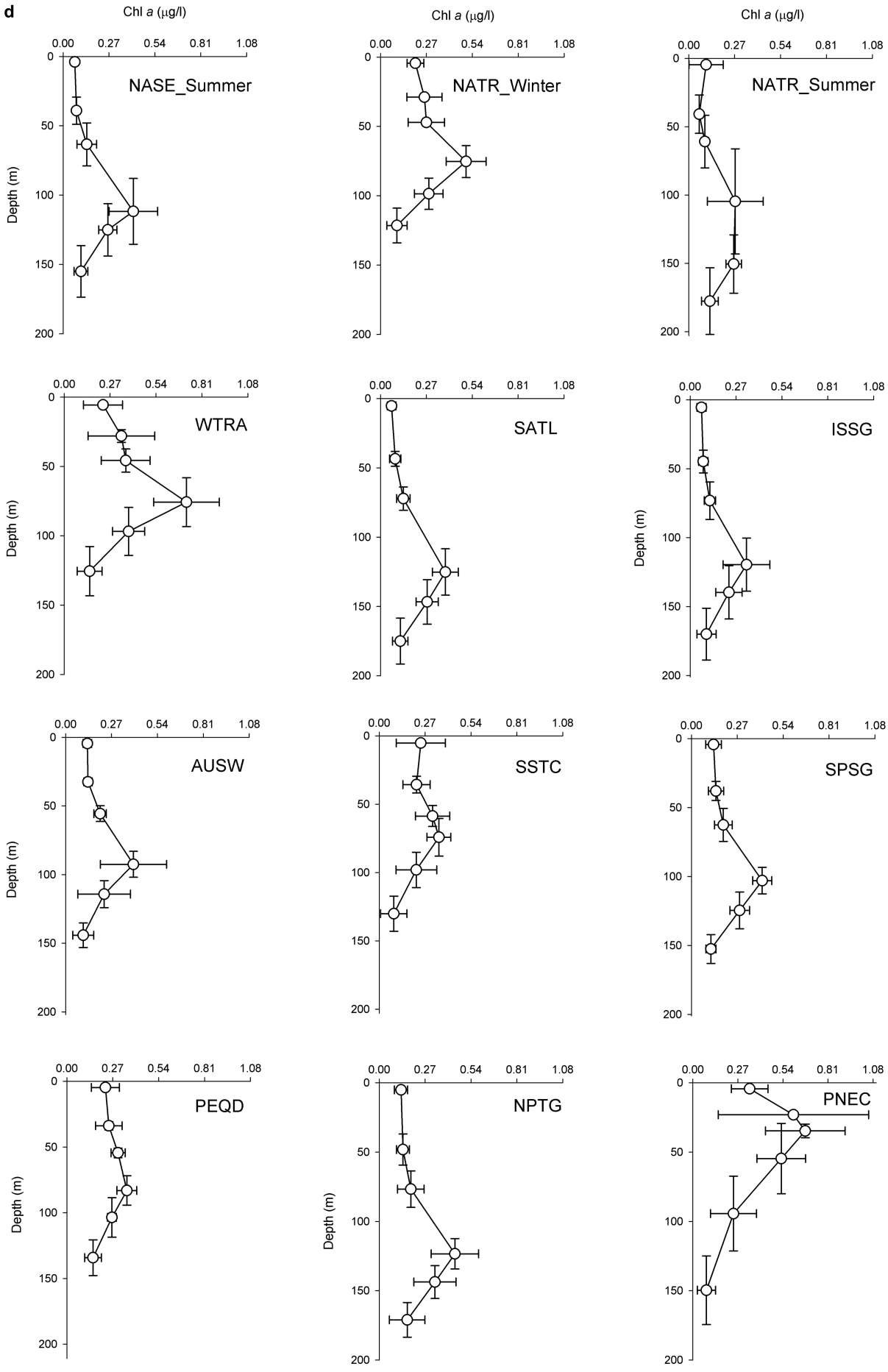
d
Chl a (μg/l)
0.00 0.27 0.54 0.81 1.08
Depth (m)
0 50 100 150 200
NASE_Summer
NATR_Winter
NATR_Summer
WTRA
SATL
ISSG
AUSW
SSTC
SPSG
PEQD
NPTG
PNEC

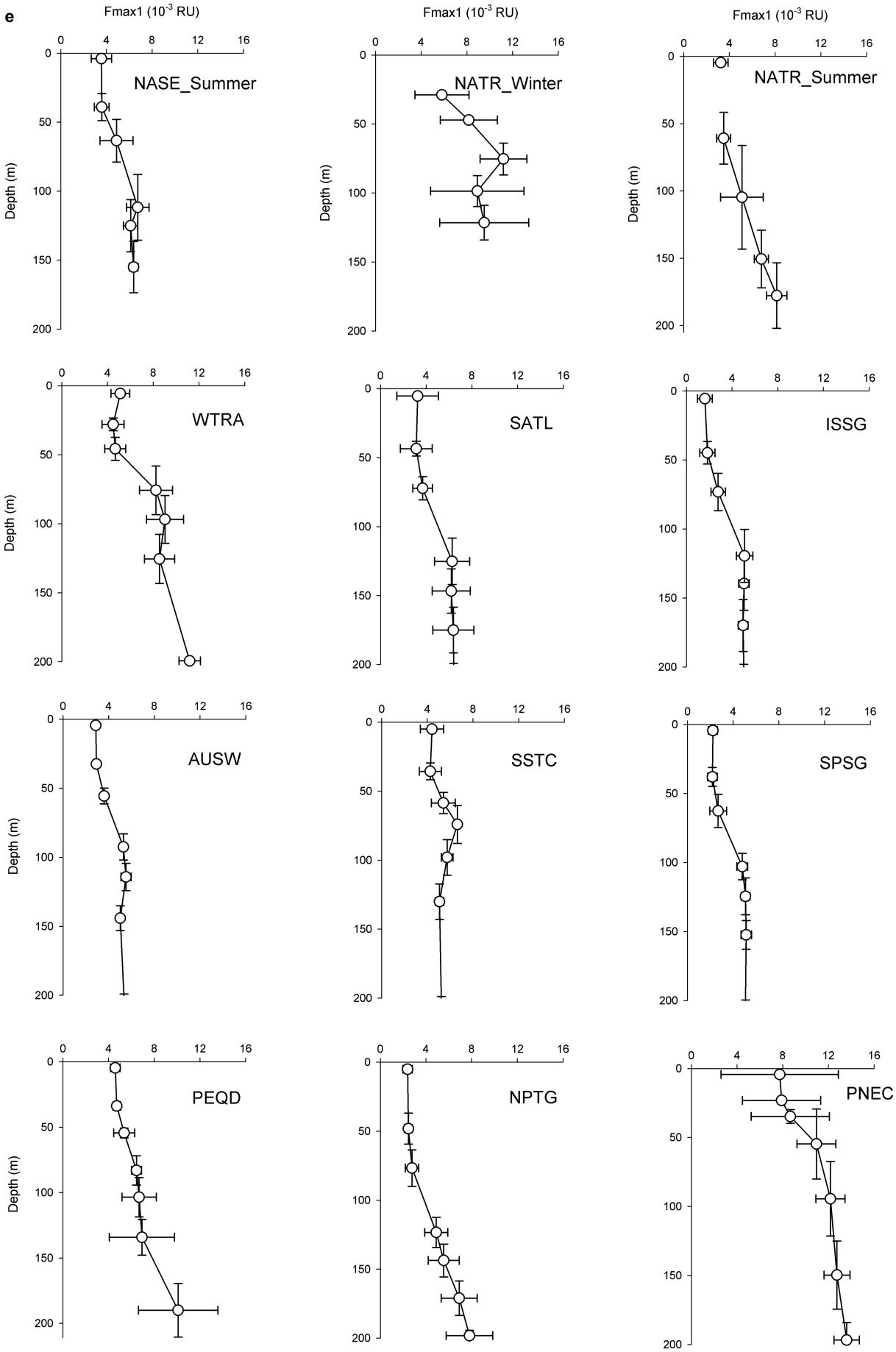
e
Fmax1 (10^{-3} RU)
Depth (m)
NASE_Summer
NATR_Winter
NATR_Summer
WTRA
SATL
ISSG
AUSW
SSTC
SPSG
PEQD
NPTG
PNEC

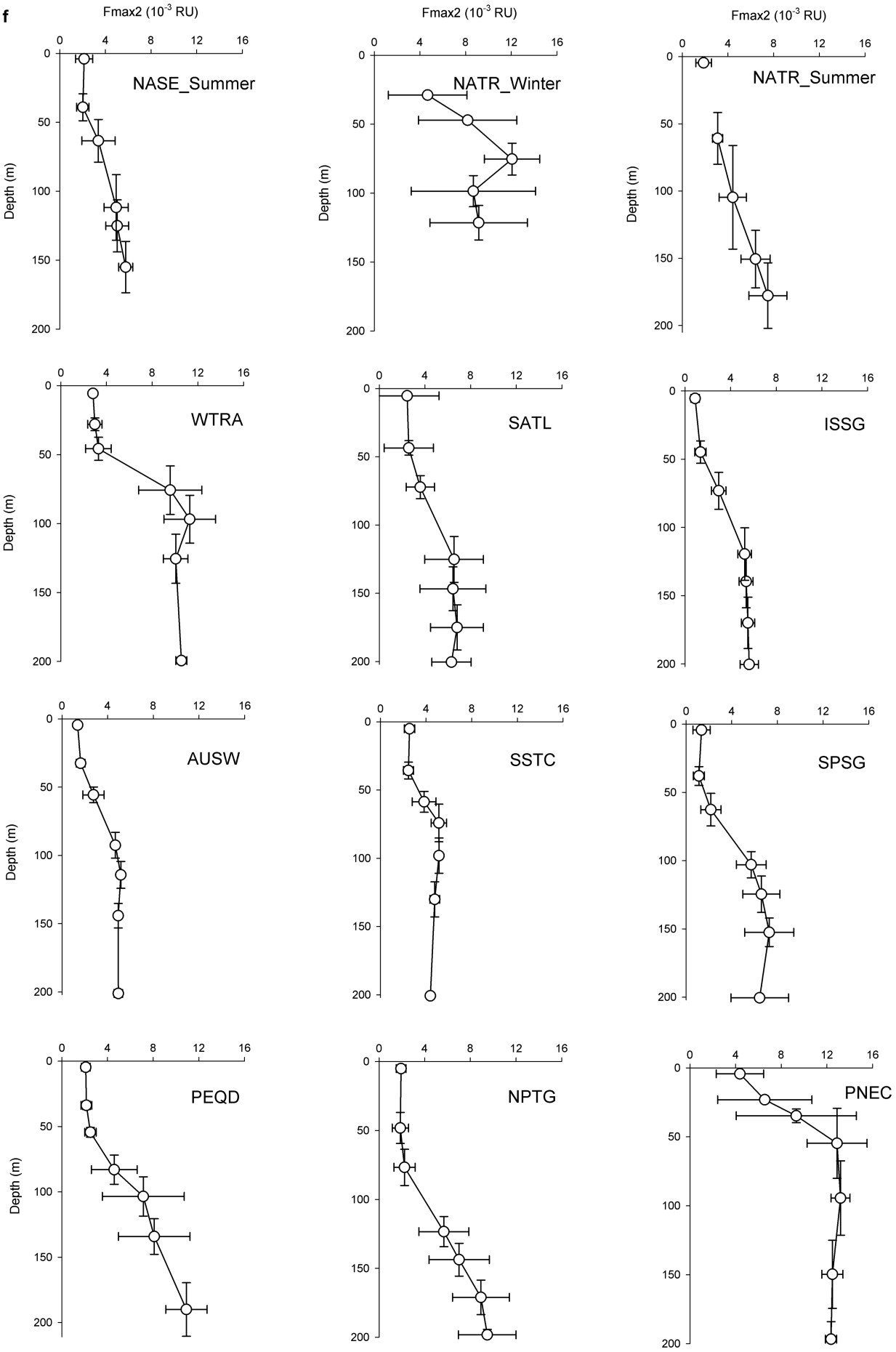
f
Fmax2 (10^{-3} RU)
Depth (m)
NASE_Summer
NATR_Winter
NATR_Summer
WTRA
SATL
ISSG
AUSW
SSTC
SPSG
PEQD
NPTG
PNEC

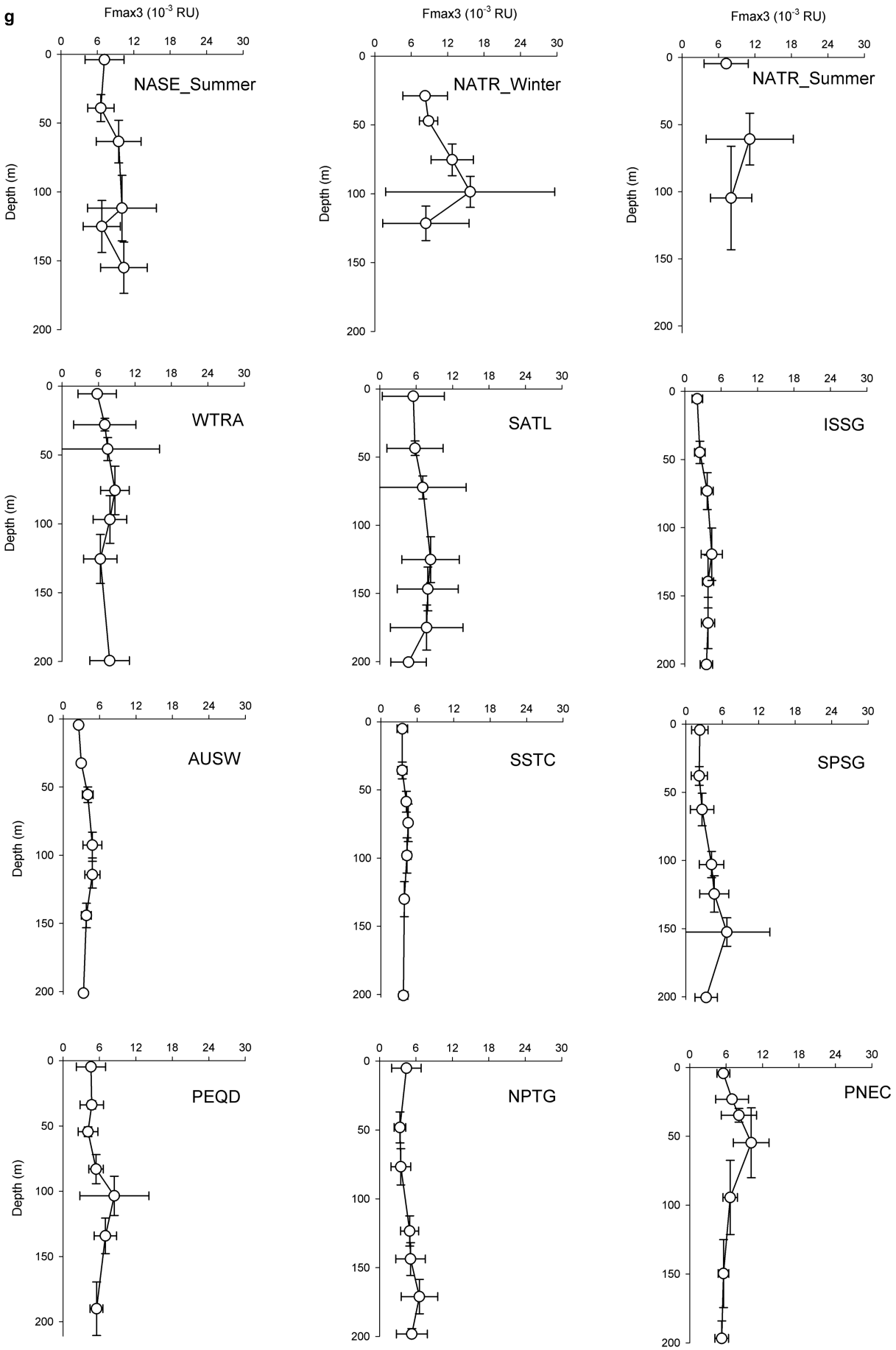
g
Fmax3 (10-3 RU)
Depth (m)
NASE_Summer
NATR_Winter
NATR_Summer
WTRA
SATL
ISSG
AUSW
SSTC
SPSG
PEQD
NPTG
PNEC

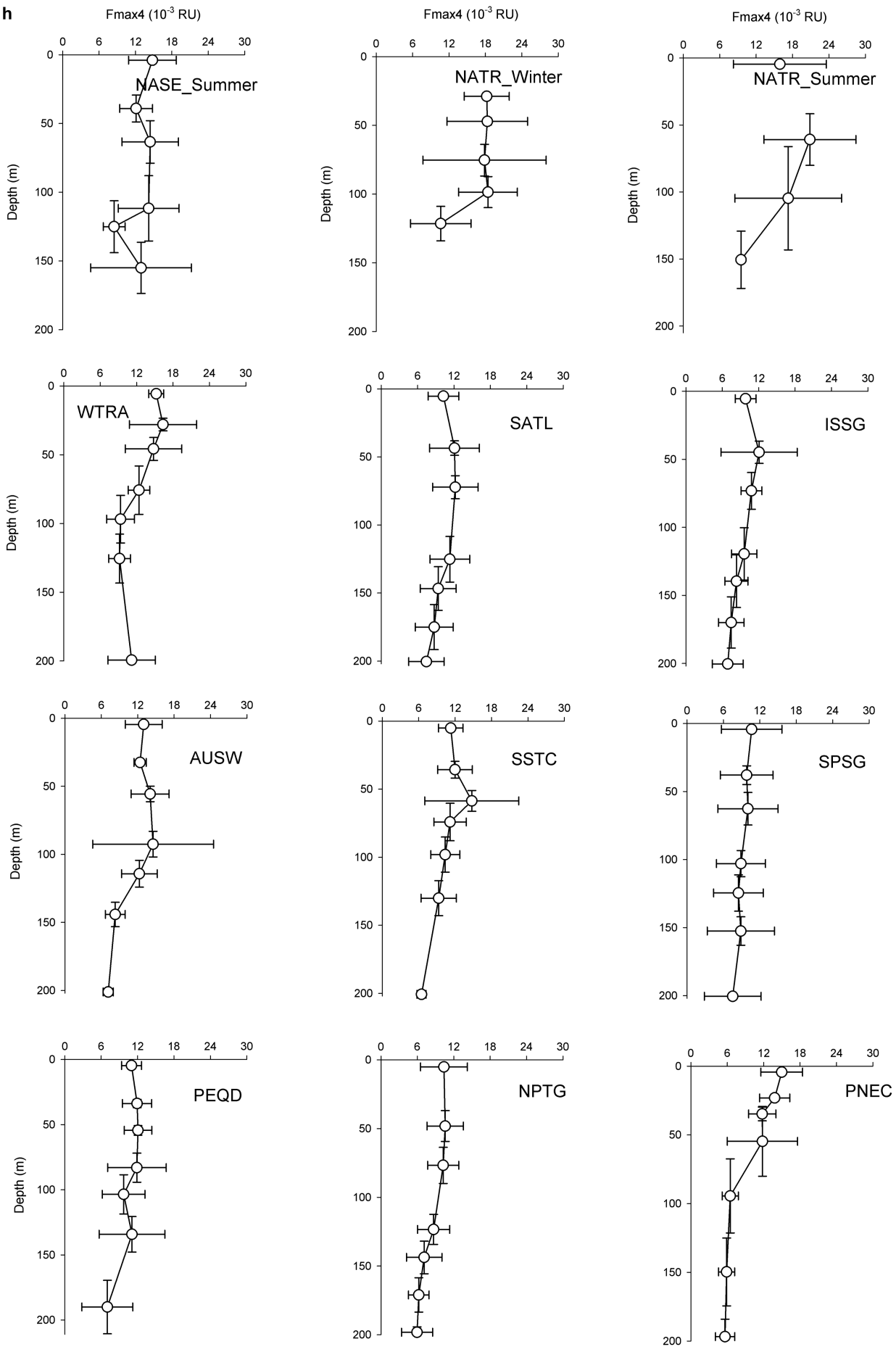
h
Fmax4 (10^{-3} RU)
Depth (m)
NASE_Summer
NATR_Winter
NATR_Summer
WTRA
SATL
ISSG
AUSW
SSTC
SPSG
PEQD
NPTG
PNEC

Fig. 1. Average profiles of the environmental parameters (a) potential temperature, θ, (b) salinity, S, (c) apparent oxygen utilization, AOU, and (d) chlorophyll *a*, Chl *a*, and the four fluorescent components (e) Fmax1, (f) Fmax2, (g) Fmax3 and (h) Fmax4 for each biogeographic province. The bars are the standard deviations of the data at each sampling depth. Note that provinces with less than four stations were not considered.

References

Aiken, G. R., McKnight, D. M., Wershaw, R. L., MacCarthy, P., 1985. An introduction to humic substances in soil, sediment, and water. In *Humic Substances in Soil, Sediment, and Wa- ter: Geochemistry, Isolation and Characterization*, eds Aiken, G. R., McKnight, D. M., Wershaw, R. L., MacCarthy, P., Wiley, New York, pp. 1-9.

Albert, D. B., Taylor, C., Martens, C. S., 1995. Sulfate reduction rates and low-molecular-weight fatty-acid concentrations in the water column and surficial sediments of the Black-Sea. *Deep-Sea Res. Pt. I*, 42, 1239–1260.

Álvarez, M., Pelejero, C., Calvo, E., Fernandez-Vallejo, P., Movilla, J., Lopez Sanz, A., Fernández Guallart, E., Horstkotte, B., Companys, B., 2012. Muestreo y análisis de oxígeno disuelto (O_2) en agua de mar. Expedición de circunnavegación Malaspina 2010: Cambio global y exploración de la biodiversidad del océano. In *Libro blanco de métodos y técnicas de trabajo oceanográfico*. E. Moreno-Ostos. Madrid, CSIC, 79–92.

Álvarez-Salgado, X.A., Álvarez, M., Brea, S., Mèmery, L., Messias, M.J., 2014. Mineralization of biogenic materials in the water masses of the South Atlantic Ocean. II: Stoichiometric ratios and mineralization rates, *Prog. Oceanogr., 123*, 24-37.

Álvarez-Salgado, X. A., Nieto-Cid, M., Álvarez, M., Pérez, F. F., Morin, P., Mercier, H., 2013. New insights on the mineralization of dissolved organic matter in central, intermediate, and deep water masses of the northeast North Atlantic, *Limnol. Oceanogr., 58*, 681-696.

Ambar, I., Howe, M. R., 1979. Observations of the Mediterranean outflow – I Mixing in the Mediterranean outflow. *Deep-Sea Res*, 26, 535–554.

Amon, R. M. W., Budéus, G., Meon, B., 2003. Dissolved organic carbon distribution and origin in the Nordic Seas: exchange with the Arctic Ocean and the North Atlantic. *J. Geophys. Res.*, 108, 3221, doi: 10.1029/2002JC001594.

Amon, R. M. W, Benner, R., 1996. Bacterial utilization of different size classes of dissolved organic matter. *Limnol. Oceanogr.,* 41, 41–51.

Anderson, T. R., Williams, P. J., 1999. A one-dimensional model of dissolved organic carbon cycling in the water column incorporating combined biological-photochemical decomposition. *Global Biogeochem. Cycles*, 13, 337–349.

Andersson, J. H., Wijsman, J. W. M., Herman, P. M. J., Middelburg, J. J., Soetaert, K., Heip, C., 2004. Respiration patterns in the deep ocean, *Geophys. Res. Lett., 31*, L03304.

Andrew, A. A., Del Vecchio, R., Subramaniam, A., Blough, N.V., 2013. Chromophoric dissolved organic matter (CDOM) in the Equatorial Atlantic Ocean: Optical properties and their relation to CDOM structure and source, *Mar. Chem., 148*, 33-43, doi:10.1016/j.marchem.2012.11.001.

Arhan, M., Heywood, K. J., King, B.A., 1999. The deep waters from the Southern Ocean at the entry of the Argentine Basin, *Deep-Sea Res.,* II, 46, 475–499.

Arístegui, J., Agustí, S., Duarte, C. M., 2003. Respiration in the dark ocean, *Geophys. Res. Lett., 30*(1041), http://dx.doi.org/10.1029/2002GL016227.

Arndt, S., Jørgensen, B. B., LaRowe, D. E., Middelburg, J. J., Pancost, R. D., Regnier, P., 2013. Quantifying the degradation of organic matter in marine sediments: a review and synthesis. *Earth-Sci. Rev.,* 123, 53–86.

Arrhenius, S.Z., 1889. Über die reaktionsgeschwindigkeit bei der inversion von rohrzucker durch säuren, *Phys. Chem., 4*, 226–248.

Arrieta, J. M., Mayol, E., Hansman, R. L., Herndl, G. J., Dittmar, T., Duarte, C. M., 2015. Dilution limits dissolved organic carbon utilization in the deep ocean, *Science*, 348, 6232, 331-333, doi: 10.1126/science.1258955.

Azam, F., Smith, D. C., Steward, G. F., Hagström, Å, 1993. Bacteria-Organic Matter Coupling and Its Significance for Oceanic Carbon Cycling. *Microb. Ecol.*, 28, 167-179.

Azam, F., Fenchel, T., Field, J. G., Gray, J.S., Meyer-Reil, L. A., Thingstad, F., 1983. The ecological role of water-column microbes in the sea. *Mar.e Ecol. Prog. Ser.*, 10, 257–263.

Bandaranayake, W.M., Des Rocher, A., 1999. Role of secondary metabolites and pigments in the epidermal tissues, ripe ovaries, viscera, gut contents and diet of the sea cucumber Holothuria atra, *Marine Biology,* 133, 163–169.

Bastviken, D. J., Persson, L, Odham, G., Tranvik, L., 2004. Degradation of dissolved organic matter in oxic and anoxic lake water. *Limnol. Oceanogr.*, 49(1), 109–116.

Bastviken D, Olsson, M., Tranvik, L., 2003. Simultaneous measurements of bacterial production and organic carbon mineralization in oxic and anoxic lake sediments. *Microbial Ecology* 46: 73–82.

Benner, R., Amon, R. M. W., 2015. The size-reactivity continuum of major bioelements in the ocean. *Annu. Rev. Mar. Sci.*, 7, 185–205.

Benner, R., Herndl, G.J., 2011. Bacterially derived dissolved organic matter in the microbial carbon pump, *Microbial carbon pump in the ocean*, eds Jiao N., Azam F., Sanders S., Science/AAAS, Washington, pp 46–48.

Benner, R., Louchouarn, P., Amon, R. M. W., 2005. Terrigenous dissolved organic matter in the Arctic Ocean and its transport to surface and deep waters of the North Atlantic. *Global Biogeochem. Cycles,* 19, GB2025, doi: 10.1029/2004GB002398.

Benner, R., Biddanda, B., 1998. Photochemical transformations of surface and deep marine dissolved organic matter: effects on bacterial growth. *Limnol. Oceanogr.*, 43, 1373–1387.

Benner, R., Pakulski, J. D., Mccarthy, M., Hedges, J. I., Hatcher, P. G., 1992. Bulk chemical characteristics of dissolved organic-matter in the ocean. *Science,* 255, 1561–1564.

Benson, B.B., Krauss, D. Jr., 1984. The concentration and isotopic fractionation of oxygen dissolved in freshwater and seawater in equilibrium with the atmosphere, *Limnol. Oceanogr.,* 29, 620–632.

Blasco, D., de la Fuente Gamero, P., Galindo, M., 2012. Muestreo y análisis de nutrientes inorgánicos disueltos en agua de mar. Expedición de circunnavegación Malaspina 2010: Cambio global y exploración de la biodiversidad del océano. In *Libro blanco de métodos y técnicas de trabajo oceanográfico*. E. Moreno-Ostos. Madrid, CSIC, 107–121.

Bidle, K. D., Falkowski, P. G., 2004. Cell death in planktonic, photosynthetic microorganisms, *Nature Reviews Microbiology*, 2, 643-655.

Bittar, T. B., Stubbins, A., Vieira, A. A. H., Mopper, K., 2015. Characterization and photodegradation of dissolved organic matter (DOM) from a tropical lake and its dominant primary producer, the cyanobacteria Microcystis aeruginosa.

Blough, N. V., Del Vecchio, R., 2002. Chromophoric DOM in the coastal environment. In *Biogeochemistry of marine dissolved organic matter*, eds Hansell, D. A., Carlson, C. A., Academic Press, San Diego, pp 509–546.

Boden, T., Marland, G., Andres, R., 2011. Global CO_2 emissions from fossil-fuel burning, cement manufacture, and gas flaring: 1751-2008 (accessed at 2011.11.10). *Oak Ridge National Laboratory, U. S. Department of Energy, Carbon Dioxide Information Analysis Center, Oak Ridge, Tenn., U. S. A. In* IPCC, 2013. Climate Change 2013: The Physical Science Basis. Contribution of Working Group I to the Fifth Assessment Report of the Intergovernmental Panel on Climate Change, eds. Stocker, T.F., Qin, D., Plattner, G.-K., Tignor, M., Allen, S.K., Boschung, J., Nauels, A., Xia, Y., Bex, V., Midgley, P.M., Cambridge University Press, Cambridge, United Kingdom and New York, NY, USA, 1535 pp.

Boehme, J., Coble, P., Conmy, R., Stovall-Leonard, A., 2004. Examining CDOM fluorescence variability using principal component analysis: seasonal and regional modeling of three-dimensional fluorescence in the Gulf of Mexico. *Mar. Chem.*, 89, 3–14.

Bostock, H. C., Opdyke, B. N., & Williams, M. J. M. (2010). Characterising the intermediate depth waters of the Pacific Ocean using δ13C and other geochemical tracers. *Deep Sea Res. Part I: Oceanographic Research Papers*, 57(7), 847–859.

Breves, W., Heuermann, R., Reuter, R., 2003. Enhanced red fluorescence emission in the oxygen minimum zone of the Arabian Sea, *Ocean. Dynam.,* 53, 86–97, doi:10.1007/s10236-003-0026-y.

Bricaud, A., Babin, M., Claustre, H., Ras, J., Tièche, F., 2010. Light absorption properties and absorption budget of Southeast Pacific waters. *J. Geophys. Res.,* 115, C08009. http://dx.doi.org/10.1029/2009JC005517.

Bricaud, A., Stramski, D., 1990. Spectral absorption coefficients of living phytoplankton and nonalgal biogenous matter: A comparison between the Peru upwelling area and the Sargasso Sea, *Limnol. Oceanogr.,* 35, 562–582.

Bricaud, A., A. Morel, Prieur, L., 1981. Absorption by dissolved organic matter of the sea (yellow substance) in the UV and visible domains, *Limnol. Oceanogr.,* 26, 43–53.

Broecker, W.S., Takahashi, T., Takahashi, T., 1985. Sources and flow patterns of deep-ocean waters as deduced from potential temperature, salinity and initial phosphate concentration, *J. Geophys. Res.*, 90, 6925–6939.

Bronk, D. A., 2002. Dynamics of DON. In *Biogeochemistry of Marine Dissolved Organic Matter*, eds Hansell, D. A., Carlson, C. A., Academic Press, San Diego, pp. 153–247.

Brown, J.H., Gillooly, J.F., Allen, A.P., Savage, V.M., West, G.B., 2004. Toward a metabolic theory of ecology, *Ecology,* 85, 1771–1789.

Brown, M., 1977. Transmission spectroscopy examinations of natural waters, *Estuar. Coast. Mar. Sci., 5*, 309–317.

Bussmann, I., 1999. Bacterial utilization of humic substances from the Arctic Ocean, *Aquat Microb. Ecol, 19*, 37–45.

Butturini, A., Ejarque, E., 2013. Technical Note: Dissolved organic matter fluorescence – a finite mixture approach to deconvolve excitation-emission matrices, *Biogeosciences*, 10, 5875–5887.

Buesseler, K.O. et al., 2007. Revisiting carbon flux through the ocean's twilight zone. *Science*, 316(5824): 567–570.

Calvert, S. E., Karlin, R. E., Toolin, L. J., Donahue, D. J., Southon, J. R., Vogel, J. S., 1991. Low organic carbon accumulation rates in Black Sea sediments. *Nature*, 350, 692–695.

Calvo-Díaz, A., Morán, X. A. G., 2006. Seasonal dynamics of picoplankton in shelf waters of the southern Bay of Biscay. *Aquat. Microb. Ecol.*, 42, 159.

Cameron, D. R., Lenton, T. M., Ridgwell, A. J., Shepherd, J. G., Marsh, R., Yool, A., 2005. A factorial analysis of the marine carbon cycle and ocean circulation controls on atmospheric CO_2. *Global Biogeochem. Cycles*, 19, GB4027, doi: 10.1029/2005GB002489.

Carder, K. L., Steward, R. G., Harvey, G. R., Ortner, P. B., 1989. Marine humic and fulvic acids: their effects on remote sensing of ocean chlorophyll. *Limnol. Oceanogr.*, 34(1), 68–81.

Carlson, C. A., Hansell, D. A., 2015. DOM Sources, Sinks, Reactivity, and Budgets. In *Biogeochemistry of Marine Dissolved Organic Matter* (Second Edition), eds Hansell, D. A., Carlson, C.A., Academic Press, Boston, pp 66–94.

Carlson, C. A., Hansell, D. A., Tamburini, C., 2011. DOC persistence and its fate after export within the ocean interior. In *Microbial Carbon Pump in the Ocean*, eds Jiao, N., Azam, F., Sanders, S., Science Booklet, Supplement to Science, pp. 57–59.

Carlson, C.A., Hansell, D.A., Nelson, N.B., Siegel, D.A., Smethie, W.M., Khatiwala, S., et al., 2010. Dissolved organic carbon export and subsequent remineralization in the mesopelagic and bathypelagic realms of the North Atlantic basin. *Deep-Sea Res. II,* 57, 1433–1445.

Carlson, C. A., 2002. Production and removal Processes. In *Biogeochemistry of Marine Dissolved Organic Matter*, eds Hansell, D. A., Carlson, C. A., pp. 91–151, Elsevier, San Diego, doi:10.1016/B978-012323841-2/50006-3.

Carlson, C. A., Ducklow, H. W., Michaels, A. F., 1994. Annual flux of dissolved organic carbon from the euphotic zone in the northwestern Sargasso Sea, *Nature, 371*, 405–408.

Carr et al., 2006. A comparison of global estimates of marine primary production from ocean color. *Deep Sea Res II*, 53(5-7): 741-770.

Castro, C. G., Pérez, F. F., Holley, S.E., Rios, A.F., 1998. Chemical characterization and modelling of water masses in the Northeast Atlantic, *Prog. Oceanogr.*, 41, 249–279.

Catalá, T.S., Mladenov, N., Echevarría, F, Reche, I., 2013. Positive trends between salinity and chromophoric and fluorescent dissolved organic matter in a seasonally inverse estuary. *Estuarine, Coastal and Shelf Science*, 133, 206–216.

Catubig, N. R., Archer, D. E., Francois, R., deMenocal, P., Howard, W., Yu, E. -F., 1998. Global deep-sea burial rate of calcium carbonate during the Last Glacial Maximum, *Paleoceanography*, 13 (3), 298–310.

Chavez, F. P., Messié, M., Pennington, J. T., 2011. Marine Primary production in relation to climate variability and change. *Ann. Rev. Mar. Sci,.* 3, 227–260.

Chen, H., Stubbins, A., Perdue, E. M., Green, N. W., Helms, J. R., Mopper, K., Hatcher, P.G. 2014. Ultrahigh resolution mass spectrometric differentiation of dissolved organic matter isolated by coupled reverse osmosis-electrodialysis from various major oceanic water masses. *Mar. Chem.*, 164, 48–59.

Chen, H., Meng, W., Zheng, B., Wang, C., An, L., 2013. Optical signatures of dissolved organic matter in the watershed of a globally large river (Yangtze River, China). *Limnologica*, 43, 482–491.

Chen, Z., Li, Y., Pan, J., 2004. Distributions of colored dissolved organic matter and dissolved organic carbon in the Pearl River Estuary, China. *Cont. Shelf. Res.*, 24, 1845–1856.

Chen, C. T. A., 2004. The Global Carbon Cycle: Integrating Humans, Climate, and the Natural World. In *Exchanges of Carbon in the Coastal Seas*, eds. Field, C. B. Raupach, M. R., pp. 341–351, Island Press, Washington DC.

Chen, R. F., Bada, J. L., 1992. The fluorescence of dissolved organic matter in seawater. *Mar.Chem.*, 37, 191–221.

Chin, W. ·C., Orellana, M. V., Verdugo, P., 1998. Spontaneous assembly of marine dissolved organic matter into polymer gels. *Nature*, 391, 568–572.

Coble, P.G., 2007. Marine optical biogeochemistry: the chemistry of ocean color. *Chem. Rev.*, 107, 402–418.

Coble, P. G., Del Castillo, C. E., Avril, B., 1998. Distribution and optical properties of CDOM in the Arabian Sea during the 1995 Southwest Monsoon. *Deep-Sea Res. II*, 45, 2195–2223.

Coble, P. G., 1996. Characterization of marine and terrestrial DOM in seawater using excitation–emission matrix spectroscopy. *Mar. Chem.*, 51, 325–346.

Conmy, R.N., Coble, P.G., Chen, R.F., Gardner, G.B., 2004. Optical properties of dissolved organic matter in the Northern Gulf of Mexico. *Mar. Chem.*, 89, 127–144.

Cory, R.M., McKnight, D.M., 2005. Fluorescence spectroscopy reveals ubiquitous presence of oxidized and reduced quinines in dissolved organic matter. *Environmental Science and Technology*, 39, 5142–8149.

Creighton, T.E., 1993. Proteins, Structure and Molecular Properties, 2nd Edition. Freeman, New York.

Dahlén, J., Bertilsson, S., Pettersson, C., 1996. Effects of UV-A irradiation on dissolved organic matter in humic surface waters. *Environ. Int.*, 22, 501–506.

Dainard, P. G., Guéguen, C., 2013. Distribution of PARAFAC modelled CDOM components in the North Pacific Ocean, Bering, Chukchi and Beaufort Seas. *Mar. Chem.*, 157, 216–223.

Davidson, E. A., Janssens, I., 2006. Temperature sensitivity of soil carbon decomposition and feedbacks to climate change, *Nature, 440*, 165·173.

Davis, X. J., Straneo, F., Kwon, Y.-O., Kelly, K. a., & Toole, J. M., 2013. Evolution and formation of North Atlantic Eighteen Degree Water in the Sargasso sea from moored data. *Deep Sea Res. Part II: Topical Studies in Oceanography*, 91, 11–24.

De La Fuente, P., Marrasé, C., Canepa, A., Álvarez-Salgado, X. A., Gasser, M., Fajar, N. M., Romera-Castillo, C., Pelegrí, J. L., 2014. Does a general relationship exist between fluorescent dissolved organic matter and microbial respiration?—The case of the dark equatorial Atlantic Ocean, *Deep-Sea Research I*, 89, 44–55.

Del Castillo, C. E., Miller, R. L., 2008. On the use of ocean color remote sensing to measure the transport of dissolved organic carbon by the Mississippi River Plume. *Remote Sens. Environ.*, 112 (3), 836–844.

del Giorgio, P., Duarte, C.M., 2002. Respiration in the open ocean, *Science, 420*, 379·384.

Del Vecchio, R., Blough, N. V., 2004a. Spatial and seasonal distribution of chromophoric dissolved organic matter and dissolved organic carbon in the Middle Atlantic Bight. *Mar. Chem.*, 89, 169–187.

Del Vecchio, R., Blough, N.V., 2004b. On the origin of the optical properties of humic substances, *Environ. Sci. Technol., 38*, 3885-3891.

Del Vecchio, R., Subramaniam, A., 2004. Influence of the Amazon River on the surface optical properties of the western tropical North Atlantic Ocean. *J. Geophys. Res.,* 109, C11001.

Del Vecchio, R., Blough, N. V., 2002. Photobleaching of chromophoric dissolved organic matter in natural waters: kinetics and modeling. *Mar. Chem.*, 78, 231–253.

Determann, S., Reuter, R., Willomm, R., 1996. Fluorescent matter in the eastern Atlantic Ocean. Part 2: vertical profiles and relation to water masses. Deep-Sea Research I, 43 (3), pp. 345–360.

DeVries, T.J., Primeau, F.W., Deursch, C.A., http://www.sgmeet.com/osm2014/viewabstract.asp? AbstractID =17345, 2014. Quantifying and Comparing the Microbial and Biological Carbon Pumps in the Ocean. Abstract, Ocean Sciences Meeting, Honolulu, Hawaii, USA.

Dittmar, T. 2015. Reasons behind the long-term stability of dissolved organic matter. In *Biogeochemistry of Marine Dissolved Organic Matter* (Second Edition), eds Hansell, D.A., Carlson, C.A., Academic Press, Boston, pp 369–385.

Dittmar, T., De Rezende, C. E., Manecki, M., Niggemann, J., Coelho Ovalle, A. R., Stubbins, A., et al., 2012. Continuous flux of dissolved black carbon from a vanished tropical forest biome. *Nat. Geosci.*, 5, 618–622.

Dittmar, T., Paeng, J., 2009. A heat-induced molecular signature in marine dissolved organic matter. *Nature Geoscience,* 2, 175–179.

Dittmar, T., Koch, B., Hertkorn, N., Kattner, G., 2008. A simple and efficient method for the solid-phase extraction of dissolved organic matter (SPE-DOM) from seawater. *Limnol. Oceanogr.: Methods*, 6, 230-235.

Dittmar, T., Kattner. G., 2003. Recalcitrant dissolved organic matter in the ocean: major contribution of small amphiphilics. *Mar. Chem.*, 82, 115–123.

Dittmar, T., Fitznar, H. P., Kattner, G., 2001. Origin and biogeochemical cycling of organic nitrogen in the eastern Arctic Ocean as evident from d- and l-amino acids. *Geochim. Cosmochim. Acta*, 65, 4103–4114.

Druffel, E.R.M., Griffin, S., Bauer, J.E., Wolgast, D., Wang, X.-C., 1998. Distribution of particulate organic carbon and radiocarbon in the water column from the upper slope to the abyssal NE Pacific Ocean. *Deep Sea Res. Part II Top. Stud. Oceanogr.,* 45, 667–687.

Druffel, E. R. M., Bauer, J. E., Williams, P. M., Griffin, S., Wolgast, D., 1996. Seasonal variability of particulate organic radiocarbon in the northeast Pacific Ocean. *J. Geophys. Res.*, 101, 20543–20552.

D'Sa, E. J., Goes, J. I., , Gomes, H., Mouw, D., 2014. Absorption and fluorescence properties of CDOM of the eastern Bering Sea. *Biogeosciences*, 11, 3225–3244,

Ducklow, H. W., Hansell, D. A., Morgan, J. A., 2007. Dissolved organic carbon and nitrogen in the Western Black Sea. *Mar. Chem.,* 105, 140–150.

Ducklow, 2003. Biogeochemical Provinces: Towards a JGOFS Synthesis. In Ocean Biogeochemistry, eds. Fasham, M. J. R., Berlin.

Ducklow, H. W., D. K. Steingberg, and K. O. Buesseler (2001), Upper Ocean Carbon Export and the Biological Pump. *Oceanography,* 14 (4), 50–58.

Dunne, J., Sarmiento, J., Gnanadesikan, A., 2007. A synthesis of global particle export from the surface ocean and cycling through the ocean interior and on the seafloor. *Global Biogeochem. Cycles,* 21, GB4006, doi: 10.1029/2006GB002907.

Ejarque-González, E., Buturini, A., 2014. Self-Organising Maps and Correlation Analysis as a Tool to Explore Patterns in Excitation-Emission Matrix Data Sets and to Discriminate Dissolved Organic Matter Fluorescence Components, *PLoS ONE*, 9(6): e99618. doi:10.1371/journal.pone.0099618.

Elderfield, H., 2002. Carbonate Mysteries. *Science*, 296, 1618–1621.

Estrada, M., 2012. Determinación fluorimétrica de la clorofila a. Expedición de circunnavegación Malaspina 2010: Cambio global y exploración de la biodiversidad del océano. In *Libro blanco de métodos y técnicas de trabajo oceanográfico*. E. Moreno-Ostos. Madrid, CSIC, 399–405.

Falkowski, P. et al., 2009. The Global Carbon Cycle: A Test of Our Knowledge of Earth as a System. *Science*, 290, 290–295.

Feely, R. A. et al., 2004. Impact of anthropogenic CO_2 on the $CaCO_3$ system in the oceans. *Science*, 305, 362–366.

Feely, R. A., C. L. Sabinelli, R. Schlitzer, J. L. Bullister, S. Mecking, and D. Greeley (2004), Remineralization in the Upper Water Column of the Pacific Ocean. *Journal of Oceanography, 60*, 45-52.

Fellman, J. B, D'Amore, D. V., Hood, E., Boone, R D., 2008. Fluorescence characteristics and biodegradability of dissolved organic matter in forest and wetland soils from coastal temperate watersheds in southeast Alaska. *Biogeochemistry*, 88, 169–184.

Fernández-Castro, B., Mouriño-Carballido, B., Benítez-Barrios, V., Chouciño, P., Fraile-Nuez, E., Graña, R., Piedeleu, M., Rodríguez-Santana, A., 2014. Microstructure turbulence and diffusivity parameterization

in the tropical and subtropical Atlantic, Pacific and Indian Oceans during the Malaspina 2010 expedition. *Deep Sea Res. I*, 94, 15–30.

Ferrari, G.M., Dowell, D., 1998. CDOM absorption characteristics with relation to fluorescence and salinity in coastal areas of the southern Baltic Sea. *Est. Coast. Shelf Sci.,* 47, 91–105.

Fiedler, P. C., Talley, L. D., 2006. Hydrography of the eastern tropical Pacific: A review. *Prog. Oceanogr.*, 69(2-4), 143–180.

Friedrichs M. A. M., McCartney, M. S., Hall, M. M., 1994. Hemispheric asymmetry of deep water transport modes in the western Atlantic. *J. Geophys. Res.*, 99, 25165–25179.

Gasol, J. M., Vázquez-Domínguez, E., Vaqué, D., Agustí, S., Duarte, C. M., 2009. Bacterial activity and diffusive nutrient supply in the oligotrophic Central Atlantic Ocean, *Aquat. Microb. Ecol.*, 56, 1–12.

Gasol, J. M., del Giorgio, P. A., 2000. Using flow cytometry for counting natural planktonic bacteria and understanding the structure of planktonic bacterial communities. *Sci. Mar.*, 64, 197–224.

Georgi, D. T., 1981. On the relationships between the large-scale property variations and fine structures of the Antarctic Circumpolar Current, *J. Geophys. Res.*, 86, 6556–6566.

Goldberg, S., Carlson, C., Hansell, D., Nelson, N., Siegel, D., 2009. Temporal dynamics of dissolved combined neutral sugars and the quality of dissolved organic matter in the Northwestern Sargasso Sea. *Deep-Sea Res. I*, 56, 672–685.

Gordon, A. L., Bosley, K.T., 1991. Cyclonic gyre in the tropical south Atlantic, *Deep-Sea Res. A*, 38 (Suppl), S323–S343.

Gram, L., Grossart, H-P., Schlingloff, A., Kiørboe, T., 2002. Possible Quorum Sensing in Marine Snow Bacteria: Production of Acylated Homoserine Lactones by Roseobacter Strains Isolated from Marine Snow. *Applied and Environmental Microbiology*, 68(8), p. 4111–4116.

Green, N. W., Michael Perdue, E., Aiken, G. R., Butler, K. D., Chen, H., Dittmar, T., Niggemann, J., Stubbins, A., 2014. An intercomparison of three methods for the large-scale isolation of oceanic dissolved organic matter. *Mar. Chem.*, 161, 14–19.

Green, S. A., Blough, N. V., 1994. Optical Absorption and Fluorescence Properties of chromophoric dissolved organic matter in natural waters, *Limnol. Oceanogr., 39*, 1903-1916.

Griffin, C. G., Frey, K. E., Rogan, J., Holmes, R. M., 2011. Spatial and interannual variability of dissolved organic matter in the Kolyma River, East Siberia, observed using satellite imagery. *J. Geophys. Res.*, 116, G03018.

Gruber, N., et al., 2009. Oceanic sources, sinks, and transport of atmospheric CO_2, *Global Biogeochem. Cycles, 23*, GB1005, doi:10.1029/2008GB003349.

Guéguen, C., C. W. Cuss, C. J. Cassels, Carmack, E. C., 2014. Absorption and fluorescence of dissolved organic matter in the waters of the Canadian Arctic Archipelago, Baffin Bay, and the Labrador Sea, *J. Geophys. Res. Oceans*, 119, 2034–2047, doi:10.1002/2013JC009173.

Guéguen, C., Kowalczuk, P., 2013. Colored dissolved organic matter in frontal zones. In *Chemical Oceanography of Frontal Zones*, Hdb Env Chem, ed Berlkin, I. M. DOI 10.1007/698_2013_244.

Guéguen, C., McLaughlin, F. A., Carmack, E. C., Itoh, M., Narita, H., Nishino, S., 2012. The nature of colored dissolved organic matter in the southern Canada Basin and East Siberian Sea. *Deep-Sea Research II*, 81–84, 102–113.

Guéguen, C., Guo, L., Yamamoto-Kawai, M., Tanaka, N., 2007. Colored dissolved organic matter dynamics across the shelf-basin interface in the western Arctic Ocean. *J. Geophys. Res.*, 112, C05038. doi:10.1029/2006JC003584.

Gundersen, K., Heldal, M., Norland, S., Purdie, D. A., Knap, A. H., 2002. Elemental C, N, and P cell content of individual bacteria collected at the Bermuda Atlantic time- series study (BATS) site. *Limnol. Oceanogr.*, 47 (5), 1525–1530.

Hansell, D. A., 2013. Recalcitrant dissolved organic carbon fractions, *Ann. Rev. Mar. Sci., 5*, 421-425, doi:10.1146/annurev-marine-120710-100757.

Hansell, D.A., Carlson, C.A., 2013. Localized refractory dissolved organic carbon sinks in the deep ocean, *Glob. Biogeoch. Cycles,* 27, 705–710.

Hansell D. A., Carlson, C. A., Schlitzer, R., 2012. Net removal of major marine dissolved organic carbon fractions in the subsurface ocean, *Glob. Biogeochem. Cycles*, *26*, GB1016.

Hansell, D. A., Carlson, C. A., Repeta, D. J., Schlitzer, R., 2009. Dissolved organic matter in the ocean. A controversy stimulates new insights. *Oceanography*, 22, 202–211.

Hansell, D. A., Carlson, C. A., 2001. Marine dissolved organic matter and the carbon cycle. *Oceanography*, 14(4), 41–49.

Hansell, D. A., Carlson, C. A., 1998. Deep-ocean gradients in the concentration of dissolved organic carbon. *Nature*, 395, 263–266.

Hansman, R. L., Dittmar, T., Herndl, G. J. Conservation of dissolved organic matter molecular composition during mixing of the deep water masses of the northeast Atlantic Ocean. *Mar. Chem.*, *in press*, http://dx.doi.org/10.1016/j.marchem.2015.06.001.

Harvey, J., 1982. θ-S relationships and water masses in the eastern North Atlantic. *Deep Sea Research Part A. Oceanographic Research Papers*, 29(8), 1021–1033.

Hayase, K., Shinozuka, N., 1995. Vertical distribution of fluorescent organic matter along with AOU and nutrients in the equatorial Central Pacific. *Mar. Chem.*, 48, 283–290.

Hedges, J. I., 2002. In *Biogeochemistry of Marine Dissolved Organic Matter*. Eds Hansell, D. A., Carlson, C. A., Academic Press: Boston, p 1–33.

Hedges, J. I., Hatcher, P. G., Ertel, J. R., Meyers-Schulte, K. J., 1992. A comparison of dissolved humic substances from seawater with Amazon River counterparts by 13C-NMR spectrometry, *Geochim. Cosmochim. Ac., 56*, 1753-1757.

Heller, M. I., Gaiero, D. M., Croot, P. L., 2013. Basin scale survey of marine humic fluorescence in the Atlantic: Relationship to iron solubility and H_2O_2. *Global Biogeochem. Cycles*, 27, 88–100, doi:10.1029/2012GB004427.

Helms, J. R., Mao, J., Stubbins, A., Schmidt-Rohr, K., Spencer, R. G. M., Hernes, P. J., Mopper, K., 2014. Loss of optical and molecular indicators of terrigenous dissolved organic matter during long-term photobleaching. Aquatic Sciences, 76 (3), 353–373.

Helms, J. R., Stubbins, A., Perdue, E. M., Green, N. W., Chen, H., Mopper, K., 2013. Photochemical bleaching of oceanic dissolved organic matter and its effect on absorption spectral slope and fluorescence. *Mar. Chem.*, 155, 81–91.

Helms, J. R., Stubbins, A., Ritchie, J.D., Minor, E.C., Kieber, D.J., Mopper, K. 2008. Absorption spectral slopes and slope ratios as indicators of molecular weight, source, and photobleaching of chromophoric dissolved organic matter, *Limnol. Oceanogr., 53*, 955-969.

Hernes, P.J., Benner, R., 2006. Terrigenous organic matter sources and reactivity in the North Atlantic Ocean and a comparison to the Arctic and Pacific oceans. *Mar. Chem.*, 100, 66–79.

Hernes, P.J., Benner, R., 2003. Photochemical and microbial degradation of dissolved lignin phenols: implications for the fate of terrigenous dissolved organic matter in marine environments. *J. Geophys Res: Oceans*, 108, 3291.

Hernes, P.J., Benner, R., 2002. Transport and diagenesis of dissolved and particulate terrigenous organic matter in the North Pacific Ocean. *Deep-Sea Research I*, 49, 2119–2132.

Hertkorn, N., Harir, M., Koch, B. P., Michalke, B., Schmitt-Kopplin, P., 2013. High-field NMR spectroscopy and FTICR mass spectrometry: powerful discovery tools for the molecular level characterization of marine dissolved organic matter. *Biogeosciences*, 10, 1583–1624.

Hertkorn, N. et al., 2006. Characterization of a major refractory component of marine dissolved organic matter. *Geochim. Cosmochim. Acta*, 70, 2990–3010.

Hong, H., Wu, J., Shang, S., Hu, C., 2005. Absorption and fluorescence of chromophoric dissolved organic matter in the Pearl River Estuary, South China. *Mar. Chem.*, 97, 78–89.

Hopkinson, C. S., Vallino, J. J., 2005. Efficient export of carbon to the deep ocean through dissolved organic matter. *Nature*, 433, 142–145.

Hudson, N., Baker, A., Reynolds, D., 2007. Fluorescence analysis of dissolved organic matter in natural, waste and polluted waters — A review. *River. Res. Applic.,* 23, 631–649.

Iglesias-Rodriquez M. D., Armstrong, R., Feely, R., Hood, R., Kleypas, J., Milliman, J. D., Sabine, C., Sarmiento, J., 2002. Progress made in study of ocean's calcium carbonate budget. Eos, 83(34), 365, 374-375.

Istoshin, Y. V., 1961. Formative area of 'eighteen-degree ' water in the Sargasso Sea Central Institute of Forecasting, 384–390.

Ito, Y., Butler, A., 2005. Structure of synechobactins, new siderophores of the marine cyanobacterium Synechococcus sp. PCC 7002. *Limnol. Oceanogr.*, 50, 1918–1923.

Ito, T., Follows, M. J., Boyle, E. A., 2004. Is AOU a good measure of respiration in the oceans?, *Geophys. Res. Lett., 31*, L17305, doi:10.1029/2004GL020900.

Jaffé, R. et al., 2013. Global charcoal mobilization from soils via dissolution and riverine transport to the oceans. *Science*, 340, 345–347.

Jankowski, J.J., Kieber, D.J., Mopper, K., 1999. Nitrate and Nitrite Ultraviolet Actinometers, *Photochemistry and Photobiology,* 70(3), 319–328.

Jannasch, H. W., 1967. Growth of marine bacteria at limiting concentrations of organic carbon in seawater. *Limnol. Oceanogr.,* 12, 264–271.

Jenkins, W.J., 1998. Studying subtropical thermocline ventilation and circulation using tritium and ^{3}He, *J. Geophys Res., 103*, 15817–15831.

Jenkins, W. J., 1982. Oxygen utilization rates in the North Atlantic subtropical gyre and primary production in oligotrophic systems, *Nature, 300*, 246–249.

Jiao et al., 2014. Mechanisms of microbial carbon sequestration in the ocean – future research directions. *Biogeosciences*, 11, 5285–5306.

Jiao, N., Azam, F., 2011. Microbial carbon pump and its significance for carbon sequestration in the ocean. In *Microbial Carbon Pump in the Ocean*, eds Jiao, N., Azam, F., Sanders, S., Science Booklet, Supplement to Science, pp. 43–45.

Jiao, N., Herndl, G. J., Hansell, D. A., Benner, R., Kattner, G., Wilhelm, S. W., Kirchman, D. L., Weinbauer, M. G., Luo, T., Chen, F., Azam, F., 2010. Microbial production of recalcitrant dissolved organic matter: long-term carbon storage in the global ocean, *Nature Reviews Microbiology, 8*, 593-599.

Johnson, G.C., 2008. Quantifying Antarctic Bottom Water and North Atlantic Deep Water volumes. *J. Geophys. Res.*, 113(C5).

Johnson, K.S., Coletti, L.J., 2002. In situ ultraviolet spectrophotometry for high resolution and long-term monitoring of nitrate, bromide and bisulfide in the ocean, *Deep-Sea Res. I*, 49, 1291–1305.

Jørgensen, L., Stedmon, C.A., Granskog, M.A., Middelboe, M. 2014. Tracing the long-term microbial production of recalcitrant fluorescent dissolved organic matter in seawater, *Geophys. Res. Lett., 41*, 2481-2488.

Jørgensen, L., Stedmon, C., Kragh, T., Markager, S., Middelboe, M., Søndergaard, M., 2011. Global trends in the fluorescence characteristics and distribution of marine dissolved organic matter. Mar. Chem. 126, 139–48.

Joos, F. et al., 2013. Carbon dioxide and climate impulse response functions for the computation of greenhouse gas metrics: a multi-model analysis. *Atmospheric Chemistry and Physics*, 13, 2793–2825.

Kaiser, K., Benner, R., 2009. Biochemical composition and size distribution of organic matter at the Pacific and Atlantic time-series stations. *Mar. Chem.*, 113, 63–77.

Kalle, K., 1949. Fluorescence and contents of yellow substance in the Gulfs of Bothnia and Finland. *Deutsche Hydrographische Zeitschrift,* 2, 9–124.

Karl, D. M., Bjorkman, K. M., 2015. Dynamics of Dissolved Organic Phosphorus. In *Biogeochemistry of Marine Dissolved Organic Matter* (Second Edition), eds Hansell, D. A., Carlson, C. A., Academic Press, Boston, pp 128–184.

Karstensen, J., Tomczak, M., 1998. Age determination of mixed water masses using CFC and oxygen data, *J. Geophys. Res., 103(C9)*, 18599-18609.

Kattner, G., Simon, M., Koch, B.P., 2011. Molecular characterization of dissolved organic matter and constraints for prokaryotic utilization, in *Microbial carbon pump in the ocean*, edited by N. Jiao, F. Azam and S. Sanders, 60–61, Science/AAAS.

Keil, R. G., and D. L. Kirchman. 1994. Abiotic transformation of labile protein to refractory protein in sea water. *Mar. Chem.*, 45, 187–196.

Khatiwala, S., Primeau, F., Holzer, M., 2012. Ventilation of the deep ocean constrained with tracer observations and implications for radiocarbon estimates of ideal mean age, *Earth and Planetary Science Letters*, 325-326, 116-125.

Khatiwala, S., Primeau, F., Hall, T., 2009. Reconstruction of the history of anthropogenic CO_2 concentrations in the ocean, *Nature, 462*, 346-349, doi:10.1038/nature08526.

Kieber, R. J., Whitehead, R. F., Reid, S. N., Willey, J. D., Seation, P. J., 2006. Chromophoric Dissolved Organic Matter (CDOM). In *Rainwater, Southeastern North Carolina*, USA. J. Atm. Chem. 54, 21–41.

Kieber, R., Hydro, L. H., Seaton, P. J., 1997. Photooxidation of triglycerides and fatty acids in seawater: Implication toward the formation of marine humic substances. *Limnol. Oceanogr.*, 42, 1454–1462.

Kieber, D.J., McDaniel, J., Mopper, K., 1989. Photochemical source of biological substrates in sea water: Implications for carbon cycling. *Nature*, 341, 637–369.

Kim, J., Kim, G., 2015. Importance of colored dissolved organic matter (CDOM) inputs from the deep sea to the euphotic zone: Results from the East (Japan) Sea. *Mar. Chem.*, 169, 33–40.

Kirchman, D. L., R. Keil, Wheeler, P. A., 1989. The effect of amino acids on ammonium utilization and regeneration by heterotrophic bacteria in the subarctic Pacific. *Deep-Sea Res.*, 36, 1763–1776.

Kishino, M., Takahashi, M., Okami, N., Ichimura, S., 1985. Estimation of the spectral absorption coefficients of phytoplankton in the sea, *Bull. Mar. Sci.,* 37, 634–642.

Kovarova-Kovar, K., Egli, T., 1998. Growth kinetics of suspended microbial cells: from single-substrate-controlled growth to mixed-substrate kinetics. *Microbiol. Mol. Biol. Rev.,* 62, 646–666.

Kowalczuk, P., Tilstone, G.H., Zablocka, M., Röttgers, R., Thomas, R., 2013. Composition of dissolved organic matter along an Atlantic meridional transect from fluorescence spectroscopy and parallel factor analysis. *Mar. Chem*., 157, 170–184.

Kowalczuk, P., Zablocka, M., Slawomir, S., Kulínski, K., 2010. Fluorescence measured in situ as a proxy of CDOM absorption and DOC concentration in the Baltic Sea. *Oceanologia*, 52 (3), pp. 431–471.

Kramer, G.D., Herndl, G.L., 2004. Photo- and bioreactivity of chromophoric dissolved organic matter produced by marine bacterioplankton, *Aquat. Microb. Ecol., 36*, 239-246.

Kritzberg, E. S., Arrieta, J. M., Duarte, C. M., 2010. Temperature and phosphorus regulating carbon flux through bacteria in a coastal marine system. *Aquat. Microb. Ecol.,* 58, 141–151.

Kujawinski, E. B. 2011. The Impact of Microbial Metabolism on Marine Dissolved Organic Matter. *Annu. Rev. Mar. Sci.*, 3, 567–599.

Kujawinski, E. B. ,Del Vecchio, R., Blough, N. V., Klein, G. C.,Marshall, A. G., 2004. Probing molecular-level transformations of dissolved organicmatter: insights from electrospray ionizationFourier-transform ion cyclotron resonance mass spectrometry. *Mar. Chem.*, 92, 23–37.

Kujawinski et al. 2009. Identification of possible source markers in marine dissolved organic matter using ultrahigh resolution electrospray ionization Fourier-transform ion cyclotron resonance mass spectrometry. *Geochim. Cosmochim. Acta,* 73, 4384–99.

Kutser, T., et al., 2005. Using satellite remote sensing to estimate the colored dissolved organic matter absorption coefficient in lakes. *Ecosystems*, 8, 709–720.

Lakowicz, J.R., 2006. Principles of Fluorescence Spectroscopy. Springer.

Lalli, C.M., Parsons, T.R., 1997. Biological Oceanography: an Introduction. Butterworth-Heinemann Ltd, Oxford England, p. 314.

Lang, S. Q., Butterfield, D. A., Lilley, M. D., Paul Johnson, H., Hedges, J. I., 2006. Dissolved organic carbon in ridge-axis and ridge-flank hydrothermal systems. *Geochim. Cosmochim. Acta,* 70, 3830–3842.

Laruelle, G. G., et al., 2009. Anthropogenic perturbations of the silicon cycle at the global scale: Key role of the land-ocean transition, *Global Biogeochemical Cycles*, 23, GB4031, doi:10.1029/2008GB003267.

Lauro, F. M. et al., 2009. The genomic basis of trophic strategy in marine bacteria, *P. Natl. Acad. Sci. USA*, 106, 15527–15533.

Lawaetz, A. J., Stedmon, C. A., 2009. Fluorescence Intensity Calibration Using the Raman Scatter Peak of Water. *Appl. Spectrosc.*, 63 (8), 936–94.

Lechtenfeld, O.J., Hertkorn, N., Shen, Y., Witt, M., Benner, R., 2015. Marine sequestration of carbon in bacterial metabolites, *Nat. Comms.,* 6, 6711, DOI: 10.1038/ncomms7711.

Lechtenfeld, O. J., Kattner, G., Flerus, R., McCallister, S. L., Schmitt-Kopplin, P., Koch, B. P., 2014. Molecular transformation and degradation of refractory dissolved organic matter in the Atlantic and Southern Ocean. *Geochimica et Cosmochimica Acta*, 126, 321–337.

Lechtenfeld, 2012. Biogeochemistry of marine dissolved organic matter: molecular composition, reactivity and new methods. PhD thesis, University of Bremen, pp. 1–311.

Lee, K., 2001. Global net community production estimated from the annual cycle of surface water total dissolved inorganic carbon. *Limnol. Oceanogr.*, 46(6), 1287–1297.

Legendre, L., Rivkin, R. B., Weinbauer, M. G., Guidi, L., Uitz, J., 2015. The microbial carbon pump concept: Potential biogeochemical significance in the globally changing ocean. *Prog. Oceanogr.*, 134, 432–450.

Letscher, R. T., Hansell, D. A., Carlson, C. A., Lumpkin, R., Knapp, A. N., 2013. Dissolved organic nitrogen in the global surface ocean: distribution and fate. *Global Biogeochem. Cycles*, 27, 141–153.

Lønborg, C., Yokokawa, T., Herndl, G. J., Álvarez-Salgado, X. A., 2015. Production and degradation of fluorescent dissolved organic matter in surface waters of the eastern north Atlantic ocean. *Deep-Sea Research I*, 96, 28–37.

Lønborg, C., Álvarez-Salgado, X. A., Davidson, K., Martínez-García, S., Teira, E., 2010. Assessing the microbial bioavailability and degradation rate constants of dissolved organic matter by fluorescence spectroscopy in the coastal upwelling system of the Ría de Vigo. *Mar. Chem.*, 119, 121–129.

Longhurst, A.R., 1998. Ecological Geography of the Sea. Academic Press, San Diego. 397p.

Longhurst, A., 1995. Seasonal cycles of pelagic production and consumption. *Prog. Oceanogr.,* 36, 77–167.

Maie, N., Yamashita, Y., Cory, R.M., Boyer, J.N., Jaffé, R., 2012. Application of excitation emission matrix fluorescence monitoring in the assessment of spatial and seasonal drivers of dissolved organic matter composition: sources and physical disturbance controls. *Appl. Geochem.*, 27 (4), 917–929.

Marañón, E., Cermeño, P., Pérez, V., 2005. Continuity in the photosynthetic production of dissolved organic carbon from eutrophic to oligotrophic waters. *Mar. Ecol. Prog. Ser.*, 299, 7–17.

Masiello, C. A., Druffel, E. R. M., 1998. Black carbon in deep-sea sediments. *Nature*, 280, 1911–1913.

Mazuecos, I.P., Arístegui, J., Vázquez-Domínguez, E., Ortega-Retuerta, E., Gasol, J.M., Reche, I., 2015. Temperature control of microbial respiration and growth efficiency in the mesopelagic zone of the South Atlantic and Indian Oceans, *Deep-Sea Res. I,* 95, 131–138.

McCartney, M. S., 1982. The subtropical recirculation of mode waters, *J. Mar. Res.*, 40, 427–464.

Mecking, S., Warner, M. J., Greene, C. E., Hautala, S. L., Sonnerup, R. E., 2004. Influence of mixing on CFC uptake and CFC ages in the North Pacific thermocline, *J. Geophys. Res.*, 109, C07014, doi:10.1029/2003JC001988.

Medeiros, P. M., Seidel, M., Powers, L. C., Dittmar, T., Hansell, D. A., Miller, W. L. 2015. Dissolved organic matter composition and photochemical transformations in the northern North Pacific Ocean. *Geophysical Research Letters*, 42, 863–870.

Melhuish, W.H., 1961. Quantum efficiencies of fluorescence of organic substances: effect of solvent and concentration of the fluorescent solute, *J. Phys. Chem., 65*, 229–235.

Menon, H. B., Sangekar, N. P., Lotliker, A. A., Vetamony, P., 2011. Dynamics of chromophoric dissolved organic matter in Mandovi and Zuari estuaries — a study through in situ and satellite data. ISPRS J. Photogramm. Remote. Sens., 66 (4), 545–552.

Middelburg, J. J., Vlug, T., Jaco W. A. van der Nat, F., 1993. Organic matter mineralization in marine systems. *Global and Planetary Change*, 8., 47–58.

Millard, R. C., Owens, W. B., Fofonoff, N.P., 1990. On the calculation of the Brunt-Väisälä frequency. *Deep Sea Res.*, 37, 167–181.

Miller, W. L., Zepp, R. G., 1995. Photochemical production of dissolved inorganic carbon from terrestrial organic matter: significance to the oceanic organic carbon cycle. *Geophys. Res. Lett.*, 22, 417–420.

Milliman, J. D., Troy, P. J., Balch, W. M., Adams, A. K., Li, Y. H., Mackenzie, F. T., 1999. Biologically mediated dissolution of calcium carbonate above the chemical lysocline? *Deep Sea Res. Part I: Oceanographic Research Papers*, 46, 1653–1669.

Montgomery, R. B., 1958. Water characteristics of Atlantic Ocean and World Ocean, *Deep-Sea Res.*, 5, 134–148.

Mopper, K., Stubbins, A., Ritchie, J.D., Bialk, H.M., Hatcher, P.G., 2007. Advanced instrumental approaches for characterization of marine dissolved organic matter: Extraction techniques, mass spectrometry, and nuclear magnetic resonance spectroscopy. *Chem. Rev.*, 107, 419–442.

Mopper, K., Kieber, D. J., 2002. Photochemistry and the cycling of carbon, nitrogen and phosphorus, in Biogeochemistry of Marine Dissolved Organic Matter, eds Hansell, D. A., Carlson, C. A., pp. 455– 489, Academic, London.

Mopper, K., Zhou, X. L., Kieber, R. J., Kieber, D. J., Sikorski, R. J., Jones, R. D., 1991. Photochemical degradation of dissolved organic carbon and its impact on the oceanic carbon cycle. *Nature*, 353, 60–62.

Moran, M. A., Zepp, R. G., 1997. Role of photoreactions in the formation of biologically labile compounds from dissolved organic matter. *Limnol. Oceanogr.*, 42, 1307–1316.

Morel, A., Claustre, H., Gentili, B., 2010. The most oligotrophic subtropical zones of the global ocean: similarities and differences in terms of chlorophyll and yellow substance. Biogeosciences, 7, 3139–3151.

Morel, A., Gentili, B., 2009. A simple band ratio technique to quantify the colored dissolved and detrital organic material from ocean color remotely sensed data. Remote Sens. Environ. 113, 998–1011.

Morel, A., Gentili, B., Claustre, H., Babin, M., Bricaud, A., Ras, J., and Tièche, F., 2007. Optical properties of the "clearest" natural waters, *Limnol. Oceanogr.*, 52, 217–229.

Morel, A., Ahn, Y-H., 1990. Optical efficiency factors of free-living marine bacteria: Influence of bacterioplankton upon the optical properties and particulate organic carbon in oceanic waters, *J. Mar. Res.,* 48, 145–175.

Murphy, K. R., Stedmon, C. A., Graeber, D., Bro. R., 2013. Fluorescence spectroscopy and multi-way techniques. PARAFAC. *Anal. Methods*, 5, 6557–6566.

Murphy, K. R., Butler, K. D., Spencer, R. G. M., Stedmon, C. A., Boehme, J. R., Aiken, G. R., 2010. Measurement of Dissolved Organic Matter Fluorescence in Aquatic Environments: An Interlaboratory Comparison. *Environ. Sci. Technol.,* 44, 9405–9412.

Murphy, K. R., Stedmon, C. A., Waite, T. D., Ruiz, G. M., 2008. Distinguishing between terrestrial and autochthonous organic matter sources in marine environments using fluorescence spectroscopy. *Mar. Chem.*, 108, 40–58.

Murphy, K. R., Ruiz, G. M., Dunsmuir, W. T. M., Waite, T. D., 2006. Optimized parameters for fluorescence-based verification of ballast water exchange by ships. *Environmental, Science & Technology*, 40, 2357–2362.

Nagata, T., Kirchman, D. L., 1996. Bacterial degradation of protein adsorbed to model submicron particles in seawater. *Mar. Ecol. Prog. Ser.,* 132, 241–248.

Nagata, T., Kirchman, D. L., 1992. Release of macromolecular organic complexes by heterotrophic marine flagellates. *Mar. Ecol. Prog. Ser.*, 83, 233–240.

Naqvi, S. W. A., H. W. Bange, L. Farías, P. M. S. Monteiro, M. I. Scranton, and J. Zhang (2010), Marine hypoxia/anoxia as a source of CH_4 and N_2O. *Biogeosciences*, 7, 2159–2190.

Nelson, N. B. and Siegel, D. A., 2013. The global distribution and dynamics of chromophoric dissolved organic matter. *Annu. Rev. Mar. Sci.,* 5, 447–476.

Nelson, N. B., Siegel, D. A., Carlson, C. A., Swan, C. M., 2010. Tracing global biogeochemical cycles and meridional overturning circulation using chromophoric dissolved organic matter, *Geophys. Res. Let., 37*, L03610.

Nelson, N. B., Siegel, D.A., Carlson, C. A., Swan, C. M., Smethie, W. M., Khatiwala, S., 2007. Hydrography of chromophoric dissolved organic matter in the North Atlantic, *Deep-Sea Res. I, 54*, 710-731.

Nelson, N. B., Siegel, D. A., 2002. Chromophoric DOM in the open ocean. *Biogeochemistry of Marine Dissolved Organic Matter*, pp. 547–578.

Nelson, N. B., Siegel, D. A., Michaels, A. F., 1998. Seasonal dynamics of colored dissolved material in the Sargasso Sea. *Deep Sea Res. I,* 45, 931–957.

Nieto-Cid, M., Álvarez-Salgado, X. A., Pérez, F. F., 2006. Microbial and photochemical reactivity of fluorescent dissolved organic matter in a coastal upwelling system. *Limnol. Oceanogr.*, 51, 1391–1400.

Nieto-Cid, M., Álvarez-Salgado, Gago, J., Pérez, F. F., 2005. DOM fluorescence, a tracer for biogeochemical processes in a coastal upwelling system (NW Iberian Peninsula). *Mar. Ecol. Prog. Ser.*, 297, 33–50.

Nikaido, H., Vaara, M. 1985. Molecular basis of bacterial outer membrane permeability. *Microbiol. Rev.,* 49, 1–32.

Obernosterer, I., Reitner, B., Herndl, G. J., 1999. Contrasting effects of solar radiation on dissolved organic matter and its bioavailability to marine bacterioplankton. *Limnol. Oceanogr.*, 44, 1645–1654.

Ogawa, H., Amagai, Y., Koike, I., Kaiser, K., Benner R., 2001. Production of refractory dissolved organic matter by bacteria, *Science*, 292, 917–20.

Omori, Y., Hama, T., Ishii, M., 2015. Photochemical bleaching of fluorescent dissolved organic matter in the subtropical North Pacific Ocean. *Geochemical Journal*, 49, 175–184.

Omori, Y., Hama, T., Ishii, M., Saito, S., 2011. Vertical change in the composition of marine humic-like fluorescent dissolved organic matter in the subtropical western North Pacific and its relation to photoreactivity. *Mar. Chem.*, 124, 38–47.

Omori, Y., Hama, T., Ishii, M., Saito, S., 2010. Relationship between the seasonal change in fluorescent dissolved organic matter and mixed layer depth in the subtropical western North Pacific. *J. Geophys. Res.*, 115, C06001, doi:10.1029/2009JC005526.

Onken, R., 1995. The spreading of Lower Circumpolar Deep Water into the Atlantic Ocean. *J. Phys. Oceanogr.*, 25, 3051–3063.

Opsahl, S., Benner, R., Amon, R. M. W., 1999. Major flux of terrigenous dissolved organic matter through the Arctic Ocean. *Limnol. Oceanogr.*, 44, 2017–2023.

Opsahl, S., Benner, R., 1997. Distribution and cycling of terrigenous dissolved organic matter in them ocean. *Nature*, 386 (3), 480–482.

Orellana, M. V., Pang, W. L., Durand, P. M., Whitehead, K., Baliga, N. S., 2013. A role for programmed cell death in the microbial loop. *PLoS One*, 8 (e62595), doi: 10.1371/journal.pone.0062595.

Orellana, M. V., Hansell, D. A., 2012. Ribulose-1,5-bisphosphate carboxylase/ oxygenase (RuBisCO): A long-lived protein in the deep ocean, *Limnol. Oceanogr.,* 57(3), 826–834.

Oren, A., Gunde-Cimerman, N., 2007. Mycosporines and mycosporine-like amino acids: UV protectants or multipurpose secondary metabolites?, *FEMS Microbiol. Lett.,* 269, 1–10.

Orsi, H., Whitworth, T., Jr, W. D. N., 1995. On the meridional extent and fronts of the Antarctic Circumpolar Current. *Deep-Sea Res.*, 42, 641–673.

Ortega-Retuerta, E., Siegel, D. A., Nelson, N. B., Duarte, C. M., Reche, I., 2010. Observations of chromophoric dissolved and detrital organic matter distribution using remote sensing in the Southern Ocean: validation, dynamics and regulation. *J. Marine Syst. 82,* 295-303.

Ortega-Retuerta, E., Frazer, T. K., Duarte, C. M., Ruiz-Halpern, S., Tovar-Sánchez, A., Arrieta, J. M., Reche, I., 2009. Biogeneration of chromophoric dissolved organic matter by bacteria and krill in the Southern Ocean. *Limnol. Oceanogr.,* 54, 1941–1950.

Osterholz, H., Niggemann, J., Giebel, H-A., Simon, M., Dittmar, T., 2015. Inefficient microbial production of refractory dissolved organic matter in the ocean. *Nat. Comms.*, 6, 7422, doi 10.1038/ncomms8422.

Pereira, D.A. Giani, A., 2014. Cell density-dependent oligopeptide production in cyanobacterial strains. *FEMS Microbiol Ecol* 88: 175–183.

Pérez-Hernández, M. D., Nuez de la Fuente, M., Vélez Belchi, P., Benitez Barrios, V. M., López Laatzen, F., Fraile Nuez, E., 2012. Análisis de muestras de salinidad. Salinómetro de laboratorio Autosal 8400B. Expedición de circunnavegación Malaspina 2010: Cambio global y exploración de la biodiversidad del océano. In *Libro blanco de métodos y técnicas de trabajo oceanográfico*. E. Moreno-Ostos. Madrid, CSIC, 67–76.

Piola, A. R., Gordon, A.L., 1989. Intermediate waters in the southwest South Atlantic, *Deep-Sea Res. A*, 36, 1–16.

Pollard, R.T., and S. PU. 1985. Structure and circulation of the upper Atlantic Ocean northeast of the Azores. *Prog. Oceanogr.*, 14, 443–462.

Pomeroy P. J., Williams, I., Azam, F., Hobbie, J. E., 2007. The microbial loop. *Oceanography*, 20, 28–33.

Prather, M. J., Holmes, C. D., Hsu, J., 2012. Reactive greenhouse gas scenarios: Systematic exploration of uncertainties and the role of atmospheric chemistry. *Geophysical Research Letters*, 39, L09803, doi:10.1029/2012GL051440.

Qiu, B., 2002. The Kuroshio Extension system: Its large-scale variability and role in the mid latitude ocean-atmosphere interaction. *J. Oceanogr.*, 58, 57–75.

R Development Core Team., 2014. R: A language and environment for statistical computing. In: R Foundation for Statistical Computing, Vienna, Austria. ISBN 3-900051-07-0, http://R-project.org.

Raven, J. A., Falkowski, P.G., 1999. Oceanic sinks for atmospheric CO_2. *Plant Cell Environ*. 22, 741–755.

Reche, I., Pulido-Villena, E., Conde-Porcuna, J. M., Carrillo, P., 2001. Photoreactivity of dissolved organic matter from high-mountain lakes of Sierra Nevada, Spain. *Arctic Antarctic and Alpine Research*, 33: 426–

434.

Reid, J. L., 1989. On the total geostrophic circulation of the South Atlantic Ocean flow patterns, tracers, and transports, *Prog. Oceanogr.*, 23, 149–244.

Repeta, D.J, 2015. Chemical Characterization and Cycling of Dissolved Organic Matter. In *Biogeochemistry of Marine Dissolved Organic Matter* (Second Edition), eds Hansell, D. A., Carlson, C. A., Academic Press, Boston, 22–58.

Repeta, D. J., Hartman, N. T., John, S., Jones, A. D., Goericke, R., 2004. Structure Elucidation and Characterization of Polychlorinated Biphenyl Carboxylic Acids as Major Constituents of Chromophoric Dissolved Organic Matter in Seawater. *Environ. Sci. Technol.*, 38, 5373–5378.

Ridgwell, A., Arndt, S., 2015. Why Dissolved Organics Matter: DOC in Ancient Oceans and Past Climate Change. In *Biogeochemistry of Marine Dissolved Organic Matter* (Second Edition), eds Hansell, D. A., Carlson, C. A., Academic Press, Boston, pp 1–18.

Rinnan, A., Andersen, C. M., 2005. Handling of first-order Rayleigh scatter in PARAFAC modeling of fluorescence excitation-emission data. *Chemom. Intel. Lab. Syst.*, 76, 91–99.

Ríos, A. F., Pérez, F. F., Fraga, F., 1992. Water masses in the upper and middle North Atlantic Ocean east of the Azores. Deep Sea Research Part A. *Oceanographic Research Papers*, 39(3-4), 645–658.

Roemmich, D., Bruce, A. N. O., 1992. The Subtropical Mode Waters of the South Pacific Ocean. *J. Phys. Oceanogr.*, 22, 1178–1187.

Romera-Castillo, C., Sarmento, H., M., Álvarez-Salgado, X. A., Gasol, J. M., Marrasé, C., 2011a. Net Production and Consumption of Fluorescent Colored Dissolved Organic Matter by Natural Bacterial Assemblages Growing on Marine Phytoplankton Exudates. *Applied and Environmental Microbiology*, pp. 7490-7498, doi:10.1128/AEM.00200-11.

Romera-Castillo, C., Nieto-Cid, M., Castro, C. Marrasé, C.G., Largier, J., Barton, E.D., Álvarez-Salgado, X.A., 2011b. Fluorescence: Absorption coefficient ratio — Tracing photochemical and microbial degradation processes affecting coloured dissolved organic matter in a coastal system. *Mar. Chem., 125*, 26-38.

Romera-Castillo, C., Sarmento, H., Álvarez-Salgado, X.A., Gasol, J.M., Marrasé, C., 2010. Production of chromophoric dissolved organic matter by marine phytoplankton. *Limnol. Oceanogr.*, 55 (1), 446-454.

Röttgers, R., Koch, B.P., 2012. Spectroscopic detection of a ubiquitous dissolved pigment degradation product in subsurface waters of the global ocean, *Biogeosciences,* 9, 2585–2596.

Röttgers. R., Doerffer, R., 2007. Measurements of optical absorption by chromophoric dissolved organic matter using a point-source integrating-cavity absorption meter. *Limnol. Oceanogr. Method.*, 5, 126–135.

Rozema, J., et al., 2002. The role of UV-B radiation in aquatic and terrestrial ecosystems – an experimental and functional analysis of the evolution of UV-absorbing compounds, *J. Photochem. Photobiol. B: Biology*, 66, 2–12.

Sallée, J.-B., Wienders, N., Speer, K., Morrow, R., 2006. Formation of subantarctic mode water in the southeastern Indian Ocean. *Ocean Dynamics*, 56(5-6), 525–542.

Santos, S. M. P., Otero, M., Duarte, R. M. B. O., Duarte, A. C., 2009. Spectroscopic characterization of dissolved organic matter isolated from rainwater. *Chemosphere*, 74, 1053–1061.

Sarmiento, J. L., Gruber, N., 2006. Ocean biogeochemical dynamics. Princeton university press, Princeton.

Sarmiento, J.L., Gruber, N., 2002. Sinks for anthropogenic carbon. *Physics Today*, 55(8), pp. 30–36.

Sarmiento, J., Thiele, G., Key, R., Moore, W., 1990. Oxygen and nitrate new production and remineralization in the North Atlantic subtropical gyre, *J. Geophys. Res., 95*, http://dx.doi.org/10.1029/90JC01049.

Seiki, T., Date, E., Izawa, H., 1991. Decomposition characteristics of particulate organic matter in Hiroshima Bay, *J. Oceangr., 47*, 207–220.

Senesi, N., Miano, T. M., Provenzano, M. R., Brunetti, G., 1989. Spectroscopic and compositional comparative characterization of IHSS reference and standard fulvic and humic acids of various origin. *Sci. Total Environ.,* 81/82, 143–156.

Sexton, P. F., Norris, R. D., Wilson, P. A., Pälike, H., Westerhold, T., Röhl, U., Bolton, C. T., Gibbs, S., 2011. Eocene global warming events driven by ventilation of oceanic dissolved organic carbon. *Nature*, 471, 349–352.

Shick, J.M., Dunlap, W.C., 2002. Mycosporine like amino acids and related gadusols: Biosynthesis, accumulation, and UV-protective functions in aquatic organisms, *Ann. Rev. of Physiology,* 64, 223–262.

Siegel, D.A., Maritorena, S., Nelson, N. B., Behrenfeld, M. J., McClain, C. R., 2005. Colored dissolved organic matter and its influence on the satellite-based characterization of the ocean biosphere, *Geophys. Res. Lett., 32*, L20605.

Siegel, D. A., Maritorena, S, Nelson, N. B., Hansell, D. A., Lorenzi-Kayser, M., 2002. Global distribution and dynamics of colored dissolved and detrital organic materials. *J. Geophys. Res.*, 107, 3228.

Siegel, D. A., Michaels, A. F., Sorensen, J. C., O'Brien M., Hammer, M. A. 1995. Seasonal variability of light availability and utilization in the Sargasso Sea. J. Geophys. Res., 100, 8675–8713.

Singh, N., Abiven, S., Torn, M. S., Schmidt, M. W. I., 2012. Fire-derived organic carbon in soil turns over on a centennial scale. *Biogeosciences*, 9(8), 2847–25857.

Sipler, R. E., Bronk, D. A., 2015. Dynamics of Dissolved Organic Nitrogen. In *Biogeochemistry of Marine Dissolved Organic Matter* (Second Edition), eds Hansell, D. A., Carlson, C.A., Academic Press, Boston, pp 234–291.

Six, K. D., Maier-Reimer, E., 1996. Effects of plankton dynamics on seasonal carbon fluxes in an ocean general circulation model, *Global Biogeochem. Cycles, 10*, 559-583.

Sokal, F. F., Rohlf, F. J., 1995. *Biometry: the principles and practice of statistics in biological research*, 3rd edition, edited by W. H. Freeman and Co., New York, 937 pp.

Sonnerup, R. E, 2001. On the relations among CFC derived water mass ages, *Geophys. Res. Lett.*, 28, 9, 1739-1742.

Speer, K. G., McCartney, M.S., 1992. Bottom water circulation in the western North Atlantic. *J. Phys. Oceanogr.*, 22, 83-92.

Spencer, R. G. M., Pellerin, B. A., Bergamaschi, B. A., 2007. Diurnal variability in riverine dissolved organic matter composition determined by in situ optical measurement in the San Joaquin River (California, USA). *Hydrol. Process.,* 21, 3181–3189.

Stedmon, C. A., Nelson, N. B., 2015. The Optical Properties of DOM in the Ocean. In *Biogeochemistry of Marine Dissolved Organic Matter* (Second Edition), eds Hansell, D.A., Carlson, C.A., Academic Press, Boston, pp 481–508.

Stedmon, C. A., Álvarez-Salgado, X. A., 2011. Shedding Light on a Black Box: UV-Visible Spectroscopic Characterization of Marine Dissolved Organic Matter. In *Microbial Carbon Pump in the Ocean*, eds Jiao, N., Azam, F., Sean, S., Science/AAAS, pp. 62–63, DOI: 10.1126/science.opms.sb0001.

Stedmon, C. A., Bro, R., 2008. Characterizing dissolved organic matter fluorescence with parallel factor analysis: a tutorial. *Limnol. Oceanogr. Methods*, 6, 572–579.

Stedmon, C.A., Markager, S., 2005a. Resolving the variability in dissolved organic matter fluorescence in a temperate estuary and its catchment using PARAFAC analysis. *Limnol. Oceanogr.*, 50 (5), 686–697.

Stedmon, C.A., Markager, S., 2005b. Tracing the production and degradation of autochthonous fractions of dissolved organic matter by fluorescence analysis. *Limnol. Oceanogr.*, 50 (5), 1415–1426.

Stedmon, C. A., Markager, S., Bro, R., 2003a. Tracing dissolved organic matter in aquatic environments using a new approach to fluorescence spectroscopy. *Mar. Chem.*, 82, 239–254.

Stedmon, C. A., Markager, S., 2003b. Behaviour of the optical properties of coloured dissolved organic matter under conservative mixing. *Estuarine, Coastal and Shelf Science*, 57, 973–979.

Steinberg, D. K., Nelson, N. B., Carlson, C. A., and Prusak, A. C., 2004. Production of chromophoric dissolved organic matter (CDOM) in the open ocean by zooplankton and the colonial cyanobacterium Trichodesmium spp. *Mar. Ecol. Progr. Ser.*, 267: 45–56.

Stramski, D., Kiefer, D.A., 1998. Can heterotrophic bacteria be important to marine light absorption?, *J. Plankton Res.,* 20, 1489–1500.

Stubbins, A., et al., 2014. What's in an EEM? Molecular Signatures Associated with Dissolved Organic Fluorescence in Boreal Canada. *Environ. Sci. Technol.*, 48, 10598–10606.

Stubbins, A., Niggemann, J., Dittmar, T., 2012. Photo-lability of deep ocean dissolved black carbon. *Biogeosciences*, 9, 1661–1670.

Stubbins, A., Uher, G., Law, C. S., Mopper, K., Robinson, C., Upstill-Goddard, R. C., 2006. Open-ocean carbon monoxide photoproduction. *Deep Sea Res. Part II*, 53 (14–16), 1695–1705.

Suga, T., Takei, Y., & Hanawa, K., 1997. Thermostad Distribution in the North Pacific Subtropical Gyre: The Central Mode Water and the Subtropical Mode Water. *J. Phys. Oceanogr.*, 27, 140–152.

Suttle, C. A., 2007. Marine viruses – major players in the global ecosystem. *Nature Reviews Microbiology*, 5, 801–812.

Stuiver, M., Quay, P.D., Ostlund, H.G., 1983. Abyssal Water Carbon-14 distribution and the Age of the World Oceans, *Science, 219*(4586), 849-851.

Swan, C.M., Nelson, N.B., Siegel, D.A., Kostadinov, T.S., 2012. The effect of surface irradiance on the absorption spectrum of chromophoric dissolved organic matter in the global ocean, *Deep-Sea Res. I,* 63, 52–64.

Takahashi, T. et al., 2009. Climatological mean and decadal change in surface ocean pCO_2, and net sea-air CO_2 flux over the global oceans. *Deep Sea Res. Part II*, 56(8-10), 554–577.

Talley L. D., 1996. Antarctic Intermediate Water in the South Atlantic. In *The South Atlantic Present and Past Circulation*, Eds. Wefer et al., Springer Verlag, 219–238.

Tanaka, K., Kuma, K., Hamasaki, K., Yamashita, Y., 2014. Accumulation of humic-like fluorescent dissolved organic matter in the Japan Sea. *Scientific Reports*, 4, 5292, DOI: 10.1038/srep05292.

Tani, H., Nishioka, J., Kuma, K., Takata, H., Yamashita, Y., Tanoue, E., Midorikaw, T., 2003. Iron(III) hydroxide solubility and humic-type fluorescent organic matter in the deep water column of the Okhotsk Sea and the northwestern North Pacific Ocean. *Deep Sea Res. Part I*, 50, 1063–1078.

Tedetti, M., Charriére, B., Bricaud, A., Para, J., Raimbault, P., Sempére, R., 2010. Distribution of normalized water-leaving radiances at UV and visible wave bands in relation with chlorophyll a and colored detrital matter content in the southeast Pacific. *J. Geophys. Res.*, 115, C02010. http://dx.doi.org/10.1029/2009JC005289.

Timko, S. A., Maydanov, A., Pittelli, S. L., Conte, M. H., Cooper, W. J., Koch, B. P., Schmitt-Kopplin, P., Gonsior, M., 2015. Depth-dependent photodegradation of marine dissolved organic matter. *Frontiers in Marine Science*, 2, 66, doi: 10.3389/fmars.2015.00066.

Tomczak, M., Liefrink, S., 2005. Interannual variations of water mass volumes in the Southern Ocean. *Journal of Atmospheric and Ocean Science*, 10(1), 31–42.

Tomczak, M., Godfrey, J.S., 2003. Regional Oceanography: an Introduction 2nd edn.

Tomczak, M., 1999. Some historical, theoretical and applied aspects of quantitative water mass analysis, *J. Mar. Res., 57*, 275-303.

Torres-Valdés, S., Roussenov, V. M., Sanders, R., Reynolds, S., Pan, X., Mather, R., Landolfi, A., Wolff, G. A., Achterberg, E. P., Williams, R. G., 2009. Distribution of dissolved organic nutrients and their effect on export production over the Atlantic Ocean. *Global Biogeochem. Cycles*, 23, GB4019, doi:10.1029/2008GB003389.

Tsuchiya, M., 1986. Thermostads and circulation in the upper layer of the Atlantic Ocean, *Progr. Oceanogr.*, 16 (4), pp. 235–267.

Tsubouchi, T., Suga, T., Hanawa, K., 2009. Indian Ocean subtropical mode water: its water characteristics and spatial distribution. *Ocean Science Discussions*, 6(1), 723–739.

Twardowski, M. S., Boss, E., Sullivan, J. M., Donaghay, P. L., 2004. Modeling the spectral shape of absorption by chromophoric dissolved organic matter. *Mar. Chem.* 89, 69–88.

Tzortziou, M., Neale, P. J., Megonigal, J. P., Pow, C. L., Butterworth, M., 2011. Spatial gradients in dissolved carbon due to tidal marsh outwelling into a Chesapeake Bay estuary. *Mar. Ecol. Prog. Ser.*, 426, 41–56.

Urban-Rich, J., Fernández, D., Acuña, J. L., 2006. Grazing impact on chromophoric dissolved organic matter (CDOM) by the larvacean Oikopleura dioica. *Mar. Ecol. Prog. Ser., 317*, 101-110.

Verdugo, 2012. Marine Microgels. *Annu. Rev. Mar. Sci.*, 4, 375–400.

Verdugo, P., Alldredge, A. L., Azam, F., Kirchman, D. L., Passow, U., Santschi, P. H., 2004. The oceanic gel phase: a bridge in the DOM-POM continuum. *Mar. Chem.*, 92, 67–85.

Vetter, E. M., Perdue, E., Ingall, E., Koprivnjak, J. -F., Pfromm, P. H., 2007. Combining reverse osmosis and electrodialysis for more complete recovery of dissolved organic matter from seawater. *Separation and Purification Technology*, 56, 383–387.

Wang, Y., Zhang, D., Shen, Z., Chen, J., Feng, C., 2014. Characterization and spatial distribution variability of chromophoric dissolved organic matter (CDOM) in the Yangtze Estuary. *Chemosphere*, 95, 353–362.

Weber, G., 1961.Enumeration of components in complex systems by fluorescence spectrophotometry. *Nature*, 90(4770), 27–29.

Wedborg, M., Hoppema, M., Skoog, A., 1998. On the relation between organic and inorganic carbon in the Weddell Sea. *J. Mar. Syst.,* 17, 59–76.

Weinbauer, M. G., Chen, F., Wihelm, S. W., 2011. Virus·mediated redistribution and partitioning of carbon in the global oceans. In *Microbial Carbon Pump in the Ocean*, eds Jiao, N., Azam, F., Sanders, S. Science Booklet, Supplement to Science, pp 54–56.

Weishaar, J. L., Aiken, G. R., Bergamaschi, B. A., Fram, M. S., Fugii, R., Mopper, K., 2003. Evaluation of specific ultraviolet absorbance as an indicator of the chemical composition and reactivity of dissolved organic carbon, *Environ. Sci. Technol.*, 37, 4702·4708.

Wood, S., 2006. Generalized Additive Models: An Introduction with R. Chapman & Hall, London.

Wüst, G., 1935. Schichtung und Zirkulation des Atlantischen Ozeans, Die Stratosphäre. Wissenschaftliche Ergebnisse der Deutschen Atlantischen Expedition auf dem Forschungsund Vermessungsschiff “Meteor” 1925–1927. 6, 180pp. English translation edited by W.J. Emery, The stratosphere of the Atlantic Ocean. Scientific Results of the German Atlantic Expedition of the Research Vessel ‘Meteor’ 1925–27. Amerind Publishing Co., 1978.

Yamashita. Y., Lu, C.·J., Ogawa, H., Nishioka, J., Obata, H., Saito, H. Application of an in situ fluorometer to determine the distribution of fluorescent organic matter in the open ocean. *Mar. Chem.*, *in press*., http://dx.doi.org/10.1016/j.marchem.2015.06.025.

Yamashita, Y., Boyer, J. N., Jaffé, R., 2013. Evaluating the distribution of terrestrial dissolved organic matter in a complex coastal ecosystem using fluorescence spectroscopy. *Continental Shelf Research*, 66, 136–144.

Yamashita, Y., Cory, R.M., Nishioka, J., Kuma, K., Tanoue, E., Jaffé, R., 2010. Fluorescence characteristics of dissolved organic matter in the deep waters of the Okhotsk Sea and the northwestern North Pacific Ocean. *Deep-Sea Res. Part II*, 57, 1478–1485.

Yamashita, Y., Tanoue, E., 2009. Basin scale distribution of chromophoric dissolved organic matter in the Pacific Ocean, *Limnol. Oceanogr., 54*, 598·609.

Yamashita, Y., Tanoue, E., 2008. Production of bio·refractory fluorescent dissolved organic matter in the ocean interior, *Nature, 1*, 579·582.

Yamashita, Y., Jaffé, R., Maie, N., Tanoue, E., 2008. Assessing the dynamics of dissolved organic matter (DOM) in coastal environments by excitation and emission matrix fluorescence and parallel factor analysis (EEM·PARAFAC). *Limnol. and Oceanogr.*, 53, 1900–1908.

Yamashita, Y., Tsujasaki, A., Nishida, T., Tanoue, E., 2007. Vertical and horizontal distribution of fluorescent dissolved organic matter in the Southern Ocean. *Mar. Chem.*, 106, 498–509.

Yamashita, Y., Tanoue, E., 2003a. Chemical characterization of protein·like fluorophores in DOM in relation to aromatic amino acids. *Mar. Chem.*, 82, 255–271.

Yamashita, Y., Tanoue, E., 2003b. Distribution and alteration of amino acids in bulk DOM along a transect from bay to oceanic waters. *Mar. Chem.*, 82, 145–160.

Yoshikawa, S., Muramoto, K., Shinzawa·Itoh, K., 2011. Proton·Pumping Mechanism of Cytochrome c Oxidase, *Annu. Rev. Biophys.,* 40, 205–223.

Zenk, W. 1975. On the Mediterranean outflow west of Gibraltar. *Meteor. Forsch.·Ergebnisse A,* 16, 23–24.

Zohary, T. et al., 2005. P·limited bacteria but N and P co·limited phytoplankton in the Eastern Mediterranean—a microcosm experiment. *Deep-Sea Res.Pt. II*, 52, 3011–3023.